PHASE AND RHEOLOGICAL BEHAVIOR OF LANGMUIR FILMS AT THE AIR/WATER INTERFACE: POLYHEDERAL OLIGOMERIC SILSESQUIOXANES (POSS), POSS/POLYMER BLENDS, AND MAGNETIC NANOPARTICLES

Wen Yin

Dissertation submitted to the faculty of the
Virginia Polytechnic Institute and State University
in partial fulfillment of the requirements for the degree of

Doctor of Philosophy
in
CHEMISTRY

Alan R. Esker, Chair

Diego Troya

Harry C. Dorn

John R. Morris

Judy S. Riffle

May 13, 2009

Blacksburg, Virginia

Keywords: Langmuir monolayers, surface light scattering, polyhedral oligomeric silsesquioxanes (POSS), polydimethylsiloxane (PDMS)

PHASE AND RHEOLOGICAL BEHAVIOR OF LANGMUIR FILMS AT THE AIR/WATER INTERFACE: POLYHEDERAL OLIGOMERIC SILSESQUIOXANES (POSS), POSS/POLYMER BLENDS, AND MAGNETIC NANOPARTICLES

Wen Yin

(Abstract)

For over a century, Langmuir films have served as excellent two-dimensional model systems for studying the conformation and ordering of amphiphilic molecules at the air/water (A/W) interface. With the equipment of Wilhelmy plate technique, Brewster angle microscopy (BAM), and surface light scattering (SLS), the interfacial phase and rheological behavior of Langmuir films can be investigated. In this dissertation, these techniques are employed to examine Langmuir films of polyhedral oligomeric silsesquioxane (POSS), polymer blends, and magnetic nanoparticles (MNPs).

In a first time, SLS is employed to study POSS molecules. The interfacial rheological properties of trisilanolisobutyl-POSS (TiBuP) indicate that TiBuP forms a viscoelastic Langmuir film that is almost perfectly elastic in the monolayer state with a maximum $\varepsilon_d \sim 50$ mN·m^{-1} prior to film collapse. This result suggests that TiBuP can serve as model nanofiller with polymers.

As an interesting next step, blends of TiBuP and polydimethylsiloxane (PDMS) with different compositions are examined via surface pressure (Π) – surface area occupied per molecule (A) isotherms and SLS. The results show that TiBuP, with its attendant water, serves as a plasticizer and lowers the dilational modulus of the films at

low Π. As Π increases, composition dependent behavior occurs. Around the collapse pressure of PDMS, the TiBuP component is able to form networks at the A/W interface as PDMS collapse into the upper layer. Blends of non-amphiphilic octaisobutyl-POSS (OiBuP) and PDMS are also studied as an interesting comparison to TiBuP/PDMS blends. In these blends, OiBuP serves as a filler and reinforces the blends prior to the collapse of PDMS by forming "bridge" structure on top of PDMS monolayer. However, OiBuP is non-amphiphilic and fails to anchor PDMS chains to the A/W interface. Hence, OiBuP/PDMS blends exhibit negligible dilational viscoelasticity after the collapse of PDMS.

Furthermore, the phase behavior of PDMS blended with a trisilanol-POSS derivative containing different substituents, trisilanolcyclopentyl-POSS (TCpP), is also investigated via the Wilhelmy plate technique and BAM. These TCpP/PDMS blends exhibit dramatically different phase behavior and morphological features from previously studied POSS/PDMS blends, showing that the organic substituents on trisilanol-POSS have considerable impact on the phase behavior of POSS/PDMS blends.

The interfacial rheological behavior of tricarboxylic acid terminated PDMS (PDMS-Stabilizer) and PDMS stabilized MNPs are investigated and compared with "regular" PDMS containing non-polar end groups. The tricarboxylic acid end group of the PDMS-Stabilizer leads to a different collapse mechanism. The PDMS stabilized MNPs exhibit viscoelastic behavior that is similar to PDMS showing all the tricarboxylic acid end groups are bound to the magnetite cores.

Studying the interfacial behavior of different Langmuir films at the A/W interface provides us insight into the impact of molecule-molecule and molecule-subphase

interactions on film morphology and rheology. These results are able to serve as important guides for designing surface films with preferred morphological and mechanical properties.

Acknowledgements

There are many people who helped me during my study at Virginia Tech. First I need to thank my advisor, Dr Alan R. Esker, for offering the opportunity to work in his group. I want to thank Alan for encouraging me and being patient for the last five years. Even beyond mentoring me on laboratory scientific research, Alan does a great job of keeping a coherent group and teaching us the language and culture which is a tremendous benefit for an international student. I would like to thank my committee members, Profs. Diego Troya, John R. Morris, Harry C. Dorn, and Judy S. Riffle for their valuable discussion and comments on my Ph. D. work,

I would like to thank my many colleagues, Jianjun Deng, Suolong Ni, Bingbing Li, Ritu Paul, Woojin Lee, Abdulaziz Kaya, Zelin Liu, Qiongdan Xie, Yang Liu, Sheila Gradwell, Hyong-Jun Kim, Sarah Huffer, Michael Swift, Jae Hyun Sim, Xiaosong Du, Chuanzi OuYang. Thanks to all of you for your help during all these years.

I need to give special thanks to my wife, Wenyan Wang, for being in my life and supporting me all the time. Without her love, I could never finish this work. I also need to thank my parents, Feisheng Yin and Lishan Tong, for always being there and giving me valuable advice.

Table of Contents

List of Figures

Chapter 2

Chapter 3

Chapter 4

Chapter 5

Chapter 6

Chapter 7

Chapter 8

Chapter 9

List of Tables

Chapter 5

CHAPTER 1

Overview

Ever since Langmuir published his studies on monolayers of amphiphilic molecules on the surface of water, the air/water (A/W) interface has become an exciting place for surface scientists to explore the interfacial behavior of numerous amphiphilic molecules.[1-6] In addition to fundamental surface pressure (Π) – area occupied per molecule (monomer) (A) measurements, many other techniques have been developed to probe the morphology, thickness, and rheological properties of these Langmuir films. Hence, equipped with these characterization methods, Langmuir films serve as complete two dimensional (2D) analogues for bulk systems where various physical phenomena including phase transitions, phase separation, crystallization, and nucleation can be studied. Furthermore, Langmuir films serve as excellent 2D model system to examine and understand the dispersion and reinforcement effect of nanofillers within polymeric thin film. In this dissertation, the interfacial phase and rheological behavior of polyhederal oligomeric silsesquioxanes (POSS), POSS/polymer blends, and magnetic nanoparticles (MNPs) are investigated via Π – A isotherms, Brewster angle microscopy (BAM), and surface light scattering (SLS). The possible conformation and ordering of molecules at the A/W interface are also discussed.

Chapter 2 provides the overall introduction and literature review. This chapter starts with a general introduction of the formation of Langmuir films, their history, their phase and rheological behavior and available theoretical approaches. Several techniques

including the Wilhelmy technique, Brewster angle microscopy (BAM), and surface light scattering (SLS) are introduced. The thermodynamics of polymer blends are also summarized in this chapter. Furthermore, the synthesis, application, and interfacial behavior of the model nanofiller, polyhedral oligomeric silsesquioxanes (POSS), are reviewed.

In Chapter 3, the materials and experimental techniques that are used in this dissertation are introduced. This information will not be repeated in the individual research chapters.

In Chapter 4, SLS is used to probe the dilational viscoelastic behavior of trisilanolisobutyl-POSS (TiBuP) in the monolayer regime. The static dilational elastic modulus is in excellent agreement with the dynamic dilational elastic modulus in the monolayer regime. The films possess a moderate maximum dynamic dilational elastic modulus (~ 50 $mN \cdot m^{-1}$) prior to film collapse. Moreover, the films exhibited small surface viscosities such that the films are almost purely elastic over the frequency range studied throughout the monolayer regime. From the study provided in Chapter 4, TiBuP is expected to be excellent model nanofiller for Langmuir film systems.

As an extension of Chapter 4, the interfacial phase and rheological behavior of TiBuP/polydimethylsiloxane (PDMS) blends with different wt% TiBuP are examined via Π – <A> isotherms and SLS at the A/W interface in Chapter 5. Single-component PDMS forms Langmuir films at the A/W interface that can be characterized by four regimes: (A) submonolayer (surface pressure $\Pi = 0$ $mN \cdot m^{-1}$), (B) monolayer ($0 < \Pi < 8$ $mN \cdot m^{-1}$), (C) a monolayer to bilayer transition ($\Pi \sim 8$ $mN \cdot m^{-1}$), and (D) multilayer ($\Pi \sim 9$ $mN \cdot m^{-1}$). For all blends, at low Π ($\Pi < 2.5$ $mN \cdot m^{-1}$) in the monolayer regime, TiBuP, with its attendant

water, serves as a plasticizer and lowers the dilational modulus of the films. At higher Π ($2.5 < \Pi < 5$ mN·m^{-1}) in the monolayer regime, ε_d for the blends is comparable to single-component PDMS. For $\Pi > 5$ mN·m^{-1}, composition dependent reinforcement of the blends occurs. The Π where reinforcement occurs decreases as the wt% TiBuP increases and may correlate with the surface fraction of TiBuP (Φ_{TiBuP}) in the layer directly in contact with water. As Φ_{TiBuP} increases, the modulus of the collapsed PDMS film increases.

In Chapter 6, PDMS blended with non-amphiphilic OiBuP is studied by Π – <A> isotherms and SLS at the A/W interface as a comparison to TiBuP/PDMS blends. Unlike TiBuP/PDMS blends, OiBuP starts to reinforce the blend thin films in the PDMS monolayer regime, likely by forming networks on top of the PDMS monolayer. However, the blend films exhibit no viscoelastic modulus after the collapse of the PDMS component because OiBuP is not surface active and cannot anchor PDMS to the A/W interface.

In Chapter 7, a trisilanol-POSS with different substituents, trisilanolcyclopentyl-POSS (TCpP), is used as a model nanofiller to blend with PDMS. The TCpP/PDMS blends are then studied via Π – <A> isotherms and BAM at the A/W interface. Compared with TiBuP/PDMS and OiBuP/PDMS blends, TCpP/PDMS blends exhibit dramatically different composition dependent phase behavior. Low wt% TCpP blends (wt% TCpP < 20) and high wt% TCpP blends (wt% TCpP > 60) exhibit phase behavior that are similar to single-component PDMS or TCpP, respectively. Blends with 20 to 60 wt% TCpP show complex phase behavior. They exhibit transitions at Π values lower than the

collapse pressures for either PDMS or TCpP, which give rise to morphological features that are similar to phase separation. All blends with 20 to 60 wt% TCpP show a kink around $\Pi \sim 13$ mN·m^{-1}. Furthermore, TCpP in blends with greater than 60 wt% TCpP form small aggregates instead of large bright aggregates observed for single-component TCpP films. These observations show that the organic substituents on trisilanol-POSS have considerable impact on the phase behavior of POSS/PDMS blend systems.

Magnetic nanoparticles (MNPs) have many potential applications in biomedical fields. Hence the interfacial properties of these MNPs at the A/W interface are of great importance as the human body is water rich. In Chapter 8, the interfacial properties of polar group terminated PDMS stabilizer and PDMS stabilized MNPs are examined via Π – A isotherms and SLS. The results are then compared with "regular" PDMS (contains non-polar end groups). It was clearly shown that the end group of amphiphilic polymers alters molecule-subphase interactions and thereby changes the interfacial phase and rheological behavior of the PDMS stabilizer. With the polar tricarboxylic acid end groups, PDMS stabilizer is capable of standing on its end during compression. As a consequence, it does not exhibit the classical PDMS monolayer to bilayer transition. In contrast, the PDMS-MNPs exhibit similar phase and rheological behavior with PDMS up to the collapsed regime once the carboxylic acid end groups are bound to the surface of the magnetite cores.

Chapter 9 summarizes the overall conclusions and provides suggestions for future work in two directions: 1) The interfacial cross-linking of PDMS/POSS blends can provide an approach to lock in the interfacial morphology of polymer blends. SLS can be used to monitor the cross-linking process by probing the dilational interfacial rheology of

the surface films. After the surface films are cross-linked, Langmuir-Schaefer (LS) or Langmuir-Blodgett (LB) transfer onto solid substrate would be possible for further characterization by atomic force microscopy (AFM) or scanning electron microscopy (SEM). This approach would yield greater detail about the film morphology. 2) The ellipsometry study of TCpP/PDMS blends will provide information about the thickness of TCpP/PDMS blends for all regions of the Π - <A> isotherms. These results should provide deeper insight into plausible mechanisms for the interesting morphologies observed in Chapter 7.

CHAPTER 2

Introduction and Review

2.1 Langmuir Films and Langmuir Monolayers

2.1.1 General Introduction for Molecular Films

Molecular films are defined as thin films with thicknesses ranging from several nanometers (one or several layers of molecules) to several hundred nanometers.[1,2,6] There are many types of molecular films arising from different film preparation procedures including spin coating,[7] direct deposition,[8] thermal deposition,[9] electrodeposition,[10] polymer brush tethering,[11] micro-imprinting,[12] laser micro-patterning,[13] self-assembly,[14,15] surface in-situ polymerization,[16] the Langmuir-Blodgett (LB) technique,[6] etc. As these techniques can apply to various of organic and polymeric materials, molecular films have shown promising applications in areas such as sensor materials,[17] electroluminescent devices,[18-20] photovoltaic cells,[21] and data storage materials.[22] Organic thin films can be easily manipulated to alter the surface energy. An example of this comes from the adhesion industry; films with high surface energy can serve as adhesive layers while films with low surface energy can be used as release layers.[23-25] Similarly, by altering the hydrophobicity or hydrophilicity of the thin organic films, a film can be either bio-compatible or bio-inert, thereby attracting increasing interest from biomedical fields.[26]

2.1.2 Terminology: Langmuir Monolayers, Langmuir Films, Gibbs Films and Langmuir-Blodgett Films

Most studies in this dissertation focus on Langmuir films and Langmuir monolayers. Langmuir monolayers, Langmuir films, and Langmuir-Blodgett films are the three most commonly used terms in this thesis. Hence, it is important to define and distinguish between these three related but different concepts.

In general, Langmuir monolayers and Langmuir films are composed of insoluble amphiphilic molecules versus Gibbs films, which are formed by soluble amphiphilic molecules.[1,2,6] A typical Langmuir film is formed at the air/water (A/W) interface with lipid molecules such as fatty acid and phospholipids. These molecules contain two dissimilar parts: long hydrophobic, hydrocarbon tails and hydrophilic heads. To achieve the lowest surface energy at the A/W interface, the hydrophilic head will anchor on the water surface with the hydrophobic portion of the molecule pointing towards the air. Here in this dissertation, Langmuir films refer to a surface film composed of amphiphilic molecules at the A/W interface while Langmuir monolayers refer to Langmuir films where the films are exactly one molecule thick.

Langmuir films have several advantageous features.[3-5] First, water is an excellent "substrate" because it has a very smooth surface (roughness around 3 ~ 5 Å).[27] In this sense, Langmuir film systems at the A/W interface are much simpler than substrates like silica or gold where higher surface roughness and grain boundaries can affect the properties of the organic film.[28] Second, with two controllable thermodynamic variables, temperature (T) and surface area occupied per molecule or monomer (A), Langmuir films serve as excellent model systems for studying ordering of molecules in two-dimensions

(2D). By examining different amphiphilic molecules and subphases (e.g. different subphase pH and ionic strength), numerous intermolecular, intramolecular, and molecule-subphase interactions can be probed at the molecular level.[29-39] Moreover, interactions between the polar head groups and the subphase make Langmuir films an excellent model system for biomedical research owing to the fact that phospholipids bilayers, which comprise the main component of cell membranes, can be regarded as two weakly coupled monolayers.[40] Furthermore, the development of various techniques like Brewster angle microscopy (BAM),[41-43] fluorescence microscopy (FM), ellipsometry,[44,45] grazing incidence X-ray diffraction (GIXD),[46] mechanically generated waves,[47] electrocapillary wave diffraction (ECWD),[48-53] surface light scattering (SLS),[54-57] interfacial stress rheometry (ISR),[11,58,59] and surface pressure relaxation studies[60] enable us to study Langmuir systems as a 2D analog to three dimensional (3D) bulk systems with respect to thermodynamic, kinetic, and mechanical properties.[3]

Langmuir-Blodgett films are molecular films prepared by transferring the Langmuir films from the A/W interface to solid substrates via LB or Langmuir-Schaefer (LS) technique.[1,2,6,61] LB-films can be either a single layer or multilayers. The LB technique is one of the best methods for preparing molecular films in the sense it retains well-ordered internal film structures. Moreover, by transferring monolayer after monolayer, it facilitates the control of thickness and layer structure at the single molecule level.

The studies in this dissertation are primarily focused on the *in-situ* study of physical properties and morphology of Langmuir films at the A/W interface. Sometimes, the LB or LS technique can be used to transfer Langmuir films onto a solid surface so that additional characterization techniques can be used to interrogate the system. However,

before proceeding to these studies, it is beneficial to review the history of Langmuir and Langmuir-Blodgett films.

2.1.3 Historical Background of Langmuir and Langmuir-Blodgett Films

Langmuir monolayers and Langmuir films are not extraordinary phenomena that can only be observed in a laboratory with expensive instruments. Actually, they are very common in everyday life and people have noticed them for thousands of years. The earliest records of spreading oil on water were written on clay tablets around the 18th century BC. By observing the spreading behavior of oil droplets on the water surface, Babylonians predicted success, marriage, birth of a child, recovery from illness, or bad luck, sickness, death, etc.[62] Ancient Greek writings also record that sailors spread oil on a rough sea to insure a smoother surface for their travel and today it is known that this phenomenon is due to a damping effect exerted by the oil layer on the underlying subphase.[63] A paper marbling technique, "suminagashi", actually means "ink-floating" or "ink-streaming". This technique originated in China over 2000 years ago and became popular 800 years later in Japan. In this technique, a protein solution forms a protein monolayer at the A/W interface and the carbon suspension within the protein is later picked up by the paper using a horizontal lifting technique. This is literally the first application of a Langmuir film and is an example of the LS-technique.[64]

In 1774, this spreading behavior of oil on water finally received scientific attention from Benjamin Franklin. In his famous Clapham pond experiment,[65] he observed that the oil films suppressed vibrations at the A/W interface. This experiment stimulated subsequent investigations focusing on the damping effect of oil films on aqueous surfaces.[63] However, it was not until one-hundred years later that Lord Rayleigh finally

realized that the oil film should be exactly one molecule thick, thereby making it possible to calculate the dimension of one molecule by measuring the volume of the oil droplet and the area it occupied at the water surface.[66] Meanwhile, Agnes Pockles set up a rudimentary surface balance in her kitchen and developed an instrument similar to the Langmuir trough we use today with "barriers" compressing the oil films on the water surface. She did a series of systematic studies to characterize the physical properties of different Langmuir films at the A/W interface and published the first surface pressure - area isotherm for stearic acid in Nature.[67]

In the early 1900's, Irving Langmuir designed a number of new devices to monitor the surface pressures of spread monolayers. One such device was later named after him (Langmuir film balance) and is still being used for monolayer research today.[68,69] Moreover, Langmuir used chemically pure substances instead of the natural oils used previously, thereby allowing him to probe the monomolecular nature of the film as well as the orientation of the molecules on the water surface. His work led to a molecular level understanding of the spreading behavior of molecules on aqueous surfaces. Several years later, together with assistance from Langmuir, Katharine Blodgett successfully transferred multiple fatty acid monolayers onto glass substrates. The deposited monolayers on solid substrates are now named as LB-films.[70,71]

2.1.4 Formation of Langmuir Monolayers

As mentioned above, Langmuir monolayers are generally formed from amphiphiles containing polar head groups (hydrophilic group) and long non-polar (hydrophobic) tails. The amphiphiles need to have very low solubility in water in order to remain at the A/W interface. Long-chain fatty acids, alcohols, esters, and phospholipids are typical

Langmuir film forming molecules (Figure 2.1).[72] All of these molecules contain one or several long alkyl chains with at least 12 to 14 carbon atoms (hydrophobic tails) and one or several alcohol or acid polar head groups. The hydrophilic groups will anchor the molecules on the water surface and the long alkyl chains prevent dissolution into the subphase. Additionally, some non-traditional materials like fluoroalkanes can also form Langmuir films. [73,74]

Some amphiphilic polymers can also form Langmuir films at the A/W interface. These include polyethers,[75-78] polyesters,[79,80] polysiloxanes,[81-86] polyacrylates and polymethacrylates,[87-89] etc. Some examples are shown in Figure 2.2. The ordering in polymeric Langmuir films is different from that of small molecules. These differences will be discussed separately from the Langmuir films of small molecules later in this thesis. There are also a larger variety of non-traditional polymeric amphiphiles that also form Langmuir and LB-films. [90-95]

Spreading solvents are frequently required for the formation of Langmuir films at the A/W interface. Some molecules can spread spontaneously from the bulk phase to form monolayers because of their low surface tension. However, most molecules require a spreading solvent to help them spread at the A/W interface. The spreading solvent needs to be volatile and must spread easily to ensure rapid evaporation while simultaneously leaving the dissolved molecules uniformly dispersed on the subphase to form a Langmuir monolayer. The spreading solvent also needs to be a good solvent to ensure that molecules are not aggregated prior to spreading. Some organic solvents like hexane, dichloromethane, and chloroform are typical spreading solvents for Langmuir films.[96]

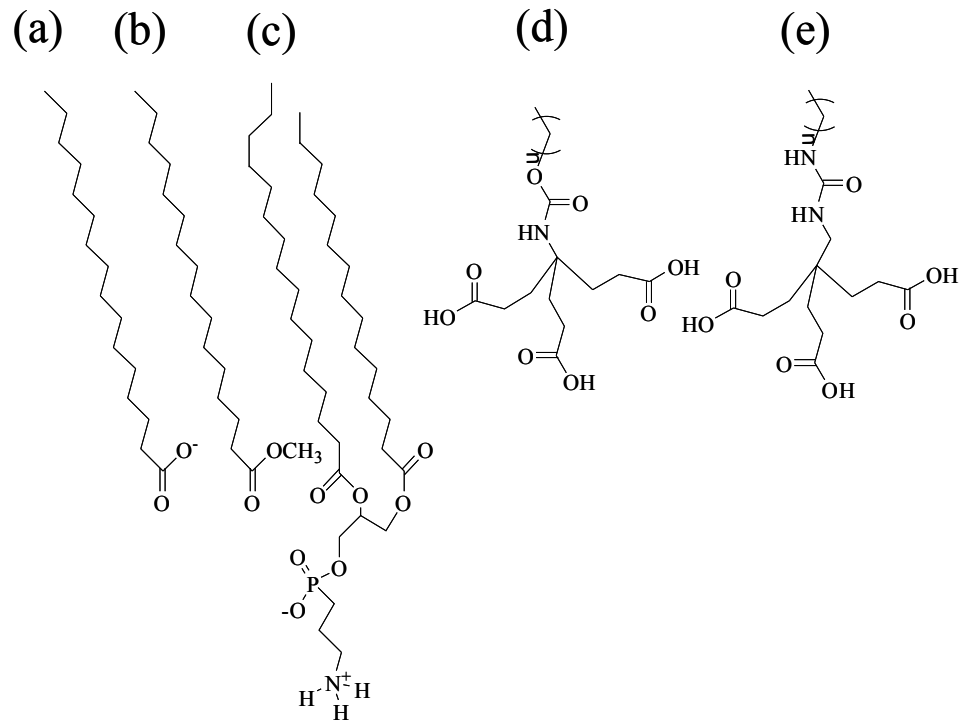

Figure 2.1. Some examples of amphiphilic molecules that can form Langmuir monolayers at the A/W interface: (a) ionized n-hexadecanoic (palmitic) acid, (b) n-hexadecanoic acid methyl ester, and various phospholipids: (c) dipalmitoylphosphatidylethanolamine, (d) tri-headed and carbamate-linked amphiphilic fatty acids (3CCb), and (e) tri-headed and ureido-linked amphiphilic fatty acids (3CUr).

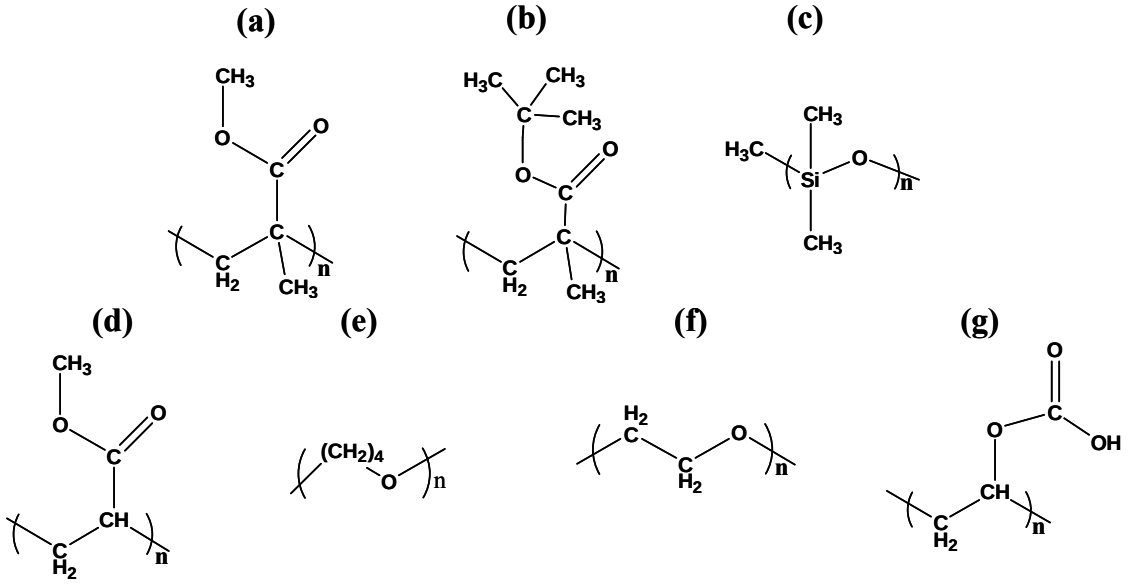

Figure 2.2. Some amphiphilic polymers that can form Langmuir monolayers at the A/W interface: (a) poly(methyl methacrylate) (PMMA), (b) poly(tert-butyl methacrylate) (PtBMA), (c) poly(dimethylsiloxane) (PDMS), (d) poly(methyl acrylate) (PMA), (e) poly(tetrahydrofuran) (PTHF), (f) poly(ethylene oxide) (PEO), and (g) poly(vinyl acetate) (PVAc).

2.2 Surface Pressure (Π) – Surface Area (A) Isotherms

2.2.1 Surface Tension (γ) and Surface Pressure (Π)

Surface tension is one of the most important concepts for surface chemistry at liquid surfaces as it essentially describes the strength of the intermolecular forces. Surface tension is responsible for numerous phenomena we can observe in everyday life including the curvature of liquid surface; the formation of drops when liquids are stretched; the formation of soap bubbles; emulsions, etc. Figure 2.3 depicts the forces exerted upon a volume element by the surrounding liquid in the bulk and at the surface. Unlike the molecules in the bulk, the absence of neighboring liquid molecules in the gas

phase means that undulations in the surface are pulled back to a planar interface because of asymmetric forces. Therefore, all molecules at the liquid surface are subject to a net force that resists an expansion of the interfacial area. This force is along the direction of the surface and is called surface tension (γ) and has units of the force per unit length.

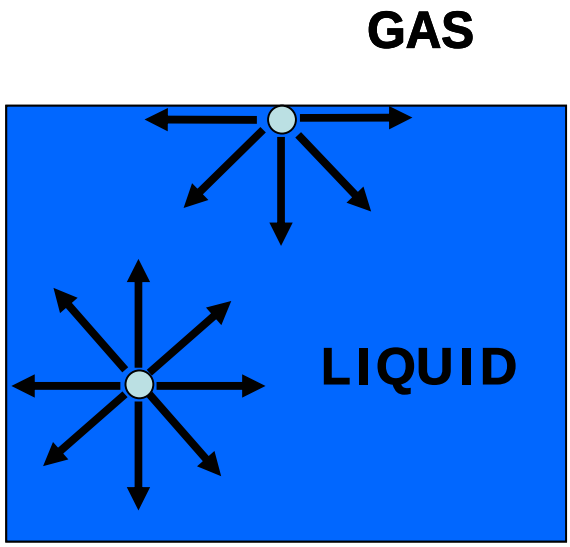

Figure 2.3. Schematic depictions of volume elements of a liquid in bulk and at the surface.

The thermodynamic definition of the surface tension is also available. In any closed system, the Gibbs free energy change for a one phase single-component system can be written as

$$dG = -SdT + VdP \qquad \text{(Eq. 2.1)}$$

where T is temperature, P is pressure, S is entropy and V is volume. For a one phase multi-component system with an interface, dG is represented as

$$dG = -SdT + VdP + \gamma dA_s + \sum_i \mu_i dn_i \qquad \text{(Eq. 2.2)}$$

γ and A_s correspond to surface tension and surface area, respectively. μ_i, and n_i refer to the chemical potential and number of moles of the *i*-th component, respectively. Hence, γ can also be interpreted as the surface free energy density where

$$\gamma = \left(\frac{\partial G}{\partial A_s} \right)_{T,P,n} \quad \text{(Eq. 2.3)}$$

Surface pressure (Π) is defined as the difference between the surface tension of a film covered surface, γ, and a pure liquid surface, γ_0:

$$\Pi = \gamma_0 - \gamma \quad \text{(Eq. 2.4)}$$

Π is also the 2D analog of the 3D pressure (P). In general, the existence of a surface film lowers the surface energy at the A/W interface, and Π is positive for Langmuir film.

The surface tension (γ) at the A/W interface can be measured by the Wilhelmy plate technique depicted in Figure 2.4. The Wilhelmy plate is most commonly made from platinum, glass, or paper.[6,97] For platinum, the surface is normally roughened to enhance wetting. Eq. 2.5 is used to calculate the surface tension from theWilhelmy plate technique.

$$\gamma = \frac{F_{obs} - W}{2(L+t)\cos\theta} \quad \text{(Eq. 2.5)}$$

In Eq. 2.5, F_{obs} is the force measured by the Wilhelmy plate, W is the gravitational force acting on the wet plate. L and t are the length and thickness of the plate, respectively, and θ is the contact angle between the liquid and the solid plate. With a surface film, the surface pressure of the Langmuir film can be calculated from the difference between the observed forces for film covered surface and pure liquid surface obtained prior to spreading:

$$\Pi = \gamma_0 - \gamma = \frac{F_{obs,\Gamma=0} - F_{obs,\Gamma}}{2(L+t)\cos\theta} \qquad \text{(Eq. 2.6)}$$

where $F_{obs,\,\Gamma=0}$ is the force observed for the pure liquid and $F_{obs,\,\Gamma}$ is the force observed for a film covered surface at a given surface concentration (Γ). Under normal conditions, the thickness of the plate is usually much smaller than the length, L >> t, and complete wetting occurs cos θ ~1, whereby, Π can be simplified to:

$$\Pi = \gamma_0 - \gamma \cong \frac{F_{obs,0} - F_{obs}}{2L} \qquad \text{(Eq. 2.7)}$$

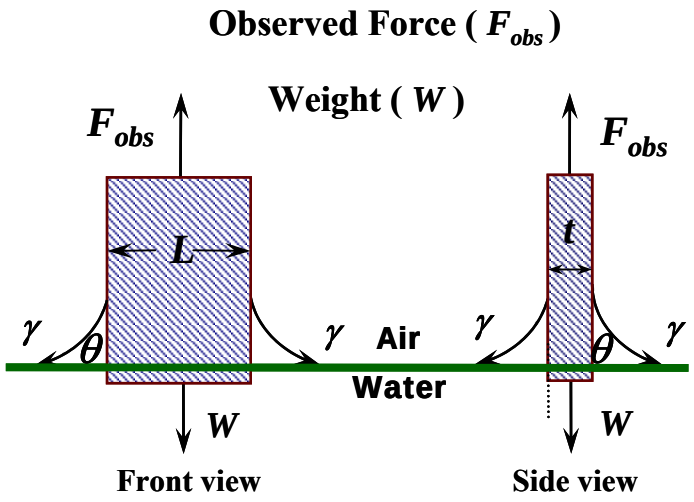

Figure 2.4: Schematic depiction of the Wilhelmy plate technique used to measure the surface tension (γ) at the A/W interface.[98]

2.2.2 Langmuir Troughs

A typical Π – A isotherm experiment is performed by spreading chloroform solutions of amphiphilic molecules onto the subphase contained in an instrument known as a Langmuir trough (Figure 2.5). Typically, a Langmuir trough has a square shape and

is constructed from polytetrafluoroethylene (PTFE), also known as Teflon^{TM}. PTFE is hydrophobic and inert to almost all chemicals. One or two movable barriers are also connected to the PTFE trough to alter the surface area (A) and hence the surface concentration (Γ).

Figure 2.5. Schematic depiction of a Langmuir trough with two barriers.

The surface area (A), an extensive quantity, is more commonly expressed as an intensive quantity, surface area per molecule or surface area per repeating unit, depending on whether or not it is a small molecule or polymer, respectively. A can be calculated from Eqs. 2.8 and 2.9:

$$A = \frac{A_{trough}}{N} = \frac{A_{trough}}{n \bullet N_A} = \frac{A_{trough}}{M \bullet V \bullet N_A} \qquad \text{(Eq. 2.8)}$$

$$A = \frac{A_{trough}}{n \bullet N_A} = \frac{A_{trough} \bullet M_0}{C \bullet m \bullet N_A} \qquad \text{(Eq. 2.9)}$$

where A_{trough} is the area of the Langmuir trough, N is the number of monomers or molecules on the surface, N_A is the Avogadro's number, n is the number of moles of the molecules on the surface, M is the molar concentration of the spreading solution, V is volume of the spreading solution, C is the mass of solute per unit mass of the spreading

solution, m is the mass of the spreading solution, and M_0 is the molar mass of the molecule for small molecules or polymer repeating unit.

2.2.3 Phase Transitions in Langmuir Films

Despite the numerous measurements that can be applied to Langmuir films at the A/W interface, Π - A isotherms provide the fundamental information about a Langmuir film's phases, phase transitions, and mechanical properties. With the reduction of one dimension, surface pressure (Π) is the 2D analog to pressure (P) in 3D bulk systems. The relationship between Π and P can be written as:

$$P(mN \bullet m^{-2}) \cong \frac{\prod(mN \bullet m^{-1})}{D(m)} \qquad \text{(Eq. 2.10)}$$

where D is the thickness of the Langmuir film. Therefore, a Π - A isotherm is the 2D analog of a P-V diagram.[1,2,6,99] Figure 2.6 compares a schematic P-V diagram of CO_2 (Figure 2.6A)[100] and an idealized Π - A isotherm for traditional amphiphiles (Figure 2.6B).[101]

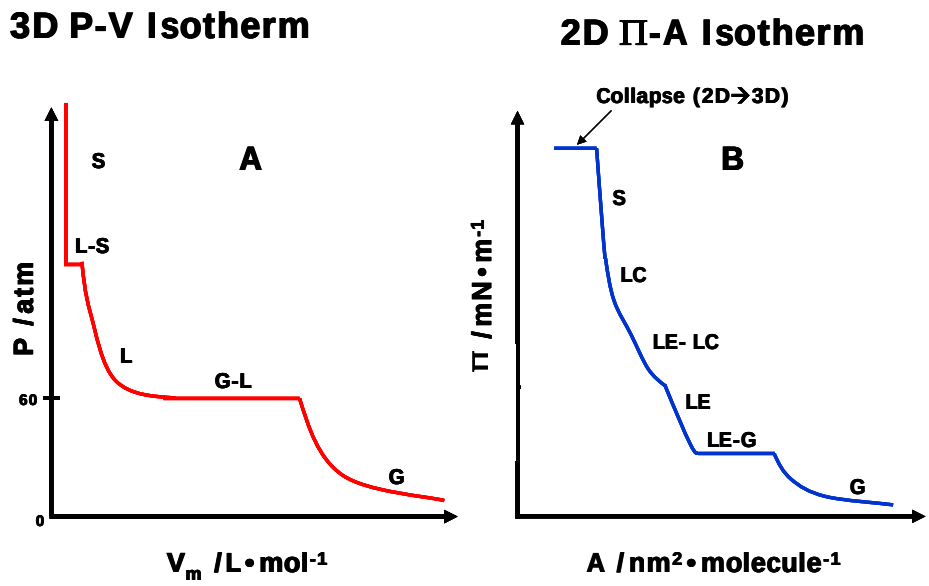

Figure 2.6. A comparison of 3D and 2D isotherms. (A) A P-V isotherm for CO_2 at 20 ^{o}C, where the letters signify G for gas, L for liquid, and S for solid. First-order gas to liquid and liquid to solid phase transitions are observed. (B) A Π-A isotherm for n-pentadecanoic acid at 25 ^{o}C on a pH = 2 subphase, where the letters correspond to G for a gas-like phase, LE for a liquid-expanded phase, LC for a liquid-condensed phase, and S for a solid phase. The G to LE and LE-LC phase transitions are first order; however, LC to S phase transitions are second order.[102]

Figure 2.7 shows an idealized Π – A isotherm for a fatty acid. At large A, molecules at the A/W interface are far apart from each other, in other words, they can not "feel" each other. At this point, interactions between these molecules are weak and Π is smaller than ~ 0.1 mN·m^{-1}. Since the molecules are non-interacting and almost randomly arranged at Π < ~ 0.1 mN·m^{-1}, this phase is defined as a 2D gas (G) phase for the Langmuir film and is comparable to a 3D gas phase. As the surface area per molecule (A)

decreases, surface concentration ($\Gamma = A^{-1}$) increases accordingly and the separation between molecules decreases while interactions between molecules increase until there is a phase transition to form a condensed phase. The least ordered condensed phase is a liquid expanded (LE) phase which was characterized by Adam.[103] The transition from G to LE is first order[4] just like the G to L phase transition in bulk systems. Alternatively, some molecules undergo a transition from a G phase to a condensed (LC) phase. For amphiphiles with long hydrocarbon tails, there are actually multiple LC phases. These phases can be distinguished by solid-like long-range order and the possibility of tilted and untilted conformations for the hydrophobic tails.[4] The G to LC phase transition is also a first order transition.[3,4] If a molecule forms a LE phase, it can also undergo a LE to LC phase transition, as depicted in Figure 2.7**.** One may suspect that the LE to LC phase transition is second order, since both have some liquid-like properties and the region for the coexisting phases on the Π – A isotherm is seldom perfectly flat.[104] However, Losche, Sackmann, and Mohwald found that the LE to LC phase transition is actually first order.[105] Under further compression, a kink is typically observed and the film reaches a solid (S) phase which was first studied by Adam in 1922.[106] The solid phase is even less compressible than the LC phase but actually possesses the same degree of translational order as the LC phase. X-ray-diffraction studies[107] showed that the difference between these two phases is the orientation of the hydrocarbon chains. In the LC phase, the hydrocarbon chains are tilted with respect to the surface normal and in the S phase they are perpendicular to the water surface. At higher surface pressure, the film is not able to withstand further compression and hence collapses into multilayer structures or dissolves

into the subphase. This 2D to 3D transition is an essential feature for Langmuir films and will be discussed separately.

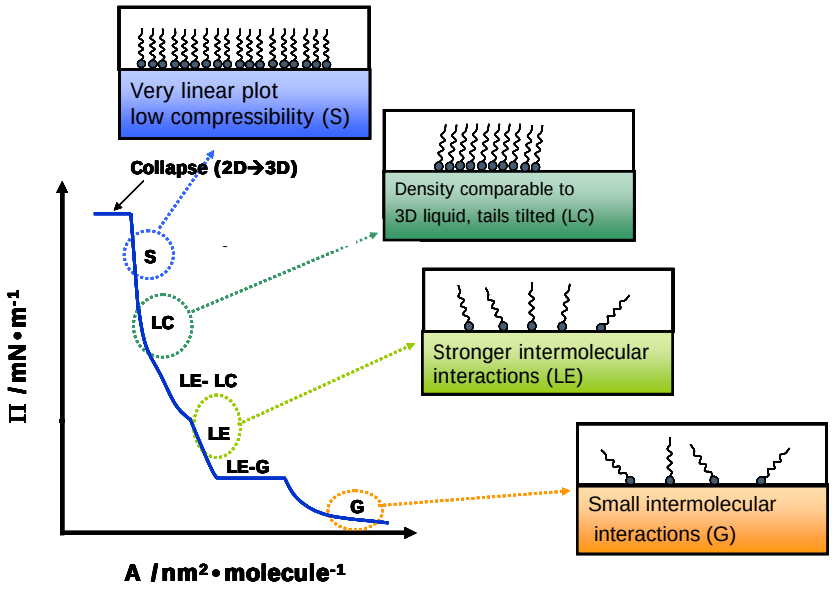

Figure 2.7: A schematic depiction of an idealized Π-A isotherm for a fatty acid Langmuir films.

2.2.4 Interfacial Rheology of Surface Films: Importance, Terminology, and Measurement.

The dilational and shear mechanical properties of surface films are crucial to many practical systems such as coatings, emulsions, and foams.[108,109] Foam and emulsion stability strongly depends on the interfacial rheology of surface films.[110] Hence, an understanding of the interfacial mechanical behavior of surfactants and amphiphilic polymers is of fundamental importance. Unfortunately, few studies have been carried out in this field because of the difficulty of measuring rheological parameters at interfaces. Furthermore, mechanical load at interfaces may alter the structure or damage thin films.

Hence, measurements of interfacial rheological properties need to be carefully designed and calibrated. As such, there are few commercialized instruments available.

As an analogue to bulk systems, several interfacial (2D) rheological parameters were summarized by Langevin:[110] 1) Compressive parameters as an analogue to the bulk modulus (K) in 3D, with an elastic modulus (ε) and viscosity (κ); 2) Shear parameters (S' and S") representing the shear elasticity and viscosity, respectively; 3) Transverse parameters (σ_d and μ) representing the elasticity and viscosity, respectively. σ_d is also known as the dynamic surface tension and μ is always negligible for thin films; and 4) Bending parameters. The elastic bending modulus is a small correction to the surface tension and is usually unimportant unless the interfacial tension is very small. A detailed explanation of these rheological parameters will be presented in the SLS instrumental section.

Several different instruments can be used to measure the shear or dilational properties of surface films. For the shear modulus, there is the canal surface viscometer which measures the shear viscosity using the bulk Hagen-Poiseuille law. By measuring how fast a film flows through a narrow canal or slit under a 2D pressure difference, the shear viscosity of the surface film can be calculated.[111-113] An interfacial stress rheometer (ISR) can also measure the dynamic interfacial shear rheology of surface films. By applying a controlled shear stress via a magnetized probe, a slender PTFE coated needle, at the A/W interface, it is possible to measure the resulting deformation (strain). As a consequence, the complex surface shear modulus (G_s*) comprised of an elastic modulus (G_s') and a loss modulus (G_s") can be deduced.[58,59] ISR is more sensitive to Langmuir films in the multilayer regime since Langmuir monolayers do not possess large shear

moduli. Other techniques like a knife-edge surface viscometer[114] and a blunt knife surface viscometer[115,116] have been developed to measure the dynamic shear modulus.

The dilational rheological parameters of surface films can be obtained by studying the damping of capillary waves at the interface. Harmonic waves are generated mechanically, thermally, or electrically. The response of the system is often mechanically or optically measured in terms of the damping of the propagating capillary waves by the surface film. Several instruments have been developed to measure dilational moduli through mechanically generated waves,[117] electrocapillary wave diffraction (ECWD),[48-53] and surface light scattering (SLS).[54-57,118,119] All of these techniques probe the dilational viscoelastic parameters over a certain frequency range, typically from several Hz to 10^4 Hz. This dissertation will focus on the last technique, surface light scattering (SLS), which utilizes spontaneous, thermally induced capillary waves to probe the high frequency rang surface films. A more detailed discussion of this technique will continue in Section 2.5.

2.2.5 2D to 3D Transitions in Langmuir Films

The collapse of Langmuir monolayers has been extensively studied and is of great importance for understanding intermolecular and molecule-subphase interactions. Two essential parameters related to Langmuir film collapse are the collapse pressure (Π_c) and the equilibrium collapse pressure (Π_e) depicted in Figure 2.8. Π_c defines the limiting pressure a Langmuir monolayer can withstand before it "breaks". This concept is analogous to the yield point for bulk materials and indicates the toughness of the materials. Π_e indicates the critical pressure above which relaxation phenomena severely alter a film's structure. As such, Π_e is the highest pressure that can be achieved during a

successive addition experiment. As seen in Figure 2.8, during compression experiments at a constant rate, the film can reach Π values between Π_e and Π_c that correspond to metastable states. To better understand this concept, it is helpful to consider a similar and common example, supersaturated water vapor. In supersaturated water vapor, water can exist as gas with a vapor pressure higher than the equilibrium vapor pressure. This case is also a metastable state. Generally speaking, metastable states are caused by inefficient packing of molecules, or in other words, incomplete relaxation of the system's structure to the equilibrium state. Therefore, in a metastable state, small perturbations can induce a phase transition. In essence, a solid surface can act as a perturbation for water vapor in a supersaturated state. The water vapor will go through a nucleation and growth process on the solid surface to form a liquid film. Langmuir film systems are similar; the amphiphilic molecules can form collapsed structures through a nucleation and growth process from the metastable monolayer. Thus, even though Π_c is defined by the onset of a plateau in a Π – A isotherm, the 2D to 3D transition can happen before Π_c.[120] Molecules with longer hydrophobic tails have greater viscosity than short chain molecules. As a consequence, long hydrophobic tails enhance the kinetic stability of the metastable regime ($\Pi_e < \Pi < \Pi_c$), and give rise to larger Π_c. Likewise, more polar head groups can increase Π_c through enhanced molecule-subphase interactions.[121] The observation that Π_c is usually compression rate dependent is not surprising, since the metastable state arises from inefficient packing of molecules, and the films are not crystalline solids in spite of their long-range order.

As depicted in Figure 2.9, the molecules will be forced to form bilayers, trilayers, and even thicker multilayers after the film collapses to dissipate extra energy added to the

system during compression. During the collapse process, the hydrophobic tails of the upper molecules will join with the hydrophobic tails of the molecules at the bottom. Poly (ethylene oxide) (PEO) represents an interesting case. While PEO is a soluble surfactant, it is possible to create stable Langmuir films below Π_c. Above Π_c, PEO is soluble and the film can loop and dissolve into the subphase during collapse.

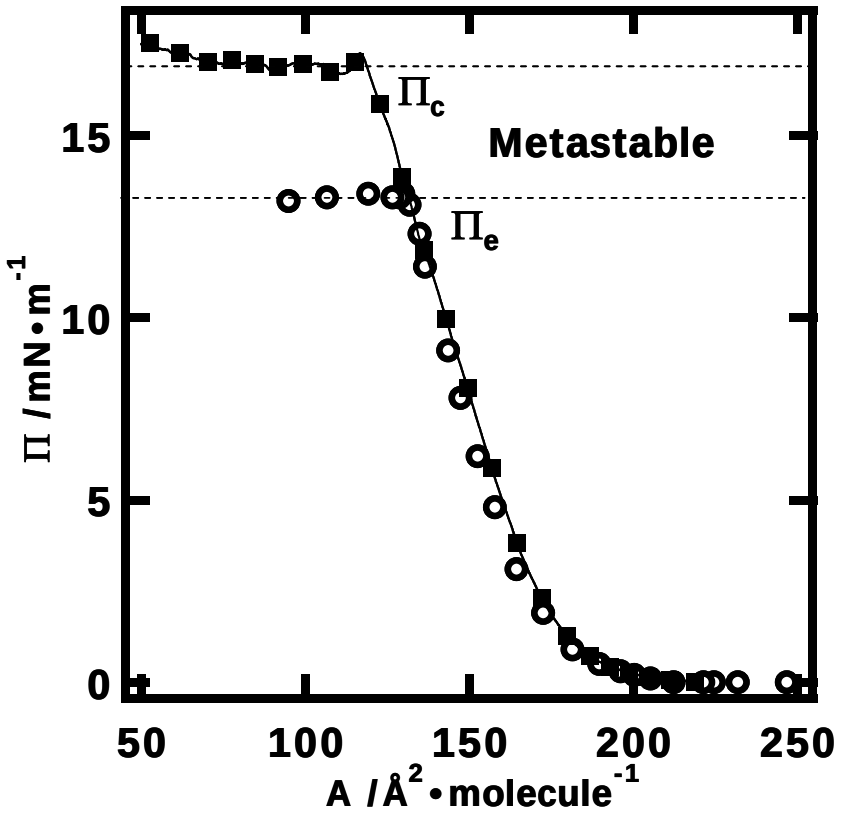

Figure 2.8: Compression Π – A isotherm (open circles) and successive addition Π – A isotherm (closed squares) for trisilanolisobutyl-POSS. Two horizontal dashed lines represent the collapse pressure (Π_c) and the equilibrium collapse pressure (Π_e).

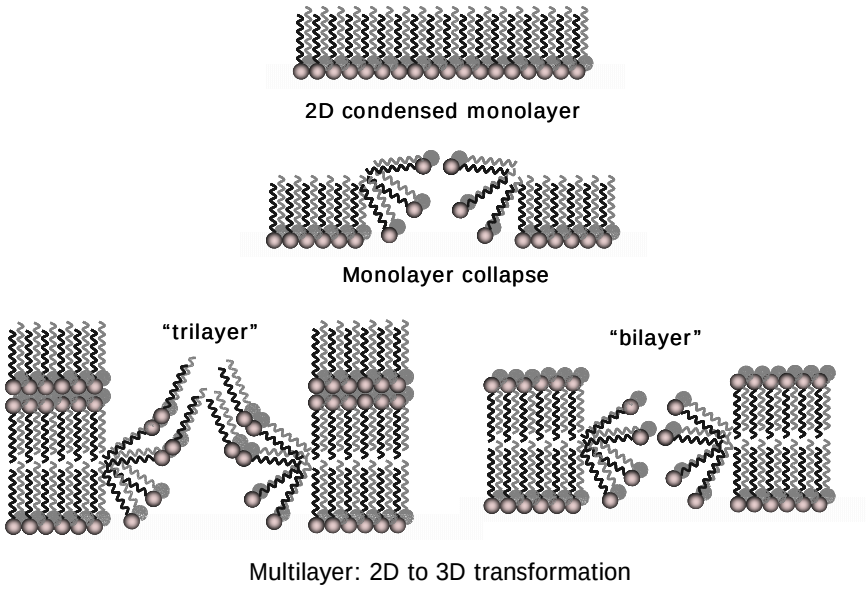

Figure 2.9. Schematic depiction of possible film mechanism.[98]

2.3 Polymeric Langmuir Films

2.3.1 Phases in Polymeric Langmuir Films

Beyond traditional surfactants, the study of amphiphilic polymers at the A/W interface has become an active research area.[31,32,34-36,57,86,89,122-125] The behavior of amphiphilic polymers at the A/W interface dramatically differs from small molecules owing to their considerably larger size. In this section, concepts from bulk polymers and polymer solutions are related to 2D polymeric Langmuir films.

The spreading behavior of flexible polymers at the A/W interface is different from small molecules. Polymer coils in a spreading solvent need to unfold so that the polar groups can hydrogen bond with the water surface. The result is 2D random coils (Figure 2.10) for flexible polymer chains. Similar to polymer solutions, the polymers at the A/W interface pass through three different regimes depicted in Figures 2.10 and 2.11. The Langmuir films start in the dilute regime where the film is in a gas-like state. With

increasing concentration there is a transition from a dilute to a semi-dilute solution at an overlap concentration (Γ*) where the polymer coils begin to touch each other. At even higher Γ, there is a second transition from a semi-dilute solution to a concentrated solution. In contrast to bulk solution, there is no evidence that polymer chains entangle in the 2D Langmuir monolayers, whereas entanglements could occur upon collapse when films undergo a 2D to 3D transition. In the dilute regime, polymers ideally exist as 2D random coils and exhibit molar mass dependent Π - Γ isotherms much like the concentration dependence of osmotic pressure of polymers in dilute 3D solutions.[126-128] In the semi-dilute regime for Langmuir films, coils can interpenetrate (Figure 2.10) and Π - Γ isotherms (Figure 2.11) exhibit molar mass independent behavior just like the concentration dependence of osmotic pressure in semi-dilute bulk polymer solutions.[129] As depicted in Figure 2.11, the collapse surface pressure ($\Pi_{collapse}$) and the subsequent Π values in the collapse regime are molar mass dependent. The molar mass dependence reflects entropic factors.[127,128]

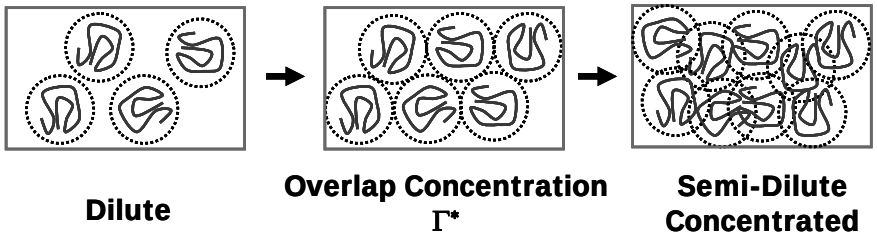

Figure 2.10: Schematic depiction of chain conformations for random coil polymers in Langmuir films.

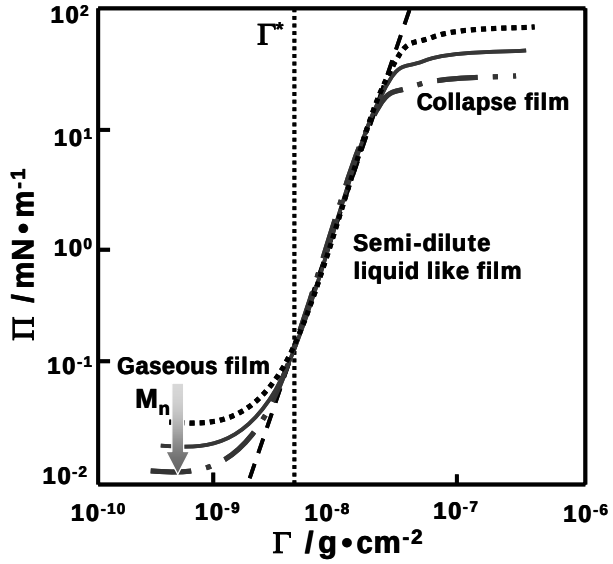

Figure 2.11: Schematic depiction of Π - Γ isotherms for Langmuir films of homopolymers with different molar masses. This graph shows a gas-like dilute regime, a liquid-like semi-dilute phase, and the collapse regime. M_n refers to the number average molar mass and Γ^* is the overlap concentration [98,128]

2.3.2 Theoretical Approaches for Polymeric Langmuir Films (2D Analog to 3D)

When surface pressure (Π) is very low (Π << 1 $mN \cdot m^{-1}$), it is valid to treat the Langmuir film as a gas film (G). Hence, the obvious first equation to consider is the ideal gas law:[127,130]

$$\Pi = \frac{RT}{A} \qquad \text{(Eq. 2.11)}$$

where R is the gas constant. If we consider the corrections for excluded area, A_0, and attractive terms, *a*, as in the van der Waals equation of the state, the direct 2D analog is:

$$\Pi = \frac{RT}{A - A_0} - \frac{a}{A^2} \qquad \text{(Eq. 2.12)}$$

Since surface pressure (Π) is nothing more than the 2D analog of osmotic pressure, a virial expansion is also valid to describe the relationship between Π and surface concentration (Γ):

$$\frac{\Pi}{\Gamma RT} = \left(\frac{1}{M_n}\right)(1 + A_2\Gamma + \cdots) \qquad \text{(Eq. 2.13)}$$

where A_2 is the second virial coefficient and the intercept is related to M_n, the number average molar mass. Using this equation, we can obtain the molar mass and second virial coefficients for various polymeric systems from their Π – A isotherms.[131,132] Nonetheless, experiments with G monolayers are sparse because of the very low Π that must be measured for ideal gases and even virial expansions.

The condensed phases for polymeric Langmuir films attract more interest and are better investigated because Π values (> 1 $mN \cdot m^{-1}$) are readily accessible experimentally. However, theoretical approaches in this regime are less convincing owing to the difficulty of defining the size of a single molecule. The actual size of molecules could be significantly affected by their orientation and order in the Langmuir films.[133] Hence, despite all of the experimental studies on condensed phase polymeric Langmuir films, a strong theoretical analysis is still lacking.

2.3.3 Scaling Theory for Polymeric Langmuir Films

The obvious parallels between 2D Langmuir film properties and polymer solutions have led researchers to modify the scaling theory of de Gennes[127] for polymer solutions to explain the Π - Γ isotherm in the semi-dilute regime:

$$\Pi = C\Gamma^z \qquad \text{(Eq. 2.14)}$$

where C is a proportionality constant and z is related to the critical exponent υ ($z = 2\upsilon / (2\upsilon-1)$).[126,130] The amphiphile-subphase interactions within a polymeric Langmuir film determine how Π scales with Γ in the semi-dilute regime. When the interface serves as good solvent, the polymer coils swell and the root mean square end to end distance, $\langle r^2 \rangle^{1/2}$ increases, whereas a theta solvent interface corresponds to an $\langle r^2 \rangle^{1/2}$ value where only the minimum amount of water necessary to fill the free volume is present in the polymer coils.[123,126] Therefore, the values of z can be related to the solvent quality of the interface: good, poor, or theta solvent conditions. For a good solvent, z values obtained from mean-field theories[134] and numerical 2D simulations are 3 and 2.86, respectively.[135] In the theta solvent limit, $z \rightarrow \infty$ for a mean field theory, whereas it ranges from 8[136] to 101[137] for numerical methods. Experimentally, many studies have focused on the scaling behavior of amphiphilic polymers at the A/W interface; both good solvent and theta solvent cases have been observed.[57,123,126,130,138]

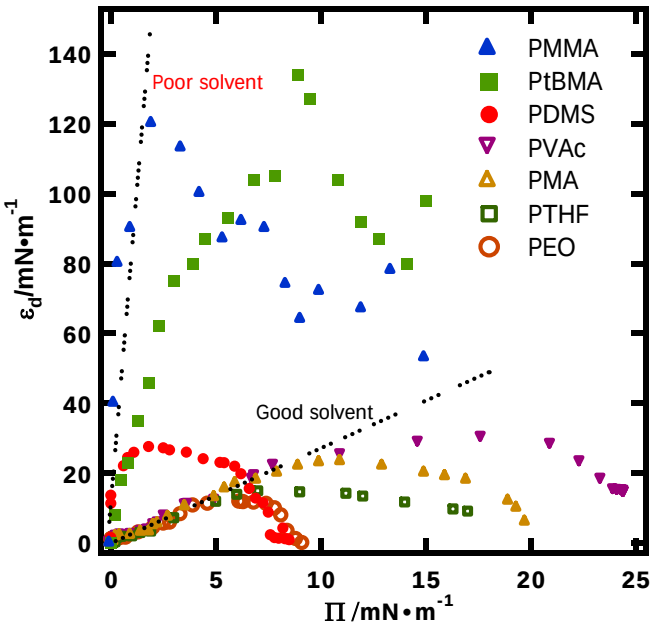

Figure 2.12. ε_d – Π isotherms for poly(methyl methacrylate) (PMMA) and poly(t-butyl acrylate) (PtBA), poly(dimethylsiloxane) PDMS, poly(vinyl acetate) (PVAc), poly(methyl acrylate) (PMA), poly(tetrahydrofuran) (PTHF) and poly(ethylene oxide) (PEO). Two labeled dotted lines signify theoretical predictions for an interface corresponding to a good solvent or poor solvent.[123]

Another approach has also been applied to understand the scaling behavior of polymers at the A/W interface with the calculation of the lateral compressibility (κ_s) and static elasticity (ε_s) of the polymer film:[123,128,139]

$$\kappa_s \equiv -\frac{1}{A}\left(\frac{\partial A}{\partial \Pi}\right)_T \qquad \text{(Eq. 2.15)}$$

$$\varepsilon_s \equiv \kappa_s^{-1} = -A\left(\frac{\partial \Pi}{\partial A}\right)_T \qquad \text{(Eq. 2.16)}$$

Here, κ_s and ε_s are analogs to the bulk isothermal compressibility (κ) and bulk modulus (K). Combining Eqs. 2.16 and Eq. 2.14, along with the assumption that $\Pi = 0$ at Γ^* yields:

$$\varepsilon_s = z\Pi \qquad \text{(Eq. 2.17)}$$

Therefore, the scaling exponent z can be obtained from the initial slope of $\varepsilon_s - \Pi$ isotherms. Figure 2.12 shows two limiting cases (good and theta solvent interface) on a plot of $\varepsilon_s - \Pi$ for various polymers. Poly(methyl methacrylate) (PMMA), poly(t-butyl methacrylate) (PtBMA), and poly(dimethylsiloxane) (PDMS) are consistent with the A/W being a near-theta solvent. In contrast, poly(vinyl acetate) (PVAc), poly(methyl acrylate) (PMA), poly(tetrahydrofuran) (PTHF) and poly(ethylene oxide) (PEO) exhibit values in the range of the predictions for good solvent scaling behavior.[126,140] In this dissertation, Figure 2.12 is adopted to analyze the dynamic elasticity (ε_d) obtained from SLS studies for different polymeric systems.

2.4 Brewster Angle Microscopy (BAM)

Most of the time, it is insufficient to draw definitive conclusions about phase transitions and collapse behavior within Langmuir film systems only on the basis of the $\Pi - A$ isotherm. Optical techniques allow one to visualize the morphology of Langmuir monolayers. Brewster angle microscopy (BAM) is an excellent optical technique for observing the microscopic structures (micron scale) in Langmuir monolayers. This technique takes advantage of the special properties of light reflected from an interface at Brewster's angle. Since its development, BAM has been widely adapted as an *in-situ* monitor for surface morphology changes. The greatest disadvantage of BAM is the

limitation of its resolution, which typically ranges from several microns to several ten microns. One way to overcome this limitation is to transfer films onto solid substrates through a LB or LS-technique whereby techniques such as atomic force microscopy (AFM) and transmission electron microscopy (TEM) can be applied.

2.4.1 Polarization of Light and Brewster's Angle

Light beams can transmit, reflect, or refract at an interface. For non-polarized light as shown in **Figure 2.13**, the light beam can be decomposed into two components. P-polarized light is parallel to the plane of incidence (the arrows), s-polarized light is perpendicular to the plane of incidence (the circles), and both components are perpendicular to the propagation direction.

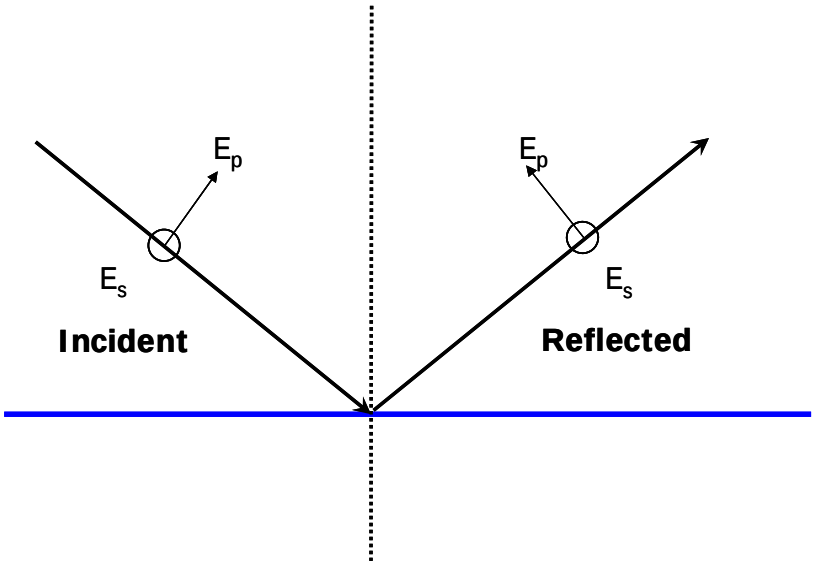

Figure 2.13: Reflection of a plane wave from a surface perpendicular to the page. The p-component of the waves is in the plane of incidence (the page), while the s component is perpendicular to the plane of incidence.

For a planar interface, the reflectivity of p-polarized light (R_p) and s-polarized light (R_s) depends on the angle of incidence (θ_i) and the refractive index (n) of the materials following Fresnel's law: [100]

$$R_p = \left(\frac{n_1 \cos\theta_t - n_2 \cos\theta_i}{n_1 \cos\theta_t + n_2 \cos\theta_i} \right)^2 = \frac{\tan^2(\theta_i - \theta_t)}{\tan^2(\theta_i + \theta_t)} \quad \text{(Eq. 2.18)}$$

$$R_s = \left(\frac{n_1 \cos\theta_i - n_2 \cos\theta_t}{n_1 \cos\theta_i + n_2 \cos\theta_t} \right)^2 = \frac{\sin^2(\theta_t - \theta_i)}{\sin^2(\theta_i + \theta_t)} \quad \text{(Eq. 2.19)}$$

where n_1 and n_2 are refractive indices of the two media; and θ_i and θ_t are the incident and refracted angles, respectively.

An important limiting case for Eqs. 2.18 and 2.19 is when $\theta_i + \theta_t = 90^o$ corresponding to Brewster's angle, $\tan(\theta_i + \theta_t)$ approaches infinity, causing R_p to go to 0, while R_s is continuous across Brewster's angle, θ_B. If one recalls Snell's law of refraction:

$$n_1 \sin\theta_i = n_2 \sin\theta_t \quad \text{(Eq. 2.20)}$$

the result is a critical incident angle (θ_B) where there is no reflection of p-polarized light (**Figure 2.14**), known as Brewster's angle:

$$\tan\theta_B = n_2 / n_1 \quad \text{(Eq. 2.21)}$$

2.4.2 Principle of BAM and Instrumental Set-Up

Fresnel's law describes the reflection of polarized light from an ideal interface between two media. However, the thickness, roughness, and anisotropic features of a real interface will all affect the reflection profile. As a consequence, the refractive index at the interface is not a fixed constant, but rather is a function of position in the system, n(Z), where Z is the distance from the defined interface between the two bulk phases. For an

interfacial layer with a thickness (D) much smaller than the wavelength of the incident light, Drude[41] derived an equation to describe the reflection of light at Brewster's angle:

$$R_p(\theta_B) = R_s(\theta_B)\overline{\rho_B}^2 \qquad \text{(Eq. 2.22)}$$

where $R_s(\theta_B)$ and $R_p(\theta_B)$ are the reflectivity for *s*-polarized and p-polarized light for a Fresnel surface at Brewster's angle, respectively, and $\overline{\rho_B}$ is the ellipticity given as:[42,43]

$$\overline{\rho_B} = \frac{\pi}{\lambda}\frac{\sqrt{n_1^2+n_2^2}}{n_1^2-n_2^2}\int_{-\infty}^{+\infty}\frac{[n(z)^2-n_1^2][n(z)^2-n_2^2]}{n(z)^2}dz \qquad \text{(Eq. 2.23)}$$

where λ is the wavelength of the incident beam.

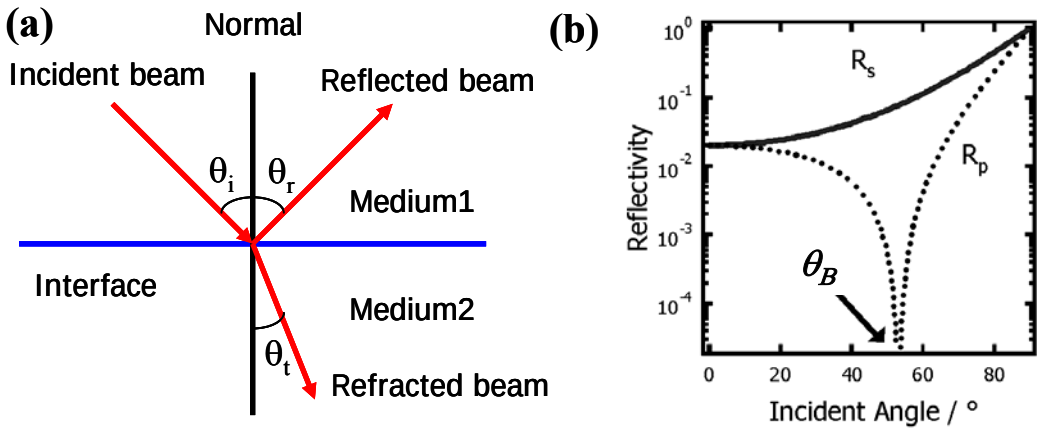

Figure 2.14: (a) Schematic depiction of reflection and refraction at an interface between two media. θ_i, θ_r, and θ_t are incident, reflected, and refracted angles. (b) Calculated reflectivities at the A/W interface from Fresnel's law at a Fresnel interface. The angle at which R_p minimizes defines Brewster's angle ($\theta_B = 53.1^o$ for water).[98]

Equation 2.22 can be rewritten in terms of the reflected light intensity (I_r) and the incident light intensity (I_i).

$$I_r = I_i R_p(\theta_B) \propto \overline{\rho_B}^2 \qquad \text{(Eq. 2.24)}$$

For a film of uniform thickness (h) and uniform refractive index (n), Eq. 2.24 becomes

$$I_r = I_i R_p(\theta) \propto \overline{\rho_B}^2 = \left(\frac{\pi h}{\lambda_0} \bullet \frac{\sqrt{n_1^2 + n_2^2}}{n_1^2 - n_2^2} \bullet \frac{(n^2 - n_1^2) \bullet (n^2 - n_2^2)}{n^2} \right)^2 \qquad \text{(Eq. 2.25)}$$

Eq. 2.25 represents the relationship between reflected light intensity and film thickness and refractive index. From Eq. 2.25, it is possible to deduce that thicker films lead to brighter images since I_r is proportional to the film thickness (h). Likewise, the greater the difference between the refractive indices of the film and the two media, the brighter the image. Eq. 2.25 also reveals that the film must have a refractive index that is different from both media to be seen. Langmuir films at the A/W interface are not always uniform with anisotropy arising from regions with different thickness or refractive index. Hence BAM can be used to probe micron scale anisotropy of film structure at the A/W interface.

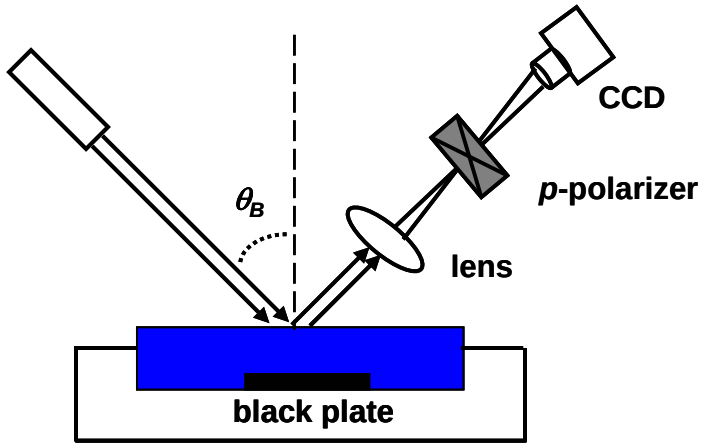

Figure 2.15: Experimental set-up for a typical BAM instrument. A *p*-polarized laser beam is incident on the water surface at Brewster's angle for water (θ_B = 53.1°). Light reflected by the interface is detected by a CCD camera. A *p*-polarizer is placed in the path of the reflected beam to remove residual s-polarized light.[102]

Figure 2.15 shows a schematic depiction of the BAM instrumental set-up, a p-polarized laser is incident on water surface at 53.1^{o} which is the Brewster's angle for the A/W interface. The reflected beam then passes through a p-polarizer, which filters out residual s-polarized light and the p-polarized light is focused onto a CCD via a lens. In a typical experiment, a tilted black glass plate is placed underneath the water surface to reflect the refracted beam away from the detector.

As discussed above, for the case of no film at the interface, no p-polarized light will be reflected at Brewster's angle and all s-polarized light will be blocked by the p-polarizer installed in front of the detector. Hence, nothing is observed at the CCD. With a Langmuir film covering the surface, the refractive index profile is altered at the A/W interface, whereby Brewster's angle for the system now deviates from the value for a bare A/W interface. Thus, some p-polarized light is reflected into the CCD to provide an image of the interface. As such, BAM has become a very sensitive tool for detecting and studying phase transitions, phase separation, crystallization, aggregation, etc. within Langmuir films.[29,34-38]

2.5 Surface Light Scattering (SLS) and the Rheological Behavior of Polymeric Langmuir Films

A surface light scattering (SLS) instrument has been designed, set-up and calibrated. The rheological behavior of several small molecules, polymers, and blends system have been studied via SLS. In this section, the background, set-up and application of SLS to investigate dilational rheological properties of Langmuir films will be discussed.

2.5.1 Surface Waves and the Propagation of Capillary Waves

The propagation of surface waves on free liquid surfaces is an everyday phenomenon. An easy way to observe it is throwing a stone into a lake; the ripples are one kind of surface wave. The tide on the sea is also a common surface wave. These two surface waves are called gravity waves in the sense gravity is the main driving force for the propagation of the surface waves. In the ripples, part of the liquid is raised up and gravity pulls it back driving the propagation of these ripples. However, gravity waves are not the only kind of surface wave. There is another type of surface wave which we are not able to observe with the naked eye, the capillary wave. Capillary waves arise from thermal fluctuations in bulk liquids and hence are present on all liquid surfaces. The driving force for the propagation of capillary waves is also the surface tension (γ). The capillary waves deform the liquid surface and hence increase its surface energy. Surface tension (γ) opposes this deformation to reduce the surface area in an attempt to restore the interface to its initial state.

Lord Kevin first studied the propagation of surface waves theoretically and derived an expression for the propagation frequency of surface waves on an ideal pure liquid (no viscosity):[141]

$$\omega_0 = \sqrt{\frac{\sigma k^3}{\rho} + gk} \qquad \text{(Eq. 2.26)}$$

where ρ is the liquid density, σ is the surface tension, (in this section, σ is used to represent surface tension to be consistent with the papers in this field), g is acceleration due to gravity, and *k* is the wave vector defined as (2π/λ) with λ equal to the wavelength of the propagating wave. The first term in Eq. 2.26 corresponds to capillary waves, while

the second term corresponds to gravity waves. From Eq. 2.26, one can infer that gravity waves are dominant for large λ, ($\omega_0 \propto k^{1/2}$) whereas capillary waves are dominant for small λ ($\omega_0 \propto k^{3/2}$). The amplitudes of capillary waves at the A/W interface are around 3~5 Å[27] with *k* around 10^4 m^{-1} or λ ~ 100 μm. Therefore, the gravitational term is negligible. Langevin provided a first order correction to Eq. 2.26 by considering the viscosity of the subphase (η):[142]

$$\omega_0 = \sqrt{\frac{\sigma k^3}{\rho}\left(1-\frac{1}{2}y^{-\frac{3}{4}}\right)} \qquad \text{(Eq. 2.27)}$$

where y is dimensionless fluid parameter that is a ratio of the relative restoring and dissipating forces at the interface:

$$y = \frac{\sigma\rho}{4\eta^2 k} \qquad \text{(Eq. 2.28)}$$

One of the most significant contributions in this area is the Lucassen-Reynders-Lucassen dispersion equation,[56] which is similar to other dispersion relationships[143] describing the dispersion relation for capillary waves at a fluid-fluid interface:

$$[\eta(k^* - m^*) - \eta'(k^* - m^{*'})]^2 = E \bullet S \qquad \text{(Eq. 2.29)}$$

where the functions E and S are given as

$$E = \left[\eta(k^* + m^*) + \eta'(k^* + m^{*'}) + \frac{\varepsilon^* k^{*2}}{i\omega^*}\right] \qquad \text{(Eq. 2.30)}$$

and

$$S = \left[\eta(k^* + m^*) + \eta'(k^* + m^{*'}) + \frac{\sigma^* k^{*2}}{i\omega^*} + \frac{g(\rho - \rho')}{i\omega^*} - \frac{\omega^*(\rho - \rho')}{ik^*}\right] \qquad \text{(Eq. 2.31)}$$

The prime terms represent the upper phase (most commonly air), while the terms with an asterisk denote complex quantities defined as

$$k^* = k - i\beta \quad \text{(Eq. 2. 32)}$$

$$\omega^* = \omega_0 + i\alpha \quad \text{(Eq. 2.33)}$$

$$\sigma^* = \sigma_d + i\omega^*\mu \quad \text{(Eq. 2.34)}$$

$$\varepsilon^* = \varepsilon_d + i\omega^*\kappa \quad \text{(Eq. 2.35)}$$

and

$$m^* = \left(k^{*2} + \frac{i\omega^*\rho}{\eta} \right)^{1/2}, \text{Re } (m^*) > 0 \quad \text{(Eq. 2.36)}$$

For the case of SLS, with temporal damping of the capillary waves, the complex wave vector, k^*, does not have an imaginary component ($\beta = 0$) and $k^* = k$ in Eq. 2.32. In contrast, the complex frequency, ω^*, has both a real frequency, ω_0, and a complex component, the temporal damping coefficient, α in Eq. 2.33. The transverse modulus, σ^*, consists of a real part, the dynamic surface tension, σ_d, and an imaginary part, the transverse viscosity, μ (Eq. 2.34). Likewise, the complex lateral modulus, ε^*, consists of a real part, the dynamic dilational elasticity, ε_d, and an imaginary part, dilational viscosity, κ, (Eq. 2.32). Additionally, a complex wave vector, m^*, represents how deeply the surface wave penetrates into the underlying liquid (Eq. 2.36). For the investigation of gas/liquid interfaces like the A/W interface, it is safe to assume the density and viscosity of air are zero ($\rho' = \eta' = 0$) in Eq. 2.31 yielding

$$\eta^2 (k - m^*)^2 = \left[\eta(k + m^*) + \frac{\varepsilon^* k^2}{i\omega^*} \right] \left[\eta(k^* + m^*) + \frac{\sigma^* k^{*2}}{i\omega^*} + \frac{g\rho}{i\omega^*} - \frac{\omega^*\rho}{ik^*} \right] \quad \text{(Eq. 2.37)}$$

2.5.2 Molecular Motion at the Interface

The damping effect on surface waves when an oil film covers a surface has been known for centuries (Section 2.1.3) We now know that the damping within a film at the A/W interface depends on energy dissipation, the viscoelastic properties of the surface film, and its coupling to the subphase liquid. Therefore, it is possible to probe the rheological properties of surface films by monitoring changes in the propagation characteristics of surface capillary waves. This approach is the basic idea behind SLS. In principle, SLS is similar to conventional rheological measurements, the difference being we use the spontaneously formed capillary waves to perturb the surface film rather than stressing or straining the system mechanically.

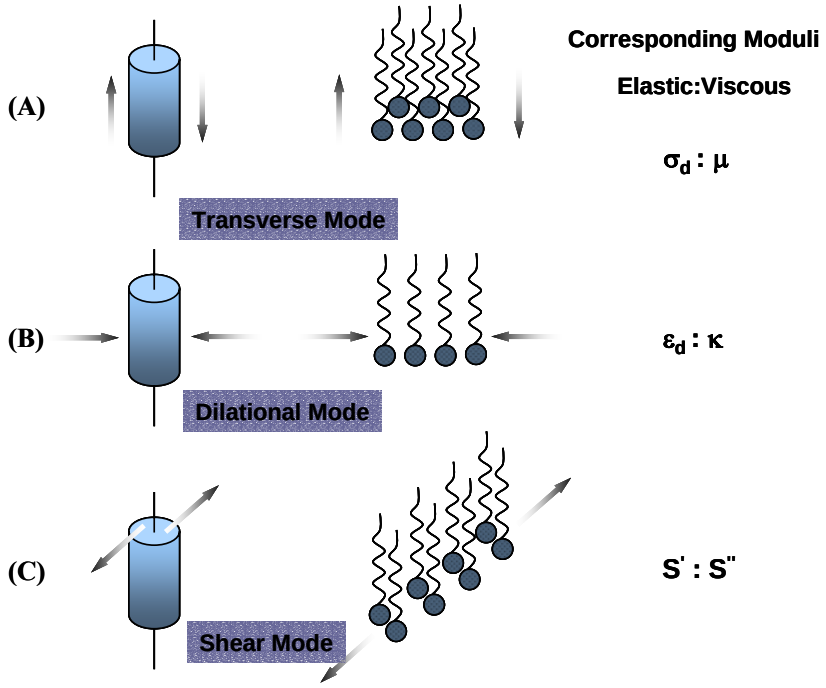

Figure 2.16. Three principal modes of monolayer motion suggested by Goodrich[144] that was relevant for SLS: (A) transverse, (B) dilational or longitudinal, and (C) shear mode.[145]

According to Goodrich,[144] there are three principle modes of motion in monolayer films with corresponding viscoelastic moduli (Figure 2.16). There are the transverse modulus, σ^*, the dilational modulus, ε^*, and the longitudinal shear modulus, S^*. Each mode has a corresponding real part representing the elasticity and an imaginary part representing viscosity. For the transverse modulus, the relevant motion is an out of plane motion with an elastic (σ_d) and viscous (μ) component (Figure 2.16A). The dynamic surface tension can deviate from the static surface tension (σ_s). The dilational or longitudinal modulus, ε_d (elastic) and κ (viscous), accounts for in-plane compressive deformation of a volume element (Figure 2.16B) and is analogous to the bulk modulus (K) in 3D systems. The shear modulus, S^* shown in Figure 2.16C, is analogous to the 3D shear modulus. The shear mode is coupled to the longitudinal mode and is impossible to separate from the dilational mode by SLS.[146] Fortunately, the magnitude of S^* is very small for a Langmuir monolayer compared with that of ε^*, thus S^* can be safely neglected.[147] For SLS experiments, it is the out of plane transverse mode that directly scatters the laser beam. However, the dilational mode couples with the transverse mode and thereby affects not only the in plane motion of capillary wave but also the out of plane motion. Hence, measurements of the capillary wave damping for a film at the A/W interface by SLS can be used to deduce the dilational viscoelastic parameters, ε_d and κ.

2.5.3 Surface Light Scattering (SLS) Instrumental Set-Up

Figure 2.17 provides a schematic depiction of the SLS set-up. A 15 mW He-Ne laser is polarized relative to the surface. The polarized electric field from the laser is parallel to the interface or perpendicular to the plane of incidence to optimize the signal to noise ratio. The transmission diffraction grating denoted as G in Figure 2.17 generates

different diffraction orders which provide reproducible local oscillators for heterodyne detection and also helps to select specific wave vectors.[128] The reference beams pass through a neutral density filter, NDF in Figure 2.17, to attenuate their intensity to a level suitable for heterodyne detection. The reference/scattered intensity I_r/I_s should be around 30 and I_r should not be too strong to avoid saturating the photomultiplier tube (PMT in Figure 2.17). The two lenses, L1 and L2, focus all the diffraction orders onto the same spot at water surface with an incident angle of 66.0°. At any given time, one of the diffraction orders along with any light scattered at the corresponding ϕ are reflected into the PMT to produce a time dependant signal. The current from the PMT is then passed through a voltage divider and high–pass filter amplifier with a cut-off frequency of 1000 Hz and 10× amplification. With the aid of a fast Fourier transform (FFT) spectrum analyzer, the power spectra are obtained, digitized, and sent to a personal computer for analysis.

A Teflon trough contains the subphase and provides the interface. A Wilhelmy plate is also mounted on the trough to simultaneously monitor the surface pressure during SLS experiments. The trough and Wilhelmy plate are both placed in a Plexiglas box to maintain the humidity on a vibration isolated optical table.

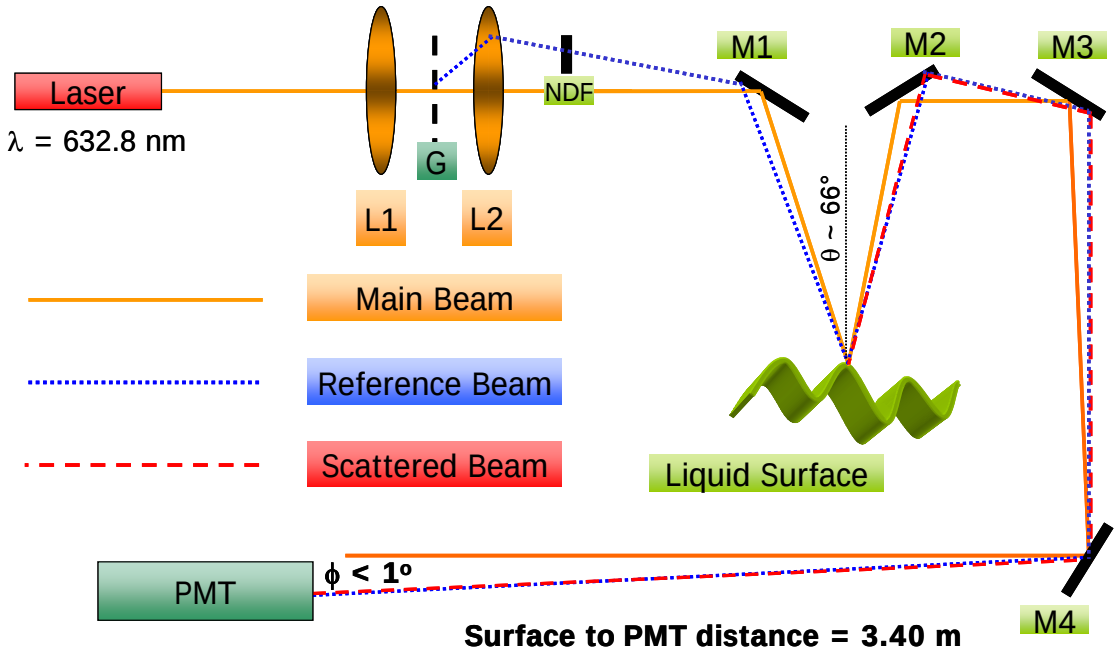

Figure 2.17. Schematic depiction of the surface light scattering instrument. The lenses, mirror, grating, neutral density filter, and photomultiplier tube are indicated by L_1 and L_2, M, G, NDF, and PMT, respectively.[145]

2.5.4 Scattering Behavior at the Interface

Figure 2.18 shows a schematic depiction of the surface light scattering measurement. At an air/liquid interface, there is a continuous distribution of capillary wave wavelengths and hence wave vectors. The incident laser beam interacts with the propagating surface wave and undergoes a Doppler shift:

$$\upsilon_{shifted} = \upsilon_{incident}\left(1 \pm \frac{\nu}{c}\right) \qquad \text{(Eq. 2.38)}$$

where $\upsilon_{shifted}$ is the shifted frequency after scattering. $\upsilon_{incident}$ is the frequency of the incident light, c is the speed of light, and ν is the velocity of the propagating capillary wave. Rearrangement of Eq. 2.26 yields:

$$v = \sqrt{\frac{g}{k} + \frac{\sigma k}{\rho}} \cong \sqrt{\frac{\sigma k}{\rho}} \qquad \text{(Eq. 2.39)}$$

Hence we have the observed frequency shift given as:

$$f_s = \left| \upsilon_{shifted} - \upsilon_{incident} \right| = \left(\frac{\nu k}{2\pi} \right) \qquad \text{(Eq. 2.40)}$$

As shown in Figure 2.18, the incident beams undergo both reflection and scattering at the A/W interface. The scattering from the diffracted beams are negligible owing to their low intensity. Only the scattering from the main laser beam is considered in SLS experiments. A PMT detector is responsible for collecting the scattering information. The light entering the PMT is a combination of the reflected diffraction order and the scattered laser beam of same wave vector represented as in Eq. 2.41:

$$k_i = \frac{2\pi}{\lambda_c} = \frac{2\pi}{\lambda_L} \cos\theta \sin\phi_i = \frac{2\pi}{\lambda_L} \cos\theta\phi_i \qquad \text{(Eq. 2.41)}$$

where k_i is the wave vector for the i^{th} diffraction order, λ_c and λ_L are the wave length of the capillary wave and laser, θ and ϕ represent the incident and scattering angle, respectively as shown in Figure 2.15.

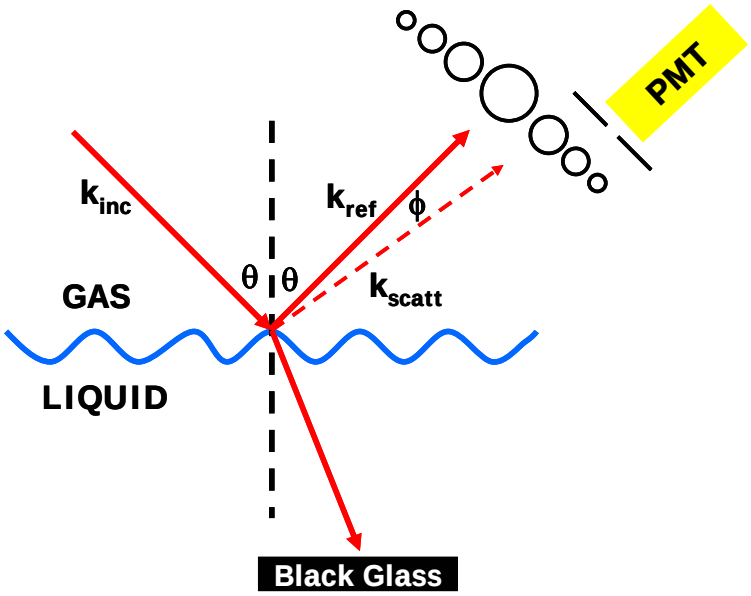

Figure 2.18. Schematic depiction of light scattered at the gas/liquid interface. The incident, reflected, and scattered wave vectors are indicated by k_{inc}, k_{ref}, and k_{scatt}, respectively. The PMT is a photomultiplier tube, while θ and ϕ correspond to the incident and scattering angle, respectively. The refracted beam is absorbed by a piece of black glass in the bottom of the trough.

2.5.5 SLS Data Analysis

SLS data analysis often takes two paths: (1) direct fitting of the heterodyne intensity correlation functions;[148-151] and (2) a Lorentzian fit of the power spectrum for the scattered light.[75,152-156] The second approach is adopted for data analysis in this dissertation. Figure 2.19 shows power spectra for different wave vectors obtained from water using the FFT analyzer. Power spectra like these are then fit with a Lorentzian function to deduce two key parameters: the frequency shift, f_s, and the experimental full width at half-maximum intensity, Δf_s.

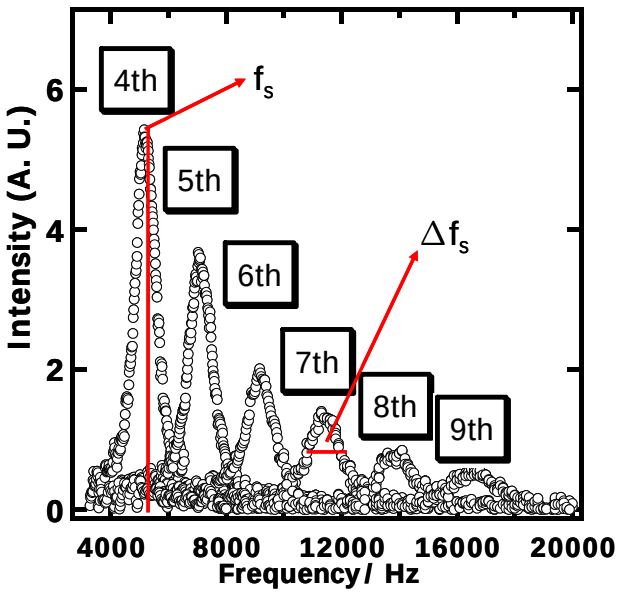

Figure 2.19. Power spectra from water at 22.5 °C corresponding to the 4th through 9th diffraction order. An example of a frequency shift, f_s, and an experimental full-width at half-maximum intensity, Δf_s, are indicated on the figure.[145]

Here, f_s is related to the propagation frequency of the capillary wave:

$$\omega_0 = 2\pi f_s \qquad \text{(Eq. 2.42)}$$

Δf_s must be corrected for instrumental broadening due to the Gaussian profile of the laser beam at the detector as done by following the procedure of Hård, *et al*:[55]

$$\Delta f_{s,c} = \Delta f_s - \frac{\Delta f_i^2}{\Delta f_s} \qquad \text{(Eq. 2.43)}$$

where Δf_i is the instrumental width and is given as:

$$\Delta f_i = \sqrt{2}\left(\frac{\Delta u_i \cos\theta_i}{R\lambda}\right)\left(\frac{\partial \omega_{0,k}}{\partial k}\right) \qquad \text{(Eq. 2.44)}$$

where θ_i is the incident angle, Δu_i is the full width at half-maximum intensity of the Gaussian laser beam profile of the i^{th} diffraction order, λ is the wavelength of the laser, R

is the distance between the detector and the interface, and $\omega_{0,k}$ is the real frequency at wave vector k.

$\Delta f_{s,c}$ is related with the damping coefficient (α) by:

$$\alpha = \pi \Delta f_{s,c} \qquad \text{(Eq. 2.45)}$$

After obtaining $\Delta f_{s,c}$, the dispersion equation Eq. 2.37 can be solved for the two dilational moduli, ε_d and κ. For pure liquid systems, f_s and $\Delta f_{s,c}$ can be used to solve for the dynamic surface tension (σ_d) and the bulk viscosity (η) of the liquid. Moreover, it is possible to use these values to calculate an equivalent frequency shift, $f_{s,eq}$, and an equivalent corrected full-width at half-maximum intensity, $\Delta f_{s,c,eq}$, at a chosen reference state. For this thesis, the reference state is chosen to be water at 25 °C. As such, the reference parameters are $\sigma_{d,ref}$ = 71.97 mN•m^{-1}, μ_{ref} = 0 mN•s•m^{-1}, k_{ref} = 324.3 cm^{-1}, ρ_{ref} = 997.0 kg•m^{-3} and η_{ref} = 0.894 Pa•s. As discussed in the next section, a common reference state allows direct comparisons for different systems to limiting cases of the dispersion equation (Eq. 2.37).

2.5.6 Polar Plot and Limiting Behavior

One very useful way to understand SLS results is to plot the $f_{s,eq}$ and $\Delta f_{s,c,eq}$ data from Section 2.5.5 onto a single polar plot containing the general solution for the dispersion equation on water at 25˚C as shown in Figure 2.20. The $\Delta f_{s,c}$-f_s are calculated for water at T = 25 ˚C. The solid curves represent ε_d in mN•m^{-1} while the dashed curves correspond to constant values of $\kappa \times 10^5$ in mN•s•m^{-1}. Six important limiting cases are obvious from this polar plot. The roman numerals (I – VI) on the figure correspond to these cases.

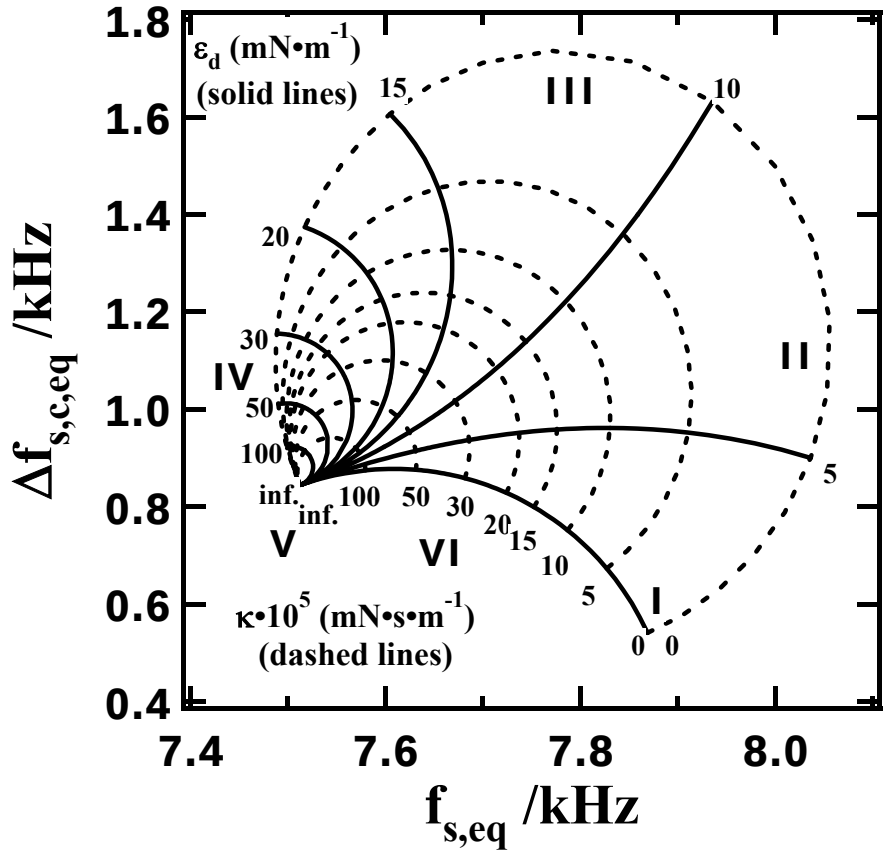

Figure 2.20. General solution for the dispersion equation on water at 25 ˚C, the reference state for this thesis. Calculated from Eq. 2.37 for k_{ref} = 324.3 cm^{-1}, $\sigma_{d,ref}$ = 71.97 mN•m^{-1}, μ_{ref} = 0 mN•s•m^{-1}, ρ_{ref} = 997.0 kg•m^{-3}, η_{ref} = 0.894 mPa•s, and g = 9.80 m•s^{-1}. The solid curves represent ε_d in mN•m^{-1} while the dashed curves correspond to constant values of $\kappa \times 10^5$ in mN•s•m^{-1}. The roman numerals (I – VI) on the figure indicate the limiting viscoelastic behavior. The limits correspond to pure liquid dynamics (I), the maximum velocity limit for a purely elastic surface film (PESF) (II), the maximum damping coefficient for a PESF (III), the minimum velocity limit for a PESF (IV), a surface film with an infinite lateral modulus (V), and the maximum damping coefficient for a purely viscous surface film (VI).[145]

I. Pure Liquid Limit (μ, ε_d, and $\kappa = 0$). Thompson (Lord Kelvin)[141] and Stokes[157] originally derived expressions for ω_o and α for capillary waves propagating on pure liquid surfaces, respectively. Langevin[142] reported corrected expressions to account for the effects of fluid viscosity and surface tension on ω_0 and α, respectively:

$$\omega_0 = 2\pi f_s = \sqrt{\frac{\sigma_d k^3}{\rho}}\left(1-\frac{1}{2}y^{-\frac{3}{4}}\right) \qquad \text{(Eq. 2.27)}$$

$$\alpha = \pi\Delta f_{s,c} = \frac{2\eta k^2}{\rho}\left(1-\frac{1}{2}y^{-\frac{1}{4}}\right) \qquad \text{(Eq. 2.46)}$$

II. Maximum Velocity Limit for a Purely Elastic Surface Film (μ and $\kappa = 0$). In this regime, the capillary wave propagates faster than on a pure liquid owing to the extra driving force ε_d can provide by coupling with the dynamic surface tension. However, the wave does experience greater damping than a pure liquid. Esker, *et al.*[89,123] treated this regime as a deviation from pure liquid dynamics (I) for ω_o and a deviation from the expression deduced by Dorrenstein[158,159] for the maximum damping coefficient for a liquid surface covered by a purely elastic surface film:

$$\omega_0 = 2\pi f_s = \sqrt{\frac{\sigma_d k^3}{\rho}}\left(1+\frac{1}{387}y^{\frac{21}{64}}\right) \qquad \text{(Eq. 2.47)}$$

$$\alpha = \pi\Delta f_{s,c} = \frac{\sqrt{2}}{2}\left(\frac{\sigma_d \eta^2 k^7}{\rho^3}\right)^{\frac{1}{4}}\left(1-\frac{2}{25}y^{\frac{5}{27}}\right) \qquad \text{(Eq. 2.48)}$$

where the valid range for y is between 210 and 490.

III. Maximum Damping Coefficient for a Purely Elastic Surface Film (μ and $\kappa = 0$). Dorrenstein originally proposed an expression for the maximum damping

coefficient for a liquid surface covered by a purely elastic surface film.[158,159] Esker, *et al.*[89,122,123] treated this regime as a deviation from pure liquid dynamics (I) for ω_o and a deviation from the expression deduced by Dorrenstein[158,159] for α:

$$\omega_0 = 2\pi f_s = \sqrt{\frac{\sigma_d k^3}{\rho}}\left(1-\frac{10}{17}y^{-\frac{9}{16}}\right) \qquad \text{(Eq. 2.49)}$$

$$\alpha = \pi\Delta f_{s,c} = \frac{\sqrt{2}}{2}\left(\frac{\sigma_d \eta^2 k^7}{\rho^3}\right)^{\frac{1}{4}}\left(1+\frac{4}{11}y^{-\frac{5}{32}}\right) \qquad \text{(Eq. 2.50)}$$

IV. Minimum Velocity Limit for a Purely Elastic Surface Film (μ and $\kappa = 0$). The capillary waves propagate with the slowest possible velocity. Esker, *et al.*[89,122,123] treated this regime as a deviation from pure liquid dynamics (I) for ω_o and a deviation from the expression deduced by Reynolds[160] for α for the damping coefficient of a surface film with a complex dilational modulus approaching infinity ($\varepsilon^* \to \infty$):

$$\omega_0 = 2\pi f_s = \sqrt{\frac{\sigma_d k^3}{\rho}}\left(1-\frac{5}{14}y^{-\frac{19}{64}}\right) \qquad \text{(Eq. 2.51)}$$

$$\alpha = \pi\Delta f_{s,c} = \frac{\sqrt{2}}{4}\left(\frac{\sigma_d \eta^2 k^7}{\rho^3}\right)^{\frac{1}{4}}\left(1+\frac{5}{3}y^{-\frac{25}{121}}\right) \qquad \text{(Eq. 2.52)}$$

V. Infinite Dilational Modulus Regime ($\mu = 0$, $\varepsilon^* \to \infty$). Reynolds[160] derived an expression for α on a liquid surface covered by a surface film with a complex dilational modulus approaching infinity ($\varepsilon^* \to \infty$). Esker, *et al.*[89,122,123] treated this regime as a deviation from pure liquid dynamics (I) for ω_o and a deviation from the expression deduced by Reynolds[160] for α as $\varepsilon^* \to \infty$:

$$\omega_0 = 2\pi f_s = \sqrt{\frac{\sigma_d k^3}{\rho}}\left(1-\frac{1}{4}y^{-\frac{1}{4}}\right) \qquad \text{(Eq. 2.53)}$$

$$\alpha = \pi \Delta f_{s,c} = \frac{\sqrt{2}}{4}\left(\frac{\sigma_d \eta^2 k^7}{\rho^3}\right)^{\frac{1}{4}}\left(1+\frac{1}{2}y^{-\frac{1}{4}}\right) \qquad \text{(Eq. 2.54)}$$

VI. Maximum Damping Coefficient for a Surface Covered by a Purely Viscous Surface Film (μ and $\varepsilon_d = 0$). Esker, *et al.*[89,122,123] treated this regime as a deviation from pure liquid dynamics (I) for ω_o and a deviation from the expression deduced by Reynolds[160] for α as $\varepsilon^* \to \infty$:

$$\omega_0 = 2\pi f_s = \sqrt{\frac{\sigma_d k^3}{\rho}}\left(1-\frac{3}{25}y^{-\frac{2}{11}}\right) \qquad \text{(Eq. 2.55)}$$

$$\alpha = \pi \Delta f_{s,c} = \frac{\sqrt{2}}{4}\left(\frac{\sigma_d \eta^2 k^7}{\rho^3}\right)^{\frac{1}{4}}\left(1+\frac{25}{22}y^{-\frac{8}{25}}\right) \qquad \text{(Eq. 2.56)}$$

Comparing SLS results with these limiting cases provides information of possible phase transitions, phase separation, and collapse phenomena for surface films.

2.6 Polymer Blends

Even before mankind started making synthetic polymers, the idea of blending two polymers had been utilized to enhance the physical properties of natural products (resins, natural rubber, cellulose, etc.). A natural resinous product, shellac, was added to nitrocellulose in the mid 1800s to improve the coating toughness. The combination of poly(vinyl chloride) PVC and butadiene-acrylonitrile (nitrile rubber: NBR) copolymer elastomer is one of the first commercialized polymer blends.[161,162] This blend has been available since the early 1940s and is still being used today. One of the most important discoveries in the history of polymer blends is the commercialization of poly (2,6-dimethyl-1,4-phenylene oxide) (PPO)/polystyrene (PS) blends by General Electric under

the trademark Noryl®. The PPO/PS blends were miscible and thus offered a property profile between these two polymers over the entire composition range.[163] The addition of PPO into PS increased the glass transition temperature (T_g), improved the toughness and mechanical strength, and also improved the flammability resistance of PS. These results catalyzed a major interest in polymer blends

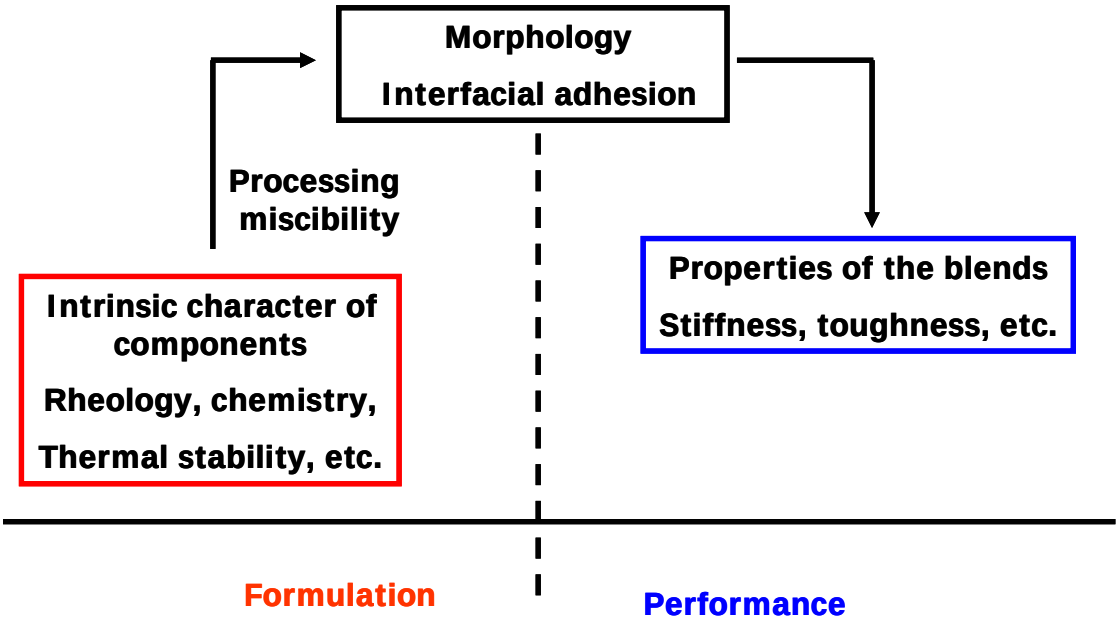

Figure 2.21: Schematic depiction of the formulation and evaluation of the performance involved in developing polymer blends

Figure 2.21 shows the procedure for developing new polymer blends, from formulation to performance evaluation. The first step is to choose the polymers with designed properties and modify the processing to insure their miscibility. Next, it is important to study the morphology and examine the interfacial adhesion of these two materials to understand their interactions. Therefore, it is necessary to characterize the physical and chemical properties of the blends to evaluate their performance under use

conditions. At the final stage property measurements feed back into the initial step to optimize performance.

2.6.1 Thermodynamics and Phase Diagrams of Polymer Blends

Miscibility is the most essential parameter in designing a polymer blends. For a perfect mixing, the polymer chains of the two polymers should be able to completely interpenetrate at a molecular level. However, most polymer blends are immiscible or only partially miscible.[129] The Gibbs free energy of mixing:

$$\Delta G_{mix} = \Delta H_{mix} - T\Delta S_{mix} \qquad \text{(Eq. 2.57)}$$

is comprised of the enthalpy of mixing (ΔH_{mix}) and the entropy of mixing (ΔS_{mix}). For most small molecule systems, ΔS_{mix} is large enough to overcome a positive ΔH_{mix}. Even when phase separation occurs, miscibility can usually be achieved by increasing the temperature. In contrast, polymers usually have relatively low translational entropy but high internal entropy relative to small molecules. Hence ΔS_{mix} is relatively small especially at high molar mass and the miscibility of polymer blends mostly depends on the enthalpic part.

The enthalpy of mixing for polymers is determined by a comparison of cohesive and adhesive forces. In other words, it depends on the interactions within the same component and the interaction between the two components. These interactions include hydrogen-bonding, dipole-dipole interactions, van der Waals interactions, electrostatic interactions, etc. ΔH_{mix} is given as

$$\Delta H_{mix} = \phi_1 \phi_2 RTn\chi_{1,2} \qquad \text{(Eq. 2.58)}$$

where ϕ_1 and ϕ_2 are the volume fraction of the two components, R is the gas constant, n is the number of moles of the monomers, and the Flory-Huggins interaction parameter, $\chi_{1,2}$ is defined as:

$$\chi_{1,2} = \frac{Z\left[\frac{(\varepsilon_{1,1} + \varepsilon_{2,2})}{2} - \varepsilon_{1,2}\right]}{k_B T} \qquad \text{(Eq. 2.59)}$$

where $\varepsilon_{i,j}$ are the interaction energies between components i and j, Z is the coordination number of the lattice, generally assumed to be 8, but it ranges from 6 to 12, and k_B and T are Boltzman's constant and the absolute temperature. Combining Eqs. 2.57 through 2.59, the Gibbs free energy of mixing is described by the Flory-Huggins equation:[134]

$$\Delta G_{mix} = RTn\left(\frac{\phi_1}{N_1}\ln\phi_1 + \frac{\phi_2}{N_2}\ln\phi_2 + \chi_{1,2}\phi_1\phi_2\right) \qquad \text{(Eq. 2.60)}$$

where N_i represents the degree of polymerization for i^{th} component. The first two terms in the Flory-Huggins equation indicate the entropy of mixing and the last one corresponds to the enthalpy of mixing.

The Flory-Huggins theory discussed above is derived under the assumption that the volume per monomer of both polymers remains the same before and after mixing. However, this is not the case for most real polymer blends. This temperature independent volume change is then lumped in to the interaction parameter $\chi_{1,2}$ with a empirical equation:

$$\chi_{1,2} \cong A + \frac{B}{T} \qquad \text{(Eq. 2.61)}$$

where the temperature independent A is referred as the "entropic part" while the temperature dependent B/T term is called the "enthalpic part". For miscibility to occur,

ΔG_{mix} must be negative. If one considers Eqs. 2.60 and 2.61 together, with a positive B, decreasing temperature causes phase separation and thereby leads to an upper critical solution temperature blend (UCST Figure 2.22a). On the other hand, a negative B leads to a lower critical solution temperature (LCST Figure 2.22b) blend. To form a stable mixture, the condition described in Eq. 2.62 also needs be met:

$$\left(\frac{\partial^2 \Delta G_{mix}}{\partial \phi_i^2}\right)_{T,P} > 0 \qquad \text{(Eq. 2.62)}$$

Negative values for Eq. 2.62 lead to phase separation of the polymer blends into a phase rich in component 1 and another phase rich in component 2. This phase separation is known as spinodal demixing. Figure 2.22 shows the unstable region which lies inside the spinodal indicated by the dotted lines. The points on the spinodal curve (dotted lines in Figure 2.22) are defined by:

$$\left(\frac{\partial^2 \Delta G_{mix}}{\partial \phi_i^2}\right)_{T,P} = 0 \qquad \text{(Eq. 2.63)}$$

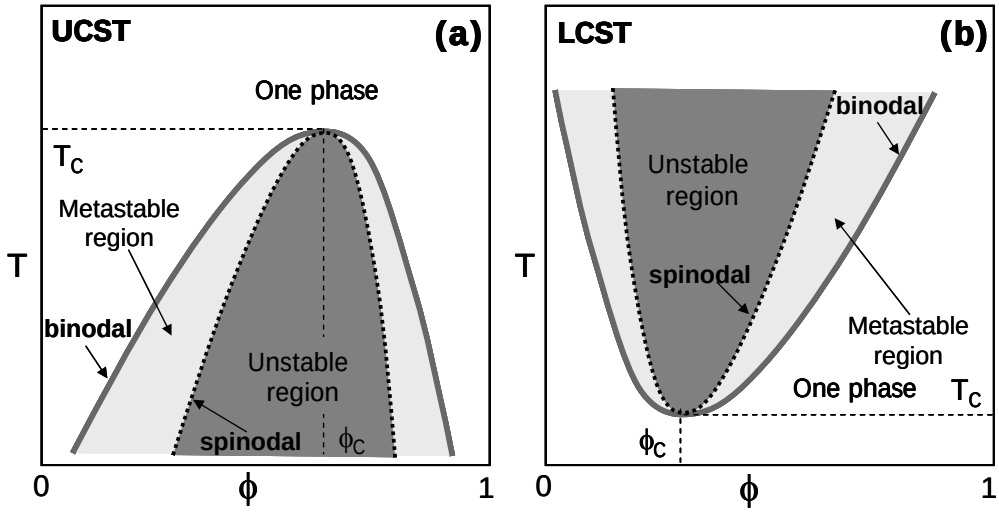

Figure 2.22: Schematic depictions of phase diagrams for polymer blends: (A) UCST and (B) LCST.

Tie lines between equivalent temperatures on the spinodal provide the compositions of the component-1 rich and component-2 rich phases. The solid lines in Figure 2.22 represent the binodal which is the equilibrium phase boundary between the single phase and the phase separated region. The region between the binodal and spinodal are metastable, where the mixture is stable against small composition fluctuations but not versus large ones. Blends in the metastable region achieve the end points of the tie lines connecting equivalent temperatures on the binodal through a nucleation and growth process. The endpoints of the tielines for the binodal are thermodynamically stable and at equilibrium. Hence, they are defined by the condition where the chemical potential of an individual component is equal in both phases:

$$\Delta\mu_1^{\,a} = \Delta\mu_1^{\,b} \qquad \text{(Eq. 2.64)}$$

where $\Delta\mu_i^j$ is the chemical potential of component i in phase j. The binodal curve can be generated by finding points that satisfy the condition:

$$\left(\frac{\partial G(\phi_j^1)}{\partial \phi_j}\right) = \left(\frac{\partial G(\phi_i^2)}{\partial \phi_i}\right) \qquad \text{(Eq.2.65)}$$

where ϕ_i^j is the composition of component i in phase j.

The critical point corresponds to the intersection of the binodal and spinodal where:

$$\left(\frac{\partial^3 \Delta G_{mix}}{\partial \phi_i^3}\right)_{T,P} = 0 \qquad \text{(Eq. 2.66)}$$

Using Eqs. 2.60, 2.65, and 2.66, it is possible to deduce the critical χ:

$$\chi_c = \frac{1}{2}\left(\frac{1}{\sqrt{N_1}} + \frac{1}{\sqrt{N_2}}\right)^2 \qquad \text{(Eq. 2.67)}$$

and the critical composition expressed in terms of component-1:

$$\phi_{1,c} = \frac{\sqrt{N_2}}{\sqrt{N_1} + \sqrt{N_2}} \qquad \text{(Eq. 2.68)}$$

For $\chi < \chi_c$, the binary blends should be completely miscible for the entire range of composition, for $\chi > \chi_c$, they will only be miscible for a region of temperature and composition space.

2.6.2 Physical Properties of Polymer Blends

Properties of interest for polymer blends include glass transition temperatures (T_g), strengths (tensile, flexural, compressive, etc.), impact strength, creep resistance, etc.[61,164-167] Many of the techniques used to characterize polymer blends ultimately relate to determining the phase behavior through T_g. Generally speaking, single phase blends will exhibit a single T_g somewhere between the T_g of the two individual components. Ideal mixtures will follow the Fox equation:

$$\frac{1}{T_{g,m}} = \frac{w_1}{T_{g,1}} + \frac{w_2}{T_{g,2}} \qquad \text{(Eq. 2.69)}$$

where $T_{g,i}$ corresponds to the T_g of i^{th} component and w_i is the weight percentage of i-th component. A T_g determination, while not a thermodynamic criterion for miscibility, is able to serve as an easy and effective method for deducing if the system is uniphasic.

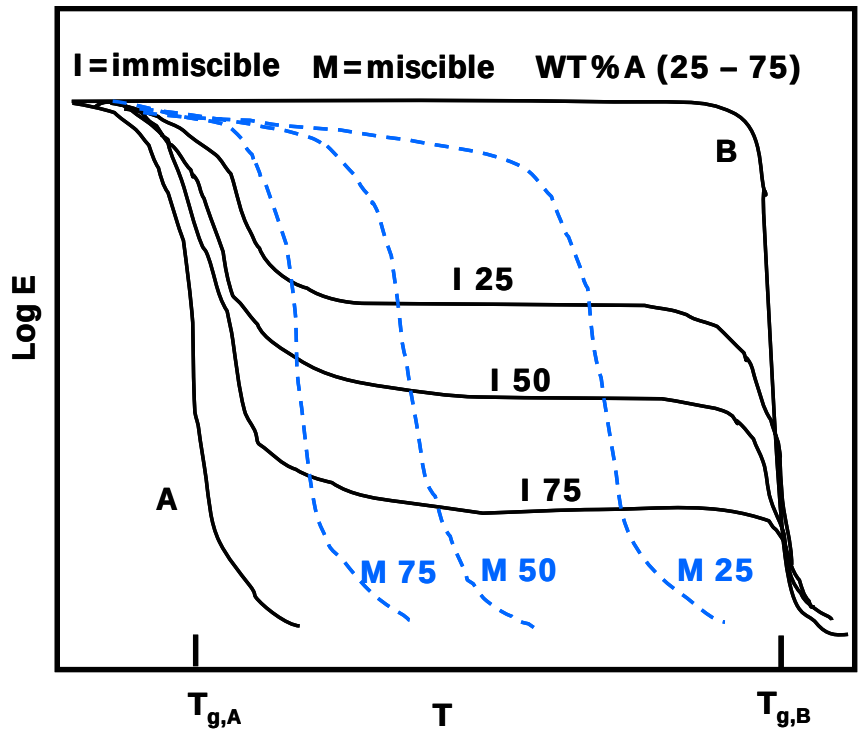

Figure 2.23: Generalized modulus-temperature behavior for single-phase and phase separated polymer blends. The leftmost (A) and rightmost curves (B) indicate tensile modulus (log E)-temperature (T) for the single components. The dotted curves (M 25 – M 75) represent log E-T for miscible polymer blends and solid curves (I 25 – I 75) represent log E-T for immiscible polymer blends. $T_{g,A}$ and $T_{g,B}$ indicate the glass transition temperature for single component A and B.

The mechanical properties of polymer blends strongly depend on phase behavior. Figure 2.23 shows generalized modulus (log E) – temperature (T) behavior for miscible and immiscible blends of two amorphous polymers with different T_g. The phase separated blends show a composition dependent plateau modulus between the T_gs of the two polymers. On the other hand, miscible blends show a single composition dependent T_g.

For miscible polymer blends, the modulus-composition behavior is strongly dependent on the T_g of the components since the T_g of the mixture is a function of the composition and modulus will exhibit a major change around T_g. For immiscible blends with a low T_g component and a high T_g component, the parallel and series models represent limiting cases for phase separated blends:

Parallel Model: $$E_b = \phi_1 E_1 + \phi_2 E_2 \quad \text{(Eq. 2.68)}$$

Series Model: $$E_b = \frac{E_1 E_2}{\phi_1 E_2 + \phi_2 E_1} \quad \text{(Eq. 2.69)}$$

Where E_1 and E_2 are the modulus of the two single components and E_b is the modulus of the blend. The parallel model provides an upper limit on E_b when the high modulus polymer is the continuous phase, whereas the series model provides a lower limit on E_b when the low modulus polymer is the continuous phase.

2.7 Polyhedral Oligomeric Silsesquioxanes (POSS) Model Nanoparticles

2.7.1 Hybrid Nanocomposite Materials

The use of composite materials dates back thousands of years when people mixed straw and mud in the form of bricks for building construction. In this composite material, straw served as the dispersed phase and reinforced the continuous phase. Although the system was ill-defined, the mixture had key features of a composite material: an engineered material made from two or more components with significantly different chemical and physical properties than any single component. Hybrid organic-inorganic materials contain both organic and inorganic components and are expected to yield materials between each extreme and also lead to unique properties that cannot be obtained from any single component system.[168] Numerous studies over the last several

decades have focused on formulating new composite materials.[169-172] Owing to the increasing demand for polymeric materials with tailored properties, the field of nanocomposite materials has generated considerable interest. Polymeric nanocomposites are polymers reinforced with nano-sized materials. The reinforcing material is defined as a nanofiller if at least one dimension is of nanometer scale.

Relative to conventional macro or micro-scale composites, the interfacial area between components can be much larger in nanocomposites. As a consequence, it is sometimes possible to obtain a desired level of property improvement with much less filler material.[173] The dispersion of the minor phase is essential to enhanced performance of composite materials since better dispersion will significantly enhance the interfacial area and consequently interfacial interactions. Sol-gel techniques have been applied to prepare emulsion polymeric composites. For this approach, the inorganic phase is well dispersed in the polymer matrix and aggregation is insignificant. However, the inorganic phase, which provides most of the mechanical strength may not be covalently attached to the organic phase and hence may only have limited interaction with the organic phase. Surface-modified clay has been studied as nanofillers to improve interactions between the organic and inorganic phases as the homogeneous dispersion of clay nanofillers is difficult. For the last two decades, a new class of slilicon based nanocomposite materials, polyhedral oligomeric silsesquioxanes (POSS), have attracted considerable interest. As a nanofiller, POSS molecules can be incorporated into polymer matrices by dissolution, polymerization, compounding, and coating.[61,174]

2.7.2 Polyhedral Oligomeric Silsesquioxanes (POSS)

Polyhedral oligomeric silsesquioxanes (POSS) are a new class of hybrid materials with an empirical chemical formula $(RSiO_{3/2})_n$ where R can be either hydrogen or an alkyl, alkenyl, aryl group, etc.[175] POSS was first reported by Scott in 1946[176] and is considered to be the smallest silica, molecular silica, to be exact.[175,177,178] The unique core-shell structure of POSS molecules (Figure 2.23) makes it compatible with numerous organic and polymeric materials. Therefore, POSS molecules can be applied in different fields such as, low-k dielectric materials,[179-181] semiconducting polymers,[182] shape memory materials,[183] space-survivable coatings,[184,185] and synthetic templates for nanostructured materials.[186-190] The incorporation of POSS molecules into polymers as a filler or through copolymerization can increase the glass transition temperature (T_g),[191,192] mechanical strength,[193-199] and thermal stability[200] of polymeric materials.

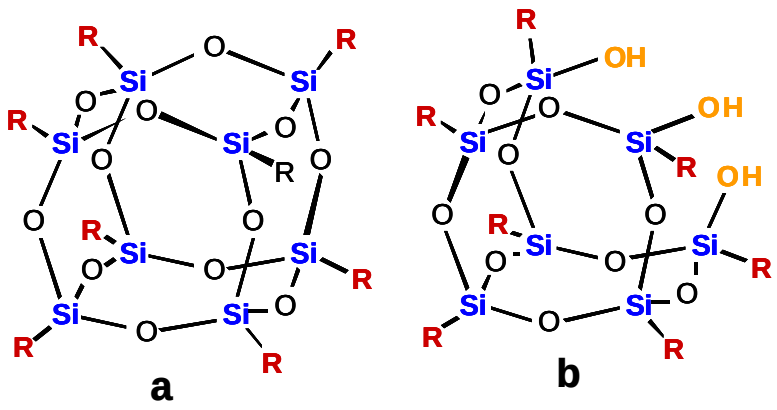

Figure 2.24: Chemical structures for (A) a closed-cage POSS, and (B) an open-cage trisilanol-POSS. R can be hydrogen or an alkyl, alkenyl, aryl group, etc.

Various chemical reactions can be used to create POSS and its derivatives.[201] The most general approach for creating POSS is the hydrolysis and condensation of monomers with formulae $XSiY_3$:[202]

$$n\mathrm{XSiY_3} + 1.5n\mathrm{H_2O} \rightarrow (\mathrm{XSiO_{1.5}})_n + 3n\mathrm{HY}$$

where X is a chemically stable ligand such as CH_3, phenyl, or vinyl, while Y can be a chemically reactive chloride or alkoxy group. This reaction frequently leads to a mixture of different POSS derivatives depending on the starting material, solvent, catalyst, and experimental conditions. Heptameric silsesquioxanes ($R_7T_7(OH)_3$) (Figure 2.23B) are the predominant trisilanol product. The products can also contain octafunctional silsesquioxanes (R_8T_8) (Figure 2.23A), larger cages, hexamers (R_6T_6), and linear and branched oligomers. $R_7T_7(OH)_3$ can be separated from the other products because of solubility differences arising from the three silanol groups. A trisilanol-POSS can be used to make a closed cage POSS where one ligand is different from the other seven by reacting $R_7T_7(OH)_3$ with R'Si(OEt)$_3$, so-called corner-capping.[202-205] R' can also be the same functional group as R to form the octafunctional POSS. Haddad first synthesized the styryl POSS polymers through AIBN-initiated free-radical polymerization from styryl-substituted POSS, $R_7(Si_8O_{12})(CH_2CH_2C_6H_4CH{=}CH_2)$, where R is either cyclohexyl or cyclopentyl group.[206] Despite the bulkiness of the POSS cage, styryl-POSS polymerized surprisingly easily and high molar mass polymers were obtained. Later, Pyun and Matyjaszewski applied atomic transfer radical polymerization (ATRP) to the synthesis of methacrylate POSS homopolymer and copolymers.[207] Most POSS polymers including norbornyl-POSS polymers,[208] vinyl-POSS polymers,[209] epoxy-POSS polymers[210] can be synthesized via similar approaches. Owing to the corner-capping

technique for preparing different POSS monomers, there are virtually limitless possibilities for synthesizing novel, functional POSS polymers. Many researches have focused on the structure-property relationships for POSS-polymers in bulk system. Mather and Haddad used POSS-norbornyl polymers as a model system to systematically study POSS interactions at the molecular level by manipulating the weight percentage and type of POSS.[208] Subsequent T_g, rheology, and TEM studies suggested slight changes in POSS domain size could cause dramatic changes in T_g. Coughlin *et al.*[211] proposed a visual model based on their morphology result of POSS-polybutadiene and polyethylene copolymers where POSS likely forms a raft-like or lamellar structure within the polymer matrix. Furthermore they proposed that 2-D POSS networks are likely present in most POSS copolymers due to the constraints imposed by the polymer chains. Wu *et. al.*[212] examined the T_g and mechanical property of styrene-*r*-styryl isobutyl-POSS copolymers where the POSS component actually serves as a plasticizer and increases the free volume of the polymer matrix owing to its finite size.

Relatively few researchers have focused on the interfacial properties of POSS polymers, but some attempts have been made. Paul *et. al.*[61,213] examined phase separation and dewetting of trisilanolphenyl-POSS (TPP)/polymer bilayer model systems as well as blend thin films on solid substrates. The results show that TPP/poly(tert-butyl acrylate) (PtBA) blend thin films exhibit LCST phase behavior with a critical temperature of ~70 °C and a critical composition (X_c) of 60 wt % PtBA with insignificant dewetting at the phase boundary. In TPP/PtBA bilayers, with short annealing time, only the upper TPP layer dewets from the underlying PtBA layer and dewetting of the lower PtBA layer is restricted to a few isolated holes even with long annealing time. In TPP/PS bilayer

system, dewetting of both the upper TPP and the lower PS layers was observed. Tuteja *et. al*.[214] systematically studied the superoleophobicity of poly(methyl methacrylate) (PMMA) thin films blended with Fluoro-POSS. The stability and optical properties of POSS/polymer blends thin films have also been studied recently.[215,216]

Since Deng, *et al.*[29,30,37,38] discovered that some trisilanol-POSS molecules are amphiphilic and are able to form insoluble monolayers at the air/water (A/W) interface, Langmuir film systems have become an excellent model system for the study of the interfacial property of POSS derivatives[29,30,37,38] and POSS/polymer blend systems.[31-33,125] Compared with conventional amphiphilic materials such as fatty acids and phospholipids, POSS derivatives exhibit much simpler phase transitions owing to their spherical structure. Trisilanolcyclohexyl-POSS forms ordered, crystal like structures with large shear moduli upon compression.[29] Furthermore, trisilanolisobutyl-POSS was used to blend with functionalized silicones including regular hydrophobically terminated PDMS,[31] poly(dimethyl-co-methylvinyl-co-2-diphenyl phosphine oxide ethyl) siloxane (PDMS-PO),[125] poly(3-cyanopropyl, methyl) (PCPMS), poly(dimethyl-co-methylhydrido-co-3-cyanopropyl, methyl) siloxane (PDMS-CN).[33] In these systems, the monolayer states were completely homogeneous, however, morphologies in the collapsed regime differed depending on whether TiBuP or the silicone collapsed first. If the silicone collapsed first, networks of nanoparticle aggregates eventually formed once the TiBuP component collapsed, whereas, discrete aggregates of TiBuP formed if TiBuP collapsed prior to the silicone. In contrast, octaisobutyl-POSS/PDMS blends[32] were also investigated where all blends exhibit similar phase behavior as PDMS and octaisobutyl-POSS likely exists as multilayer at all Π. Ring-like structures were also captured during

the expansion isotherm showing that the non-amphiphilic octaisobutyl-POSS might also form networks via a different mechanism. A direct investigation of the reinforcing behavior of POSS derivatives as nanofiller material should be a natural next step and is the main focus of this thesis.

CHAPTER 3

Materials and Experimental Methods

This chapter introduces the materials and experimental techniques that are used in this dissertation. The description of materials and experimental methods will not be repeated in subsequent chapters.

3.1 Materials

3.1.1 Polyhedral Oligomeric Silsesquioxanes (POSS)

Trisilanolisobutyl-POSS (TiBuP), trisilanolethyl-POSS (TEtP), trisilanolphenyl-POSS (TPP), trisilanolcyclopentyl-POSS (TCpP), trisilanolcyclohexyl-POSS (TCyP), and octaisobutyl-POSS (OiBuP) obtained from Hybrid Plastics, Inc. are dried in a vacuum oven for 3 days at 40°C before use. All POSS samples are dissolved in chloroform (0.02-0.5 $mg \cdot g^{-1}$ HPLC grade) solution. All samples are sonicated (Fisher Scientific FS140H) for an hour and are sealed in special glass vials for 24 to 36 hours to allow dissolution.

3.1.2 Poly(dimethylsiloxane) (PDMS), PDMS-stabilizer, and PDMS Stabilized Magnetic Nanoparticles (PDMS-MNPs).

Trimethylsilyl-terminated PDMS (PDMS, number average molar mass, M_n = 7.5 $kg \cdot mol^{-1}$, and polydispersity index, M_w/M_n = 1.09), initiated with sec-butyl lithium was obtained from Polymer Source, Inc. and was used without further purification. The TiBuP/PDMS, OiBuP/PDMS, and TCpP/PDMS blends described in Chapter 5, 6 and 7

are prepared by solvent mixing. The PDMS-stabilizer and PDMS-MNPs (Figure 3.1) were synthesized by the Riffle research group at Virginia Tech following published procedures.[217] ^{1}H-NMR yielded M_n = 2.5 kg·mol^{-1} for the PDMS-stabilizer. For the PDMS-MNPs, the graft density of PDMS chains calculated from transmission electron microscopy (10 nm diameter particles) and thermal gravimetric analysis (50 wt% magnetite) was ~1.25 PDMS-Stabilizers per nm^2. Spreading solutions were prepared with nominal concentrations of ~0.5 mg·mL^{-1} in HPLC grade chloroform.

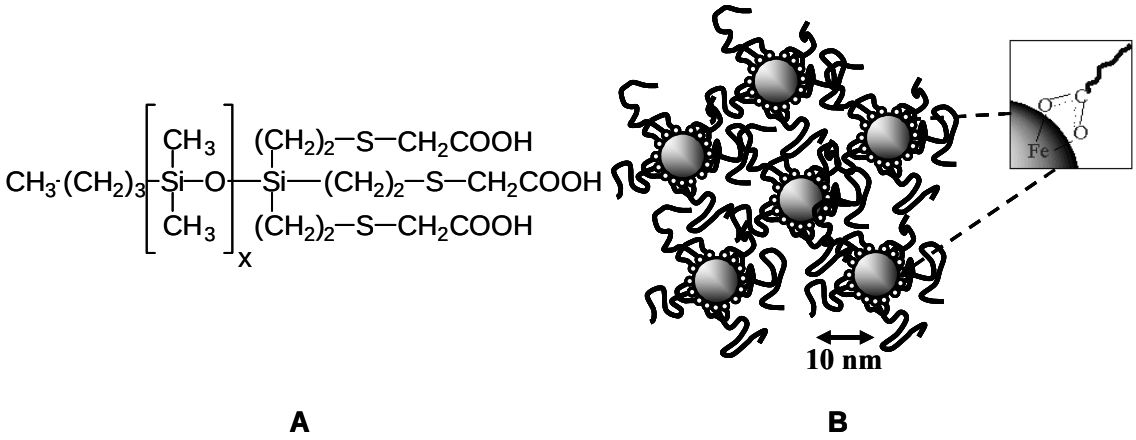

Figure 3.1. (A) Molecular structure of the PDMS-stabilizer (x = 28). (B) A schematic depiction of PDMS-MNPs. The dots symbolize carboxylic acid groups and squiggly lines represent PDMS chains. The inset shows carboxylic acid binding to the magnetite surface.

3.2 Experimental Methods

3.2.1 Π-A Isotherm Measurements

The Langmuir trough (700 cm^2, Nima Technology Ltd. 601 or 701 BAM) made of hydrophobic Teflon® was cleaned by dichloromethane and Millipore water. Two

movable barriers made of a hydrophilic acetal resin polymer (Delrin®) are cleaned with isopropanol. The Langmuir trough is then filled with ultrapure 18.2 MΩ·cm water (Millipore, Milli-Q Gradient A-10, 10 ppb organic impurities). Prior to Π-A isotherm measurement, the barriers were automatically closed to collect dust and surface active compounds at the A/W interface. Then a glass pipette connected to vacuum pump is used to suction off these impurities. This procedure is repeated several times until the surface pressure change is less than 0.1 $mN \cdot m^{-1}$ when closing the barriers. 20 to 30 mins are allowed prior to spreading the film to ensure that the temperature of the subphase (water) reaches equilibrium. Chloroform solutions of desired samples with predetermined mass concentrations are then spread via a glass MICROLITER* syringe (Hamilton) onto the subphase. A completely wetted paper plate is used to record the surface pressure via Wilhelmy plate technique to ± 0.1 $mN \cdot m^{-1}$ as described in Section 2.2.1. The trough areas and surface pressures are collected by a computer through a Nima IU4 interface to obtain the Π-A isotherms.

3.2.2 Constant Compression Rate Experiments

Constant compression rate experiments are the most fundamental Π-A isotherm measurements. They are used to identify possible phase transitions and deduce molecular orientation for amphiphilic materials. Constant compression rate experiments can also be adopted to probe the collapse behavior of amphiphilic materials by manipulating the compression rate. For this type of experiment, the two opposing barriers compress the surface film at a constant rate, typically from 10 – 40 $cm^2 \cdot min^{-1}$. Unless otherwise mentioned, all compression experiments presented in this dissertation use a compression rate of 10 $cm^2 \cdot min^{-1}$.

3.2.3 Successive Addition Experiments

In contrast to constant compression rate experiments that may yield non-equilibrium Π-A isotherms, successive addition experiments are used to probe the "equilibrium" phase behavior of the Langmuir films by allowing enough time between concentration points for the Langmuir film to relax to a constant Π value. The apparent difference between these two methods is described in Section 2.2.5. For successive addition experiments, the trough area is held constant (the barriers stay at a predetermined position). Surface area occupied per molecule (A) is manipulated by successive additions of sample solution. After each addition, the Langmuir film is allowed to relax until $\Delta\Pi < 0.1$ mN·m^{-1} over a 15 min period.

3.2.4 Brewster Angle Microscopy (BAM)

BAM studies (MicroBAM, NanoFilm Technologie, Ltd., lateral resolution of 8 μm) were carried out simultaneously during isotherm measurements, and BAM images were taken by a charge-coupled device (CCD). The original size of all BAM images taken during the measurements was 3.6×4.8 mm^2, while some BAM images presented in this dissertation with smaller sizes were cut from the original images utilizing imaging software.

3.2.5 Surface Light Scattering (SLS)

A homemade SLS instrument was constructed based on the design of Sano *et al.*[54] that incorporated the advances made by Hård and Neuman.[124] The instrument uses a 15 mW He:Ne laser with a wavelength of 632.8 nm, an incident angle of $\theta_i = 66.00^\circ$ and a distance of R = 3.40 m from the air/liquid interface to the detector. The transmission

diffraction grating generated different diffraction orders that serve as reference beams for heterodyne detection. Water calibration was used to determine the wave vector q and Δu_i (the full width at half-maximum intensity of the Gaussian laser beam profile of the i-th diffraction order) for 7^{th} through 9^{th} order diffraction: 404.3 cm^{-1} and 0.0519 cm, 459.0 cm^{-1} and 0.0531 cm, and 512.6 cm^{-1} and 0.051 cm, respectively. For SLS measurements, the solutions were spread onto the surface of a home built Langmuir trough (174 cm^2) maintained at 22.5 ^oC and Π was measured simultaneously by the Wilhelmy plate technique. The surface concentration is controlled by successive additions of chloroform solution and SLS measurements commenced once a stable Π value was obtained ($\Delta\Pi <$ 0.1 mN • m^{-1} over a 15 minute period), with a minimum waiting time of 20 minutes to allow for spreading solvent evaporation.

CHAPTER 4

Surface Rheology of Trisilanolisobutyl-POSS at the Air/Water Interface

Most of this chapter is reproduced with permission from: **Yin, W.**; Deng, J.; Esker, A. R. "Surface Rheology of Trisilanolisobutyl-POSS at the air/water interface" accepted by Langmuir.

4.1 Abstract

Trisilanol polyhedral oligomeric silsesquioxane (POSS) derivatives have recently been reported as a new class of amphiphilic molecules that form stable Langmuir monolayers at the air/water interface and exhibit interesting phase transitions and aggregation behavior. In this chapter, surface light scattering (SLS) has been used to probe the dilational viscoelastic behavior of trisilanolisobutyl-POSS in the monolayer regime of its surface pressure-area per molecule isotherm at 22.5 °C. Results showed that the static dilational elastic modulus is in excellent agreement with the dynamic dilational elastic modulus in the monolayer regime over the limited wave vector range of 404.3 to 512.6 cm^{-1}. The films possessed a moderate maximum dynamic dilational elastic modulus (~ 50 $mN \cdot m^{-1}$) prior to film collapse. Moreover, the films exhibited small surface viscosities such that the films are almost purely elastic over the frequency range studied throughout the monolayer regime.

4.2 Introduction

Polyhedral oligomeric silsesquioxanes (POSS), hybrid organic-inorganic materials, were first reported by Scott in 1946.[176] POSS materials have since attracted considerable interest because of potential applications in semiconducting polymers,[182] shape memory materials,[218] space-survivable coatings,[184] and as synthetic templates for nanostructured materials.[187] The unique inorganic-organic core-shell structure also made it possible to incorporate POSS into different polymers for reinforcement,[219,220] or improved physical and chemical properties like low-k dielectric constants,[179] increased glass transition temperatures,[192] superoleophobicity,[214] and thermal stability.[221] The size of POSS molecules, ~ 1.5 nm in diameter,[177] leads to large surface area to volume ratios that should make the interfacial properties of POSS important for their use in nanomaterials. However, relatively few early studies concentrated on the surface behavior of POSS materials.[222-225] Since Deng, *et al.*[38] discovered that some POSS molecules form insoluble Langmuir films at the air/water (A/W) interface, subsequent studies have probed the phase behavior of multilayer POSS films and POSS/polymer blends by Brewster angle microscopy (BAM).[29-32,38,226] Furthermore, surface studies on solid substrates have followed.[61,213-216,227,228]

A natural extension of surface pressure-area (Π-*A*) isotherms and BAM studies at the A/W interface is rheological studies. An understanding of the rheological properties of Langmuir films is essential for Langmuir-Blodgett (LB) film formation and the dynamic stability of gas/liquid and liquid/liquid interfaces. Many different techniques have been applied to study the interfacial rheology of Langmuir films, including mechanically generated waves,[117] electrocapillary wave diffraction (ECWD),[49,229] canal

viscometry,[113] interfacial stress rheometry (ISR),[29,58,59] surface pressure relaxation studies,[230] and surface light scattering (SLS).[118,122,123,126,147,148,153,154,231] In this chapter, SLS and Π-A isotherms were employed to study the dynamic dilational rheology of trisilanolisobutyl-POSS molecules at the A/W interface. SLS was chosen to probe dilational viscoelastic behavior in the monolayer over methods for probing shear moduli because a previous ISR study showed that shear moduli for trisilanolcyclohexyl-POSS (a homologous compound that should actually be more rigid on the basis of the Π-A isotherm) in the monolayer regime are small (~1 x 10^{-3} mN·m^{-1} for both the storage and loss moduli).[29]

4.3 Results and Discussion

A Π - A isotherm obtained by successive addition for trisilanolisobutyl-POSS is provided in Figure 4.1. Trisilanolisobutyl-POSS formed an insoluble Langmuir film at the A/W interface.[38,226] The POSS isotherm exhibited three different regimes: [38,226] (A) A > $A_{lift\text{-}off}$ = 230 $Å^2$·$molecule^{-1}$ (where $A_{lift\text{-}off}$ is the *A* value where Π starts to increase) corresponding to the end of submonolayer regime (Π = 0 mN·m^{-1}) where POSS films are likely biphasic with the coexistence of gaseous and liquid-like domains; (B) 140 < A < 230 $Å^2$·$molecule^{-1}$ corresponding to a condensed (LC) monolayer, and (C) A < 140 $Å^2$·$molecule^{-1}$ where POSS films collapse into multilayers at Π ~ 12.5 mN·m^{-1}. Treatment of the POSS molecule as a sphere at the on-set of the collapse transition yielded the diameter of the molecule. A value of ~134 $Å^2$ at the on-set of the collapse transition deduced from the cross-sectional area of the sphere versus the value of ~160 $Å^2$ estimated from the extrapolated limiting area of the molecule,[38,226] indicated that the open cage

POSS structure is moderately compressible. SLS measurements that will be provided later confirmed this interpretation.

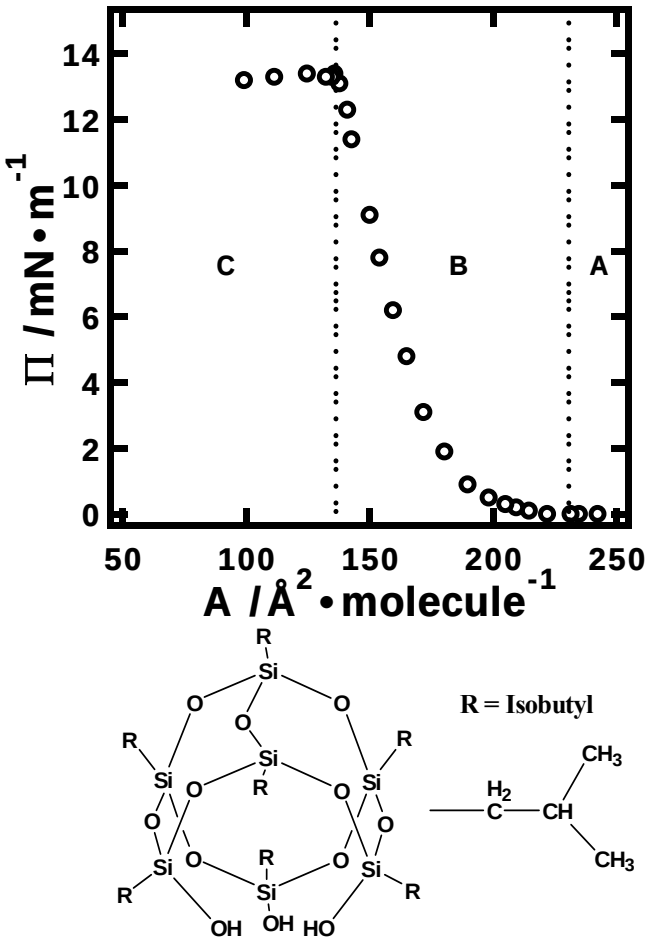

Figure 4.1. Π–A addition isotherm at T = 22.5 °C and the chemical structure of trisilanolisobutyl-POSS. Vertical dotted lines indicate boundaries for Regimes A through C.

SLS data presented in Figure 4.2 were analyzed using the approach of Esker *et al.*,[39] which is based on the method used by Hård and Neuman.[55] f_s and $\Delta f_{s,c}$ data were obtained at three different wave vectors corresponding to k = 404.3, 459.0 and 512.6 cm^{-1} (7^{th}

through 9th order diffraction). These values, along with surface tension data, were used to calculate ε_d and κ with the aid of a dispersion equation[56] for capillary wave propagation at the A/W interface.[123] After observing that ε_d and κ were frequency independent, all SLS data were converted to a common reference state. In this procedure, the deduced ε_d and κ, along with the dispersion equation at different k, were used to calculate viscoelastically equivalent values of the frequency shift ($f_{s,eq}$) and full-width at half-maximum intensity ($\Delta f_{s,c,eq}$) at a reference state corresponding to a reference wave vector (k_{ref} = 324.3 cm^{-1}), surface tension ($\sigma_{d,ref}$ = 71.97 $mN \cdot m^{-1}$), subphase density (ρ_{ref} = 997.0 $kg \cdot m^{-3}$), bulk shear viscosity (η_{ref} = 0.894 mPa·s), and transverse viscosity (μ_{ref} = 0). As these data were frequency independent, the data points for $f_{s,eq}$ and $\Delta f_{s,c,eq}$ in Figure 4.2 represent an average of the three wave vectors with one standard deviation error bars. The two vertical dotted lines in Figure 4.2 correspond to the boundaries between Regime A and Regime B and between Regime B and Regime C as defined in Figure 4.1. The three horizontal dotted lines represent three different limiting cases for viscoelastic behavior: (I) pure liquid behavior (ε_d, κ, and $\mu = 0$), (III) the maximum damping coefficient for a purely elastic film (where damping of capillary waves is the strongest), and (IV) the minimum velocity for a purely elastic surface film (where capillary wave velocity is the slowest).[122,123,231] Two other important limits for perfectly elastic films: (II) the maximum velocity and (V) the infinite lateral modulus limit have been omitted for clarity.

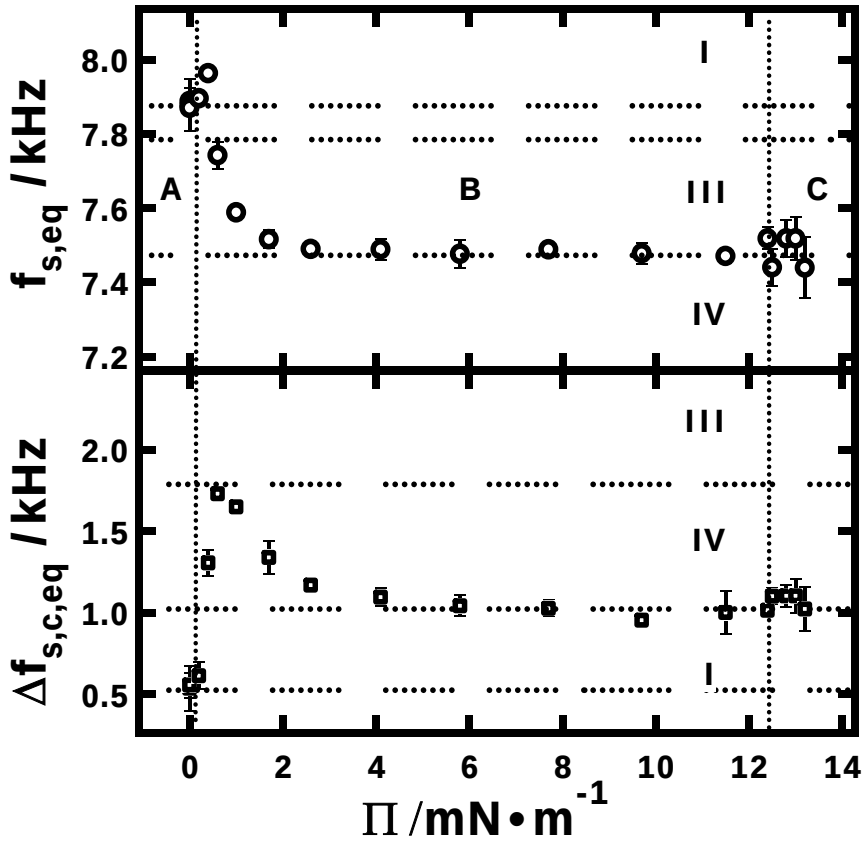

Figure 4.2. Plots of $f_{s,eq}$ - Π (top, circle) and $\Delta f_{s,c,eq}$ − Π (bottom, square) for trisilanolisobutyl-POSS. Data points represent an average of three wave vectors with one standard deviation error bars. Vertical dotted lines indicate Regimes A through C defined in Figure 4.1. Horizontal dotted lines correspond to limiting behavior[39,40,44] of the dispersion relation:[47] (I) pure liquid limit, (III) the maximum damping coefficient for a perfectly elastic surface film, and (IV) the minimum velocity for a perfectly elastic surface film.

In Regime A, trisilanolisobutyl-POSS behaved as a pure liquid (I). As surface concentration increased, a monolayer formed at the A/W interface (crossover from Regime A to B). Around this transition, two things happened. First, $f_{s,eq}$ reached a maximum before starting a monotonic decay. This maximum is consistent with the

formation of an elastic film with a small dilational elasticity and viscosity. Likewise, $\Delta f_{s,c,eq}$ increased quickly and reached a maximum at $\Pi \sim 0.6$ mN·m^{-1}. As was previously noted,[123,126] a peak in the $\Delta f_{s,c,eq} - \Pi$ plot where the value of $\Delta f_{s,c,eq}$ approaches the limiting case of the maximum damping coefficient for a perfectly elastic surface film (III) means $\varepsilon_d/\sigma_d \sim 0.17$. Hence, trisilanolisobutyl-POSS Langmuir films have $\varepsilon_d \sim 10$ mN·m^{-1} at $\Pi \sim 0.6$ mN·m^{-1}. For many polymeric Langmuir film systems,[123,231] the corresponding peaks for $\Delta f_{s,c,eq}$ appeared instantly as Π deviated from 0 mN·m^{-1}. Here, the more gradual increase in $\Delta f_{s,c,eq}$ is attributed to hydrogen bonding between the three silanol groups of trisilanolisobutyl-POSS and water molecules which are squeezed out of the film during monolayer formation around the boundary between Regimes A and B. After the transition (Regime B), both $f_{s,eq}$ and $\Delta f_{s,c,eq}$ exhibited a monotonic decay with values approaching those of a perfectly elastic surface film with dilational viscoelastic characteristics that are consistent with the minimum velocity limit of the dispersion equation (IV) over the range of $\sim 3 < \Pi < \sim 12.5$ mN·m^{-1}. In Regime C, BAM studies showed that trisilanolisobutyl-POSS films collapse into a heterogeneous film with multilayer regions.[38,226] After collapse of the film begins, Π remains constant at ~ 12.5 mN·m^{-1}. Furthermore, $f_{s,eq}$ and $\Delta f_{s,c,eq}$ values do not change and the film retained dilational dynamics that are consistent with a liquid covered by a perfectly elastic film in the minimum velocity limit (IV).

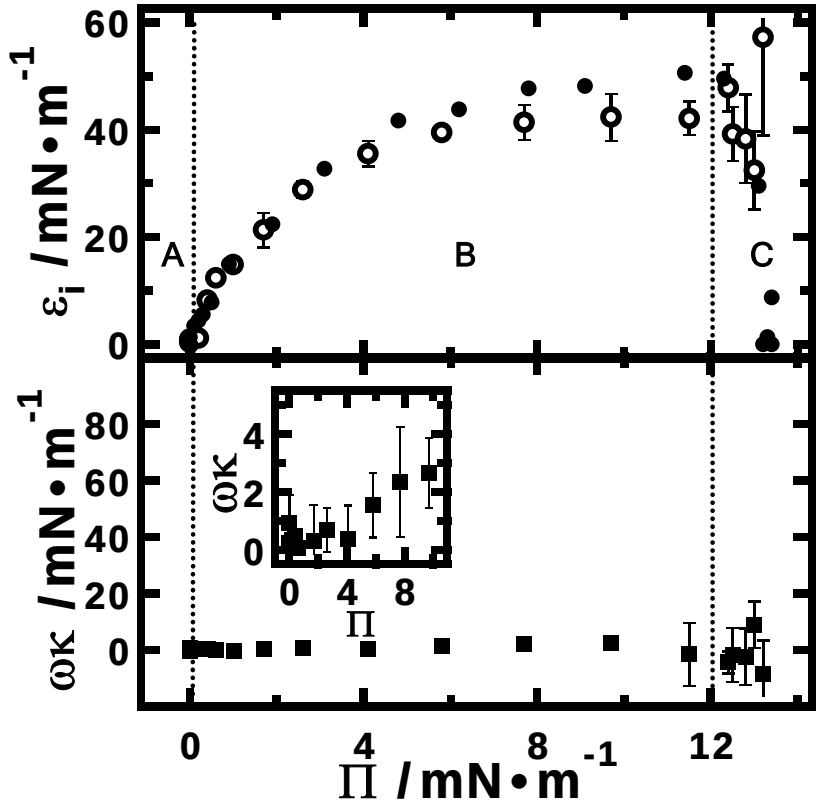

Figure 4.3. Plots of ε_i-Π (top) and ωκ-Π (bottom, filled triangles) for trisilanolisobutyl-POSS. ε_s values (top, filled circles) are deduced from Figure 4.1. ε_d (top, open circles) and ωκ values represent the average of three different wave vectors with one standard deviation error bars. Dotted vertical lines indicate the boundaries of the same regimes defined in Figure 4.1. The inset of the bottom graph expands ωκ vs. Π to show the small but continuous increase in ωκ with respect to Π in the monolayer regime.

Dynamic dilational viscoelastic parameters deduced from SLS measurements of trisilanolisobutyl-POSS films at the A/W interface as a function of Π are presented in Figure 4.3. The upper panel of Figure 4.3 contains ε_d and is compared to the corresponding static dilational elasticity calculated from Figure 4.1

using $\varepsilon_s = -A\left(\partial\Pi/\partial \mathrm{A}\right)_T$. The lower panel of Figure 4.3 shows the dilational loss modulus ($\omega\kappa$) as a function of Π. In the sub-monolayer regime (A), incomplete surface coverage led to a film lacking viscoelastic character (ε_d and $\omega\kappa \sim 0$). In Regime B, the monolayer state, both ε_d and ε_s rose sharply with increasing Π and agreed closely up to Regime C, the collapsed state. The maximum values of ε_d and ε_s before film collapse were ~ 43 and ~ 49 $mN \cdot m^{-1}$, respectively. Furthermore, $\omega\kappa$ exhibited small values, $\omega\kappa < 3$ $mN \cdot m^{-1}$, that rose gently with Π (inset of the lower panel of Figure 4.3) until film collapse (Regime C), where the $\omega\kappa$ values exhibit large scattering. $\omega\kappa$-Π plot allowed the loss tangent ($\tan\delta = \omega\kappa/\varepsilon_d$) to be easily deduced. ε_d and $\omega\kappa$ values in Figure 4.3 yielded $\tan\delta \sim 1$ (a balance of the viscous and elastic contribution) for submonolayer coverage and values of $\tan\delta < 0.1$ (elastic dominant films) in Regime B (the monolayer at $\Pi < 9$ $mN \cdot m^{-1}$). At the end of Regime B, $\tan\delta$ values rose to $\tan\delta \sim 0.5$ as $\omega\kappa$ increased. Within Regime C, ε_s fell to zero, whereas ε_d, $\omega\kappa$, and consequentially $\tan\delta$ maintained values comparable to those at the collapse transition.

The excellent agreement between ε_d and ε_s in the monolayer state (Regime B), along with small $\omega\kappa$ values, are consistent with a monolayer that is almost perfectly elastic. Another interesting feature of Regime B is the large initial slope $\left(d\varepsilon_d/d\Pi\right) \sim 13$. The slope in this region of the monolayer is controlled by two main factors: amphiphile-water and amphiphile-amphiphile interactions. In traditional small molecule amphiphiles, large initial slopes for ε_d-Π indicate rigid films with efficient packing of the hydrophobic portions of the molecules as one may see for stearic or arachidic acid.[67,232] In contrast, smaller slopes occur in systems like oleic acid[233] where cis-unsaturation in the

hydrophobic tail hinders packing to create a more compressible monolayer. For polymeric systems, the changes in slope correlate with good solvent (water-swollen polymer chains) and poor or theta solvent (films with minimal water) conditions.[130] When the A/W interface behaves as a good solvent, $\left(d\varepsilon_d/d\Pi\right) \sim 3$, whereas $\left(d\varepsilon_d/d\Pi\right) \sim$ 8-100 when the A/W interface behaves as a poor solvent. Some examples of polymers where the A/W interface is reported to be a good solvent include: polymers (poly(vinylacetate) (PVAc), poly(methylacrylate) (PMA), poly(tetrahydrofuran) (PTHF), and poly(ethylene oxide) (PEO).[123,126] In contrast, polymers such as poly(*t*-butylmethacrylate) (PtBMA), poly(methylmethacrylate) (PMMA) and poly(dimethylsiloxane) (PDMS) represent classical examples of polymers for which the A/W interface acted as a poor solvent.[57,123,126] Considering the structural similarity between trisilanolisobutyl-POSS and PDMS, amphiphile-water interactions should be substantially less important than intermolecular interactions for explaining both the Π-A isotherm and dilational viscoelastic behavior of trisilanolisobutyl-POSS once the LC monolayer has formed. In fact, the large initial slope of $\left(d\varepsilon_d/d\Pi\right)$, the small κ in the monolayer regime, and the maximum ε_d corresponding to a moderately rigid film for trisilanolisobutyl-POSS are similar in magnitude to PDMS,[57,229,234] although the trisilanolisobutyl-POSS film is more rigid.

At the start of Regime C, trisilanolisobutyl-POSS films have been shown to collapse into multilayer domains.[38,226] During film collapse, the trisilanolisobutyl-POSS films are unable to store any additional energy. Energy added to the system by further compression of the film converts regions of the monolayer into multilayer. In this regime, $\varepsilon_s = 0$ reflects the fact that matter is lost from the monolayer to the multilayer domains

and does not necessarily reflect a change in the elasticity of the film itself. As seen in Figure 4.3, ε_d did not return to zero. ε_d obtained from SLS represents the locally averaged elasticity of the film on length scales of a few hundred microns. Hence, even though the film is no longer uniform, ε_d maintains its large value upon collapse reflecting the local elasticity. This feature is consistent with the fact that a continuous POSS layer still contacts the water surface, even if parts of it have additional material on top in the form of multilayer. Furthermore, it shows that the act of making non-invasive SLS measurements does not induce additional multilayer formation in contrast to further decreases in A during compression of a film for static Π - A isotherm measurements. Thus, SLS shows that the heterogeneous trisilanolisobutyl-POSS film is still rigid after it collapses. Upon further addition of spreading solution, the film becomes even more heterogeneous and the assumptions for SLS measurements may no longer be valid. As a consequence, the ε_d and $\omega\kappa$ values in Regime C exhibit greater scatter with larger error bars than in the monolayer (Regime B).

4.4 Conclusions

In summary, SLS has been employed for the first time study of interfacial dilational viscoelastic properties of a POSS molecule. Trisilanolisobutyl-POSS formed a viscoelastic Langmuir film which is almost perfectly elastic in the monolayer state for the wave vector range of 404.3 to 512.6 cm^{-1}. Previous studies have suggested that POSS molecules may serve as model 2D nanofillers (nanoscale objects that can enhance the elastic modulus of a material) in Langmuir film studies.[29,30,38,226] If one considers that the maximum dilational elasticity of trisilanolisobutyl-POSS is ~ 50 $mN \cdot m^{-1}$ prior to film collapse, one might expect reinforcement (increased elastic moduli for the composite film

relative to the polymer film) in the monolayer state for compatible polymer blends where the A/W interface can be regarded as a good solvent, and plasticization (enhanced fluidity of a polymer through the addition of a small molar mass additive) in the monolayer state in compatible polymer blends where the A/W interface is a poor solvent. Further SLS studies of POSS derivatives as 2D nanofillers in polymeric Langmuir films are underway.

CHAPTER 5

Phase and Rheological Behavior of Trisilanolisobutyl-POSS/PDMS Blends at the Air/Water Interface

5.1 Abstract

The work presented in Chapter 4 showed that surface light scattering (SLS) can be used to probe the rheological properties of trisilanol-POSS derivatives. As a potential model nanofiller, trisilanolisobutyl-POSS (TiBuP) forms Langmuir films with moderate rigidity and negligible interfacial viscosity. In this chapter, the interfacial phase and rheological behavior of TiBuP/polydimethylsiloxane (PDMS) blends with different wt% TiBuP are examined at the air/water (A/W) interface to connect rheological properties with previously completed morphological studies. PDMS forms Langmuir films at the A/W interface that are ideal for SLS studies and can be characterized by four regimes: (A) submonolayer (surface pressure $\Pi = 0$ mN·m^{-1}), (B) monolayer ($0 < \Pi < 8$ mN·m^{-1}), (C) a monolayer to bilayer transition ($\Pi \sim 8$ mN·m^{-1}), and (D) multilayer ($\Pi \sim 9$ mN·m^{-1}). For all blends, at low Π ($\Pi < 2.5$ mN·m^{-1}) in the monolayer regime, TiBuP, with its attendant water, serves as a plasticizer and lowers the dilational modulus of the films. At higher Π ($2.5 < \Pi < 5$ mN·m^{-1}) in the monolayer regime, ε_d for the blends is comparable to pure PDMS. This feature is consistent with water being squeezed out of the film and TiBuP being unable to plasticize PDMS on its own. For $\Pi > 5$ mN·m^{-1}, composition dependent reinforcement of the blends occurs. The Π where reinforcement occurs

decreases as the wt% TiBuP increases and may correlate with the surface fraction of TiBuP (Φ_{TiBuP}) in the layer directly in contact with water. As Φ_{TiBuP} increases, the modulus of the collapsed PDMS film increases. This observation likely reflects the formation of TiBuP networks which restrict PDMS mobility.

5.2 Introduction

5.2.1 TiBuP and PDMS as Model Filled Polymer System

Recently, the field of polymeric nanocomposite materials has generated considerable interest owing to an increasing demand for improved performance and tailored properties.[235-239] Polymeric nanocomposites are polymers reinforced with nano-sized or even molecular level nanostructured materials.[240] The reinforcing material is defined as a nanofiller as long as at least one dimension is on the order of 100 nm or smaller. Polyhederal oligomeric silsesquioxanes (POSS), silica-based nanofiller materials, were first reported by Scott in 1946.[176] The unique core-shell structure of POSS molecules (Figure 5.1) makes them compatible with numerous organic and polymeric materials.[177,201,241] Therefore, POSS based materials can be used as semiconducting polymers,[182] shape memory materials,[183] space-survivable coatings,[184,185] and for synthetic templates nanostructured material.[186-189] The incorporation of POSS molecules into a polymer can increase its glass transition temperature (T_g)[191,192] and thermal stability.[242] Due to their size (diameters around 1.5 nm), POSS molecules are described as the smallest silica particles[243] or "molecular silica". Furthermore, the well-defined and easily modified chemical structure makes POSS molecules excellent model fillers for exploring filler-polymer interactions. The mechanical, optical, and thermal

properties of POSS copolymers and POSS/polymer blends have been extensively studied.[196,199,212,244-246] However, relatively little research has been done to probe the behavior of POSS derivatives as nanofiller materials within thin films, even as thin film polymer blends grow more important for diverse applications including lithography,[247] dielectric layers,[248] gas separation membranes,[249] biocompatible coatings,[250] and drug delivery systems.[251] Several attempts have been made in this area. Paul *et al.*[61,213,227] examined phase separation and dewetting of trisilanolphenyl-POSS incorporated into polymeric thin films on solid substrates. Tuteja *et al*. systematically studied the superoleophobicity of poly(methyl methacrylate) (PMMA) thin films blended with flourous POSS derivatives.[214] The stability and optical properties of POSS/polymer blends have also been studied recently.[215,216] Since Deng, *et al.*[38] discovered that some trisilanol-POSS molecules are amphiphilic and are able to form insoluble monolayers at the air/water (A/W) interface, Langmuir film systems have become an excellent model system for studying the interfacial properties of POSS derivatives[29,30,38,226] and POSS/polymer blends.[31-33,125]

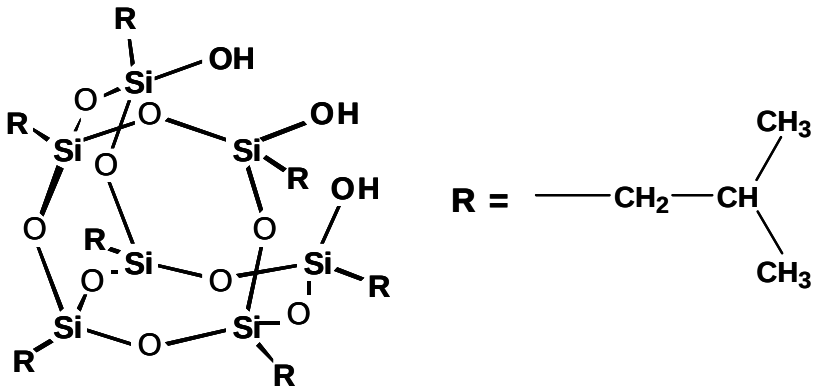

Figure 5.1. Molecular structure of trisilanolisobutyl-POSS (TiBuP) where R is an isobutyl group.

Polydimethylsiloxane (PDMS) is the most widely used silicon based polymer. The extremely flexible Si-O bonds render a very low glass transition temperature (T_g).[252] Also, as an organic-inorganic polymer, PDMS is thermally stable at high temperature and has a small thermal expansion coefficient that arises from its inorganic backbone. Therefore, PDMS has found uses in many fields such as adhesives and sealant materials,[253,254] silicon based lubricants,[255,256] anti-foaming agents,[257] damping fluids,[258] etc.

Beyond its unique bulk properties, PDMS is one of the first class of polymers that has been investigated extensively at the A/W interface. Ever since Fox *et al.*[83] reported that PDMS is able to form a uniform Langmuir monolayer at the A/W interface and exhibit interesting interfacial behavior, subsequent studies have focused on the interfacial properties of silicones in Langmuir films.[57,124,229,259] With a smooth water subphase and two controllable thermodynamic variables: temperature (T) and surface area per molecule

(A), Langmuir films are excellent model systems for studying phase transitions and ordering in different fields of chemistry, physics, and life sciences.[3-5,72] With the introduction of Brewster angle microscopy (BAM),[29-32,38,39,42,43,226] fluorescence microscopy (FM),[44,45] ellipsometry,[229] and grazing incidence X-ray diffraction (GIXD), [46] these two-dimensional (2D) Langmuir films can provide information completely analogous to three dimensional (3D) bulk systems.[1,6] Previous morphological studies from the Esker group have investigated the phase behavior of polydimethylsiloxane (PDMS) blended with trisilanolisobutyl-POSS (TiBuP) at the A/W interface.[31] Judging from a thermodynamic analysis of the $\Pi - A$ isotherms and BAM images, the blends likely form uniform monolayers at the A/W interface with no detectable phase separation upon spreading at submonolayer coverage ($\Pi \sim 0$ mN·m^{-1}). At Π comparable to the collapse pressure of TiBuP, aggregates could be seen during compression of the film and aggregates start to coalesce with further increases in surface concentration, especially for blends with high wt% TiBuP. Expansion of these highly compressed multilayer films revealed ring-like structures that are reminiscent of idealized depictions of nanofiller networks proposed for explaining reinforcement in filled polymer composites. Hence, one might expect that TiBuP could work as a nanofiller to reinforce the PDMS matrix. A natural next step would be rheological studies of TiBuP/PDMS blends at the A/W interface. The static and dynamic rheological behavior of a fair number of amphiphilic polymeric and small molecule monolayers can be obtained from several techniques including mechanically generated waves,[47] electrocapillary wave diffraction (ECWD),[49,229] surface light scattering (SLS),[118,122,123,126,153,231,234] interfacial stress

rheometry (ISR),[29,58,59] and surface pressure relaxation studies.[60] In this paper, SLS will be employed to probe the dynamic dilational rheology of the TiBuP/PDMS blends.

5.2.2 Surface Light Scattering (SLS) Measurements

SLS monitors the propagation of spontaneously formed capillary waves on air/liquid or liquid/liquid interfaces which arise from density fluctuations within the liquid subphase. The amplitude and wavelength (λ) of the relevant fluctuations are 3-5 Å for water,[260] and a few hundred μm, respectively. Most SLS instruments utilize a transmission diffraction grating[55] to generate different diffraction orders and detect scattered light through heterodyne beating. Two different paths are generally taken for subsequent data analysis: (1) direct fitting of the heterodyne intensity correlation functions,[148] and (2) a Lorentzian fit of the power spectrum for the scattered light.[122,123,153,231,234] In the second approach (used in this study), the power spectrum yields a frequency shift (f_s) and an experimental full-width at half-maximum intensity (Δf_s). The experimental full-width is usually corrected for the Gaussian beam profile of the laser:[73]

$$\Delta f_{s,c} = \Delta f_s - \frac{\Delta f_i^2}{\Delta f_s} \qquad \text{(Eq. 5.1)}$$

where the instrumental full-width at half-maximum intensity for the i^{th} diffraction order of the transmission diffraction grating is defined as

$$\Delta f_i = \sqrt{2}\left(\frac{\Delta u_i \cos\theta_i}{R\lambda}\right)\left(\frac{d\omega_o}{dk}\right) \qquad \text{(Eq. 5.2)}$$

Here, Δu_i is the full width at half-maximum intensity of the Gaussian laser beam profile for the i^{th} diffraction order of the transmission diffraction grating, θ_i is the incident angle, $k = 2\pi/\lambda$ is the spatial wave vector, and R is the distance from the interface to the detector. f_s is proportional to the capillary wave propagation rate ($\omega = 2\pi f_s$) and $\Delta f_{s,c}$ is related to the capillary wave damping coefficient ($\alpha = \pi \Delta f_{s,c}$). ω and α can be used to solve the Lucassen-Reynders-Lucassen dispersion relation for a monomolecular film at the A/W interface:[56]

$$\left[\eta\left(k - m^*\right)\right]^2 = \left(\frac{\varepsilon^* k^2}{i\omega^*} + \eta(k + m^*)\right)\left(\eta(k + m^*) + \frac{\sigma^* k^2}{i\omega^*} + \frac{g\rho}{i\omega^*} - \frac{\omega^* \rho}{ik}\right) \quad \text{(Eq. 5.3)}$$

where ε^*, σ^*, ω^*, and m^* correspond to the complex dilational modulus, complex surface tension, complex frequency, and the complex wave vector in the z-direction, respectively. These complex quantities correspond to Eqs. 5.4 through 5.7, respectively.

$$\varepsilon^* = \varepsilon_d + i\omega^* \kappa \quad \text{(Eq. 5.4)}$$

$$\sigma^* = \sigma_d + i\omega^* \mu \quad \text{(Eq. 5.5)}$$

$$\omega^* = \omega_o + i\alpha \quad \text{(Eq. 5.6)}$$

$$m^* = \left(k^2 + \frac{i\omega^* \rho}{\eta}\right)^{1/2}, \ \mathrm{Re}(m^*) > 0 \quad \text{(Eq. 5.7)}$$

In Eqs. 5.3 through 5.7, ε_d is the dynamic dilational elasticity, κ is the dilational viscosity, σ_d is the dynamic surface tension, μ is the transverse viscosity, g is acceleration due to gravity, and ρ and η are the density and viscosity of the subphase (water), respectively. In principle, ε_d and κ also contain a shear component, although this seems to be negligible.[146] The solution of Eq. 5.3 is complicated by the fact that only two quantities are measured, f_s and $\Delta f_{s,c}$, but four parameters, ε_d, κ, σ_d, and μ need to be determined.

For the case of direct analysis of the correlation function, these terms serve as fitting parameters, whereas, during routine analysis of power spectra μ is normally assumed to be zero and σ_d is replaced by the static surface tension, (σ_s), which can be measured simultaneously by the Wilhelmy plate technique. Hence, ε_d and κ can be deduced from Eq. 5.3.

In the remainder of this chapter, SLS will be used to deduce the dilational viscoelastic parameters, ε_d and κ, for TiBuP/PDMS blends at the A/W interface. This information along with a previous morphological study will be used to propose plausible molecular conformations at the A/W interface.

5.3 Results and Discussion

5.3.1 $\Pi - A$ Addition Isotherm of PDMS

Figure 5.2 shows a Π-A isotherm for PDMS obtained by the successive addition method. Here, A stands for the area occupied per dimethylsiloxane repeat unit (monomer for short). The isotherm exhibits four classical regimes as reported by Fox, *et al.*:[83] (A) $A > A_{lift\text{-}off} = 18$ Å^2•monomer^{-1} (where Π starts to increase) indicating the submonolayer regime ($\Pi = 0$ mN•m^{-1}). Here the PDMS films are likely biphasic with the coexistence of gaseous and liquid-like domains;[81] (B) 14 Å^2•monomer^{-1} < A < 18 Å^2•monomer^{-1} corresponding to a PDMS monolayer with oxygen and silicon atoms from the repeating unit adsorbed at the A/W interface; (C) 8 Å^2•monomer^{-1} < A < 14 Å^2•monomer^{-1}, the first plateau regime ($\Pi \sim 8.0$ mN•m^{-1}), and (D) A < ~ 8 Å^2•monomer^{-1}, the second plateau regime ($\Pi \sim 9.0$ mN•m^{-1}). In the original paper, Regimes C and D have been described through the successive coiling of PDMS chains to form helical structures. Subsequent

ellipsometry studies suggested that Regimes C and D actually correspond to a monolayer to bilayer transition and a bilayer to multilayer transition, respectively.[229] In this chapter, the bilayer model will be adopted to be consistent with a previously published study on this blend system.[31] Π at the border between Regimes B and C defines the collapse pressure of PDMS, $\Pi_{c,PDMS}$. The small rise in Π at the end of Regime C signifies the end of the bilayer regime.

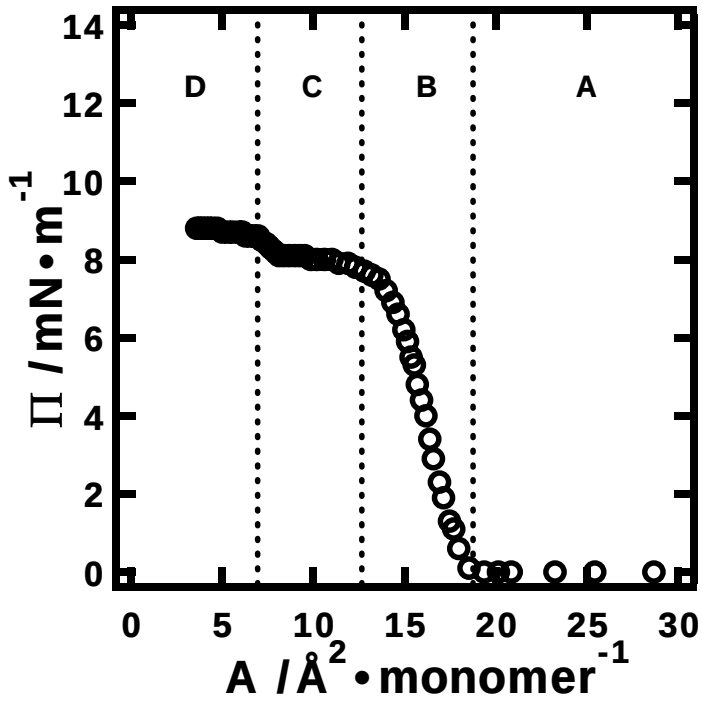

Figure 5.2. Π-A isotherms for PDMS at T = 22.5 °C. Obvious transitions in the PDMS isotherm define the boundaries (vertical dotted lines) for Regimes A through D.

5.3.2 SLS Results for PDMS

Esker *et al.*[123,231] reported that for frequency independent viscoelastic behavior, it is convenient to normalize all viscoelastic data to a common reference state. The approach

is essentially the same one used by Hård and Neuman.[55] After obtaining f_s and $\Delta f_{s,c}$ from SLS, and σ_s from the Wilhelmy plate technique, respectively, Eq. 5.3 is used to deduce the viscoelastic parameters ε_d and κ. Next, the values of ε_d and κ are used along with Eq. 5.3 to calculate the equivalent values of the frequency shift ($f_{s,eq}$) and corrected full-width at half-maximum intensity ($\Delta f_{s,c,eq}$) at an arbitrary reference state. For this study, the reference state is chosen to be water at 25 °C ($\sigma_{d,ref}$ = 71.97 mN•m^{-1}, μ_{ref} = 0, ρ_{ref} = 997.0 kg•m^{-3}, and η_{ref} = 0.894 mPa•s) and a reference wave vector of k_{ref} = 324.3 cm^{-1}. After verifying that these values are frequency independent, it is possible to average them for the different wave vectors and provide error estimates. Figure 5.3 shows $f_{s,eq}$ and $\Delta f_{s,c,eq}$ plotted as a function of Π for PDMS where data points represent an average of three wave vectors (7th through 9th diffraction orders) with one standard deviation error bars.

The horizontal dotted lines in Figure 5.3 represent several limiting cases of the dispersion equation for a viscoelastic film discussed in Chapter 2.5. There are totally six important limiting cases for the viscoelastic behavior of Langmuir films at the A/W interface: (I) pure liquid behavior (ε^* and $\mu = 0$), where a pure liquid surface or a submonolayer coverage film may exist; Purely elastic surface films (μ = 0 and κ = 0) yield three limiting cases (II) the maximum velocity limit (where capillary wave propagates the fastest), (III) the maximum damping coefficient limit (where the damping effect of the film reaches a maximum), and the (IV) the minimum velocity limit (where capillary waves propagate with their slowest velocity); The other two limits correspond to (V) the infinite lateral modulus limit (μ = 0 and $\varepsilon^* \rightarrow \infty$), and (VI) the maximum damping coefficient for a purely viscous surface film (ε_d = 0 and μ = 0).[123,231] For PDMS Langmuir

films, limits (I), (III), and (IV) are the most important of these limits and are the horizontal dotted lines included on Figure 5.3**.** Comparing the $f_{s,eq}$ and $\Delta f_{s,c,eq}$ data with these limiting cases provides useful information about the viscoelastic behavior of PDMS films at the A/W interface.

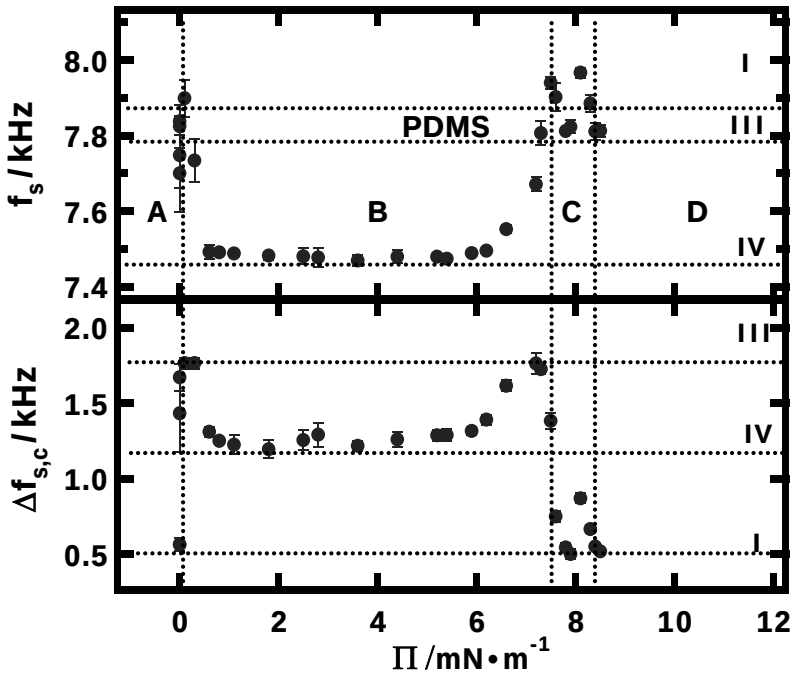

Figure 5.3. $f_{s,eq}$ - Π (top panel) and $\Delta f_{s,c,eq}$ - Π (bottom panel) isotherms for PDMS at T = 22.5 °C. Data points represent an average from three wave vectors with one standard deviation error bars. Vertical dotted lines indicate Regimes A through D defined in Figure 5.2. The horizontal dotted lines correspond to limiting behavior of the dispersion relation: (I) pure liquid limit, (III) the maximum damping coefficient for a perfectly elastic surface film, and (IV) the minimum velocity limit for a perfectly elastic surface film discussed in Chapter 2.

In Regime A, the submonolayer regime, the viscoelastic profile of the PDMS film is consistent with the pure liquid limit (I). At the very beginning of Regime B, both $f_{s,eq}$ and $\Delta f_{s,c,eq}$ quickly approach the maximum damping coefficient limit for a perfectly elastic surface film (III). The scattering of data points between limit (I) and limit (III) at this regime boundary arises from coexisting liquid (L) and gas (G) phase at $\Pi = 0$ for PDMS Langmuir films.[261] As SLS measures the viscoelastic properties averaged over an approximate area of several square microns, these measurements can probe the liquid domains (L), the gas domains (G), or a combination of both L and G for biphasic films. The corresponding $f_{s,eq}$ and $\Delta f_{s,c,eq}$ values will be consistent with limit (III), limit (I), or lie somewhere between limits (I) and (III) as a result of temporally averaging the amount of time L or G domains are in the scattering volume. In the middle of Regime B, the global minimum in $f_{s,eq}$ and the local minimum of $\Delta f_{s,c,eq}$ correspond to the viscoelastic behavior of a perfectly elastic film in the minimum velocity limit (IV). At the high Π end of Regime B, $f_{s,eq}$ starts to rise, and $\Delta f_{s,c,eq}$ shows another maximum matching the maximum damping coefficient for a perfectly elastic surface film (III). It is clear from $\Delta f_{s,c,eq}$ - Π that the viscoelastic properties in Regimes C and D are essentially those of a pure liquid (I), except for a small enhancement of the surface viscoelasticity at the boundary between Regimes C and D.

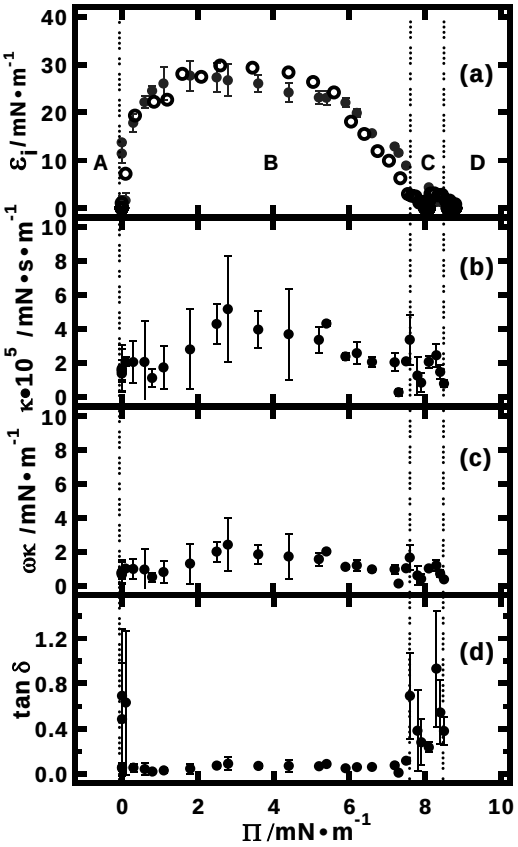

Figure 5.4. Plots of (a) ε_d - Π (filled circles) and ε_s - Π (open circles), (b) κ – Π, (c) ωκ – Π, and (d) tan δ – Π for PDMS at T = 22.5 °C. ε_s is deduced from the addition Π – A isotherm via equation $\varepsilon_s = -A(\partial\Pi/\partial A)_T$. ε_d, κ, ωκ, and tan δ values represent the average of three different wave vectors with one standard deviation error bars. The dotted vertical lines indicate the boundaries of the regimes defined in Figure 5.2.

5.3.3 Surface Viscoelastic Properties for PDMS

Figure 5.4 shows dilational viscoelastic parameters (ε_d, ε_s, κ, ωκ, and tan δ) as a function of Π. ε_d, κ, ωκ, and tan δ represent the average of three wave vectors with one standard deviation error bars. In Figure 5.4a, ε_d values deduced from SLS measurements

agree well with ε_s values deduced from Figure 5.2 over the entire Π range, suggesting that PDMS forms almost purely elastic films at the A/W interface. Both ε_d and ε_s values for PDMS films (Figure 5.4a) start from 0 $mN \cdot m^{-1}$ in Regime A and increase sharply before reaching a maximum value of $\varepsilon_{d,\,max} \sim 30$ $mN \cdot m^{-1}$ over a range from $2 \leq \Pi \leq 5$ $mN \cdot m^{-1}$ in Regime B. At the latter half of Regime B, ε_d decreases slowly and returns to 0 $mN \cdot m^{-1}$ again as the film collapses from a monolayer into a heterogeneous bilayer at a collapse pressure of $\Pi_{c,PDMS} \sim 8$ $mN \cdot m^{-1}$. In Regime C, the dilational elasticity for PDMS shows a small increase upon the formation of a bilayer before retuning to 0 $mN \cdot m^{-1}$ in Regime D. The interfacial dilational viscosity κ (Figure 5.4b) exhibits a trend that is similar to ε_d, reaching a global maximum in the middle of Regime B and showing a local maximum between Regimes C and D. Compared to ε_d values, however, κ is small and nearly zero within experimental error at all Π indicating the PDMS film can be regarded as nearly purely elastic. Figure 5.4c provides information for the loss modulus ($\omega\kappa$) that is similar to Figure 5.4b. For the dilational viscosity, the absence of any significant frequency dependence is expected for the narrow frequency range probed. Figure 5.4d shows the loss tangent, $tan\delta = \omega\kappa/\varepsilon_d$, for the PDMS film. In Regime A, C, and D, the scattered values reflect the absence of an elastic film. In contrast, values in Regime B and at the boundary between Regimes C and D are < 1 (approaching 0) and less scattered reflecting the formation of a highly elastic film with an almost negligible viscosity. Figure 5.4 is consistent with previous studies of PDMS Langmuir films where PDMS is regarded as a nearly purely elastic film.[57,86,124,234,259]

There are several important features one can observe from Figure 5.4. First, $\varepsilon_{d,}$ rises dramatically at the beginning of Regime B. If ε_d is plotted versus Π, the initial slope defines the scaling exponent z ($\varepsilon = z\Pi$) that can be related to molecule-subphase interactions.[130] If the A/W interface is a "good solvent", z = 2.86,[135] whereas values of z from 8 to 101 are consistent with "theta solvent" conditions.[135,136] The term "good solvent" and "theta solvent" refer to how water swells a polymer chain in 2D with "good solvent" conditions implying swelling by water and "theta solvent" conditions implying that water only fills the excluded volume. For a PDMS film, z ~ 30 suggests that the A/W interface is a theta or near theta solvent for PDMS with only the minimum amount of water needed to fill the excluded volume present in the monolayer film. This result is consistent with previous work by Granick, *et al.* where he concluded that the A/W interface is a near theta solvent for PDMS from a Π – A isotherm study.[57] Hence, the impact of water on the interfacial viscoelastic properties of PDMS thin films at the A/W interface should be negligible. Second, PDMS films reach their maximum ε_d of $\varepsilon_{d,max}$ ~ 30 mN•m^{-1} at Π ~ 2 mN•m^{-1} and maintain this value until ε_d begins to decrease for Π > ~ 5 mN•m^{-1}. Classically, collapse of the PDMS film would be assigned to the on-set of the first plateau in the Π - A isotherm around Π ~ 8 mN•m^{-1}. As we will discuss later in this chapter, the point where ε_d starts to decrease and deviate considerably from $\varepsilon_{d,max}$ (Π ~ 6 mN•m^{-1}) must already signify the on-set of film collapse with some segments of the polymer chain leaving the A/W interface. Third, most polymer films exhibit smaller dilational viscoelastic moduli after the film starts to collapse; however, few of them achieve ε_d ~ 0 in the collapsed regime. The fact ε_d ~ 0 in the multilayer regime for PDMS reflects weak molecule-subphase interactions as well as weak intermolecular and

intramolecular interactions. As a consequence, PDMS can spread on itself[81,229] and exists as a liquid even after collapsing into multilayer domains. Apparently, any compressive force applied to the system in the multilayer regime causes more multilayer to form without storage or loss of energy through the dilational mode of the film.

5.3.4 Addition Π – <A> Isotherms of TiBuP/PDMS Blends

The phase behavior of TiBuP and TiBuP/PDMS blends is studied through successive addition Π-A isotherms. TiBuP starts to form a monolayer at A ~ 230 $Å^2$·molecule^{-1}. As discussed in Chapter 4, TiBuP exists as a liquid condensed (LC) monolayer between 145 < A < 230 $Å^2$·molecule^{-1} before collapsing at $\Pi_{c,TiBuP}$ ~ 12.5 mN·m^{-1}. Even though its modulus is consistent with an LC phase in the monolayer regime, TiBuP films are not as rigid as PDMS. The fact that Π increases more gradually than PDMS in the low Π regime for TiBuP indicates that water likely plasticizes the TiBuP monolayer. This feature is attributed to hydrogen bonding between silanol groups of TiBuP and water where more water molecules need to be squeezed out of Langmuir film of TiBuP than PDMS before forming a condensed film (180 < A < 230 $Å^2$·molecule^{-1}). As surface concentration increases further (A < 180 $Å^2$·molecule^{-1}), Π rises faster, a feature that is consistent with the formation of a condensed film with viscoelastic properties that are comparable to PDMS.

There are several remarkable features in the Π - A isotherms of TiBuP/PDMS blends. First, their isotherms lie between pure PDMS and TiBuP. Second, the transition plateaus for PDMS become less clear as the wt% of TiBuP in the blends increases. For 20 and 40 wt% TiBuP blends, the transition regions appear as flat plateaus. For higher wt% TiBuP blends, the "plateaus" are not as well defined. Third, the transition pressures

($\Pi_{transition}$), related to the collapse of the PDMS component in the blends (indicated by the black arrows on Figure 5.5b), increase as the wt% TiBuP increases. For 20 and 40 wt% TiBuP blends, $\Pi_{transition}$ for the PDMS component is similar to pure PDMS. However, for 60 and 80 wt% TiBuP blends, $\Pi_{transition}$ is significantly higher, ~ 9 and 10 $mN \cdot m^{-1}$, respectively. These observations are consistent with previous work from the Esker group.[44] In that study, Brewster angle microscopy (BAM) and a thermodynamic analysis were used to conclude that TiBuP/PDMS blends form uniform monolayers at the A/W interface and the POSS component likely helps anchor the PDMS component to the A/W interface resulting in higher $\Pi_{transition}$. The change in the isotherms around the monolayer to bilayer transition for PDMS may indicate mechanistically different transition behavior. Further discussion of these differences will rely on SLS studies.

5.3.5 SLS Results for TiBuP/PDMS Blends

Figures 5.6 and 5.7 show $f_{s,eq} - \Pi$ and $\Delta f_{s,c,eq} - \Pi$ plots for PDMS, TiBuP, and blends with different wt% TiBuP, respectively. In comparison to PDMS, $f_{s,eq}$ for TiBuP in Figure 5.6 increases more gradually around the transition from Regime A to Regime B and decreases to the minimum velocity limit for a perfectly elastic surface film (IV) over a wider Π range (0 to 2 $mN \cdot m^{-1}$ for TiBuP vs. 0 to 0.5 $mN \cdot m^{-1}$ for PDMS). Likewise, $\Delta f_{s,c,eq}$ in Figure 5.7 does reach the maximum damping coefficient for a perfectly elastic surface film (III) until $\Pi \sim 0.6$ $mN \cdot m^{-1}$, whereas as PDMS does so at $\Pi \sim 0$. It was pointed out in the paper of Kawagauchi *et al.*[126] that a peak in $\Delta f_{s,c,eq} - \Pi$ plot means $\varepsilon_d/\sigma_\sigma \sim 0.17$. This feature suggests that the TiBuP Langmuir film is not as rigid as PDMS at low Π. This observation is consistent with our discussion of the Π – A isotherms and the supposition that more water molecules are present in the Langmuir film at low

Π, thereby softening the TiBuP film. Beginning from the middle of Regime B, both $f_{s,eq}$ and $\Delta f_{s,c,eq}$ for TiBuP approach the minimum velocity limit for a perfectly elastic surface film and remain there until the collapse pressure ($\Pi_{c,TiBuP} \sim 12.5$ mN·m^{-1}) .

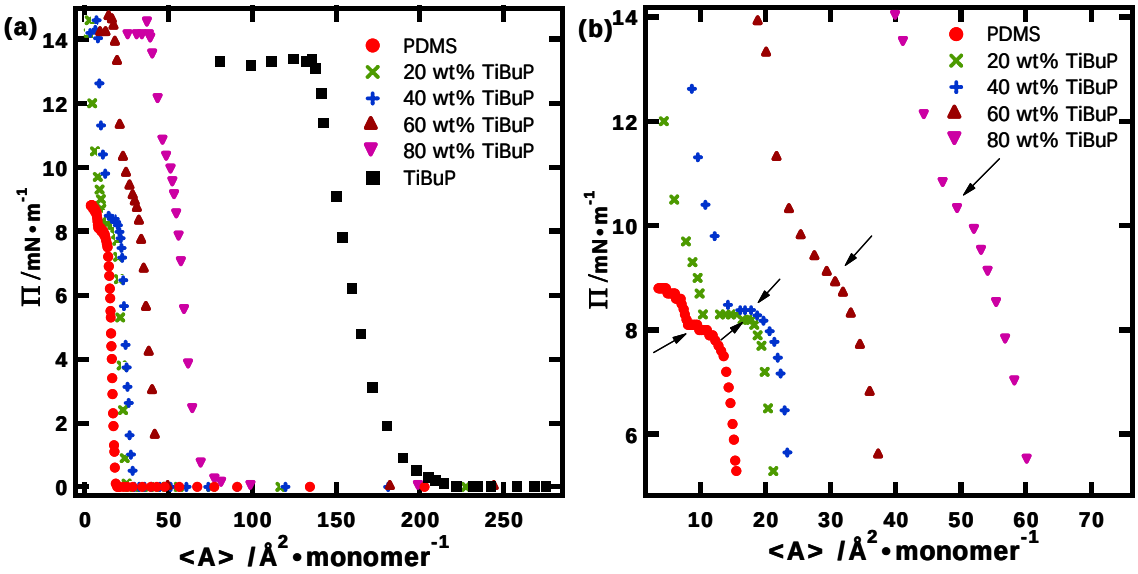

Figure 5.5. Π-A isotherms for TiBuP/PDMS blends from successive addition experiment at T = 22.5 °C. **(a)** The left-most isotherm is 100 wt% PDMS (red ●) while the right-most isotherm is 100 wt% TiBuP (black ■). The intermediate isotherms from left to right correspond to blends with 20 (green ×), 40 (blue +), 60 (brown ▲), and 80 (purple ▼) wt% TiBuP. **(b)** Expansion of the Π-A isotherms in the region where PDMS would be expected to undergo the monolayer to bilayer transition. The arrows indicate the collapse pressures for the monolayer to bilayer transition, $\Pi_{transition}$, of the PDMS component in the blends.

The rheological behavior for TiBuP/PDMS blends is composition dependent. All blends share similar behavior prior to Regime C. In comparison to PDMS, $f_{s,eq}$ for the blends in Figure 5.6 decreases more slowly and reaches the minimum velocity limit for a

perfectly elastic surface film (IV) at larger Π with increasing wt% TiBuP. This feature is more obvious for $\Delta f_{s,c,eq} - \Pi$, where, correspondingly, $\Delta f_{s,c,eq}$ only approaches the minimum velocity limit for a perfectly elastic surface film (IV) in the middle of regime B.

In Regime C, 20 and 40 wt% TiBuP blends exhibit the same qualitative features as PDMS with respect to $f_{s,eq} - \Pi$ and $\Delta f_{s,c,eq} - \Pi$. $f_{s,eq}$ reveals a local minimum while $\Delta f_{s,c,eq}$ exhibits a local maximum. These features are consistent with the 20 and 40 wt% blends undergoing bilayer formation through a mechanism similar to PDMS.

For 60 and 80 wt% TiBuP blends, the characteristic features in $f_{s,eq} - \Pi$ and $\Delta f_{s,c,eq} - \Pi$ plots for Regime C are absent. While $f_{s,eq}$ appears to approach the pure liquid limit (I) in Figure 5.6d, it really approaches the maximum velocity limit (II) for a perfectly elastic surface film. Figure 5.7d clearly shows that the 60 wt% TiBuP blend does not behave as a pure liquid with respect to $\Delta f_{s,c,eq}$. For the 80 wt% TiBuP blends, any transitions analogous to Regime C in PDMS are delayed to higher Π in Figures 5.6f and 5.7f and never approach pure liquid behavior. Instead, the film behaves like a film at the minimum velocity limit for a perfectly elastic film (IV). The features for the 60 and 80 wt% TiBuP blends are consistent with different rheological behavior as the PDMS component collapses.

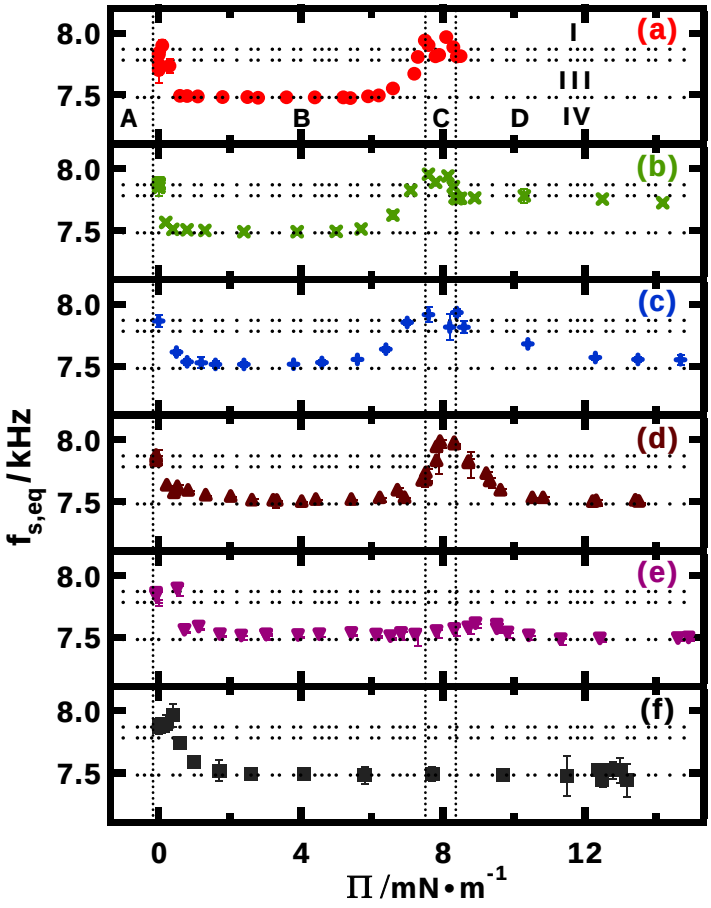

Figure 5.6. $f_{s,eq}$ – Π for (a) 0 (PDMS, red ●), (b) 20 (green ×), (c) 40 (blue +), (d) 60 (brown ▲), (e) 80 (purple ▼), and (f) 100 (black ■) wt% TiBuP at T = 22.5 °C. Data points represent an average of three wave vectors with one standard deviation error bars. Vertical dotted lines indicate Regimes A through D defined in Figure 5.2. The three horizontal dotted lines correspond to limiting cases of the dispersion relation for a purely elastic surface film: (I) the pure liquid limit, (III) the maximum damping coefficient, and (IV) the minimum velocity limit as labeled by roman numerals on (a).

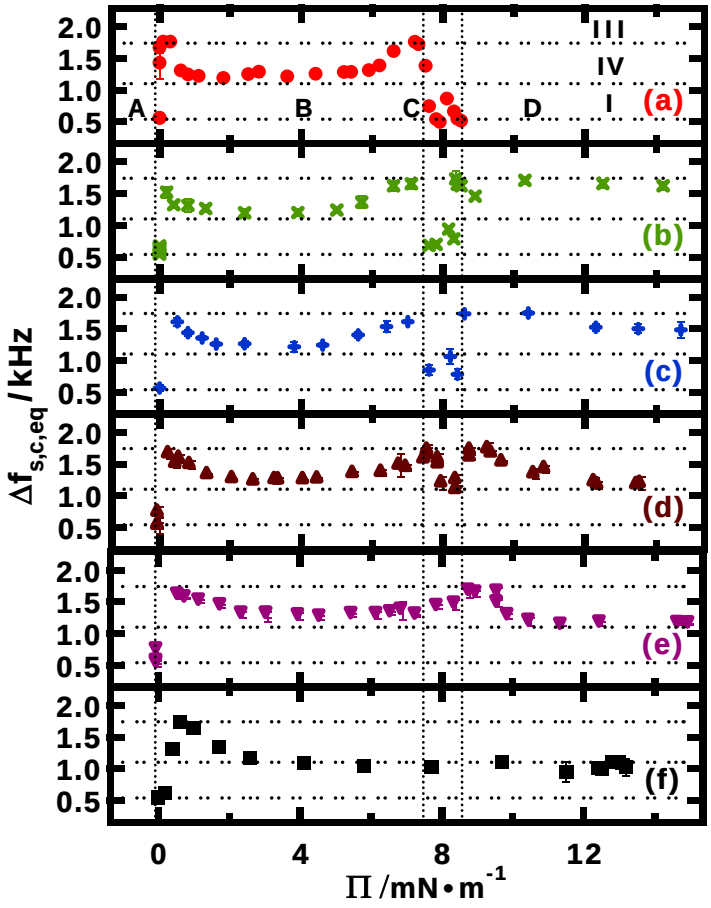

Figure 5.7. $\Delta f_{s,c,eq}$ – Π for (a) 0 (PDMS, red ●), (b) 20 (green ×), (c) 40 (blue +), (d) 60 (brown ▲), (e) 80 (purple ▼), and (f) 100 (black ■) wt% TiBuP at T = 22.5 °C. Data points represent an average of three wave vectors with one standard deviation error bars. Vertical dotted lines indicate Regimes A through D defined in Figure 5.2. The three horizontal dotted lines correspond to limiting cases of the dispersion relation for a perfectly elastic surface film: (I) the pure liquid limit, (III) the maximum damping coefficient, and (IV) the minimum velocity limit as labeled by roman numerals on (a).

After the monolayer to bilayer transition for PDMS (Regime C) has occurred, all blends exhibit rheological behavior that deviates from PDMS in Regime D. As seen in

Figure 5.6 and 5.7 for $\Pi_{transition} < \Pi < \Pi_{c,TiBuP}$ there is systematic deviation from pure liquid dynamics (I) for PDMS to a film with rheological properties approaching the minimum velocity limit for perfectly elastic surface film (IV) with increasing wt% TiBuP. In Regime D, it appears TiBuP reinforces the PDMS film.

5.3.6 Rheological Behavior of PDMS and TiBuP

$\varepsilon_d - \Pi$ for PDMS, TiBuP, and all blends are plotted in Figure 5.8. The average standard deviation for ε_d is ~ 5%. Focusing first on the pure components, ε_d increases more gradually and exhibits lower values for TiBuP than PDMS for $\Pi <$ ~ 2.5 mN·m^{-1}. This behavior is consistent with the trends observed for $f_{s,eq}$ - Π and $\Delta f_{s,eq}$ - Π in Figure 5.6 and 5.7, respectively, where we proposed that this feature likely arises from additional water in the TiBuP monolayer that effectively plasticizes the film (also discussed in Chapter 4). Although the initial slope of ε_d - Π for TiBuP (~ 13) is smaller than PDMS (~ 30), it appears that water is squeezed out of the film for $\Pi >$ ~ 2.5 mN·m^{-1} as the TiBuP film forms a more condensed monolayer with ε_d that are greater than PDMS. Unlike PDMS where ε_d returns to zero after reaching its maximum value, ε_d of TiBuP continues to increase as Π increases and reaches and maintains its maximum value (~ 45 mN·m^{-1}) even after the film collapses. The scatter of the TiBuP data points after collapse (Π ~ 12.5 mN·m^{-1}) is attributed to the heterogeneous nature of the TiBuP Langmuir film where experimental conditions may invalidate the dispersion equation.

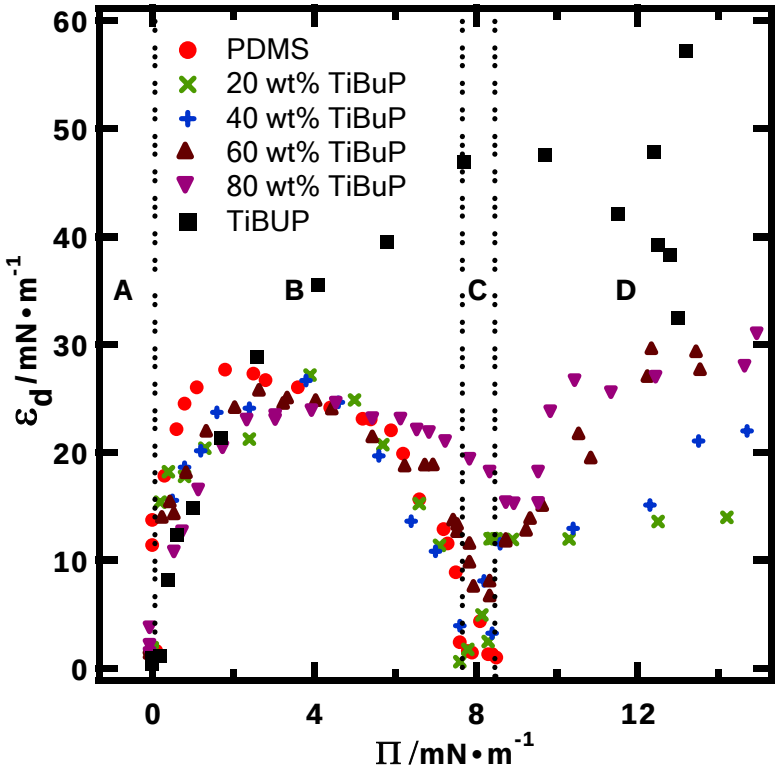

Figure 5.8. ε_d – Π for 0 (PDMS, red ●), 20 (green x), 40 (blue +), 60 (brown ▲) and 80 (purple ▼) and 100 (black ■) wt% TiBuP at T = 22.5 °C. Data points represent an average of three wave vectors. Vertical dotted lines indicate Regimes A through D defined in Figure 5.2. One standard deviation error bars of ~ ± 5% have been omitted for clarity.

5.3.7 Observations for the Rheological Behavior of TiBuP/PDMS Blends

ε_d – Π for the blends in Figure 5.8 is obviously more like PDMS than TiBuP before $\Pi_{c,PDMS}$ even at high TiBuP loading. Therefore, it is reasonable to treat TiBuP as the additive when analyzing the rheological behavior of the blends in Regime B (monolayer). For $\Pi < 2.5$ mN·m^{-1}, ε_d of blends lies between the corresponding values for PDMS and

TiBuP. In essence, TiBuP and its attendant water plasticize the PDMS film and effectively make the A/W interface a better solvent for the blends. ε_d of all the blends are comparable to PDMS for $2.5 < \Pi < 5$ mN·m^{-1} showing that the plasticizing effect disappears when water is squeezed out from the film. From $5 < \Pi < \sim 8$ mN·m^{-1} ($\Pi_{c,PDMS}$), distinct, composition dependent differences in ε_d emerges. Figure 5.9 expands the plot of $\varepsilon_d - \Pi$ in the vicinity of Regime C. As seen in Figure 5.9, ε_d for 20 and 40 wt% TiBuP blends with PDMS from $5 < \Pi < 8$ mN·m^{-1} are comparable to or slightly smaller than PDMS at corresponding Π value. In contrast, ε_d for 60 and 80 wt% TiBuP blends are greater than for PDMS over the same Π range, whereby the TiBuP acts as a filler instead of a plasticizer, reinforcing the film in this regime.

Next, the transition region at the end of Regime C where Π increases slightly before the film enters Regime D ($7.5 < \Pi < 8.5$ mN·m^{-1} for PDMS) will be considered. As seen in Figure 5.9, PDMS films show a slight increase in ε_d (~ 5 mN·m^{-1}) and return to zero in Regime D. This behavior is quantitatively similar for the 20 wt% TiBuP blend, and qualitatively similar for the 40 wt% TiBuP blend although the local maximum in ε_d is twice as large (~ 10 mN·m^{-1}) compared to PDMS. At this point, the TiBuP no longer acts as a plasticizer in the 20 wt% blend, and has actually crossed over to acting as a filler in the 40 wt% TiBuP blend. Furthermore, the 60 and 80 wt% TiBuP blends do not go to zero in the transition region nor do they exhibit a local maximum in ε_d. Rather, the minima in ε_d for the shift outside the region defined as Regime C for PDMS and these blends show filler behavior in Regime C and D, reinforcing the PDMS film at all Π.

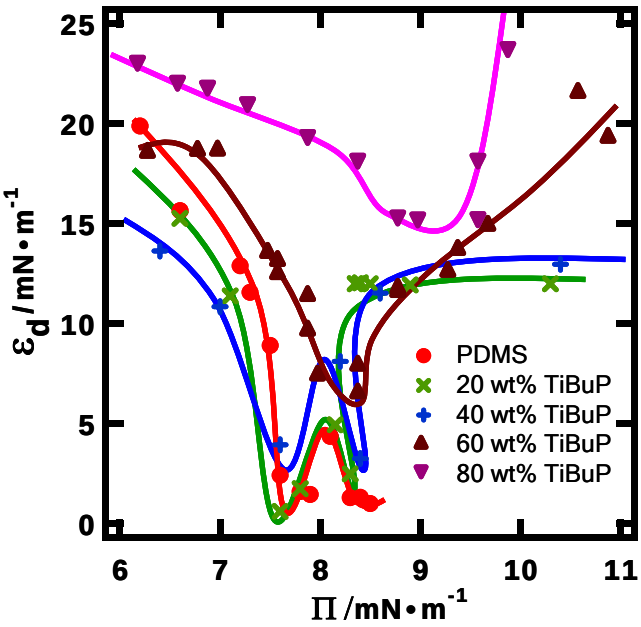

Figure 5.9. ε_d – Π in the vicinity of Regime C for 0 (PDMS, red ●), 20 (green x), 40 (blue +), 60 (brown ▲), 80 (purple ▼), and 100 wt% TiBuP (black ■) at T = 22.5 °C. Data points represent an average of three wave vectors. Solid lines of the corresponding color are trend lines used to highlight features of the ε_d – Π plots.

Finally, the behavior of all blends in Regime D is considered. As seen in Figure 5.9, two things are obvious for Regime D (Π > 8.5 mN·m^{-1}): 1) Π for the blends is able to exceed the maximum Π value for PDMS in the second plateau (~ 8.5 mN·m^{-1}); and 2) ε_d exhibits a systematic increase for all blends. Clearly, the addition of TiBuP converts the PDMS film into a viscoelastic object at high Π.

Figure 5.10 presents plots of ωκ – Π for all blends, the κ – Π isotherm is omitted owing to the similarity between these two plots. ωκ for TiBuP exhibit small values until

film collapse ($\Pi_{c,TiBuP}$ ~ 12.5 mN·m^{-1}). After $\Pi_{c,TiBuP}$, ωκ exhibit large scatter indicating the formation of TiBuP multilayer aggregates. ωκ for all blends are similar to PDMS prior to $\Pi_{c,PDMS}$, exhibiting small values that are essentially zero, i.e. the films are nearly purely elastic. ωκ values for higher wt% TiBuP blends are slightly larger in the monolayer regime with maximum values of ωκ ~ 4 mN·m^{-1} for 60 and 80 wt% TiBuP blends versus ~ 2 mN·m^{-1} for 20 and 40 wt% TiBuP blends and PDMS. This observation is consistent with the features in Figures 5.8 and 5.9 where the 60 and 80 wt% TiBuP blends show filler behavior even before $\Pi_{c,\ PDMS}$. In Regime D, ωκ for all of the blends remain small (~ 4 – 10 times smaller) even after collapse of the TiBuP component ($\Pi_{c,TiBuP}$ ~ 12.5 mN·m^{-1}).

tan δ - Π for PDMS, TiBuP, and all blends are presented in Figure 5.11 The scatter of tan δ values for TiBuP in Regime A (Π ~ 0) indicates a submonolayer film. The fact that tan δ values for TiBuP remain small (approaching 0) in the monolayer regime is consistent with the discussion in Chapter 4 that TiBuP forms a nearly purely elastic film at the A/W interface. tan δ for TiBuP start increasing after $\Pi_{c,TiBuP}$, indicating the formation of TiBuP multilayers and an enhancement of loss behavior. All blends show similar tan δ - Π as PDMS in the monolayer regime. In the transition regime (7.5 < Π < 8.5 mN·m^{-1}), 20 and 40 wt% TiBuP blends exhibit scatter that is similar to PDMS indicating the film is weakly elastic when PDMS undergoes the monolayer to bilayer transition. In contrast, tan δ values for 60 and 80 wt% TiBuP remain small (essentially zero), indicating that these films remain strongly elastic at all Π.

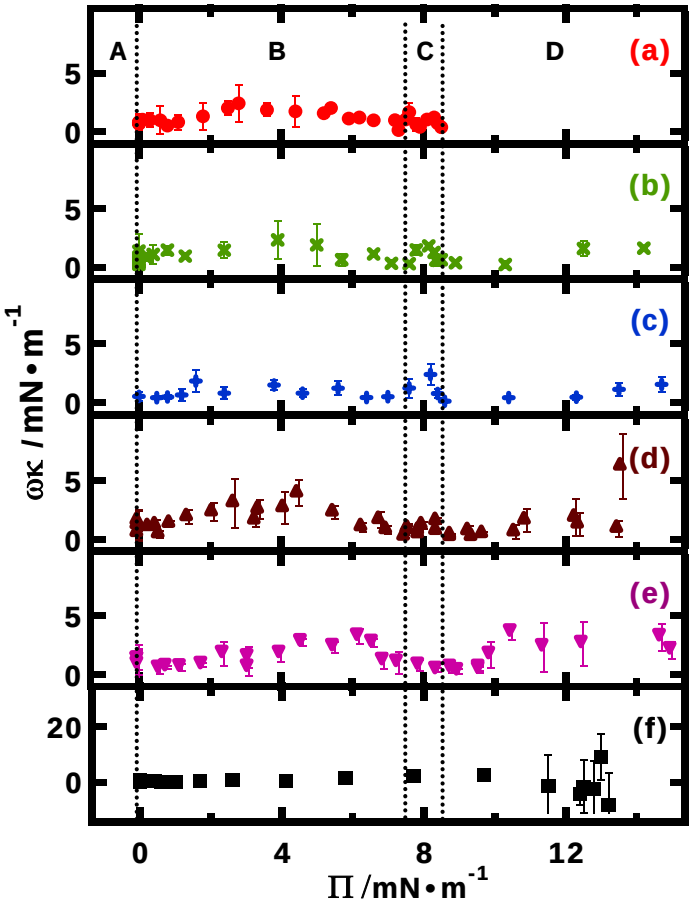

Figure 5.10. ωκ – Π for (a) 0 (PDMS, red ●), (b) 20 (green ×), (c) 40 (blue +), (d) 60 (brown ▲), (e) 80 (purple ▼), and (f) 100 (black ■) wt% TiBuP at T = 22.5 °C. Data points represent an average of three wave vectors with one standard deviation error bars. Vertical dotted lines indicate Regimes A through D defined in Figure 5.2.

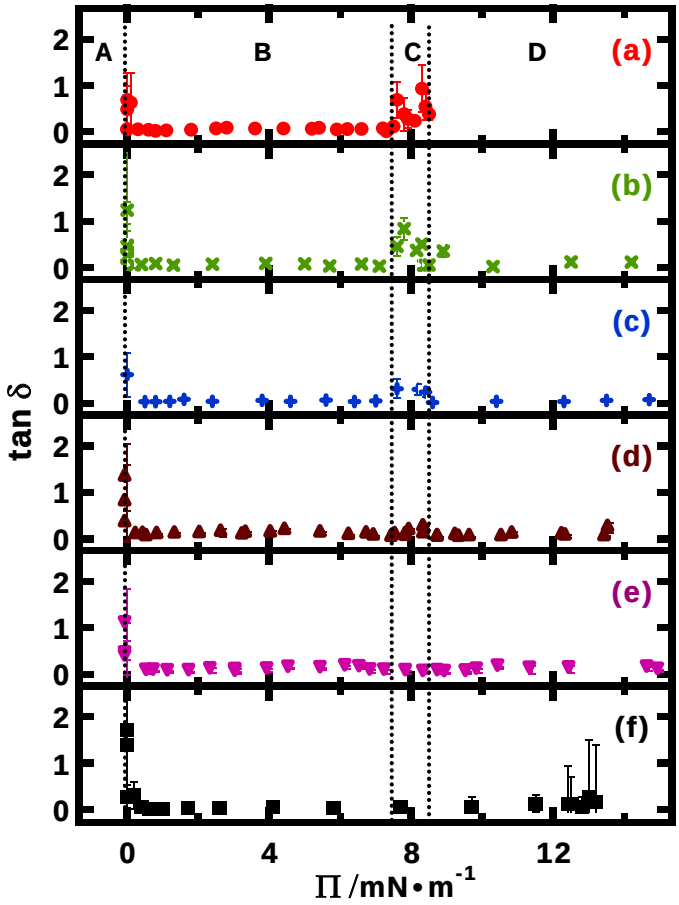

Figure 5.11. tan δ – Π for (a) 0 (PDMS, red ●), (b) 20 (green ×), (c) 40 (blue +), (d) 60 (brown ▲), (e) 80 (purple ▼), and (f) 100 (black ■) wt% TiBuP at T = 22.5 °C. Data points represent an average of three wave vectors with one standard deviation error bars. Vertical dotted lines indicate Regimes A through D defined in Figure 5.2.

5.3.8 A Model for Explaining the Rheological Behavior of TiBuP/PDMS Blends at the A/W Interface

Any model for the interaction between TiBuP and PDMS at the A/W interface must explain TiBuP plasticization of PDMS between $0 < \Pi < 2.5$ mN·m^{-1}, the disappearance of this effect between $2.5 < \Pi < 5$ mN·m^{-1}, and the cross-over from plasticization to filler reinforcement at higher Π. In Figure 5.12a, the dashed lines around a PDMS chain represent the area occupied by a single chain for a polymer in theta solvent conditions. Voids between chains are filled with water. However, the conformation of the chain should be consistent with an unperturbed chain in two dimensions. Upon the addition of TiBuP, there must be an expansion of the PDMS chain to accommodate TiBuP and its attendant H-bonded water molecules. This behavior implies TiBuP is miscible with PDMS and is consistent with the negative excess Gibbs free energies of mixing reported by Hottle, *et al.*[31] for this system. In essence, TiBuP increases the fractional free area in the polymer (analogous to how a plasticizer increases the free volume in bulk polymer systems) leading to enhanced polymer chain mobility and smaller elastic moduli (Figure 5.12b). This behavior is similar to the decrease in the glass transition temperature (T_g) reported by Wu *et al.*[212] for statistical copolymers of styrene and styryl-isobutyl-POSS.

Between $2.5 < \Pi < 5$ mN·m^{-1}, the effective plasticization of the PDMS film decreases and disappears. As already noted in the discussion of the viscoelastic properties of TiBuP, there is a much stronger increase in ε_d with respect to Π for this Π range. This feature has been explained by squeezing water out of the POSS film in Chapter 4. In this regime, ε_d for the blends is comparable to PDMS, showing that TiBuP alone is not able to

plasticize PDMS in this regime. In essence, PDMS chains should occupy approximately the same area as in theta solvent condition. Hence, all films have similar rheological properties in the vicinity of the maximum ε_d (Figure 5.12c).

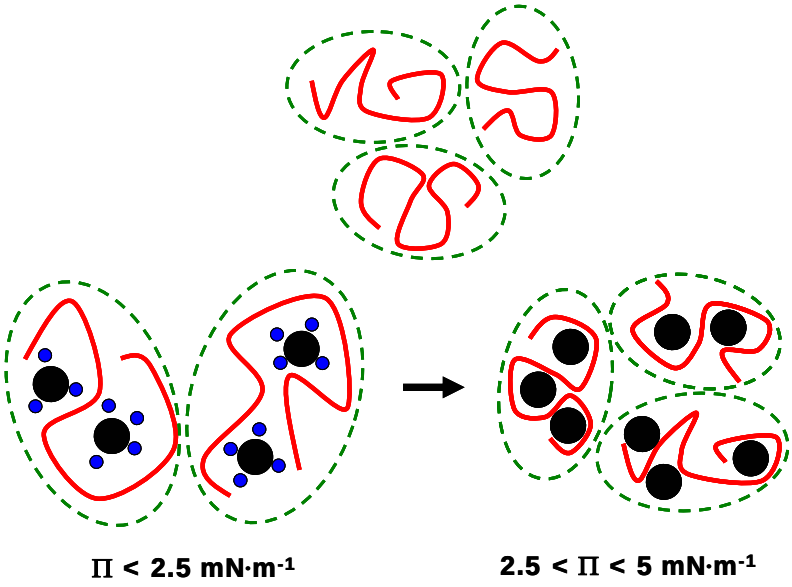

Figure 5.12. Schematic depiction of possible molecular conformations for TiBuP/PDMS blends at the A/W interface where red solid curves represent the PDMS polymer chains, black spheres represent TiBuP molecules, small blue spheres represent the attendant water molecules within the films, and green dashed lines represent the area PDMS chains occupy at the A/W interface.

As already noted in this chapter, the on-set of monolayer collapse is normally regarded as the point on a Π – A isotherm where a flat plateau begins. This definition must be restricted further to distinguish between monolayer phase transitions such as the liquid expanded (LE) to condensed (LC) phase transition observed in fatty acid and phospholipids systems,[72] and plateaus that originated from true collapse processes: the desorption of polymer chains into the subphase (soluble surfactants like polyethylene

oxide)[75,126] or the formation of 3D multilayer structures (insoluble surfactants like PDMS). In reality, the collapse of the Langmuir films occurs over a range of Π instead of at one specific Π value. If one considers the dynamic elastic modulus, ε_d, is a measure of the rigidity of the surface film, a decrease in ε_d must indicate the on-set of the monolayer to multilayer transition. For PDMS, ε_d stays at its maximum over a range of ~ $2 < \Pi < 5$ $mN \cdot m^{-1}$. ε_d starts to deviate significantly from $\varepsilon_{d,\,max}$ at $\Pi \sim 5$ $mN \cdot m^{-1}$ where compression of the film is already causing some of the dimethylsiloxane repeat units of PDMS to leave the A/W interface. Recognizing this feature, and the fact that collapse of the TiBuP film starts at higher Π ($\Pi\,(\varepsilon_{d,max}) \sim 11 < \Pi < \Pi_c \sim 12.5$ $mN \cdot m^{-1}$) allows one to formulate a model for explaining the viscoelastic behavior of TiBuP/PDMS blends for $\Pi > 5$ $mN \cdot m^{-1}$.

Starting from the premise that PDMS collapses before TiBuP, it is reasonable to propose that there will be a change in surface composition of the film directly bound to water once some PDMS molecules move away from the A/W interface. Since TiBuP is more stable at the A/W interface, the amount of TiBuP at the A/W interface should stay constant at $\Pi < \Pi_{c,\,PDMS}$ for the blends. As a consequence:

$$\Phi_{TiBuP,\Pi\,(\varepsilon_{d,max})} \cdot \langle A\,(\varepsilon_{d,max})\rangle = \Phi_{TiBuP,\Pi} \cdot \langle A\,(\Pi)\rangle \qquad \text{Eq. 5.8}$$

$\Phi_{TiBuP,\,\Pi\,(\varepsilon_{d,max})}$ is the surface area fraction of TiBuP at the maximum ε_d ($\Pi \sim 4$ $mN \cdot m^{-1}$). $\langle A\,(\varepsilon_{d,max})\rangle$ is the corresponding average area per repeat unit (monomer) at $\varepsilon_{d,max}$. $\Phi_{TiBuP,\Pi}$ and $\langle A\,(\Pi)\rangle$ represents the surface area fraction for TiBuP and the average area per repeating unit at any given Π between $\Pi\,(\varepsilon_{d,max})$ and $\Pi_{c,TiBuP}$ for a 100 wt% TiBuP film, respectively. The initial $\Phi_{TiBuP,\Pi\,(\varepsilon_{d,max})}$ can be calculated using the initial mole

fraction (X_{POSS}) and the areas occupied by TiBuP and PDMS at their maximum ε_d (where all molecules are closely packed together), $A_{TiBuP,\varepsilon d,max}$, and $A_{PDMS,\varepsilon d,max}$, respectively.

$$\Phi_{TiBuP,\Pi(\varepsilon_{d,\max})} = \frac{X_{TiBuP} \bullet A_{TiBuP,\varepsilon_{d,\max}}}{X_{TiBuP} \bullet A_{TiBuP,\varepsilon_{d,\max}} + X_{PDMS} \bullet A_{PDMS,\varepsilon_{d,\max}}} \qquad \text{Eq. 5.11}$$

The mole fraction of both components can be calculated from the initial wt% TiBuP of the blend. $A_{TiBuP,\varepsilon d,max}$ and $A_{PDMS,\varepsilon d,max}$ are ~ 160 Å^2 and ~16 Å^2, respectively. Using Eq. 5.11, it is possible to estimate $\Phi_{TiBuP,\,\Pi\,(\varepsilon d,max)}$ for blends at $\Pi > \Pi\,(\varepsilon_{d,max})$. Values for these calculations at several Π are provided in Tables 5.1 Values of $\Phi_{TiBuP,\Pi} > 1$ are indicative of $\Pi > \Pi\,(\varepsilon_{d,max})$ for TiBuP.

Table 5.1. Calculated TiBuP surface fractions for TiBuP/PDMS blends at $\Pi > \Pi_{c,PDMS}$

wt% TiBuP	$\Phi_{TiBuP,\Pi\,(\varepsilon d,max)}$	$\Phi_{TiBuP,\,\Pi\,=\,9}$	$\Phi_{TiBuP,\Pi\,=\,10}$	$\Phi_{TiBuP,\Pi\,=\,11}$
20	0.19	0.42	0.59	0.76
40	0.38	0.76	0.78	0.96
60	0.58	0.83	0.93	1.01
80	0.79	0.88	0.93	1.05

Table 5.2. Calculated TiBuP surface fractions for TiBuP/PDMS blends at $\Pi < \Pi_{c,\,PDMS}$

wt% POSS	$\Phi_{TiBuP,\Pi\,(\varepsilon d,max)}$	$\Phi_{POSS,\,\Pi=6}$	$\Phi_{POSS,\Pi=7}$	$\Phi_{POSS,\Pi=8}$
20	0.19	0.20	0.20	0.21
40	0.38	0.42	0.43	0.46
60	0.58	0.63	0.65	0.67
80	0.79	0.81	0.82	0.88

As seen in Tables 5.1 and 5.2 there is an enrichment of TiBuP in the layer directly bound to water as soon as Π exceeds Π (ε_d,max) for PDMS. Furthermore, at very high Π, all films have a high TiBuP composition in the layer directly bound to water. Φ_{TiBuP} values over 1 are attributed to the fact that TiBuP starts to transform into multilayer aggregates at Π > ~ 11 $mN \cdot m^{-1}$. The enrichment of the layer directly bound to the water in the TiBuP component is interesting in terms of classical theories for the enhancement of viscoelastic moduli by filler and nanofillers. The increase of modulus for polymeric materials when incorporated with filler materials usually involves several factors: (1) a hydrodynamic effect arising from the introduction of rigid particles, (2) the increase of cross-linking density by polymer-filler interactions, and (3) the formation of filler aggregates or networks through filler-filler interactions that trap polymer chains inside. In our system, both the high Φ_{TiBuP} values and previous BAM results[44] suggest the formation of TiBuP networks at high Π. Figure 5.13 presents the top and side views of possible surface morphologies for blends during and after PDMS forms bilayers. In Figure 5.13, red solid curves represent PDMS polymer chains, black spheres represent TiBuP molecules, and blue rectangles represent the subphase (water). In Figure 5.13a before PDMS collapses, TiBuP serves as the phase dispersed in the PDMS matrix (also depicted in Figure 5.12). In Figure 5.13b and c, collapse of PDMS increases the fraction of TiBuP at the surface fraction (Table 5.1 and 5.2), and the TiBuP molecules likely form networks with increasing surface fraction that restrict PDMS mobility at the A/W interface, thereby reinforcing the polymer matrix. Figure 5.13b depicts lightly networked TiBuP with comparatively low Φ_{TiBuP} where PDMS would form bilayers only within PDMS domains. As Φ_{TiBuP} increases, some collapsed PDMS chains may spread over the

top of TiBuP domains as depicted in Figure 5.13c. Characteristic interfacial morphologies like those depicted in Figure 5.13 probably occur at different Π values for different blend composition. In order for the TiBuP networks to form, a critical percolation threshold must be exceeded. On the basis of the SLS results for ε_d, this value is likely on the order of $\Phi_{TiBuP} \sim 0.5$. In essence, the TiBuP component must become the major phase in the layer directly bound to the water surface before significant reinforcement occurs. On the basis of this threshold, reinforcement of the 20 wt% TiBuP blends would not occur until $\Pi > 9$ mN·m^{-1}, whereas the 40 wt% TiBuP blend would already exhibit reinforcement in Regime C ($\Pi > 8$ mN·m^{-1}) , and 60 and 80 wt% TiBuP blends would show reinforcement for $\Pi \geq 6$ mN·m^{-1}.

5.4 Conclusions

In this chapter, the viscoelastic behavior of PDMS, TiBuP, and their blends were studied via addition Π – A isotherms and SLS at the A/W interface. The blends exhibit interesting rheological behavior depending on both composition and surface pressure. At low Π ($\Pi < 2.5$ mN·m^{-1}), TiBuP and its attendant water act as a plasticizer of the PDMS films. In the regime $2.5 < \Pi < 5$ mN·m^{-1}, ε_d for the blends is comparable to pure PDMS. This observation may indicate that water is being squeezed out from the film and TiBuP is not able to plasticize PDMS on its own. For $\Pi > 5$ mN·m^{-1}, composition dependent reinforcement of the blends occurs. The Π where reinforcement occurs decreases as the wt% TiBuP increases and may correlate with the point where TiBuP becomes the major component in the layer directly in contact with water. As such, TiBuP networks may be

forming that restrict PDMS mobility and enhance the modulus of the collapsed PDMS film.

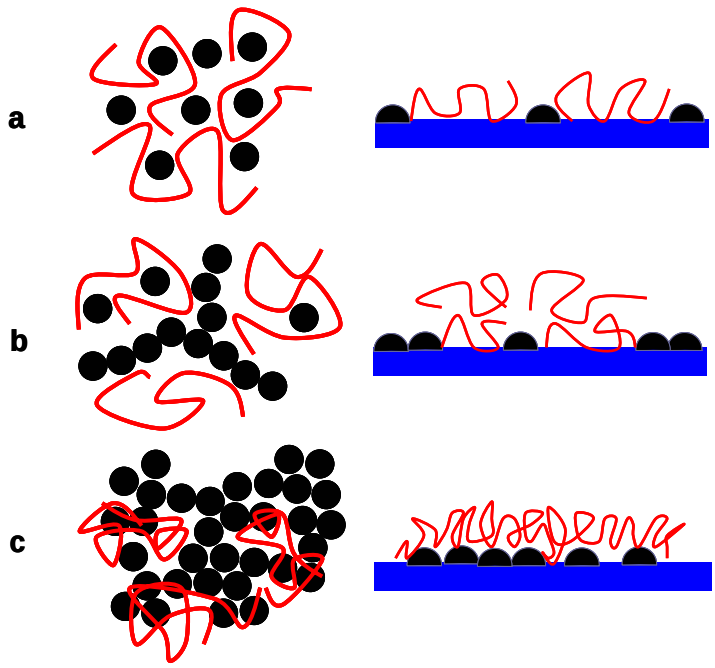

Figure 5.13. A schematic depiction of the top view (left) and side view (right) of possible interfacial morphologies of PDMS (solid curves) reinforced with TiBuP (black spheres) at the A/W interface: (a) a PDMS monolayer with dispersed TiBuP, (b) lightly networked TiBuP with collapsed PDMS, and (c) heavily networked TiBuP with collapsed PDMS.

CHAPTER 6

Phase and Rheological Behavior of Octaisobutyl-POSS/PDMS Blends at the Air/Water Interface

6.1 Abstract

In Chapter 5, trisilanolisobutyl-POSS (TiBuP)/polydimethylsiloxane (PDMS) blends exhibited interesting phase and rheological behavior depending both on the wt% TiBuP in the film and surface pressure. In this chapter, blends of non-amphiphilic octaisobutyl-POSS (OiBuP) and PDMS are investigated via successive addition surface pressure (Π) – average area per repeat unit (<A>) isotherm and surface light scattering (SLS). OiBuP/PDMS blends exhibit dramatically different phase and rheological behavior than TiBuP/PDMS blends. Before the PDMS component collapses, OiBuP reinforces the PDMS matrix by forming networks and an overall "bridge structure" on top of PDMS monolayer. During the monolayer to bilayer transition for the PDMS component, the blends show composition dependent viscoelastic behavior. After collapse of the PDMS component, few OiBuP are likely left at the A/W interface and the films exhibit negligible viscoelastic behavior just like single-component PDMS films.

6.2 Introduction

The increasing interest in nanocomposite materials have led to a renewed interest in polyhederal oligomeric silsesquioxanes (POSS), silica based nanofiller materials.[44-47] POSS was first reported by Scott in 1946.[48] POSS molecules are composed of a Si-O inorganic cage and an organic corona as shown in Figure 6.1. Generally there are two primary species of POSS derivatives: closed cage POSS, the most common of which are octameric POSS (R_8T_8) (Figure 6.1A) and open cage POSS, like trisilanol-POSS ($R_7T_7(OH)_3$) (Figure 6.1B) derivatives where one corner of the cage is replaced by three silanol groups. Deng *et al.*[62] first reported that trisilanolisobutyl-POSS (TiBuP) forms uniform Langmuir monolayers and exhibits much simpler phase transitions relative to fatty acids at the air/water (A/W) interface. Subsequent morphological studies of phase behavior as well as viscoelastic properties of trisilanol-POSS derivatives followed.[62-64] Furthermore, interfacial morphology studies of some POSS/polydimethylsiloxane (PDMS) blends at the A/W interface also followed.[65-67] On the basis of a thermodynamic analysis of the Π – A isotherms and Brewster angle microscopy (BAM) images, Hottle *et al.*[65] pointed out that TiBuP/PDMS blends form uniform monolayers at the A/W interface. No detectable phase separation or aggregation was observed until TiBuP began to collapse. At that point, ring-like structures were observed during the expansion of the films. In another paper by Hottle *et al.*,[66] octaisobutyl-POSS (OiBuP)/PDMS blends were studied at the A/W interface as a comparison to TiBuP/PDMS blends. Unlike PDMS blends with amphiphilic TiBuP which formed uniform monolayers at the A/W interface, OiBuP blends with PDMS are heterogeneous at all surface concentrations. However, the OiBuP/PDMS blends were "homogenously" heterogeneous films relative to single-

component films of OiBuP at the A/W interface. Apparently, PDMS is capable of breaking up large OiBuP aggregates in this system. Furthermore, ring-like networks or morphologies like "shattered glass" were observed during expansion Π – <A> isotherms that are consistent with POSS networks forming in the PDMS/POSS films. A natural extension for these two blend systems would be interfacial rheology studies. In Chapter 5, the viscoelastic behavior of TiBuP/PDMS blends were studied via SLS at the A/W interface. The blends exhibited interesting rheological behavior depending on film composition and surface pressure. At low Π (Π < 2.5 mN·m^{-1}), TiBuP and its attendant water act as a plasticizer for the PDMS. In the regime 2.5 < Π < 5 mN·m^{-1}, ε_d for the blends is comparable to pure PDMS. At higher Π for all blends, TiBuP likely networks in the layer directly bound to water, thereby restricting PDMS chain mobility and enhancing the modulus of the collapsed PDMS film. Considering the obvious structural difference between amphiphilic TiBuP and non-amphiphilic OiBuP, a SLS study of OiBuP/PDMS blends should provide insight into how different POSS derivatives work as nanofillers to reinforce the polymer matrix and how POSS-subphase interactions play a role in the rheological behavior of the blends at the A/W interface.

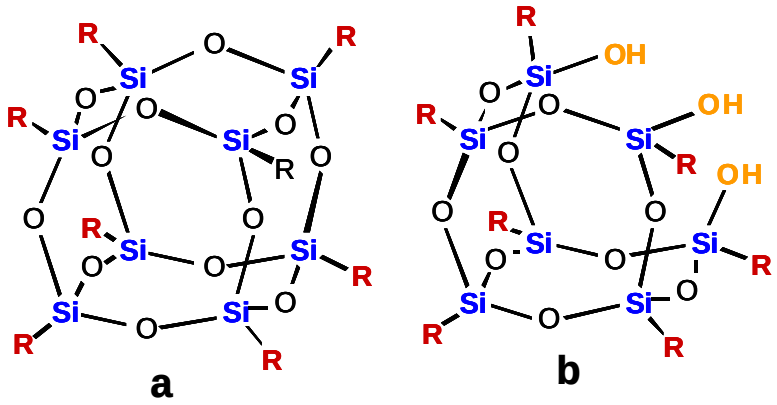

Figure 6.1. Chemical structures for (a) a closed cage octameric-POSS, and (b) an open cage trisilanol-POSS. R can be hydrogen, alkyl, alkenyl, aryl, etc.

In the remainder of this chapter, the interfacial viscoelastic behavior of OiBuP/PDMS blends will be studied via SLS measurements. With a non-amphiphilic OiBuP instead of amphiphilic TiBuP as the model nanofiller, the blends are expected to exhibit different rheological behavior arising from different OiBuP versus TiBuP interactions with water. This information along with previous morphological study will be used to propose possible molecular conformations at the A/W interface.

6.3 Results and Discussion

6.3.1 Phase and Rheological Behavior of PDMS

The understanding of the phase and rheological behavior of PDMS is essential for interpreting studies of OiBuP/PDMS blends. In Chapter 5, both addition isotherm and SLS results were presented and several essential conclusions were drawn. First, PDMS forms Langmuir films at the A/W interface and can be characterized by four regimes: (A) submonolayer (surface pressure $\Pi = 0$ mN·m^{-1}), (B) monolayer ($0 < \Pi < 8$ mN·m^{-1}), (C) a

monolayer to bilayer transition ($\Pi_{c,PDMS}$ ~ 8 mN·m^{-1}), and (D) multilayer (Π ~ 9 mN·m^{-1}).[83] Second, static dilational elasticity (ε_s) values deduced from the Π – A isotherm are in excellent aggrement with dynamic dilational elasticities (ε_d) deduced from SLS measurements. This conclusion was consistent with small dynamic dilational viscosities (κ) and the loss modulus ($\omega\kappa$) at all Π. Furthermore, the loss tangent, $tan\delta = \omega\kappa/\varepsilon_d$ < 1 (approaching 0) at most Π except the start of Regime A, and Regime C and Regime D where the PDMS film lacks viscoelastic character. All of these results are consistent with the fact that PDMS films are essentially purely elastic. Third, the scaling exponent z (ε = zΠ) that describes the molecule-subphase interactions is ~ 30, which suggests that the A/W interface is near theta solvent for PDMS and only the minimum amount of water needed to fill the excluded volume is present in the film upon the formation of a monolayer. Fourth, ε_d for PDMS is zero in the collapsed regime owing to weak molecule-subphase interactions as well as weak intermolecular and intramolecular interactions. In this chapter, these conclusions will serve as a starting point for analyzing the phase and rheological behavior of OiBuP/PDMS blends.

6.3.2 Addition Π - <A> Isotherms of OiBuP/PDMS Blends

Figure 6.2 presents plots of Π as a function of the average area per monomer, <A>, for PDMS and OiBuP/PDMS blends of different composition. The isotherm for pure OiBuP is not included because OiBuP is non-amphiphilic and is unable to form a stable Langmuir film at the A/W interface.[32] There are several important features one can observe in Figure 6.3. All isotherms lift off at almost same area (<A>) and share similar shape up to Π ~ 6 mN•m^{-1}. This feature implies that OiBuP has a traditional filler effect for $\Pi \leq$ 6 mN•m^{-1}. In this regime, OiBuP resides at the A/W interface, but the surface

tension properties are similar to single-component PDMS. Furthermore, as mentioned in Chapter 5, the isotherms of TiBuP/PDMS blends lie between those of TiBuP and PDMS. Considering OiBuP should have a similar cross-sectional area to TiBuP, this feature also suggests that OiBuP exists as a multilayer at all Π. The other remarkable feature is that all blends start to deviate from pure PDMS behavior from Π ~ 6 $mN \cdot m^{-1}$, around the middle of Regime B. The inset in Figure 6.2 expands the monolayer to bilayer transition regime where the transition behavior is composition dependent. For 20 and 40 wt% OiBuP blends, the isotherms still exhibit a relatively clear plateau similar to pure PDMS. However, the plateau is not as well defined for 60 and 80 wt% OiBuP blends. Instead, they exhibit a change of slope from Π ~ 6 to 9 $mN \cdot m^{-1}$. These observations are consistent with previous work and the heterogeneous film observed by BAM.[32] In this chapter, interfacial rheological properties of OiBuP/PDMS blends are probed through SLS measurements.

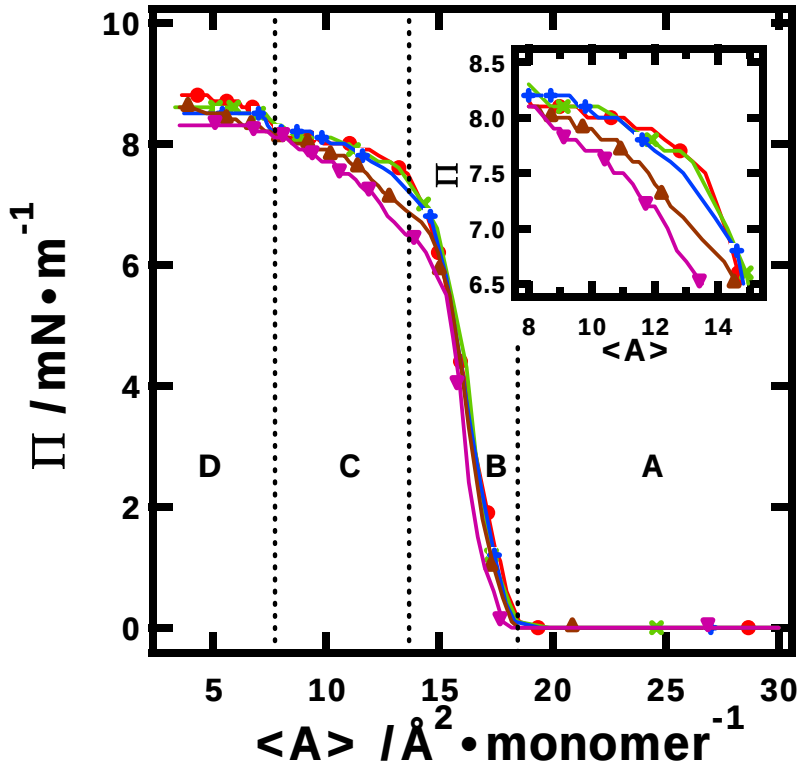

Figure 6.2. Successive addition Π - <A> isotherms for octaisobutyl-POSS/PDMS blends with 0 (PDMS, red ●), 20 (green ×), 40 (blue +), 60 (brown ▲) and 80 (purple ▼) wt% OiBuP at T = 22.5 °C. The inset expands Regime C, the first plateau. The dotted vertical lines indicate the boundaries between different PDMS regimes.[8]

6.3.3 SLS Results for OiBuP/PDMS Blends

The SLS data analysis scheme is the same one used in Chapter 5. Frequency shift (f_s) and full-with at half-maximum intensity corrected for instrumental broadening ($\Delta f_{s,c}$) values obtained from three diffraction orders (with wave vectors of k = 404.3 cm^{-1}, 459.0 cm^{-1}, and 512.6 cm^{-1}) are converted to an arbitrary reference state (water at 25 °C with a surface tension of $\sigma_{d,ref}$ = 71.97 $mN \cdot m^{-1}$,a transverse viscosity of μ_{ref} = 0, a density of ρ_{ref} = 997.0 $kg \cdot m^{-3}$, a viscosity of η_{ref} = 0.894 mPa•s, and k_{ref} = 324.3 cm^{-1}) to deduce

equivalent frequency shifts ($f_{s,eq}$) and corrected full-widths at half-maximum intensity ($\Delta f_{s,c,eq}$). After verifying that these values are frequency independent, it is possible to average them for the different wave vectors and provide error estimates as shown in Figures 6.3 and 6.4. The horizontal dotted lines in Figure 6.3 and 6.4 represent several limiting cases of the dispersion equation for a viscoelastic film as discussed in Chapter 2: (I) pure liquid behavior, (II) the maximum velocity for a purely elastic film, (III) the maximum damping coefficient for purely elastic film, (IV) the minimum velocity for purely elastic film, (V) the infinite modulus limit, and (VI) the maximum damping coefficient for a purely viscous surface film.[123,231] For OiBuP/PDMS blend Langmuir films, limits (I), (III), and (IV) are the most important and correspond to the horizontal dotted lines included on Figure 6.3 and 6.4 Comparing the $f_{s,eq}$ and $\Delta f_{s,c,eq}$ data with these limiting cases provides useful information about the viscoelastic behavior of OiBuP/PDMS blends at the A/W interface.

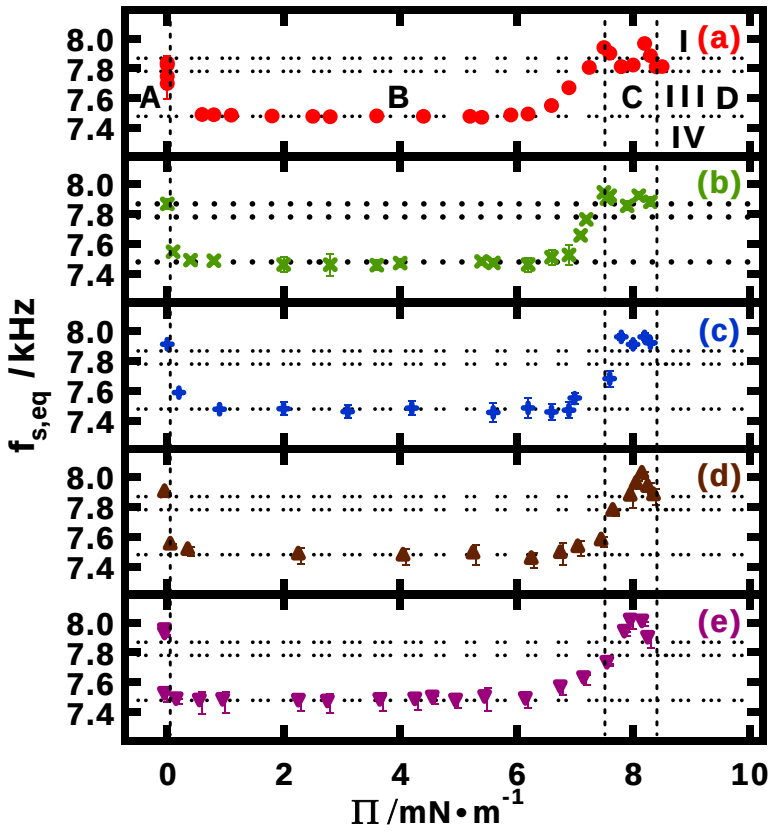

Figure 6.3. $f_{s,eq}$ – Π for (a) 0 (PDMS, red ●), (b) 20 (green ×), (c) 40 (blue +), (d) 60 (brown ▲), and (e) 80 wt% OiBuP (purple ▼) blends at T = 22.5 °C. Data points represent an average of three wave vectors with one standard deviation error bars. Vertical dotted lines indicate Regimes A through D defined in Figure 6.2. The three horizontal dotted lines correspond to limiting cases of the dispersion relation: (I) pure liquid limit, and (III) the maximum damping coefficient, and (IV) the minimum velocity limit for perfectly elastic surface films.

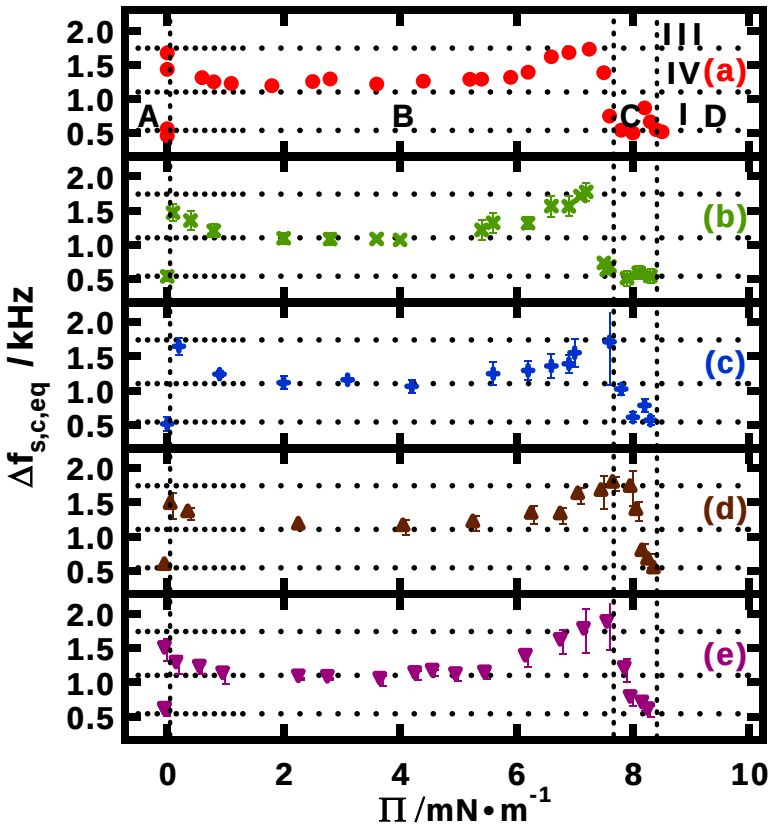

Figure 6.4. $\Delta f_{s,c,eq}$ – Π for (a) 0 (PDMS, red ●), (b) 20 (green ×), (c) 40 (blue +), (d) 60 (brown ▲), and (e) 80 wt% OiBuP (purple ▼) blends at T = 22.5 °C. Data points represent an average of three wave vectors with one standard deviation error bars. Vertical dotted lines indicate Regimes A through D defined in Figure 6.2. The three horizontal dotted lines correspond to limiting cases of the dispersion relation: (I) pure liquid limit and (III) the maximum damping coefficient, and (IV) the minimum velocity limit for perfectly elastic surface films.

Figure 6.3 and 6.4 show $f_{s,eq} - \Pi$ and $\Delta f_{s,c,eq} - \Pi$ plots, respectively, of PDMS and blends containing different wt% POSS. $f_{s,eq}$ and $\Delta f_{s,c,eq}$ exhibit trends that are similar to PDMS films prior to Regime C for all blends. In Regime A, the viscoelastic profile for all blends is consistent with the pure liquid limit (I). At the very beginning of Regime B, both $f_{s,eq}$ and $\Delta f_{s,c,eq}$ quickly approach the maximum damping coefficient limit for a perfectly elastic surface film (III). The scattering of data points between limit (I) and limit (III) at this regime boundary arises from the biphasic nature of the coexisting liquid (L) and gas (G) phases at $\Pi = 0$ for PDMS[261] and OiBuP/PDMS[32] blend Langmuir films. In the middle of Regime B, the global minimum in $f_{s,eq}$ and the local minimum of $\Delta f_{s,c,eq}$ correspond to the viscoelastic behavior of a perfectly elastic film in the minimum velocity limit (IV). At the high Π end of Regime B, $f_{s,eq}$ starts to rise, and $\Delta f_{s,c,eq}$ shows another maximum matching the maximum damping coefficient for a perfectly elastic surface film (III).

Around Regime C, OiBuP/PDMS exhibit composition dependent viscoelastic behavior. The $f_{s,eq} - \Pi$ and $\Delta f_{s,c,eq} - \Pi$ plots for 20 and 40 wt% OiBuP blend are similar to single-component PDMS. All of the blends reach the pure liquid limit (I) at the border of Regime B and C, and some exhibit a local minimum ($f_{s,eq}$) and maximum ($\Delta f_{s,c,eq}$) in Regime C. This behavior is attributed to the formation of a bilayer. At the end of Regime C and the beginning of Regime D, both $f_{s,eq}$ and $\Delta f_{s,c,eq}$ return to pure liquid behavior (I) upon the formation of PDMS multilayers. For 60 and 80 wt% OiBuP, the local maximum in $\Delta f_{s,c,eq}$ and local minimum in $f_{s,eq}$ for single-component PDMS films are

absent. $\Delta f_{s,c,eq}$ and $f_{s,eq}$ for 60 and 80 wt% OiBuP blends only approach the pure liquid limit (I) near the end of Regime C. In Regime D, none of the blend films are viscoelastic.

These observations suggest that prior to the monolayer to bilayer transition, OiBuP/PDMS films exhibit viscoelastic properties that are similar to single-component PDMS films. Apparently, OiBuP behaves as a traditional filler. At higher Π, OiBuP/PDMS show composition dependent viscoelastic behavior which may be indicative of PDMS collapsing through somewhat different mechanism.

6.3.4 Rheological Behavior of OiBuP/PDMS Blends

Figure 6.5 shows $\varepsilon_d - \Pi$ for all four blends and pure PDMS with an inset amplifying the transition regime. For all blends, ε_d starts from zero in Regime A (submonolayer regime) and increases sharply as Π increases in a fashion similar to a single-component PDMS film. At the start of Regime B, ε_d for all of the blends starts to exceed PDMS at small Π, ~ 1 to 2 $mN \cdot m^{-1}$. ε_d values then reach maximum moduli around $\varepsilon_{d,max} \sim 35$ $mN \cdot m^{-1}$ in the middle of Regime B. As the films begin to collapse, ε_d also decreases (end of Regime B). During the start of the collapse process at the end of Regime B, all of the blend films have viscoelastic moduli that are greater than or equal to single-component PDMS films. In the monolayer to bilayer transition regime ($\Pi \sim 8$ $mN \cdot m^{-1}$), the blends exhibit composition dependent behavior as shown in the inset. ε_d for 20 and 40 wt% OiBuP blends exhibit features that are similar to single-component PDMS films: $\varepsilon_d \rightarrow 0$ at the boundary between Regime B and C, exhibits a local maximum in ε_d in Regime C, and $\varepsilon_d \rightarrow 0$ at the end of Regime C. In contrast, ε_d for 60 and 80 wt%

OiBuP blends monotonically decrease across Regime C with increasing Π and $\varepsilon_d \rightarrow 0$ at the end of Regime C.

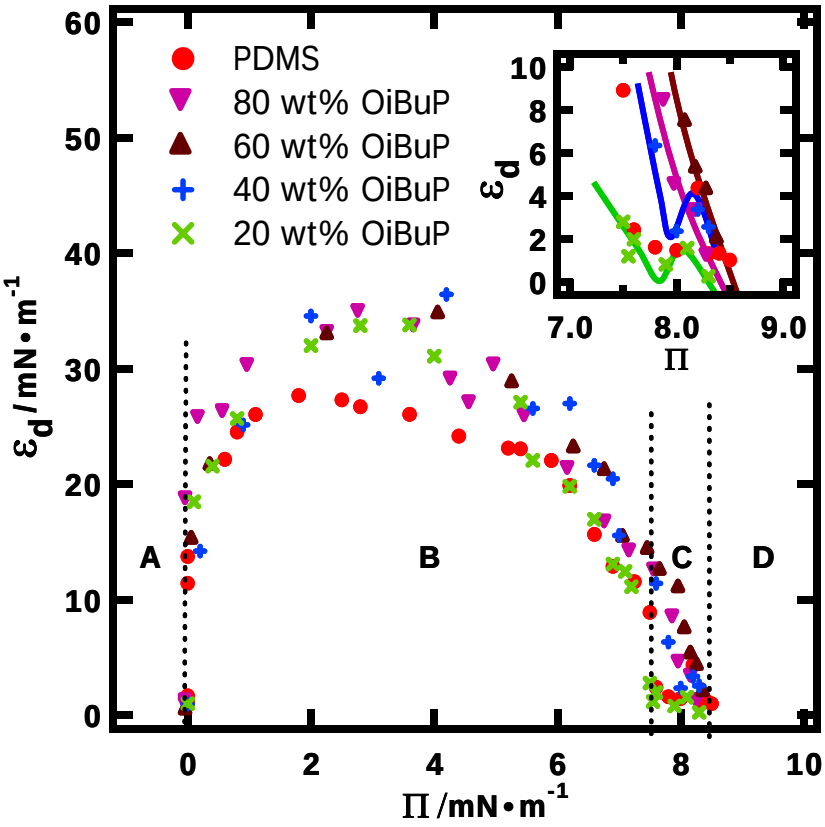

Figure 6.5. ε_d – Π for 0 (PDMS red ●), 20 (green ×), 40 (blue +), 60 (brown ▲), and 80 wt% OiBuP (purple ▼) blends at T = 22.5 °C. Data points represent an average of three wave vectors. Vertical dotted lines indicate Regimes A through D defined in Figure 6.2**.** One standard deviation error bars (~ 5%) are omitted for clarity. The inset expands the collapsed regime (Π ~ 8 mN•m^{-1}) and the curves highlight the trends for the blends in this regime.

Several interesting features can be observed when comparing $\varepsilon_d - \Pi$ behavior for OiBuP/PDMS blends with TiBuP/PDMS blends discussed in Chapter 5. First, ε_d increases more gradually for all TiBuP/PDMS blends than single-component PDMS films. This behavior is attributed to hydrogen bonding between silanol groups of TiBuP and water, where more water molecules need to be squeezed out of the Langmuir film. In contrast, all of the initial slopes for OiBuP/PDMS blends on $\varepsilon_d - \Pi$ plots are as large as or larger than the value for PDMS. As OiBuP is non-amphiphilic, we hypothesize that excess bound water is absent in the blend films leading to enhanced rigidity. Second, TiBuP/PDMS blends have approximately the same $\varepsilon_{d,max}$ values as PDMS at $2.5 < \Pi < 5$ $mN \cdot m^{-1}$, whereas, $\varepsilon_{d,max}$ values for all OiBuP/PDMS blends are greater than PDMS (~ 35 vs. ~ 30 $mN \cdot m^{-1}$). This observation shows OiBuP reinforces the PDMS films. Third, similar to TiBuP/PDMS blends, the OiBuP/PDMS blends exhibit composition dependent viscoelastic behavior during the monolayer to bilayer transition. However, unlike TiBuP/PDMS blends where all blends exhibit reinforcement in Regime D, none of the OiBuP/PDMS blends exhibit viscoelastic behavior in Regime D. The absence of viscoelastic behavior in Regime D for OiBuP/PDMS blends supports the conjecture that TiBuP reinforces PDMS blends in Regime D by forming network-like structures that anchor the collapsed PDMS film to the interface. As OiBuP is non-amphiphilic, it is unable to anchor the collapsed PDMS film to the A/W interface.

Plots of surface dilational loss moduli ($\omega\kappa$) versus Π plots are presented in Figure 6.6 while plots of dilational viscosity (κ) are omitted owing to the similarity between $\omega\kappa$ and κ. Some $\omega\kappa$ values are negative with large standard deviation, which is consistent

with the fact that the blend films are heterogeneous at all Π. However, the absolute values of ωκ remain small for all Π showing that the films are still elastic dominant.

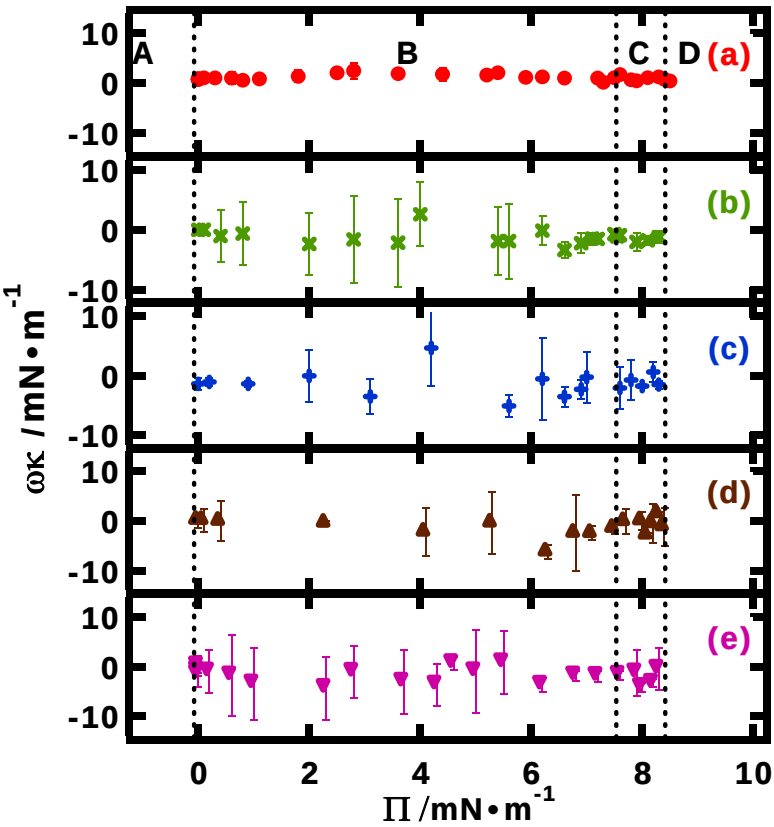

Figure 6.6. ωκ – Π for (a) 0 (PDMS, red ●), (b) 20 (green ×), (c) 40 (blue +), (d) 60 (brown ▲), and (e) 80 wt% OiBuP (purple ▼) blends at T = 22.5 °C. Data points represent an average of three wave vectors with one standard deviation bars. Vertical dotted lines indicate Regimes A through D defined in Figure 6.2**.**

6.3.5 Possible Molecular Conformation of OiBuP/POSS Blends at the A/W Interface

Figure 6.7 provides a schematic depiction of possible OiBuP aggregation within OiBuP/PDMS blends. Unlike amphiphilic TiBuP, the non-amphiphilic OiBuP exists as multilayers at $\Pi < \Pi_{c,PDMS}$ (~8 $mN \cdot m^{-1}$) and PDMS occupies most of the A/W interface. Significant amounts of OiBuP likely reside on top of the PDMS layer with only a small fraction directly bound to water. Those OiBuP in the upper layer are able to form networks and serve as "bridges" between OiBuP molecules that still reside directly at the A/W interface and serve as the "bridge pier". Hence, OiBuP is able to reinforce the PDMS matrix in its monolayer regime the same way TiBuP reinforce the TiBuP/PDMS blends in Regime D after the PDMS component has collapsed. However, after the PDMS collapses into bilayer and multilayer films, OiBuP cannot form a viscoelastic film like TiBuP and hereby the blends films exhibit no viscoelastic properties even if the "bridge structure" still remains.

During the monolayer to bilayer transition for PDMS, there are likely two parallel processes taking place in the blend films: PDMS undergoing the transition in regions where there is no OiBuP on top, (Figure 6.8a) and PDMS underneath OiBuP molecules undergoing the transition (Figure 6.8b). During the second process, the OiBuP molecules on top of PDMS chains are able to hinder the collapse of PDMS. As a result, blends with high wt% OiBuP have higher ε_d during bilayer formation that masks the local maximum on the $\varepsilon_d - \Pi$ plots signifying completion of a PDMS bilayer. For 20 and 40 wt% OiBuP blends, the collapse behavior of these blends is essentially the same as PDMS and a local maximum in ε_d is observed on the corresponding $\varepsilon_d - \Pi$ plot for Regime C (Figure 6.8a).

For 60 and 80 wt% OiBuP blends, the second process is likely dominant during the monolayer to bilayer transition owing to the fact more OiBuP is present in the film leading to greater coverage of the PDMS by OiBuP prior to collapse of the PDMS component. The blends thereby exhibit viscoelastic behavior that differs from single-component PDMS films. This hypothesis is partially supported by BAM studies by Hottle *et al.*[32] During film expansion, OiBuP/PDMS blends with higher wt% OiBuP exhibit "shattered glass" morphologies that are consistent with OiBuP covering most of the surface. In contrast lower wt% OiBuP blends exhibit ring-like structures. The ring-like morphology indicates that open space in the layer above PDMS must be present even at high Π.

6.4 Conclusions

In this chapter, the viscoelastic behavior of OiBuP/PDMS blends with different wt% OiBuP is studied via SLS at the A/W interface. OiBuP likely networks in the upper layer and reinforces the PDMS matrix at the A/W interface via a "bridge" structure prior to collapse of the PDMS component. During the monolayer to bilayer transition of PDMS, blends exhibit composition dependent viscoelastic behavior. After the collapse of PDMS, there are likely few OiBuP molecules left at the A/W interface and all blend films exhibit no dilational viscoelastic behavior. These results suggest that POSS-subphase interactions play an important role on the interfacial behavior of POSS/PDMS blends at the A/W interface.

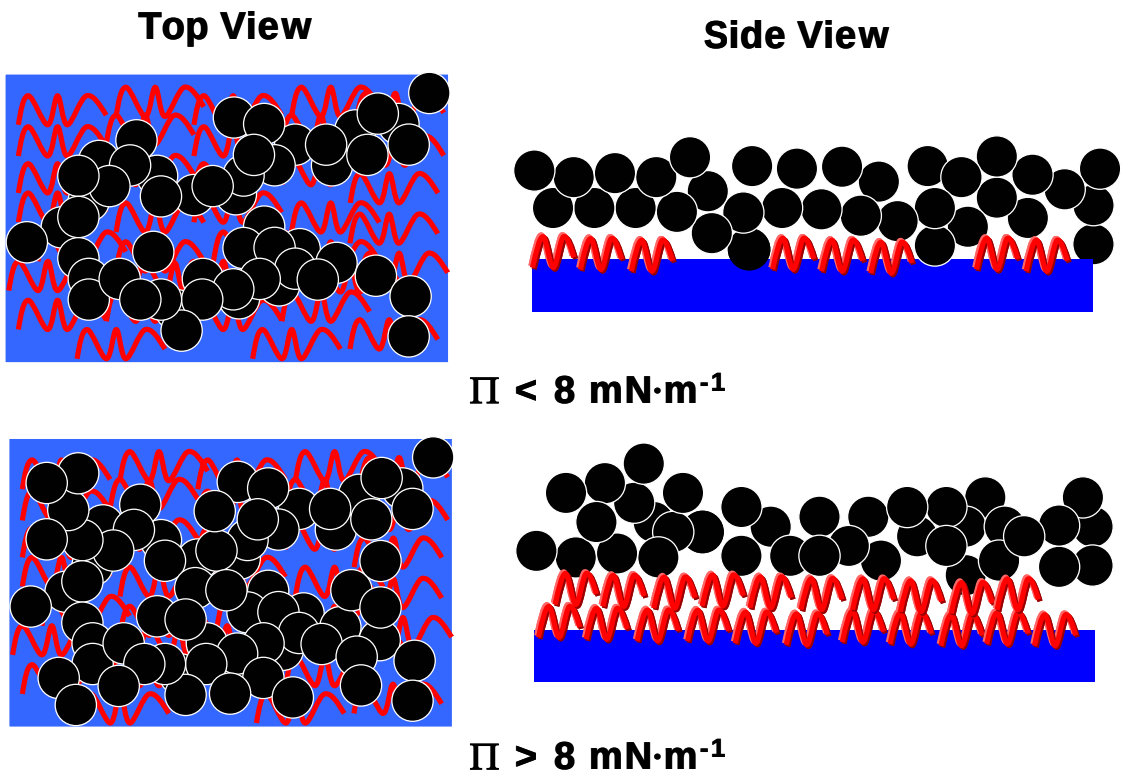

Figure 6.7. Depiction of the top and side view of OiBuP/PDMS blends at the A/W interface for (top) $\Pi < 8$ mN•m^{-1} and (bottom) $\Pi > 8$ mN•m^{-1}. The red coils represent PDMS polymer chains, black spheres represent OiBuP molecules, and the blue background represents the A/W interface.

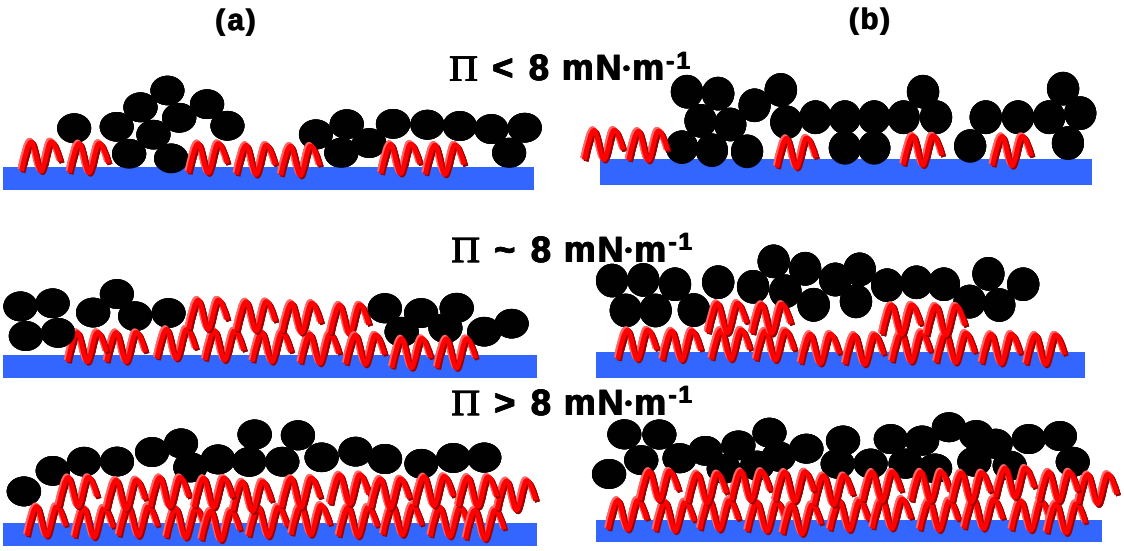

Figure 6.8. Schematic graph representing the transition mechanism for blends around the collapse pressure ($\Pi \sim 8$ mN•m^{-1}) for (a) 20 and 40 wt% OiBuP/PDMS blends and (b) 60 and 80 wt% OiBuP/PDMS blends. The red coils stand for PDMS polymer chains, the black spheres represent OiBuP molecules, and the blue bars represent the water surface.

CHAPTER 7

Morphological Study of Trisilanolcyclopentyl-POSS/PDMS Blends at the Air/Water Interface

7.1 Abstract

In Chapters 5 and 6, the interfacial phase and rheological behavior of two polyhederal oligomeric silsesquioxane (POSS) blended with polydimethylsiloxane (PDMS), trisilanolisobutyl-POSS (TiBuP)/PDMS and octaisobutyl-POSS (OiBuP)/PDMS blends, respectively, were investigated via surface pressure (Π) – averaged surface area per monomer (<A>) isotherms and surface light scattering (SLS) at the air/water (A/W) interface. The results reveal the impact of POSS-subphase interactions on the reinforcing behavior of POSS derivatives within a thin film polymeric matrix. In this chapter, a trisilanol-POSS with different substituents, trisilanolcyclopentyl-POSS (TCpP), is used as a model nanofiller to blend with PDMS. Compared with TiBuP/PDMS and OiBuP/PDMS blends discussed in Chapters 5 and 6, TCpP/PDMS blends exhibit dramatically different composition dependent phase behavior. According to the thermodynamic analysis of the Π – <A> isotherms and Brewster angle microscopy (BAM) images, all blends likely form uniform monolayers at the A/W interface. Low wt% TCpP blends (wt% TCpP < 20) exhibit phase behavior that is similar to single-component PDMS. Blends with 20 to 60 wt% TCpP show complex phase behavior. They exhibit transitions at Π values lower than the collapse pressures for

either PDMS or TCpP. These transitions give rise to morphological features that are strikingly similar to phase separation. Plateaus in the Π – <A> isotherms may indicate the PDMS monolayer to bilayer transition is either distorted (20 or 40 wt% TCpP) or delayed (60 wt% TCpP). All blends with 20 to 60 wt% TCpP also show a kink around Π ~ 13 $mN \cdot m^{-1}$. Blends with greater than 60 wt% TCpP exhibit TCpP-like phase behavior but form small aggregates instead of the large aggregates observed for single-component TCpP films. These observations are dramatically different from any previously studied POSS/PDMS blends and suggest that substituents of trisilanol-POSS have considerable impact on the phase behavior of POSS/PDMS blends.

7.2 Introduction

The overriding motivation for the studies presented in this dissertation is to understand how molecule-subphase and intermolecular interactions affect the dispersion of nanofillers within a Langmuir film and to understand how the dispersion of the nanofiller affects the rheological behavior of the blend films. In Chapter 5 and 6, the interfacial phase and rheological behavior of two polyhederal oligomeric silsesquioxane (POSS)/PDMS blends, trisilanolisobutyl-POSS (TiBuP)/PDMS blends and octaisobutyl-POSS (OiBuP)/polydimethylsiloxane (PDMS) blends, were investigated via surface pressure (Π) – average area per monomer (<A>) isotherms and surface light scattering (SLS). These two POSS derivatives with identical substituents (isobutyl) exhibit dramatically different reinforcing behavior as nanofillers within a PDMS matrix. The difference apparently arises from different molecule-subphase interactions considering

TiBuP is amphiphilic, able to hydrogen bond with water, while OiBuP exhibits no surface activity. Hence, an interesting next step is to investigate the effect different substituents have on the nanofiller behavior of POSS within a PDMS matrix. In this chapter, trisilanolcyclopentyl-POSS (TCpP) will be used as a model nanofiller to blend with PDMS. Π – <A> isotherms and Brewster angle microscopy (BAM) will be employed to investigate the phase behavior of TCpP/PDMS blend films.

7.3 Results and Discussion

7.3.1 Interfacial Behavior of TiBuP versus TCpP

Trisilanolcyclopentyl-POSS (TCpP) shows different phase and rheological behavior than TiBuP (Chapter 4) at the A/W interface. In Figure 7.1A, Π undergoes a gentle increase initially from ~ 200 $Å^2$·molecule^{-1} before reaching a plateau around A ~ 130 $Å^2$·molecule^{-1} corresponding to the on-set of the collapse transition for TiBuP. For TCpP, Π increases more sharply from A ~ 160 $Å^2$·molecule^{-1}, with film collapse at A ~ 130 $Å^2$·molecule^{-1}, essentially the same value as TiBuP. On the basis of the definition of the static dilational elasticity ($\varepsilon_s = -A\left(\partial\Pi/\partial \mathrm{A}\right)_T$), one expects the TCpP film to be more rigid than TiBuP in the monolayer with less water in the film. Furthermore, the lower collapse Π for TCpP (~ 8 mN·m^{-1} vs. ~17 mN·m^{-1} for TiBuP) is also consistent with weaker TCpP interactions with the aqueous subphase relative to TiBuP. As seen in Figure 7.1B, plots of the dynamic dilational elasticity (ε_d) deduced from SLS as a function of Π for TCpP and TiBuP show the dynamic dilational elasticity of TCpP rises more quickly at low Π and achieves a larger maximum value ~ 100 mN·m^{-1} than TiBuP. In other words, TCpP is much "harder" than TiBuP and should serve as an interesting

comparison to TiBuP for understanding the effects substituents have on POSS nanofillers.

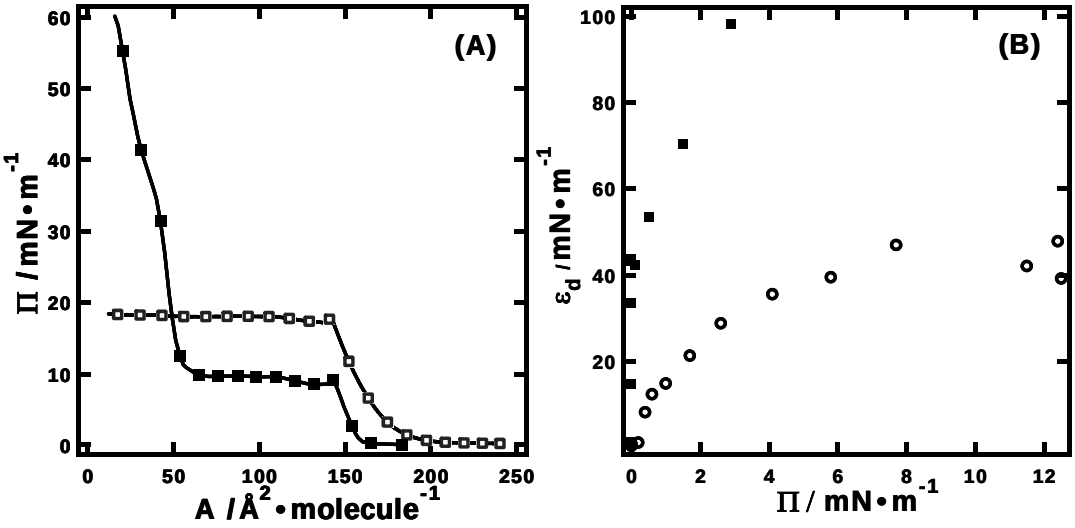

Figure 7.1. (A) Π – A for TiBuP (open squares) and TCpP (filled squares) measured at T = 22.5 °C with a constant compression rate of 10 $cm^2 \cdot min^{-1}$. (B) ε_d – Π for TiBuP (open squares) and TCpP (filled squares) measured via SLS at T = 22.5 °C. The surface concentration was controlled by the successive addition method.

7.3.2 Π – <A> Compression Isotherms of TCpP/PDMS Blends

Figure 7.2 shows compression Π – <A> isotherms for TCpP/PDMS blends with the wt% TCpP increasing from left to right. For the sake of clarity, Figure 7.3A and B show TCpP/PDMS blends with 0 to 60 wt% TCpP and 80 to 100 wt% TCpP, respectively. A reasonable expectation would be that the TCpP/PDMS blend system should be similar to the TiBuP/PDMS blends in Chapter 5 as both TiBuP and TCpP are amphiphilic. Unlike the TiBuP/PDMS blends where all blends progressively change from single-component PDMS to single-component TiBuP behavior, TCpP/PDMS blends exhibit very complex

composition dependent Π – <A> isotherms. On the basis of the shapes of the Π - <A> isotherms, TCpP/PDMS blends can be divided into three different classes: A) blends with less than 20 wt% TCpP, B) blends with 20 to 60 wt% TCpP, and C) blends with greater than ~80 wt% TCpP.

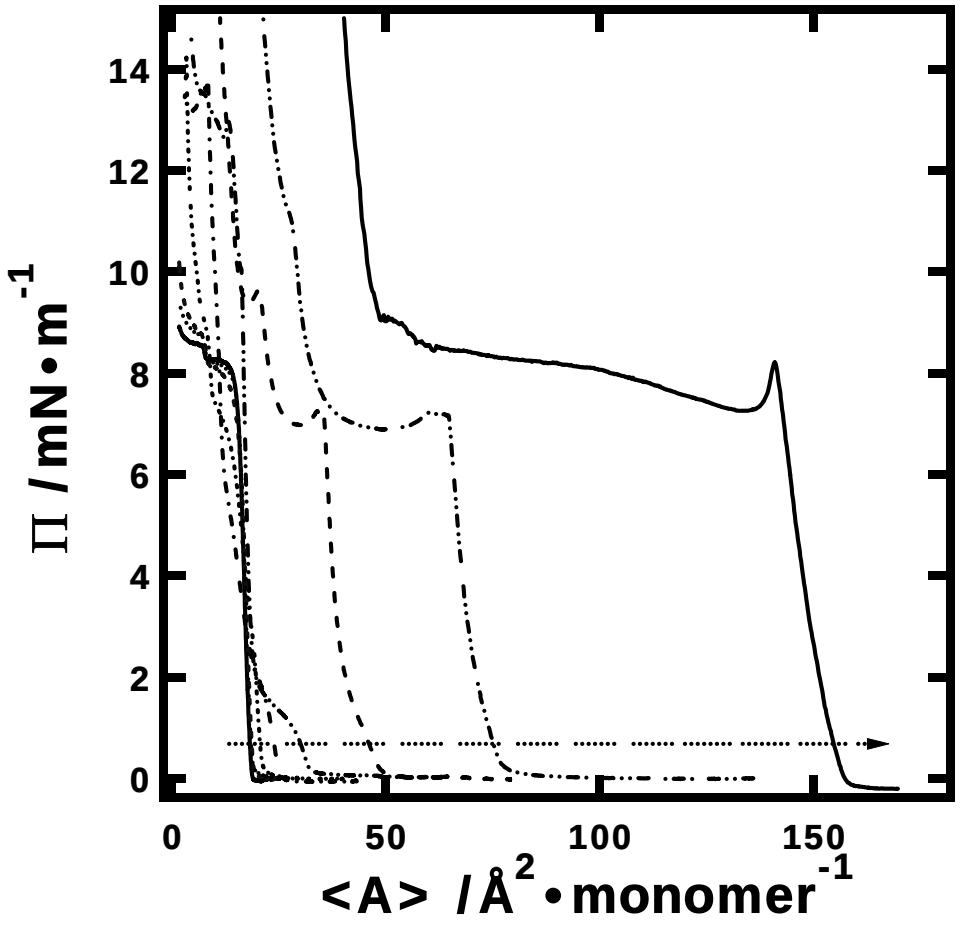

Figure 7.2. Π – <A> compression isotherms for TCpP/PDMS blends at T = 22.5 °C with a constant compression rate of 10 $cm^2 \cdot min^{-1}$. The wt% TCpP in the blends increase from left to right along the arrow: 0 (PDMS), 2, 5, 20, 40, 60, 80, 91, and 100 wt% TCpP.

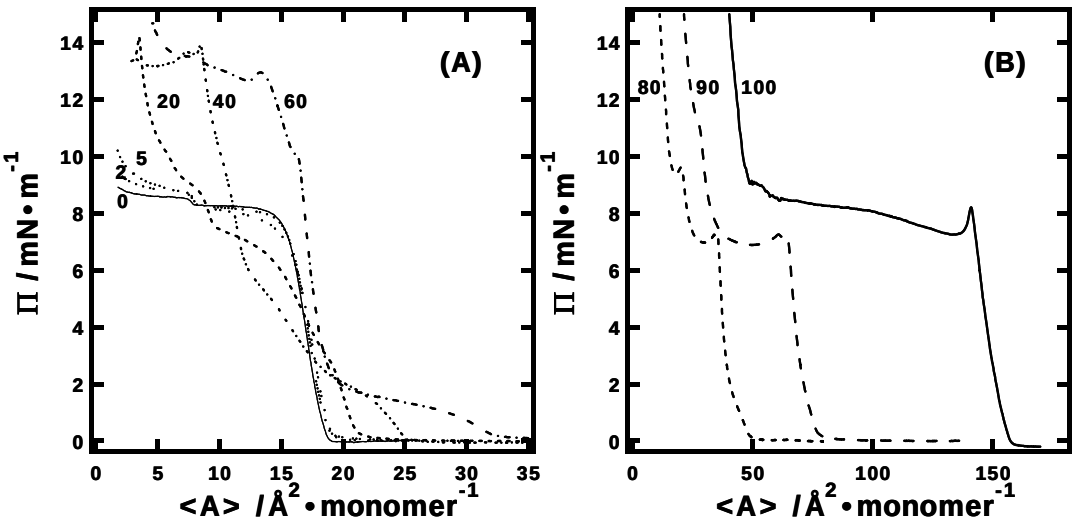

Figure 7.3. Π – <A> compression isotherms for TCpP blends with PDMS at T = 22.5 °C and a compression rate of 10 $cm^2 \cdot min^{-1}$. (A) TCpP/PDMS blends with 0 (PDMS), 2, 5, 20, 40, and 60 wt% TCpP. (B) TCpP/PDMS blends with 80 to100 wt% TCpP.

For blends with less than 20 wt% TCpP, the Π – <A> isotherms are identical to single-component PDMS films up to Π ~ 6 $mN \cdot m^{-1}$ and qualitatively similar thereafter. Deviation around the collapse transition for single-component PDMS films (Π ~ 8 $mN \cdot m^{-1}$) is characterized by lower Π for 2 and 5 wt% TCpP blends relative to a single-component PDMS film. In contrast, the second plateaus have higher Π values than for single-component PDMS films. Both the first and second plateaus are more irregularly defined with increasing wt% TCpP. Similar features were also observed in the isotherms of OiBuP/PDMS blends presented in Chapter 6, where the OiBuP exists as multilayers at all Π. Considering TCpP has a lower collapse pressure than PDMS, this feature may arise from the existence of TCpP aggregates while PDMS undergoes a monolayer to bilayer

transition. Moreover, for small <A>, all blends show elevated Π relative to single-component PDMS films even at the smallest wt% TCpP.

The phase behavior of TCpP/PDMS blends with 20 to 60 wt% TCpP differ dramatically from single-component PDMS films. All of these blends exhibit a transition at Π values below the collapse pressure of either component. With increasing wt% TCpP, the surface pressure of this transition decreases. Furthermore, the plateaus that are indicative of PDMS multilayer formation are significantly distorted (20 and 40 wt% TCpP) or absent (60 wt% TCpP) suggesting that the collapse mechanism in these blends is very different from either single-component PDMS or TCpP films. Both the 40 and 60 wt% TCpP blends exhibit a kink around Π ~ 13 $mN \cdot m^{-1}$. It is interesting to note that TiBuP/PDMS blends also exhibited a kink around Π ~ 15 $mN \cdot m^{-1}$ corresponding to the collapse pressure of TiBuP.[226] However, TCpP has an even lower collapse pressure (Π ~ 7 $mN \cdot m^{-1}$) than PDMS. Clearly, the physical meaning of this feature must be different in the TiBuP/PDMS system than in the TCpP/PDMS system.

When the blend composition is 80 wt% TCpP or greater, the TCpP/PDMS blends exhibit Π - <A> isotherms similar to TCpP. They collapse at Π ~ 7 $mN \cdot m^{-1}$, close to the collapse pressure of single-component TCpP films. After a short plateau where the PDMS component in the films is believed to undergo a monolayer to bilayer and bilayer to multilayer transitions, Π increases sharply with decreasing <A>, much like rigid TCpP films.

7.3.3 Thermodynamic Analysis of TCpP/PDMS Compression Isotherms

Although TCpP/PDMS blends exhibit strong composition dependent phase behavior, the area where Π starts to increase ($A_{lift\text{-}off}$) for all of the blends lie between single-component PDMS and single-component TCpP suggesting that both components spread at the A/W interface. Hence, a thermodynamic study of the isotherms should provide insight into the mixing behavior for TCpP/PDMS blends. An equation relating <A> to the pure components for ideal mixing is given as:

$$< A_{mix,ideal}(\Pi) >= X_{TCpP} A_{TCpP}(\Pi) + X_{PDMS} A_{PDMS}(\Pi) \qquad \text{Eq. 7.1}$$

where $A_{TCpP}(\Pi)$ and $A_{PDMS}(\Pi)$ are the values of A at a given Π value for single-component TCpP and PDMS, respectively, and X_{TCpP} and X_{PDMS} represent the mole fraction of TCpP and PDMS, respectively. Hence, the area change upon mixing (ΔA_{mix}), the 2D analog of the change in volume upon mixing in 3D at constant pressure is written as

$$\Delta A_{mix}(\Pi) =< A_{mix}(\Pi) > - < A_{mix,ideal}(\Pi) > \qquad \text{Eq. 7.2}$$

where $<A_{mix}(\Pi)>$ is the experimental <A> at a given Π. The molar Gibbs excess free energy of mixing as a function of Π ($\Delta G_{excess}(\Pi)$) is also useful for understanding the thermodynamic behavior of blends. $\Delta G_{excess}(\Pi)$ values for binary mixtures can be calculated according to

$$\Delta G_{excess}(\Pi) = \int_0^{\Pi} \Delta A_{mix}(\Pi) d\Pi \qquad \text{Eq. 7.3}$$

Figure 7.4 shows plots of $<A_{mix}(\Pi)>$ and $<A_{mix,\ ideal}(\Pi)>$ vs. X_{TCpP} for TCpP/PDMS blend films from $\Pi = 0$ (at $A_{lift\text{-}off}$) to 7 $mN \cdot m^{-1}$. At $A_{lift\text{-}off}$, $\Pi = 0$ $mN \cdot m^{-1}$, $<A_{mix}(\Pi)>$ is consistent with ideal mixing for all compositions. As Π increases, $<A_{mix}(\Pi)>$ values for high wt% TCpP blends (> 60 wt%, > 10 mol%) start to show negative deviation from $<A_{mix,\ ideal}(\Pi)>$. Correspondingly, the $\Delta G_{excess}(\Pi)$ values in Figure 7.5 become more negative at higher wt% TCpP as Π increases. The good agreement between $<A_{mix}(\Pi)>$ and $<A_{mix,\ ideal}(\Pi)>$ and the near-zero $\Delta G_{excess}(\Pi)$ values for blends containing less than 60 wt% TCpP (~ 10 mol% TCpP) is consistent with uniphasic mixtures. For mixtures containing higher wt% TCpP, the negative deviation of $<A_{mix}(\Pi)>$ from ideal mixing and the negative $\Delta G_{excess}(\Pi)$ values may suggest an attraction between the two components at elevated surface pressure. However, the thermodynamic analysis is only valid under the condition that all films are monolayers. It is still not clear if the low Π transition for 20 to 60 wt% TCpP blends involves any multilayer transitions. Hence, the negative $\Delta G_{excess}(\Pi)$ values above the transition (Π = 1.5 to 4 $mN \cdot m^{-1}$ for 20 to 60 wt% TCpP blends, respectively) could also arise from multilayer transitions where the surface area decreases simply because some molecules move to an upper layer. At this stage, the only conclusion we can draw from ΔG_{excess} analysis is that the TCpP/PDMS blends of all composition likely form compatible films $\Pi < 1.5$ $mN \cdot m^{-1}$. Further interpretations of the thermodynamic analysis of this blend system require imaging of films.

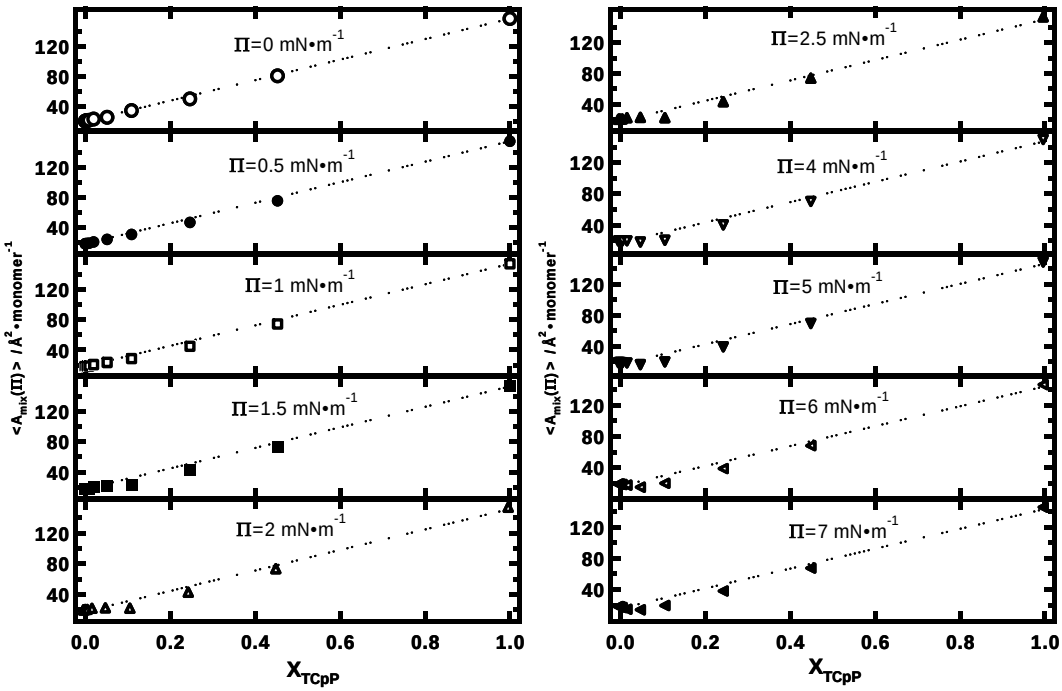

Figure 7.4. $\langle A_{mix}(\Pi)\rangle$ - X_{TCpP} for TCpP/PDMS blends with different compositions at T = 22.5 °C and different Π as indicated on the graphs. Experimental values (symbols) are compared with ideal mixing ($\langle A_{mix,ideal}(\Pi)\rangle$ from Eq. 7.1, dotted lines).

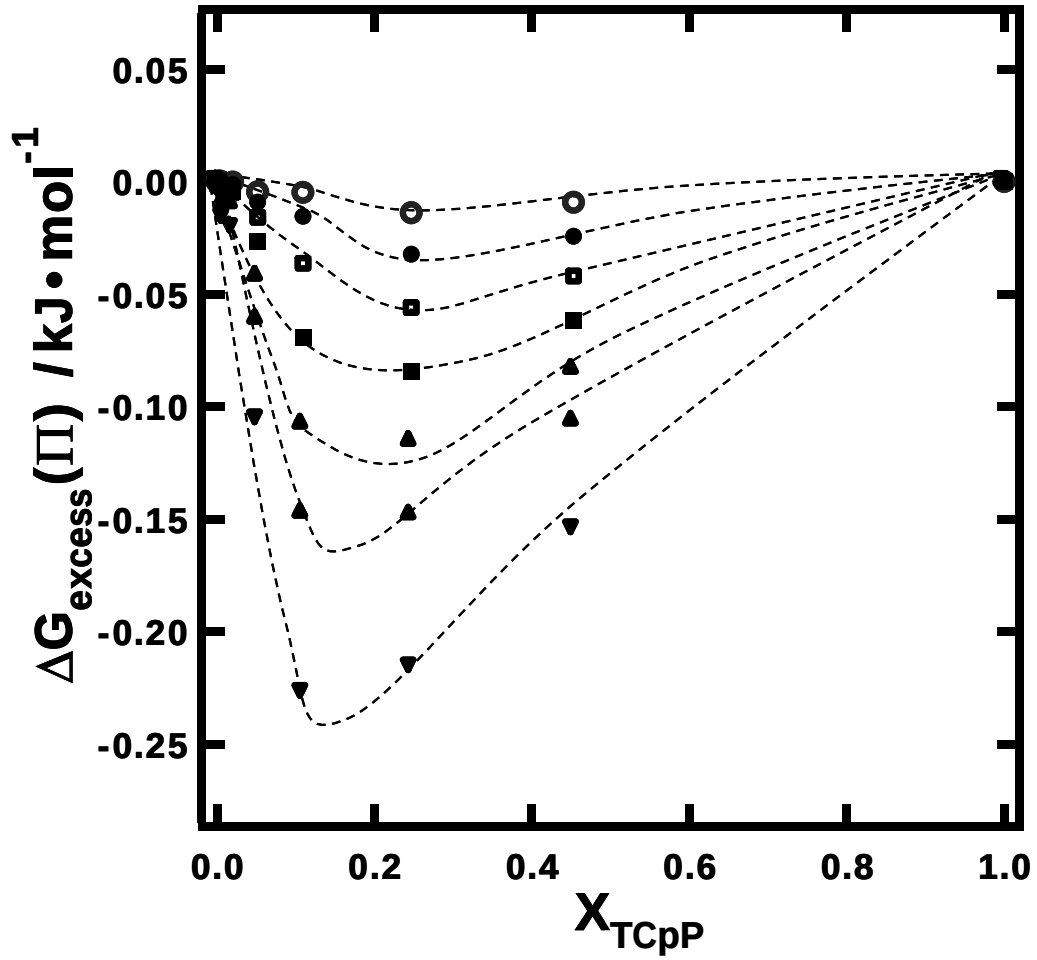

Figure 7.5. $\Delta G_{excess}(\Pi)$ - X_{TCpP} calculated from Π - <A> isotherms at T = 22.5 °C and Π = 0.5 (open circles), 1 (filled circles), 1.5 (open square), 2 (filled squares), 2.5 (open triangles), 3 (filled triangles), and 4 mN·m^{-1} (inverted triangles) plotted as a function of X_{TCpP}. The dotted curves highlight the trends for different Π. As noted in the text, data for Π > 1.5 mN·m^{-1} may be invalid if the low Π transitions for intermediate X_{TCpP} reflect monolayer to multilayer rather than monolayer to monolayer phase transitions.

7.3.4 BAM Analysis of TCpP/PDMS Blends

BAM studies provide in-situ morphology of Langmuir films at the A/W interface. Figure 7.6 provides representative BAM images for a single-component PDMS film. PDMS forms a uniform film upon spreading and the only heterogeneous features BAM detects are small circular aggregates at <A> corresponding to the second plateau where PDMS undergoes a bilayer to multilayer transition (Figure 7.6 F – H). Figure 7.7 shows representative BAM images for a single-component TCpP film. TCpP can form nearly uniform monolayers at the A/W interface. The white arrow highlights the boundary between coexisting liquid and gas phases in the TCpP films prior to monolayer formation. Some solid-like domains in the BAM images (white arrow in Figure 7.7D) can be observed just before the TCpP films begins to collapse. Around its collapse pressure ($\Pi \sim 7$ mN·m^{-1}), TCpP forms large bright aggregates (Figure 7.7 E – H) that are dramatically different from the small spherical domains observed in single-component PDMS films.

Figures 7.8 and 7.9 show that 20 and 40 wt% TCpP blends exhibit similar morphologies. Features of liquid/gas coexistence can be seen for both blends at low Π (white arrows in Figure 7.8B and 7.9B). For the transition ranging between $\Pi = 5.5$ and 7.5 mN·m^{-1}, BAM images of 20 wt% TCpP blends exhibit morphologies that are similar to phase separation (Figures 7.8E and F). A similar transition appears in the 40 wt% TCpP blends (Figure 7.9) but at lower Π (between ~ 3.5 and 6.5 mN·m^{-1}). More detailed images of the transition region are provided in Figure 7.10 where one can clearly see the formation of small domains and features that are reminiscent of spinodal phase separation

as Π increases. The blend films become uniform after this transition and stay homogeneous until the kinks and plateau in the Π – <A> isotherm at Π ~ 13 mN·m^{-1} (Figure 7.9H).

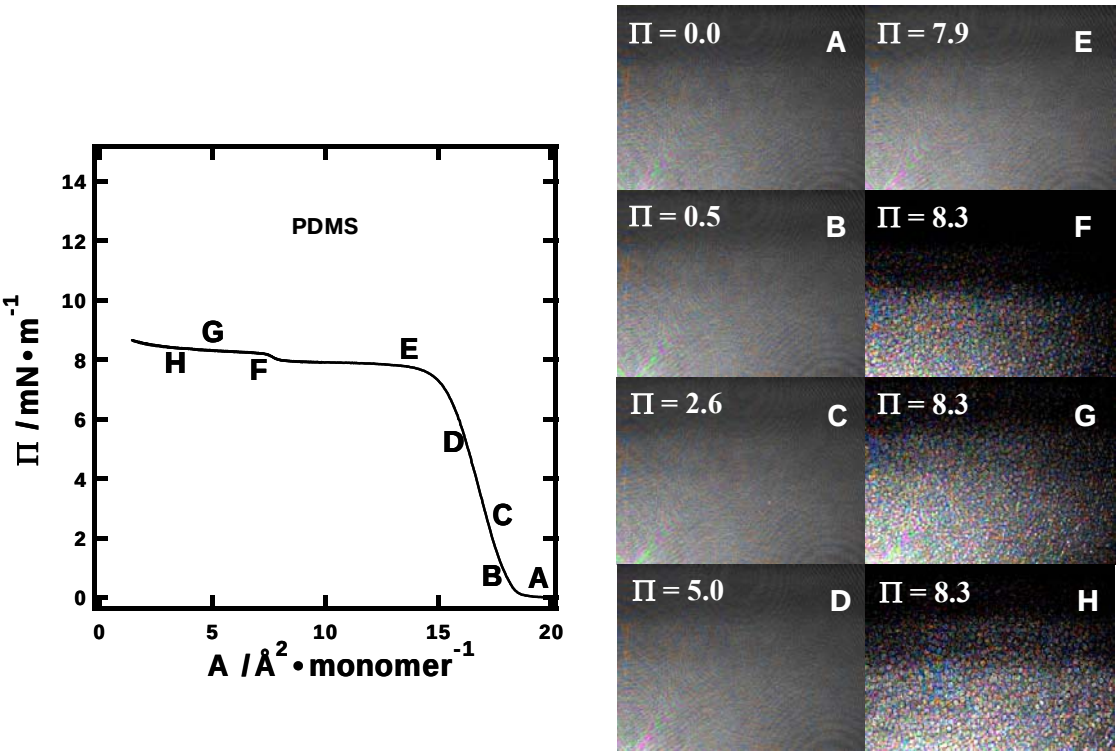

Figure 7.6. BAM images for a single-component PDMS (M_w = 7.5 kg·mol^{-1}) film obtained at T = 22.5 °C and a compression rate of 10 cm^2·min^{-1}. The letters on the isotherm indicate where the BAM images were taken during the compression experiment and correspond to various surface pressures (Π / mN·m^{-1}): A (0.0), B (0.5), C (2.6), D (5.0), E (7.9), F (8.3), G (8.3), and H (8.3).

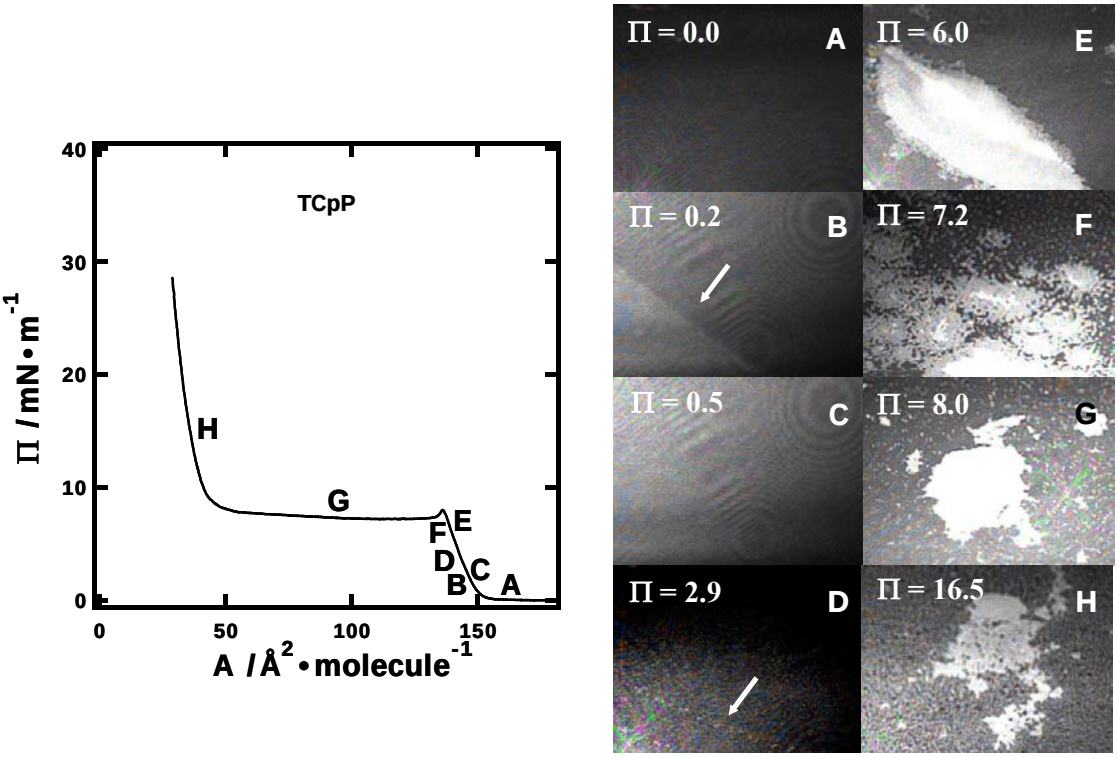

Figure 7.7. BAM images for a single-component TCpP film obtained at T = 22.5 °C and a compression rate of 10 $cm^2 \cdot min^{-1}$. The letters on the isotherm indicate where the BAM images were taken during the compression experiment and correspond to various surface pressures (Π /$mN \cdot m^{-1}$): A (0.0), B (0.2), C (0.5), D (2.9), E (6.0), F (7.2), G (8.0), and H (16.5). The white arrow in B points to the boundary between coexisting liquid and gas phases. The white arrow in D points to a solid-like domain.

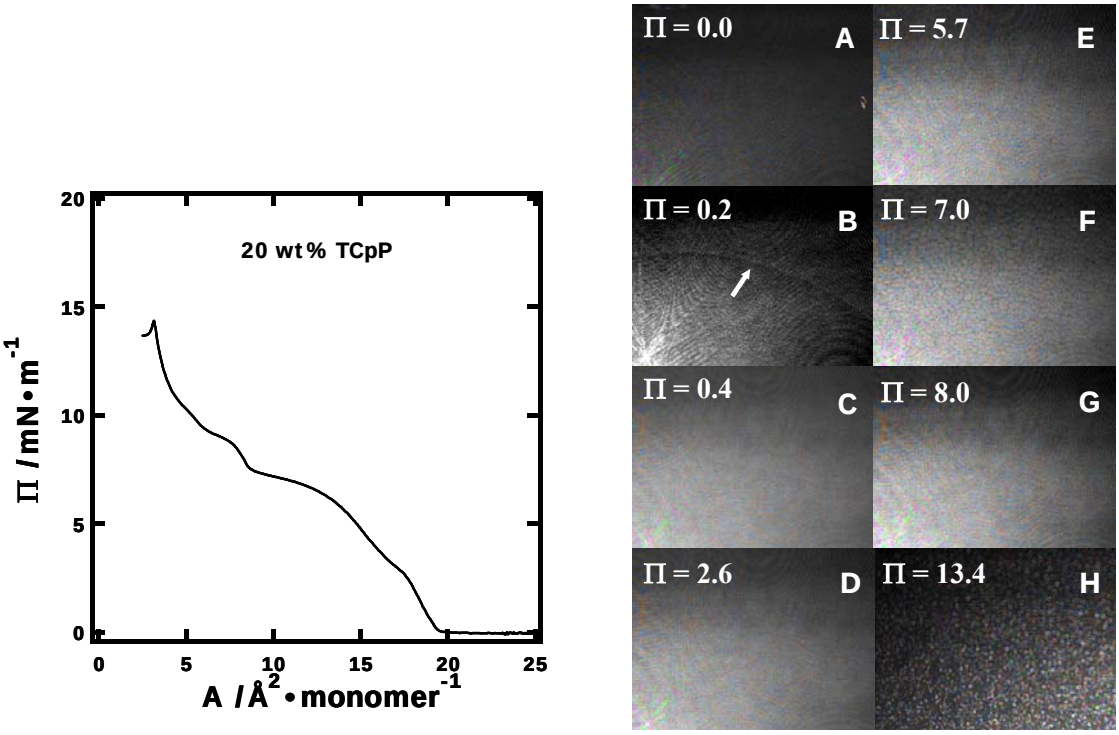

Figure 7.8. BAM images for a $X_{TCpP} \sim 0.20$ TCpP/PDMS (M_w = 7.5 kg·mol^{-1}) blend film obtained at T = 22.5 °C and a compression rate of 10 cm^2·min^{-1}. The letters on the isotherm indicate where the BAM images were taken during the compression experiments and correspond to various surface pressures (Π /mN·m^{-1}): A (0.0), B (0.2), C (0.4), D (2.6), E (5.7), F (7.0), G (8.0), and H (13.4). The arrow in B points to the boundary between liquid and gas phases.

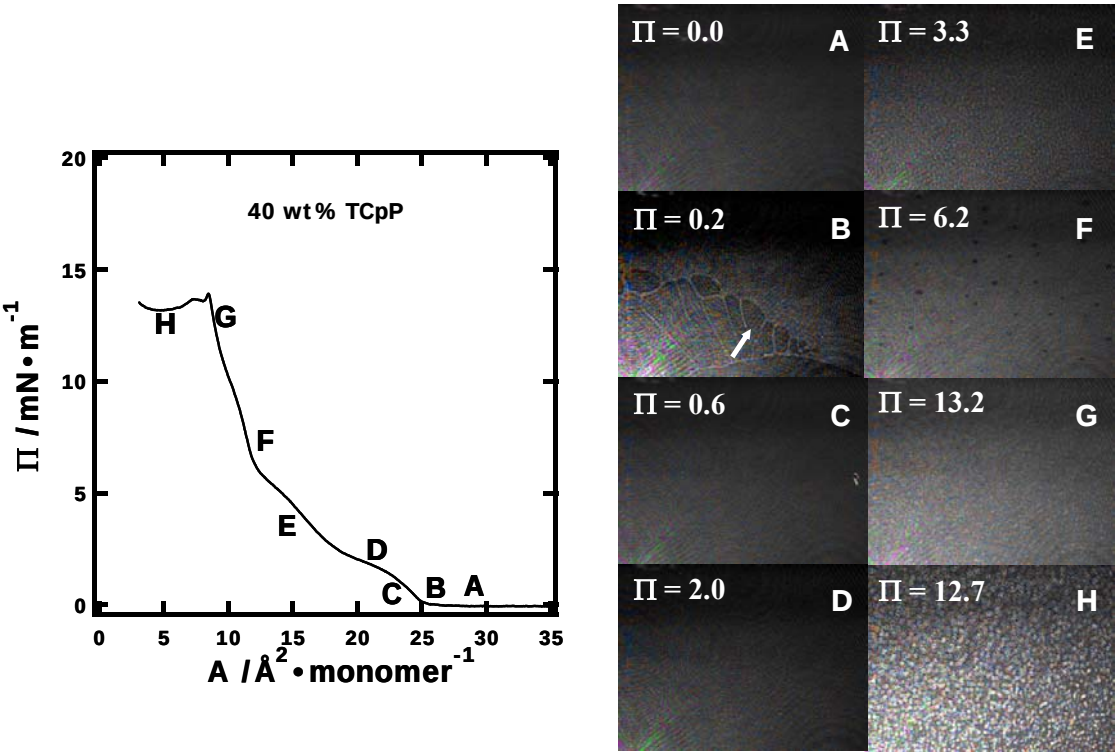

Figure 7.9. BAM images for a X_{TCpP} ~ 0.40 TCpP/PDMS (M_w = 7.5 kg·mol^{-1}) blend film obtained at T = 22.5 °C and a compression rate of 10 cm^2·min^{-1}. The letters on the isotherm indicate where the BAM images were taken during the compression experiments and correspond to various surface pressures (Π / mN·m^{-1}): A (0.0), B (0.2), C (0.6), D (2.0), E (3.3), F (6.2), G (7.4), and H (13.2). The arrow in B points to the boundary between liquid and gas phases.

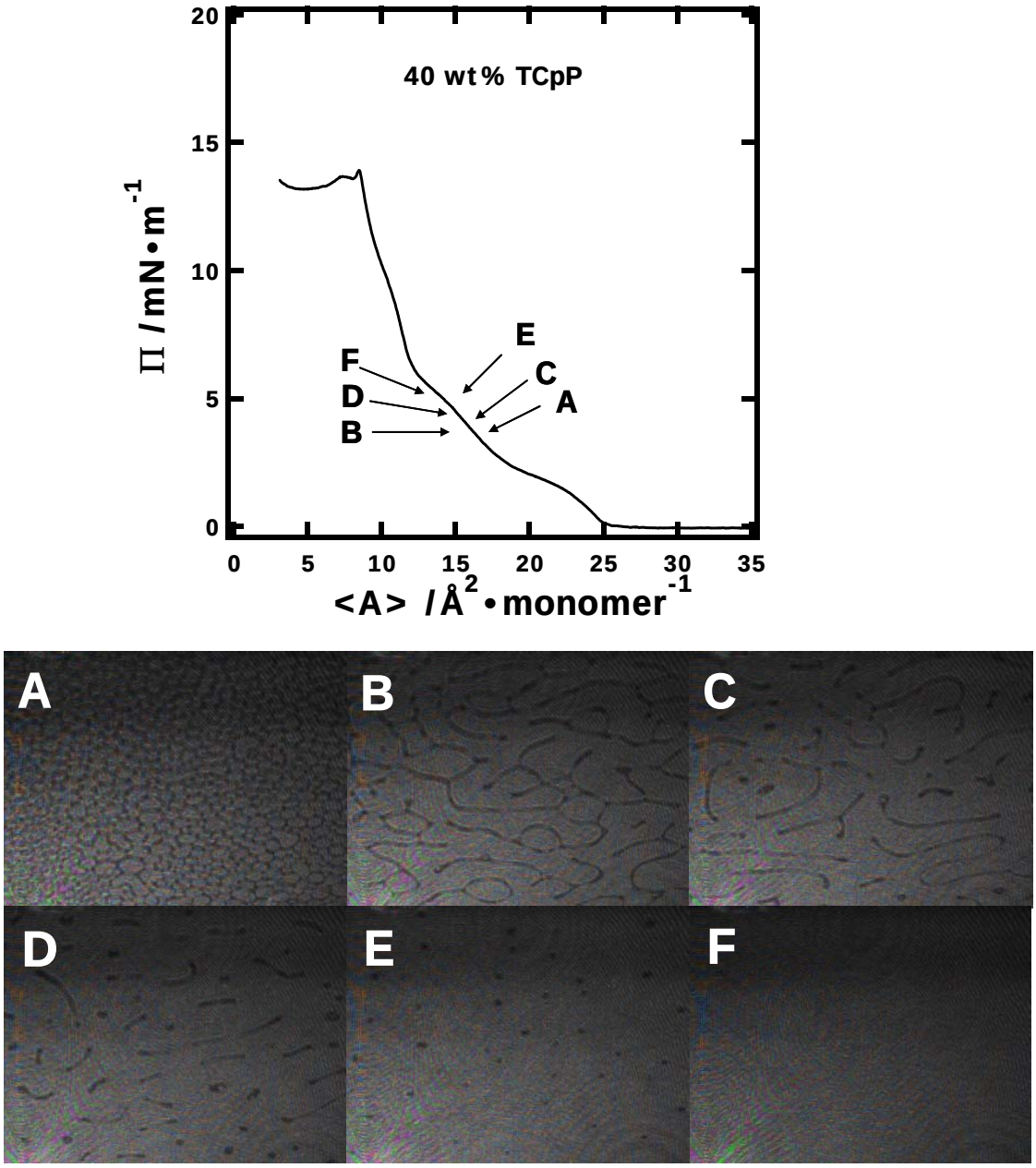

Figure 7.10. BAM images for a X_{TCpP} ~ 0.40 TCpP/PDMS (M_w = 7.5 kg·mol^{-1}) blend film obtained at T = 22.5 °C and a compression rate of 10 cm^2·min^{-1}. The letters on the isotherm indicate where the BAM images were taken during the compression experiments.

For the 60 wt% TCpP blend, bright solid-like features can be seen at all surface concentrations even though most of the film remains uniform and liquid/gas phase coexistence can be observed at low surface pressure (Figure 7.11 B). The isolated solid-like domains grow brighter during compression of the film suggesting that their thickness is increasing. Π – <A> isotherms for 80 wt% TCpP blends are similar to single-component TCpP. However, BAM images taken during compression of the 80 wt% TCpP blend with PDMS (Figure 7.12) show the morphology is different from single-component TCpP films. Solid-like domains for 80 wt% TCpP are much smaller than those observed for single-component TCpP films (Figure 7.7).

The morphology studies of the TCpP/PDMS blends reveal many interesting features. All blends likely form uniform monolayers at the A/W interface although some solid-like features are observed for blends containing at least 60 wt% TCpP even at low Π. If one compares the morphology for single-component TCpP (Figures 7.7) and 80 wt% TCpP/PDMS blend films (Figure 7.12), it is clear that TCpP in 80 wt% TCpP does not form large bright aggregates like it does in single-component TCpP films. This feature suggests that PDMS breaks up large TCpP aggregates, leading to smaller TCpP aggregates dispersed throughout the PDMS.

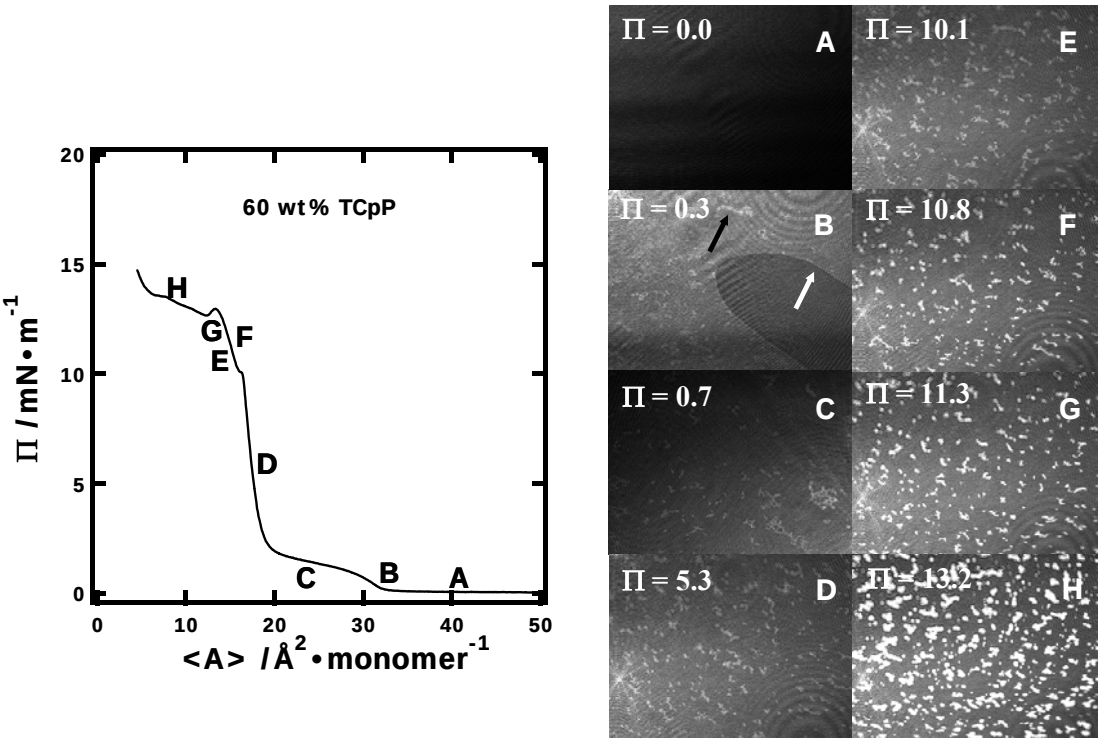

Figure 7.11. BAM images for X_{TCpP} ~ 0.60 TCpP/PDMS (M_w = 7.5 kg·mol^{-1}) blend film obtained at T = 22.5 °C and a compression rate of 10 cm^2·min^{-1}. The letters on the isotherm indicate where the BAM images were taken during the compression experiments and correspond to various surface pressures (Π / mN·m^{-1}): A (0.0), B (0.3), C (0.7), D (5.3), E (10.1), F (10.8), G (11.3), and H (13.2). The white arrow in B points to the boundary between liquid and gas phases. The black arrow in B points to a solid-like domain.

During the low Π transition for 20 and 40 wt% TCpP blends, there is no clear evidence from BAM images for multilayer formation. As shown in Figure 7.13, successive addition isotherms for TCpP, TCpP collapse around Π ~ 4.5 mN·m^{-1} with a plateau at Π ~ 2.5 mN·m^{-1} after the kink. Interestingly, these transitions occur in the same Π range as the low Π transition for 20 and 40 wt% TCpP blend with PDMS. It is possible

that PDMS helps disperse the TCpP phase and leads to small TCpP aggregates that are beyond the resolution of BAM for blends containing low wt% TCpP. Hence, excluding the possibility of multilayer formation at this time may be dangerous. In fact, multilayer structures can be seen from low Π (Π ~ 0.3 $mN \cdot m^{-1}$) for 60 wt% TCpP blends and the size and number density of these aggregates increase as Π increases. Clearly, the low Π transition for 60 wt% TCpP blends could arise from collapse of TCpP component.

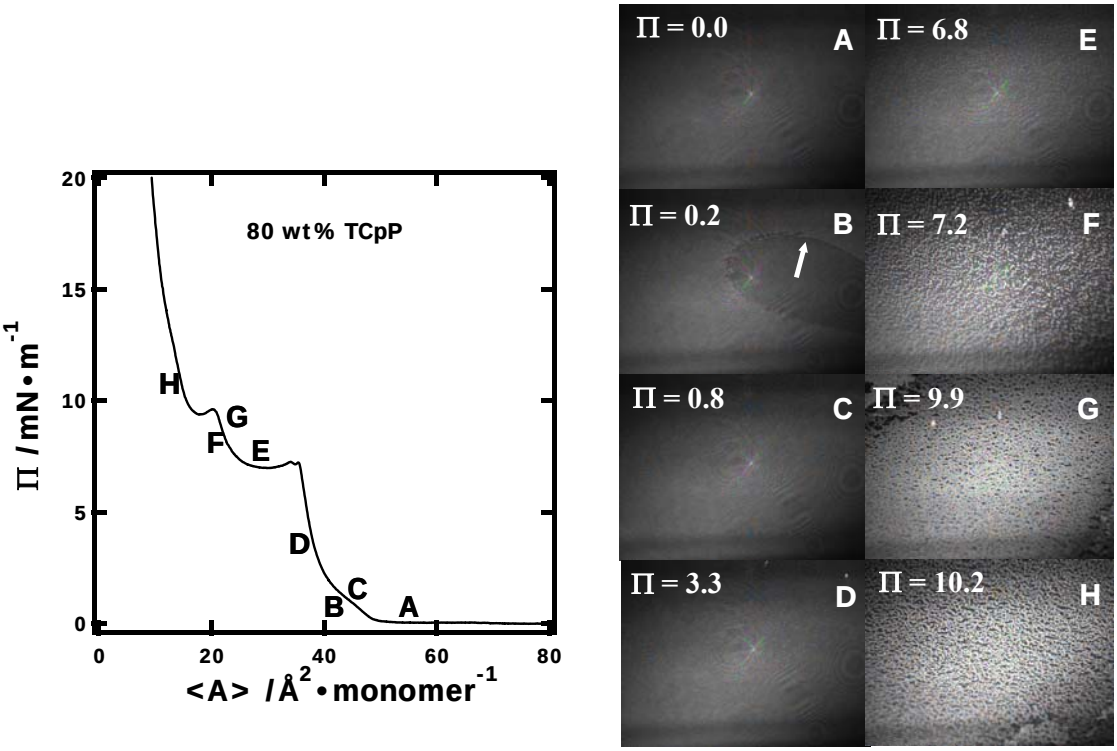

Figure 7.12. BAM images for a X_{TCpP} ~ 0.80 TCpP/PDMS (M_w = 7.5 $kg \cdot mol^{-1}$) blend film obtained at T = 22.5 °C and a compression rate of 10 $cm^2 \cdot min^{-1}$. The letters on the isotherm indicate where the BAM images were taken during the compression experiment and correspond to various surface pressures (Π / $mN \cdot m^{-1}$): A (0.0), B (0.2), C (0.8), D (3.3), E (6.8), F (7.2), G (9.9), and H (10.2). The white arrow in B points to the boundary between liquid and gas phases.

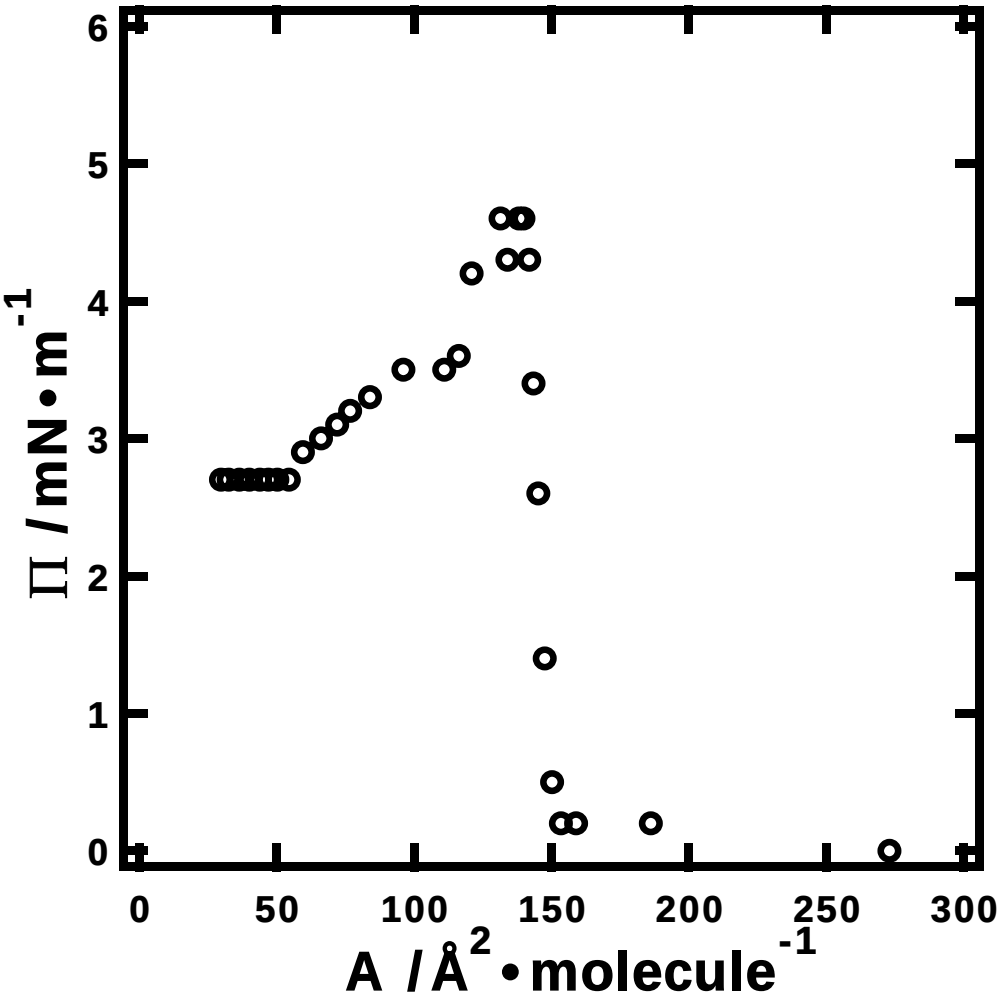

Figure 7.13. Π – A isotherm for TCpP at T = 22.5 °C obtained by the successive addition method.

Considering the fact that PDMS undergoes a monolayer to bilayer transition at Π ~ 8 $mN \cdot m^{-1}$, the high Π transitions of 20 to 40 wt% TCpP blends likely relate to this process even though the shapes of the plateaus are not as regular as single component PDMS films and the corresponding Π is lower than PDMS. The brighter liquid-like domains in BAM images may indicate the formation of PDMS bilayer. As Π increases,

the thicker PDMS domains grow larger and finally occupy the entire surface where the films again appear uniform.

The physical meaning of the kinks at $\Pi \sim 13$ mN·m^{-1} for 20 to 60 wt% TCpP blends is still unclear at this stage. From the BAM images of 20 and 40 wt% TCpP blends, the blend films have small bright spherical domains (Figure 7.8H and 7.9H) after the kinks that are similar to PDMS multilayer structures (Figures 7.6G and 7.6H). However, the BAM images for 60 wt% TCpP do not exhibit dramatic changes before or after the kink at $\Pi \sim 13$ mN·m^{-1}. One thing worth noticing is that the TCpP aggregates are much thicker and thereby much brighter than PDMS multilayers in BAM images. Hence, it is possible that the PDMS multilayers with weak optical contrast will not be observable in BAM images for 60 wt% TCpP blends in the presence of bright TCpP aggregates.

7.4 Conclusions

In this chapter, the phase behavior of TCpP/PDMS blends with different wt% TCpP is studied via Π – <A> isotherms and BAM. Compared with TiBuP/PDMS and OiBuP/PDMS blends discussed in Chapters 5 and 6, respectively, TCpP/PDMS blends exhibit dramatically different composition dependent phase behavior. According to the thermodynamic analysis of the Π – <A> isotherms and BAM images, all blends likely form uniform monolayers at the A/W interface at low Π. For low and high wt% TCpP, blends exhibit Π – <A> isotherms with transitions and morphological features that are consistent with PDMS-like and TCpP-like behavior, respectively. At intermediate compositions, 20 to 60 wt% TCpP blends, unique surface morphologies are observe that may represent monolayer to monolayer or monolayer to multilayer phase transitions. At

present, it is not possible to distinguish between the two. Suggestions for ways to resolve these differences are provided in Chapter 9.

CHAPTER 8

Viscoelastic Behavior of Polydimethylsiloxane Stabilized Magnetite Magnetic Nanoparticle Complexes

Most of this chapter is reproduced with permission from: **Yin, W.;** Xie, Q.; Deng, J.; Goff, j. D.; Vadala, P.; Riffle, J. S.; Esker, A. R. "Viscoelastic Behavior of Polydimethylsiloxane Stabilized Magnetite Magnetic Nanoparticle Complexes" accepted by *ACS Symposium Series*.

8.1 Abstract

In Chapters 5 and 6, blends of polydimethylsiloxane (PDMS) with amphiphilic trisilanolisobutyl-POSS and non-amphiphilic octaisobutyl-POSS have been studied via successive addition surface pressure (Π) – average surface area per monomer (<A>) isotherms and surface light scattering (SLS). The results show interesting phase and rheological behavior owing to different molecule – subphase interactions. The study in this chapter examines the interfacial viscoelastic properties of PDMS stabilized magnetic nanoparticle complexes (PDMS-MNPs) via surface light scattering (SLS) and the Wilhelmy plate technique at the air/water (A/W) interface. Trimethylsilyl-terminated polydimethylsiloxane (PDMS) and tricarboxylic acid-terminated polydimethylsiloxane (PDMS-Stabilizer) provide suitable reference compounds for comparative studies. Results show that PDMS, PDMS-Stabilizer, and PDMS-MNPs are ideal systems for SLS studies. The SLS data reveal that PDMS and PDMS-MNPs have similar phase transitions and viscoelastic behavior from the gaseous state through bilayer formation. In contrast,

the viscoelastic properties of the PDMS-Stabilizer show marked differences starting in the collapsed regime. The differences between PDMS-Stabilizer and PDMS-MNPs are consistent with complete coupling of the carboxylic acid groups to the magnetite surfaces in PDMS-MNPs.

8.2 Introduction

Magnetic materials have attracted considerable interest for modifying the optical properties of films[262] and as catalyst carriers.[263] Recently, magnetic nanoparticles (MNPs) have enabled additional potential applications in biomedical fields like separations, biosensing, targeted drug delivery, magnetic resonance imaging contrast agents, and hyperthermia based cancer treatments.[264-268] For all of these potential applications, stabilizers are required to prevent MNP aggregation in solution. The polymers should contain at least two segments: a functionalized segment that adheres to the metal or metal oxide surface of the MNP, and at least one flexible segment that prevents MNP aggregation through steric stabilization. There are numerous studies on the stabilization of MNPs in aqueous fluids using poly(methacrylic acid),[269] dextran,[270] poly(vinyl alcohol),[270] carboxylic acid-functionalized poly(ethylene oxide),[271-274] sodium poly(oxyalkylene diphosphonate)s,[275] block copolymer stabilizers like poly(ethylene oxide-b-methacrylic acid),[276] and graft copolymers such as poly(alkylene oxide-g-acrylic acid).[277] In addition, silicone stabilizers have been considered for direct use inside the eye for treating detached retinas.[277-280] For other non-polar fluids, oleic acid is probably the most common stabilizer.[281,282] Interestingly, many of these stabilizers render the particles surface active at the air/water (A/W) interface.

In this study, surface pressure (Π) – surface area per dimethylsiloxane repeat unit (A_{DMS}) isotherms and surface light scattering (SLS) is used to probe the viscoelastic properties of a trimethylsilyl-terminated polydimethylsiloxane (PDMS), a tricarboxylic acid-terminated PDMS stabilizer (PDMS-Stabilizer, Figure 8.1A), and PDMS stabilized magnetite magnetic nanoparticle complexes (PDMS-MNPs, Figure 8.1B) at the A/W interface. This study shows that differences in viscoelastic behavior between PDMS and PDMS-Stabilizer during collapse change when the PDMS-Stabilizer is coupled to magnetite MNPs to form the PDMS-MNPs.

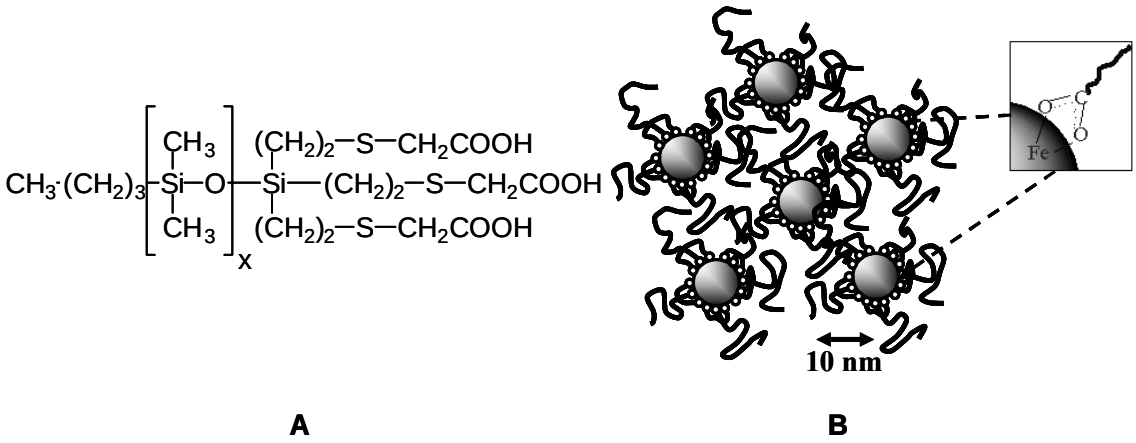

Figure 8.1. (A) Molecular structure of the PDMS-Stabilizer (x = 28). (B) A schematic depiction of PDMS-MNPs. The dots symbolize carboxylic acid groups and squiggly lines represent PDMS chains. The inset shows carboxylic acid binding to the magnetite surface.

8.3 Results and Discussion

8.3.1 Successive Π - A_{DMS} Addition Isotherms for PDMS, PDMS-Stabilizer, and PDMS-MNPs

Figure 8.2 shows Π-A_{DMS} isotherms for PDMS, PDMS-Stabilizer, and PDMS-MNPs. Here A_{DMS} represents the area per dimethylsiloxane repeat unit (monomer for short). For the case of the PDMS-MNPs, the A_{DMS} values only reflect the silicone component in the complex (i.e., if there was 1 g of PDMS-MNPs on the surface, 0.5 g was used for the calculation of A_{DMS} because the MNPs are 50 wt% magnetite). The PDMS isotherm in Figure 8.2 exhibits the four classical regimes originally reported by Fox, *et al.*:[83] (A) $A_{DMS} > A_{lift\text{-}off,DMS}$ = 18 $Å^2$·monomer^{-1} (where Π starts to increase) corresponding to the end of the submonolayer regime (Π = 0 mN·m^{-1}). In this regime, PDMS films are biphasic with the coexistence of gaseous and liquid-like domains;[81] (B) 14 $Å^2$·monomer^{-1} < A_{DMS} < 18 $Å^2$·monomer^{-1} corresponding to a PDMS monolayer with adsorbed oxygen and silicon atoms from the repeating unit adsorbed on water; (C) ~ 8 $Å^2$·monomer^{-1} < A_{DMS} < 14 $Å^2$·monomer^{-1}, the first plateau regime (Π ~ 8.0 mN·m^{-1}) where it was postulated that PDMS underwent progressive coiling into helical structures; and (D) A_{DMS} < ~ 8 $Å^2$·monomer^{-1}, the second plateau (Π ~ 9.0 mN·m^{-1}), where the helical structures undergo collapse. While the interpretation of Regime A and B is widely accepted, newer measurements have suggested that the plateaus correspond to the formation of bilayers and multilayers as PDMS spreads easily upon the underlying hydrated PDMS monolayer and the films can be heterogeneous.[81,229]

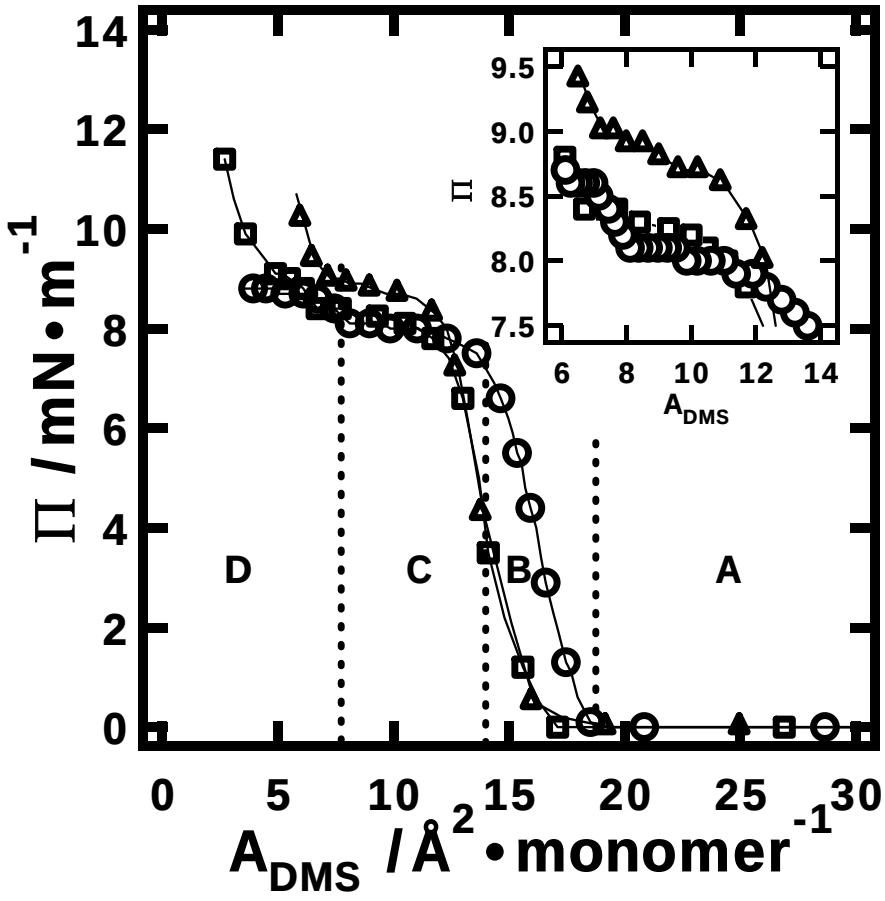

Figure 8.2. Π-A_{DMS} isotherms (T = 22.5 °C) for PDMS (circles), PDMS-Stabilizer (triangles), and PDMS-MNPs (squares). The solid lines between points are only trend lines. Transitions in the PDMS isotherm define the boundaries (vertical dotted lines) for Regimes A through D. The inset expands Regime C, the first plateau.

Qualitatively, the isotherm for the PDMS-Stabilizer is similar to PDMS in Regimes A and B, with a few quantitative differences. First, $A_{lift\text{-}off}$ shifts from 18 to ~ 17 $Å^2$•monomer^{-1} for the PDMS-Stabilizer reflecting the fact that the end groups make a more significant contribution to the calculation of A_{DMS} for the 2.5 kg·mol^{-1} PDMS-Stabilizer than the 7.5 kg·mol^{-1} PDMS. The second difference is a larger plateau pressure

($\Pi \sim 8.7$ mN•m^{-1}) for the PDMS-Stabilizer in Regime C. Third, there is a steeper upturn in the PDMS-Stabilizer isotherm starting at the end of what is Regime C for PDMS. The upturn in Π out of Regime C has been reported previously for other polar terminated silicone oligomers,[82] and reflects a more traditional surfactant like structure as the collapsing polymer starts to "stand" on the hydrophilic anchor. The isotherm for PDMS-MNP is identical to the PDMS-Stabilizer through Regime A and most of Regime B. This result suggests that grafting flexible PDMS-Stabilizer to the magnetite surfaces at densities of the order ~1.25 per nm^2 has little effect on the ability of the dimethylsiloxane repeating units to interact with water, a likely consequence of the relatively long linking group (Figure 8.1A). Interestingly, the PDMS-MNPs' isotherm agrees with PDMS in Regime C. Apparently, tethering the polar portion of the PDMS-Stabilizer to the magnetite core causes the PDMS-MNP to behave more like hydrophobically terminated PDMS during collapse. In Regime D, the PDMS-MNPs exhibit behavior that lies between PDMS and PDMS-Stabilizer. As the polar end groups of the stabilizer are not available for anchoring PDMS to the A/W interface, one interpretation would be that the PDMS-MNPs do not undergo multilayer formation as easily as hydrophobic PDMS. The subsequent discussion of viscoelastic behavior will make use of the regimes defined in Figure 8.2.

8.3.2 SLS Results for PDMS, PDMS-Stabilizer, and PDMS-MNPs

Esker, *et al.*[123,231] recently noted that in the absence of frequency dependent viscoelastic behavior, it is convenient to reduce all viscoelastic data from SLS down to a common reference state. The approach is essentially the same one used by Hård and Neuman.[55] One starts by deducing the frequency shift (f_s), full-width at the half

maximum intensity corrected for instrumental broadening ($\Delta f_{s,c}$) from power spectra in SLS at different wave vectors (k), and the static surface tension (σ_s) from the Wilhelmy plate technique. These parameters along with Eq. 5.3 are used to calculate the dynamic dilational elasticity (ε_d) and corresponding viscosity (κ). Next, the values of ε_d, κ, and σ_s are used along with Eq. 5.3 to calculate the equivalent values of the frequency shift ($f_{s,eq}$) and corrected full-width at half-maximum intensity ($\Delta f_{s,c,eq}$) at an arbitrary reference state. For this study, the reference state is chosen to correspond to water at 25 °C (k = 324.3 cm^{-1}, dynamic surface tension of σ_d = 71.97 $mN \cdot m^{-1}$, transverse viscosity of $\mu = 0$, density of $\rho = 997.0$ $kg \cdot m^{-3}$, and bulk viscosity η = 0.894 mPa·s). Figure 8.3 shows $f_{s,eq}$ plotted as a function of Π for PDMS, PDMS-Stabilizer, and PDMS-MNPs. The assignment of the regimes in Figure 8.4 is in accord with the regimes of Figure 8.2 for PDMS. Figure 8.4 provides similar data for $\Delta f_{s,c}$ as a function of Π. The use of logarithmic x-axes for $\Pi < 1$ $mN \cdot m^{-1}$ and linear scales for $\Pi > 1$ $mN \cdot m^{-1}$ in Figures 8.3 and 8.4 provides a convenient way to plot the data and has no physical significance. The data points in Figures 8.3 and 8.4 represent an average for three wave vectors (7^{th} through 9^{th} diffraction orders corresponding to wave vectors of k = 404.3 cm^{-1}, 459.0 cm^{-1}, and 512.6 cm^{-1}) with one standard deviation error bars.

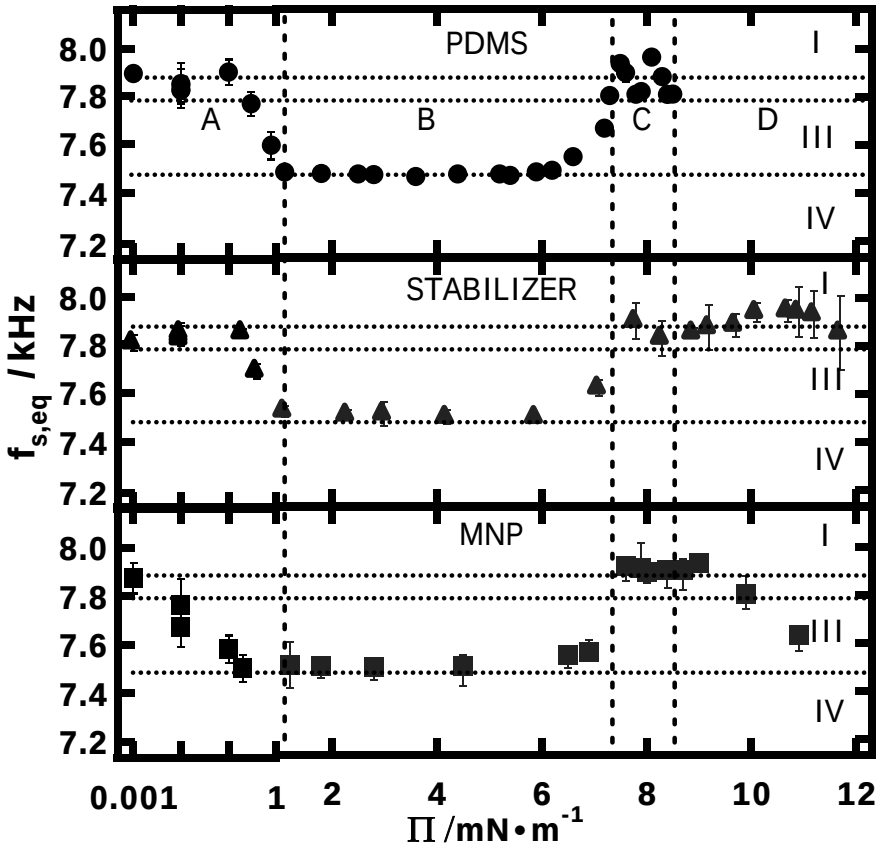

Figure 8.3. $f_{s,eq}$–Π for PDMS (circles), PDMS-Stabilizer (triangles), and PDMS-MNPs (squares). The x-axis uses a logarithmic scale for Π < 1 mN·m^{-1}, and a linear scale for Π > 1 mN·m^{-1}. Data points represent an average of three wave vectors with one standard deviation error bars. Data points at Π = 0.001 mN·m^{-1} correspond to water (Π = 0), while points at Π = 0.01 mN·m^{-1} correspond to submonolayer films that do not have a detectable Π (Π < 0.1 mN·m^{-1}). Vertical dotted lines indicate Regimes A through D defined in Figure 8.2. The three horizontal dotted lines correspond to limiting behavior of the dispersion relation: (I) the pure liquid limit, (III) the maximum damping coefficient for a perfectly elastic surface film, and (IV) the minimum velocity limit for a perfectly elastic surface film.

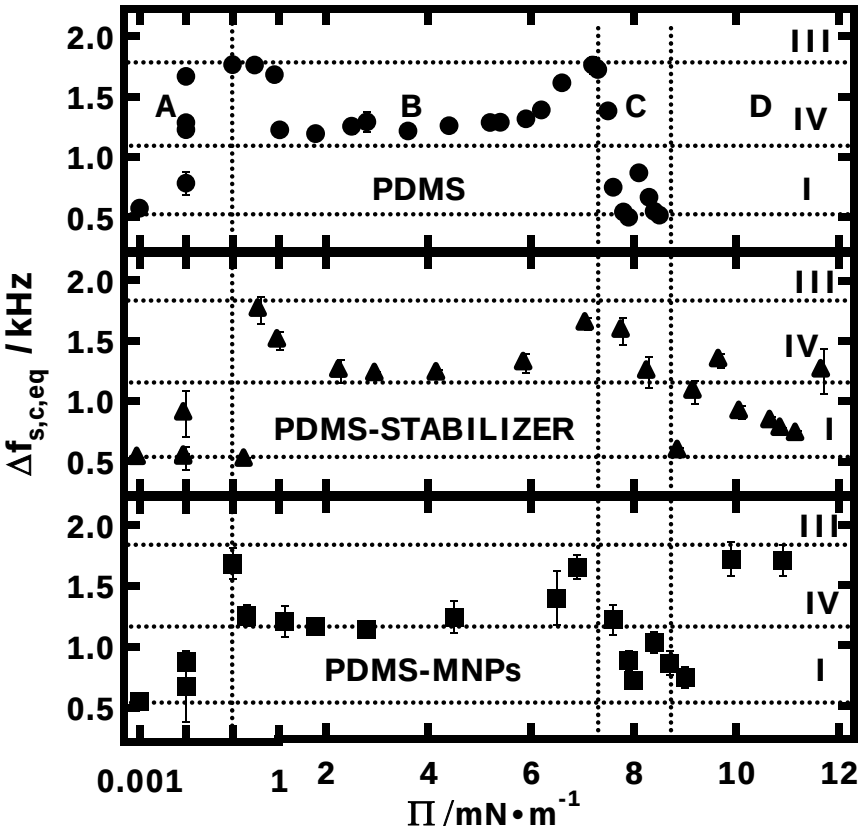

Figure 8.4. $\Delta f_{s,c,eq}$-Π for PDMS (circles), PDMS-Stabilizer (triangles), and PDMS-MNPs (squares). The x-axis uses a logarithmic scale for Π < 1 mN·m^{-1}, and a linear scale for Π > 1 mN·m^{-1}. Data points represent an average of three wave vectors with one standard deviation error bars. Data points at Π = 0.001 mN·m^{-1} correspond to water (Π = 0), while points at Π = 0.01 mN·m^{-1} correspond to submonolayer films that do not have a detectable Π (Π < 0.1 mN·m^{-1}). Vertical dotted lines indicate Regimes A through D defined in Figure 8.2. The three horizontal dotted lines correspond to limiting behavior of the dispersion relation: (I) the pure liquid limit, (III) the maximum damping coefficient for a perfectly elastic surface film, and (IV) the minimum velocity limit for a perfectly elastic surface film.

Plotting the data as done in Figures 8.3 and 8.4 facilitates easy comparisons between the experimental data and important limiting behavior of the dispersion equation.[123,231] There are six important limiting cases for the viscoelastic behavior of Langmuir films at the A/W interface: (I) Pure liquid behavior (ε^* and $\mu = 0$), purely elastic surface films ($\kappa = 0$ and $\mu = 0$) which yield – (II) the maximum velocity limit, (III) the maximum damping coefficient, and (IV) the minimum velocity limit, (V) films with an infinite lateral modulus ($\varepsilon^* \rightarrow \infty$), and (VI) the maximum damping coefficient for a purely viscous surface film ($\varepsilon_d = 0$ and $\mu = 0$). As PDMS forms perfectly elastic surface films, the three most important limits are (I), (III), and (IV). These limits are included on Figures 8.3 and 8.4.

In Regime A, submonolayer coverage, as seen in Figures 8.3 and 8.4, PDMS behaves as a pure liquid (I). With increasing concentration, the monolayer forms, $\Pi \sim 0$, leading to a sharp drop in $f_{s,eq}$ and a sharp increase in $\Delta f_{s,c,eq}$. Figure 8.4 clearly shows that as the monolayer forms the damping of the PDMS monolayer is consistent with the maximum damping coefficient of a perfectly elastic surface film (III) and indicates that $\varepsilon_d/\sigma_s \sim 0.17$.[123,231] In the middle of Regime B, the global minimum in $f_{s,eq}$, and the local minimum in $\Delta f_{s,c,eq}$ indicate the viscoelastic properties of the film are similar to those of a perfectly elastic surface film in the minimum velocity limit (IV). Such a film is characterized by intermediate $\varepsilon_d \sim 30$ to 50 $mN \cdot m^{-1}$ and negligible κ. At the high Π end of Regime B, $f_{s,eq}$ starts to rise, and $\Delta f_{s,c,eq}$ shows another maximum that is in agreement with the maximum damping coefficient for a perfectly elastic surface film (III). The appearance of a second maximum indicates that as the film collapses, ε_d/σ_s is again ~ 0.17 and more importantly that ε_d is decreasing in the collapsing film. In Regimes C and D, the viscoelastic properties are essentially those of a pure liquid (I), except for a small enhancement of viscoelastic behavior at the boundary between Regimes C and D.

It is interesting to note how the PDMS-Stabilizer and PDMS-MNPs differ from PDMS in Figures 8.3 and 8.4. In Regime A, all systems are roughly the same. As the monolayer forms during compression ($\Pi \sim 0$), the behavior is similar as all the films are essentially perfectly elastic, and the maximum in $\Delta f_{s,c,eq}$ occurs at $\Pi \sim 0$. This observation is consistent with the facts that $\varepsilon_d/\sigma_s \sim 0.17$ at the maximum $\Delta f_{s,c,eq}$ [126] and the A/W interface is theta solvent for PDMS.[57] The behavior of the PDMS-Stabilizer starts to depart from that of PDMS and PDMS-MNPs at the high Π end of Regime B. As

seen in Figure 8.4, the second maximum in $\Delta f_{s,c,eq}$ shifts to a higher Π value. This feature is likely due to a different collapse mechanism as the hydrophilic tricarboxylic acid end group inhibits PDMS-Stabilizer multilayer formation by the same mechanism as PDMS. Differences become even more apparent when the PDMS-Stabilizer fails to exhibit a local maximum in $\Delta f_{s,c,eq}$ at the boundary between Regimes C and D. Again, this feature shifts to higher Π. It is notable that PDMS-MNPs exhibit essentially PDMS behavior in Regimes A through C. Given the isotherms in Figure 8.2, it is not surprising that PDMS, PDMS-Stabilizer, and PDMS-MNPs exhibit the largest differences in Regime D. In Regime D, PDMS-Stabilizer and PDMS-MNPs exhibit different $f_{s,eq}$ and $\Delta f_{s,c,eq}$ that do not conform to any particular limiting behavior, thereby warranting an analysis of the surface viscoelastic parameters through the dispersion equation.

8.3.3 Surface Viscoelastic Parameters for PDMS, PDMS-Stabilizer, and PDMS-MNPs

ε_d probed by SLS is a high frequency (kHz) analog to the static dilational modulus (0 Hz, a 2D analog to the bulk modulus):

$$\varepsilon_S = C_S^{-1} = -A_{DMS}\left(\frac{\partial \Pi}{\partial A_{DMS}}\right)_T \qquad \text{(Eq. 8.1)}$$

where C_s is the surface compressibility, the 2D analog to the isothermal compressibility in 3D. Figure 8.5 shows ε_s obtained from Figure 8.2 and Eq. 8.1, and ε_d (an average of the three different wave vectors) plotted as a function of Π for PDMS, PDMS-Stabilizer, and PDMS-MNPs. For PDMS, there is excellent agreement between ε_d and ε_s throughout the entire range of Π. This behavior is consistent with negligible κ. Figure 8.6 shows, κ vs. Π for PDMS, PDMS-Stabilizer, and PDMS-MNPs. κ is indeed small for PDMS and

is nearly zero within experimental error. This result is consistent with previous studies.[124,153,234,259] Furthermore, Esker *et al.* noted that $\varepsilon_s = z\Pi$ where z is the scaling exponen.[123] For PDMS, the initial slope yields z ~ 30, i.e. the A/W interface is a near theta solvent for PDMS.[57] Another important feature of Figure 8.5, is that the maximum $\varepsilon_d \sim 30$ mN·m^{-1} occurs in the center of Regime B as expected. Finally, ε_d shows a small peak at the boundary between Regimes C and D for PDMS. One interpretation is the collapse of a helical monolayer,[83] although a bilayer to multilayer transition is more probable.[229] These observations are all consistent with the discussion of Figures 8.3 and 8.4.

As seen in Figures 8.5 and 8.6, the viscoelastic properties of the PDMS-Stabilizer and PDMS-MNPs are nearly identical to PDMS up to the end of Regime B. The first key difference is that PDMS-Stabilizer, does not exhibit $\varepsilon_d = 0$, until $\Pi \sim 9$ mN·m^{-1} during the initial collapse of the film. Moreover, Regime C is essentially absent for the PDMS-Stabilizer. This feature must arise from stronger anchoring of the PDMS-Stabilizer to the subphase by the hydrophilic tricarboxylic acid terminal group.[121] Interestingly, Regime C is present for PDMS-MNPs after the stabilizer is coupled to the magnetite surface and film collapse as measured by the point where ε_d returns to zero is the same as PDMS ($\Pi \sim 8$ mN·m^{-1}). The other main differences all occur in Regime D. For PDMS, pure liquid behavior is observed in Regime D ($\varepsilon_d = 0$ and $\kappa = 0$). In contrast, both PDMS-Stabilizer and PDMS-MNPs exhibit non-zero ε_d and κ in Regime D. Moreover, the PDMS-Stabilizer film is more viscous than the PDMS-MNPs in Regime D. This enhancement in the film's viscosity is attributed to multilayer formation for PDMS-MNPs, similar to

PDMS, whereas collapse in PDMS-Stabilizer leads to chains standing on their hydrophilic anchor.

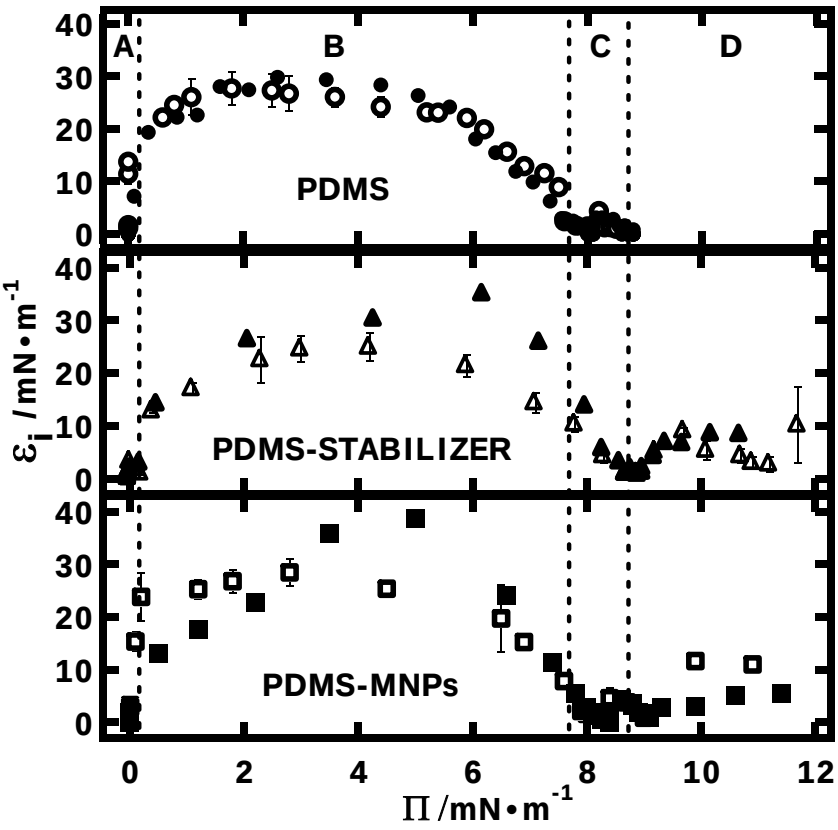

Figure 8.5. Plots of ε_i-Π for PDMS (circles), PDMS-Stabilizer (triangles), and PDMS-MNPs (squares). Figure 8.2 and Eq. 8.1 yield ε_s values (filled symbols). ε_d values (open symbols) represent the average of three different wave vectors with one standard deviation error bars. The dotted vertical lines indicate the boundaries of the regimes defined in Figure 8.2.

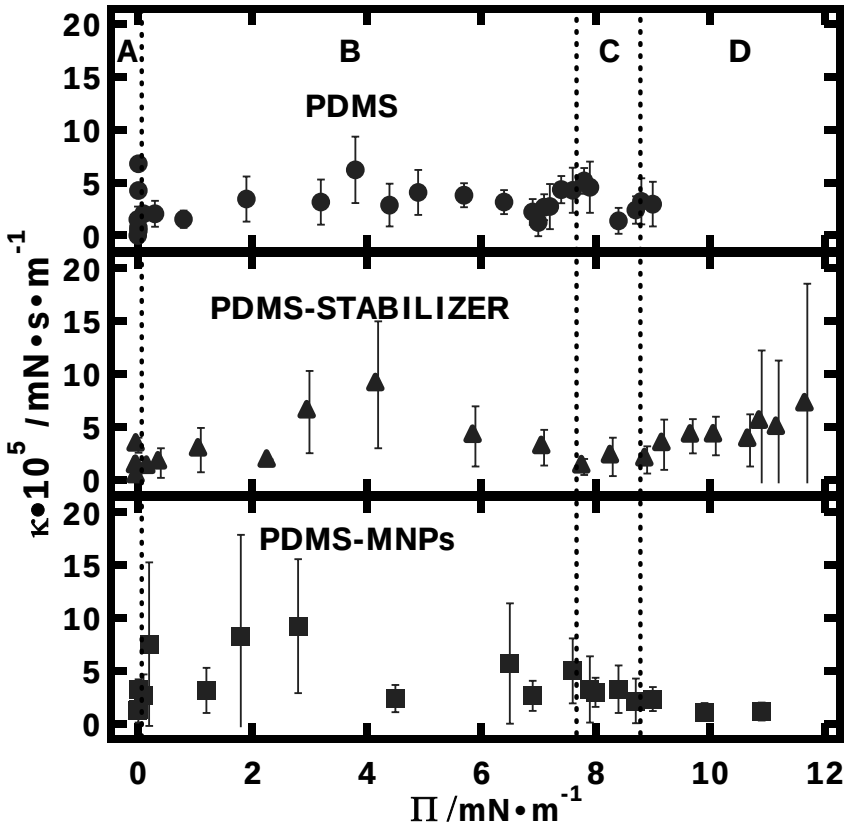

Figure 8.6. Plots of κ-Π for PDMS (circles), PDMS-Stabilizer (triangles), and PDMS-MNPs (squares). κ values represent the average of three different wave vectors with one standard deviation error bars. The dotted vertical lines indicate the boundaries of the regimes defined in Figure 8.2.

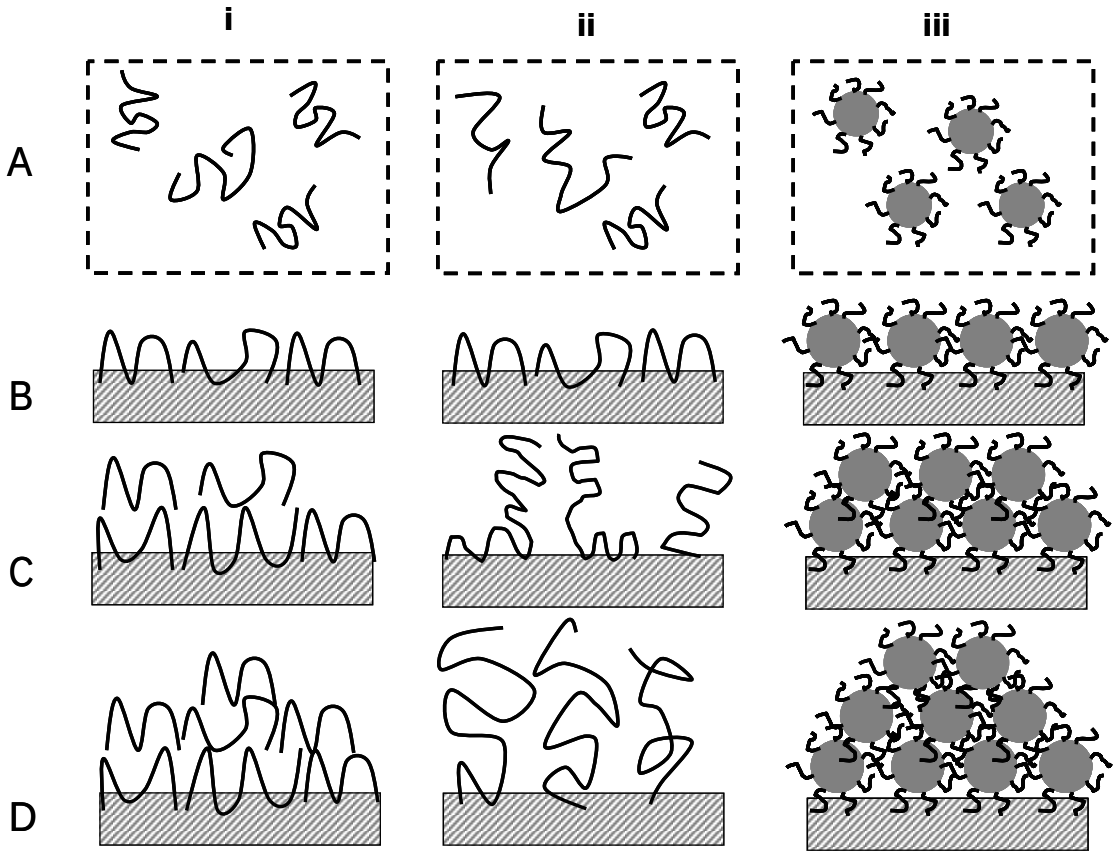

Figure 8.7. Schematic depictions of conformations within Regimes A (top views) and B through D (side views) for (i) PDMS, (ii) PDMS-Stabilizer, and (iii) PDMS-MNPs.

8.4 Conclusions

As already known, PDMS exhibits four distinct regimes at the A/W interface (schematically depicted in Figure 8.7). In Regime A, PDMS films can be heterogeneous,[81,229] representing a coexistence of liquid-like PDMS and gas domains. In Regime A, PDMS chains should have two dimensional (2D) coil conformations. The addition of the polar end group (PDMS-Stabilizer), or the tethering of the PDMS-Stabilizer to the magnetite to form PDMS-MNPs should have little effect on the observed behavior in Regime A relative to PDMS. In Regime B, a semi-dilute 2D liquid-like film forms at low Π and scaling behavior is consistent with poor solvent behavior for the A/W

interface. As expected for a semi-dilute solution, PDMS, PDMS-Stabilizer and PDMS-MNPs all exhibit similar behavior. During film collapse in Regime C, we favor bilayer formation (depicted in Figure 8.7)[81,229] for both PDMS and PDMS-MNPs rather than the elaborate coil to helix transition model.[83] However, the tricarboxylic acid end group of the PDMS-Stabilizer leads to a different collapse mechanism. As depicted in Figure 8.7, the PDMS chains can now stand on end during further compression yielding a viscoelastic film.[121] Consequently, Regime C and Regime D are essentially one and the same for the PDMS-Stabilizer. In contrast, both PDMS and PDMS-MNPs should be forming multilayers in Regime D. For PDMS, the absence of viscoelastic behavior or an increase in Π indicates there is no energy penalty for forming thicker PDMS layers. In contrast, SLS clearly shows that the PDMS-MNPs are less able to form multilayers during compression with both a rise in Π and viscoelastic responses from the film. Hence, even though PDMS-Stabilizer shows deviation from PDMS-like behavior in Regime C, PDMS-MNPs behave like PDMS from Regime A through Regime C and only deviate in Regime D. This response to film compression is consistent with complete anchoring of the carboxylic acid end groups to the magnetite cores of the PDMS-MNPs.

CHAPTER 9

Conclusions and Future Work

9.1 Conclusions

9.1.1 Surface Light Scattering (SLS) for Non-invasive Interfacial Rheology Measurements

A home-made surface light scattering (SLS) apparatus was used to study the interfacial rheology of Langmuir films at the A/W interface in this dissertation. As mentioned in Chapter 2, several techniques can measure the interfacial dilational modulus of thin films at the A/W interface. Studies of mechanically generated capillary waves[117] and electrocapillary wave diffraction (ECWD)[48-51] share similar features with SLS[118,119,123,147,231] in the sense the dilational viscoelastic properties of the surface waves are probed through their wave damping characteristics. The static dilational elasticity (ε_s) of Langmuir films can also be deduced from surface pressure (Π) – area per molecule or repeat unit (A) isotherms as described in Chapter 4 via $\varepsilon_s = -A\left(\partial\Pi/\partial \mathrm{A}\right)_T$.[29] Relative to the non-invasive SLS technique, this approach can provide misleading results especially during film collapse when compression of the film causes the conversion of monolayer into multilayer. One example was shown in Chapter 4 (Figure 8.1) where $\varepsilon_s \sim 0$ around the collapse pressure of trisilanolisobutyl-POSS (TiBuP) but the dynamic dilational elasticity (ε_d) retained a value close to the maximum dynamic dilational elasticity ($\varepsilon_{d,max}$).

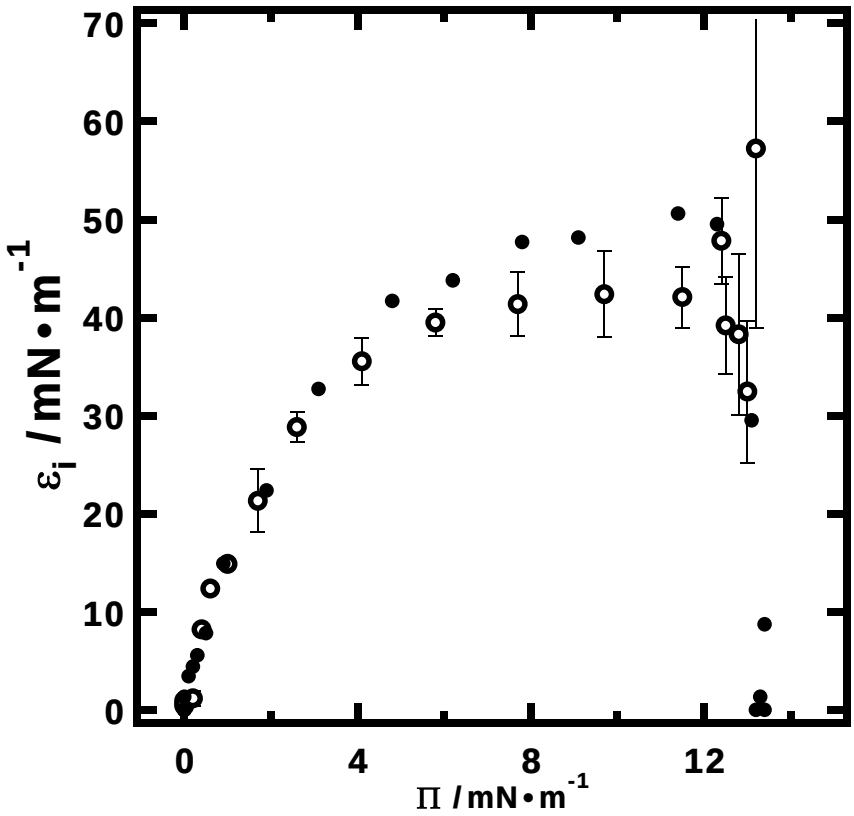

Figure 9.1. Plots of ε_i-Π (top) for TiBuP. ε_s values (filled symbols) are deduced from the Π-A isotherm (Figure 4.1). ε_d values (open symbols) represent the average of three different wave vectors with one standard deviation error bars.

9.1.2 POSS Derivatives as Model Nanofillers

POSS/polymer blend Langmuir films provide excellent model systems for studying the phase and rheological behavior of ultrathin polymer blends. With a water subphase, POSS-subphase interactions serve as an important variable that can significantly affect the interfacial morphology and rheology of the polymeric films. In TiBuP blends with polydimethylsiloxane (PDMS) in Chapter 5, the interaction between amphiphilic TiBuP and the water subphase helped TiBuP molecules disperse within the PDMS matrix.

Moreover, TiBuP and its attendant water are able to plasticize PDMS and hence lower the dilational modulus at the air/water (A/W) interface. On the other hand, blends of PDMS with octaisobutyl-POSS (OiBuP) in Chapter 6 did not form uniform monolayers at the A/W interface because OiBuP is non-amphiphilic. Hence, OiBuP does not introduce excess water into the blends and PDMS films at the A/W interface. As a result, OiBuP never plasticize PDMS at any Π.

One more interesting feature for Langmuir films of blends is that with two different components having different collapse pressure, one component can leave the water surface before the other one, thereby altering the surface composition as surface pressure changes. In TiBuP/PDMS blends, TiBuP has a collapse pressure of ~12 $mN \cdot m^{-1}$, higher than the collapse pressure of PDMS (~ 8 $mN \cdot m^{-1}$). As a consequence, at Π = ~ 8 $mN \cdot m^{-1}$, some PDMS chains are leaving the water surface because TiBuP is more stable. The TiBuP surface fraction at the layer directly bound to water thereby increases and TiBuP molecules are able to network and reinforce the blends. In OiBuP/PDMS blends, PDMS is more stable at the A/W interface and the OiBuP component is squeezed into the upper layer for Π below the collapse pressure of PDMS. As a consequence, enrichment of the PDMS component at the A/W interface occurs prior to the collapse pressure for PDMS. After the PDMS component began to collapse, the blends exhibit viscoelastic properties similar to collapsed single-component PDMS films, i.e. films lacking viscoelastic character.

In Chapter 7, trisilanolcyclopentyl-POSS (TCpP), is used as a model nanofiller to blend with PDMS. Compared with TiBuP/PDMS and OiBuP/PDMS blends discussed above, TCpP/PDMS blends exhibit dramatically different composition dependent phase

behavior. According to the thermodynamic analysis of the surface pressure (Π) – average area per monomer (<A>) isotherms and Brewster angle microscopy (BAM) images, all blends likely form uniform monolayers at the A/W interface. Low wt% TCpP blends (wt% TCpP < 20) exhibit phase behavior that is similar to single-component PDMS and high wt% TCpP (wt% TCpP > 60) exhibit phase behavior that is similar to single-component TCpP. Blends with 20 to 60 wt% TCpP exhibit transitions at Π values lower than the collapse pressures for either PDMS or TCpP. Plateaus in the Π – <A> isotherms indicate the PDMS monolayer to bilayer transition is either distorted (20 or 40 wt% TCpP) or delayed (60 wt% TCpP). All blends with 20 to 60 wt% TCpP also show a kink around Π ~ 13 $mN \cdot m^{-1}$ which physical meaning is still unclear considering both single-component PDMS and TCpP have collapse pressure at Π ~ 7 $mN \cdot m^{-1}$. Proposed experiments for further analysis of this system will be presented as suggested future work.

9.1.3 Phase and Rheological Behavior of PDMS-Stabilizer and PDMS- MNPs

In Chapter 8, the interfacial phase and rheological behavior of hydrophobically terminated PDMS, tricarboxylic acid terminated PDMS (PDMS-stabilizer), and PDMS stabilized magnetic nanoparticles (PDMS-MNPs) were compared via addition Π – A_{DMS} isotherms and SLS measurements where A_{DMS} is the surface area per dimethylsiloxane repeat units. It was clearly shown that the end group of amphiphilic polymers alter molecule-subphase interactions and thereby change the interfacial phase and rheological behavior of the PDMS stabilizer. With the polar tricarboxylic acid end groups, PDMS stabilizer stands on its end during further compression and does not exhibit the classical

PDMS monolayer to bilayer transition. In contrast, the PDMS-MNPs exhibit similar phase and rheological behavior with PDMS up to the collapsed regime once the carboxylic acid end groups are bond to the surface of the magnetite cores.

9.2 Suggestions for Future Work

9.2.1 Photo Cross-linking of PDMS/POSS Blends at the A/W Interface

As described in Chapters 5 to 7, Langmuir films serve as excellent model systems for studying the dispersion and reinforcement of nanofillers within polymeric matrices. Typically, the Langmuir-Schaefer (LS) and Langmuir-Blodgett (LB) techniques can be employed to transfer the Langmuir film onto solid substrates so that subsequent measurements such as atomic force microscopy (AFM) and scanning electron microscopy (SEM) can be applied to the thin films. However, for blend systems, LS or LB-transfer may alter the dispersion of the nanofillers within the polymeric matrix. Moreover, some polymers (i.e. PDMS) cannot be efficiently transferred owing to their extremely low surface energy. The cross-linking of amphiphilic polymers at the A/W interface would serve as a good solution for the above challenges. Dubault *et al.* first formed two-dimensional (2D) cross-linked monolayers by polymerization of dimethacrylates and several other difunctional reactive amphiphiles under UV irradiation at the A/W and oil/water interface.[283] Such a strategy has been applied by other research groups to investigate many types of reactions at the A/W interface.[284-286] Recently, Matmour *et al.*[287] reported a study on the cross-linking of polybutadiene at the A/W interface where morphology studies confirmed the formation of a cross-linked monolayer about 1 nm thick. Therefore, it is reasonable to expect the interfacial cross-linking may be

able to lock-in the surface morphology of Langmuir films for blends and also facilitate LS or LB-transfer.

Clearly, the first step is to examine the phase and rheological behavior of the blends of POSS and PDMS with photosensitive cross-linkable function groups (diphenylsiloxane, vinylmethylsiloxane groups, etc).[288] The type and density of cross-linkable groups are two variables that can be manipulated. The blends of POSS and PDMS with low density of cross-linking groups are expected to share similar phase and rheological behavior as blends of POSS and regular PDMS. The second step is inducing UV cross-linking at the A/W interface. Typically, Π is kept stable via an isobaric experiment. Simultaneously, SLS can be used to probe the dilational modulus of the Langmuir film and thereby monitor the cross-linking process. When the photo cross-linking process has finished (usually corresponding to the point in an isobaric experiment where movement of the barriers ceases), LB or LS-transfer can be applied to transfer the Langmuir films onto solid substrate where AFM or SEM can be employed to examine the surface morphology in greater detail.

9.2.2 In-situ Ellipsometry Study of TCpP/PDMS Blend Thin Films at the A/W Interface

In Chapter 7, the morphology of TCpP/PDMS blends is studied via in-situ BAM measurements at the A/W interface. TCpP/PDMS blends exhibit phase behavior and morphology that is dramatically different from other POSS/PDMS blends. The most striking feature is the phase transitions appeared in the isotherms of TCpP/PDMS blends with intermediate wt% TCpP (20 to 60 wt% TCpP) that are below the transition Π for

either single-component TCpP or PDMS. However, owing to the resolution of BAM images, it is not clear whether these transitions are monolayer to monolayer or monolayer to multilayer in origin.Mann *et al.*[229] employed in-situ ellipsometry to investigate the phase transition of PDMS by measuring the thickness change during the Π – A isotherm. The results show the thickness of PDMS films doubled after the first plateau (described in Chapter 5) where they believe PDMS undergoes monolayer to bilayer transition. The same approach can be adopted here to monitor the thickness change of TCpP/PDMS blend films during the phase transitions. As discussed in Chapter 7, if there is formation of TCpP multilayers during the phase transitions, the thickness of the film should increase and should be observable by in-situ ellipsometry. Hence, the ellipsometric information of TCpP/PDMS blend films can provide insight into the physical meaning of those phase transitions in Π - <A> isotherms.

Reference:

(1) Ulman, A. *Introduction to Ultrathin Organic Films: From Langmuir-Blodgett to Self-Assembly*; Academic Press: Boston, 1991.

(2) Gaines, G. L. *Insoluble Monolayers at Liquid-Gas Interfaces*; Interscience: New York, 1966.

(3) Dutta, P. *Stud. Interface Science* **2002**, *16*, 1-12.

(4) Knobler, C. M.; Desai, R. C. *Annu. Rev. Phys. Chem.* **1992**, *43*, 207-236.

(5) McConnell, H. M. *Annu. Rev. Phys. Chem.* **1991**, *42*, 171-195.

(6) Petty, M. C. *Langmuir-Blodgett Films*; Cambridge University Press: London, 1996.

(7) Moreau, W. M. *Rev. Sci. Instrum.* **1970**, *41*, 1251.

(8) Vozzi, G.; Flaim, C.; Ahluwalia, A.; Bhatia, S. *Biomaterials* **2003**, *24*, 2533-2540.

(9) Moriguchi, I.; Maeda, H.; Teraoka, Y.; Kagawa, S. *J. Am. Chem. Soc.* **1995**, *117*, 1139-1140.

(10) White, M. *Coatings Technology Handbook*; CRC Press: Boca Raton, 2006.

(11) Halperin, A.; Tirrell, M.; Lodge, T. P. *Adv. Polym. Sci.* **1992**, *100*, 31-71.

(12) Miller, C.; Shanks, H.; Witt, A.; Rutkowski, G.; Mallapragada, S. *Biomaterials* **2001**, *22*, 1263-1269.

(13) Lu, Y.; Chen, S. C. *Adv. Drug Delivery Rev.* **2004**, *56*, 1621-1633.

(14) Trankhtenberg, S. *Thin Films and Nanostruct.* **2007**, *34*, 639-664.

(15) Coffee, S. S.; Winkenwarder, W. A.; Stanley, S. K.; Davood, S.; Banerjee, S. K.; Ekerdt, J. G. *Mater. Res. Soc. Symp. Proc.* **2006**, *921E*,

(16) Jennings, G. K.; Brantley, E. L. *Adv. Mater.* **2004**, *16*, 1983-1994.

(17) Locklin, J.; Bao, Z. *Anal. Bioanal.Chem.* **2006**, *384*, 336-342.

(18) Burroughes, J. H.; Bradley, D. D. C.; Brown, A. R.; Marks, R. N.; Mackay, K.; Friend, R. H.; Burns, P. L.; Holmes, A. B. *Nature* **1990**, *347*, 539-541.

(19) Muccini, M. Nat. Mater. **2006**, *5*, 605-613.

(20) Sirringhaus, H.; Tessler, N.; Friend, R. H. *Science* **1998**, *280*, 1741-1744.

(21) Yu, G.; Gao, J.; Hummelen, J. C.; Wudl, F.; Heeger, A. J. *Science* **1995**, *270*, 1789-1791.

(22) Brown, A. R.; Pomp, A.; Hart, C. M.; de Leeuw, D. M. *Science* **1995**, *270*, 972-974.

(23) Koszewski, A.; Rymuza, Z.; Reuther, F. *Microelectron. Eng.* **2008**, *85*, 1189-1192.

(24) Ben Ali, M.; Bessueille, F.; Chovelon, J. M.; Abdelghani, A.; Jaffrezic-Renault, N.; Maaref, M. A.; Martelet, C. *Mater. Sci. Eng., C* **2008**, *28*, 628-632.

(25) Mittal, K. L.; Editor *Adhesion Aspects of Thin Films, Volume 3*, 2007.

(26) Sigal, G. B.; Mammen, M.; Dahmann, G.; Whitesides, G. M. *J. Am. Chem. Soc.* **1996**, *118*, 3789-3800.

(27) Braslau, A.; Deutsch, M.; Pershan, P. S.; Weiss, A. H.; Als-Nielsen, J.; Bohr, J. *Phys. Rev. Lett.* **1985**, *54*, 114-117.

(28) Karapanagiotis, I.; Evans, D. F.; Gerberich, W. W. *Colloids Surf., A* **2002**, *207*, 59-67.

(29) Deng, J. V., Brent D.; Esker, Alan R.; Anseth, Jay W.; Fuller, Gerald G. *Langmuir* **2005**, *21*, 2375.

(30) Deng, J.; Farmer-Creely, C. E.; Viers, B. D.; Esker, A. R. *Langmuir* **2004**, *20*, 2527-2530.

(31) Hottle, J. R.; Kim, H.-J.; Deng, J.; Farmer-Creely, C. E.; Viers, B. D.; Esker, A. R. *Macromolecules* **2004**, *37*, 4900-4908.

(32) Hottle, J. R.; Deng, J.; Kim, H.-J.; Farmer-Creely, C. E.; Viers, B. D.; Esker, A. R. *Langmuir* **2005**, *21*, 2250-2259.

(33) Kim, H.-J. D., Jianjun; Lalli, Jennifer Hoyt; Riffle, Judy S.; Viers, Brent D.; Esker, Alan R. *Langmuir* **2005**, *21*, 1908-1916.

(34) Li, B.; Esker, A. R. *Langmuir* **2007**, *23*, 574-581.

(35) Li, B.; Wu, Y.; Liu, M.; Esker, A. R. *Langmuir* **2006**, *22*, 4902-4905.

(36) Li, B.; Marand, H.; Esker, A. R. *J. Polym. Sci., Part B: Polym. Phys.* **2007**, *45*, 3300-3318.

(37) Deng, J. H., John R.; Polidan, Joseph T.; Kim, Hyong-Jun; Farmer-Creely, Catherine E.; Viers, Brent D.; Esker, Alan R. *Langmuir* **2004**, *20*, 109-115.

(38) Deng, J. P., J. T.; Hottle, J. R.; Farmer-Creely, C. E.; Viers, B. D.; Esker, A. R. *J. Am. Chem. Soc.* **2002**, *124*, 15194-15195.

(39) Ni, S. L., Woojin; Li, Bingbing; Esker, Alan R. *Langmuir* **2006**, *22*, 3672-3677.

(40) Lopez-Montero, I.; Arriaga, L. R.; Monroy, F.; Rivas, G.; Tarazona, P.; Velez, M. *Langmuir* **2008**, *24*, 4065-4076.

(41) Drude, P. *Ann. Physik* **1891**, *279*, 126-157.

(42) Hoenig, D.; Moebius, D. *J. Phys. Chem.* **1991**, *95*, 4590-4592.

(43) Henon, S.; Meunier, J. *Rev. Sci. Instrum.* **1991**, *62*, 936-939.

(44) Bercegol, H.; Gallet, F.; Langevin, D.; Meunier, J. *J. Phys.* **1989**, *50*, 2277-2289.

(45) Moy, V. T.; Keller, D. J.; Gaub, H. E.; McConnell, H. H. *J. Phys. Chem.* **1986**, *90*, 3198-3202.

(46) Dutta, P.; Peng, J. B.; Lin, B.; Ketterson, J. B.; Prakash, M.; Georgopoulos, P.; Ehrlich, S. *Phys. Rev. Lett.* **1987**, *58*, 2228-2231.

(47) Bernett, M. K.; Zisman, W. A. *Macromolecules* **1971**, *4*, 47-53.

(48) Skarlupka, R.; Seo, Y.; Yu, H. *Polymer* **1997**, *39*, 387-392.

(49) Seo, Y.; Skarlupka, R.; Yu, H. *Polym. Eng. Sci.* **1998**, *38*, 741-748.

(50) Gau, C. S.; Yu, H.; Zografi, G. *J. Colloid Interface Sci.* **1994**, *162*, 214-221.

(51) Sohn, D.; Yu, H.; Nakamatsu, J.; Russo, P. S.; Daly, W. H. *J. Polym. Sci., Part B: Polym. Phys.* **1996**, *34*, 3025-3034.

(52) Stenvot, C.; Langevin, D. *Langmuir* **1988**, *4*, 1179-1183.

(53) Safouane, M.; Langevin, D.; Binks, B. P. *Langmuir* **2007**.

(54) Sano, M.; Kawaguchi, M.; Chen, Y. L.; Skarlupka, R. J.; Chang, T.; Zografi, G.; Yu, H. *Rev. Sci. Instrum.* **1986**, *57*, 1158-1162.

(55) Hård, S.; Neuman, R. D. *J. Colloid Interface Sci.* **1981**, *83*, 315-334.

(56) Lucassen-Reynders, E. H.; Lucassen, J. *Adv. Colloid Interface Sci.* **1970**, *2*, 347-395.

(57) Granick, S. *Macromolecules* **1985**, *18*, 1597-1602.

(58) Brooks, C. F.; Fuller, G. G.; Frank, C. W.; Robertson, C. R. *Langmuir* **1999**, *15*, 2450-2459.

(59) Naumann, C. A.; Brooks, C. F.; Fuller, G. G.; Knoll, W.; Frank, C. W. *Langmuir* **1999**, *15*, 7752-7761.

(60) Monroy, F.; Ortega, F.; Rubio, R. *J. Phys. Chem. B* **1999**, *103*, 2061-2071.

(61) Paul, R.; Karabiyik, U.; Swift, M. C.; Esker, A. R. *Langmuir* **2008**, *24*, 5079-5090.

(62) Tabor, D. *J. Colloid Interface Sci.* **1980**, *73*, 294.

(63) Scott, J. C. *Oil on Troubled Waters. A Bibliography on the Effects of Surface-active Films on Surface-wave Motions*; Multi-Science Publishing Co. Ltd: London, 1979.

(64) Dynarowicz-Latka, P.; Dhanabalan, A.; Oliveira, O. N., Jr. *Adv Colloid Interface* **2001**, *91*, 221-293.

(65) Franklin, B. *Phil. Trans.* **1774**, *64*, 445.

(66) Rayleigh, L. J. S. *Proc. Phys. Soc. London* **1890**, *47*, 364.

(67) Pockels, A. *Nature* **1891**, *43*, 437.

(68) Langmuir, I. *T. Faraday Soc.* **1920**, *15*, 62-74.

(69) Langmuir, I. *J. Am. Chem. Soc.* **1917**, *39*, 1848-1906.

(70) Blodgett, K. B.; Langmuir, I. *Phys. Rev.* **1937**, *51*, 964-982.

(71) Blodgett, K. B. *J. Am. Chem. Soc.* **1935**, *57*, 1007-1022.

(72) Kaganer, V. M.; Mohwald, H.; Dutta, P. *Rev. Mod. Phys.* **1999**, *71*, 779-819.

(73) Broniatowski, M.; Sandez Macho, I.; Dynarowicz-Latka, P. *Thin Solid Films* **2005**, *493*, 249-257.

(74) Takiue, T.; Vollhardt, D. *Colloids Surf., A* **2002**, *198-200*, 797-804.

(75) Sauer, B. B.; Yu, H. *Macromolecules* **1989**, *22*, 786-791.

(76) Shuler, R. L.; Zisman, W. A. *J. Phys. Chem.* **1970**, *74*, 1523-1534.

(77) Watanabe, M.; Kosaka, Y.; Oguchi, K.; Sanui, K.; Ogata, N. *Macromolecules* **1988**, *21*, 2997-3003.

(78) Watanabe, M.; Kosaka, Y.; Sanui, K.; Ogata, N.; Oguchi, K.; Yoden, T. *Macromolecules* **1987**, *20*, 452-454.

(79) Lee, W.; Nowak, R. W.; Gardella, J. A. *Langmuir* **2002**, *18*, 2309-2312.

(80) Lee, W.; Gardella, J. A. *Langmuir* **2000**, *16*, 3401-3406.

(81) Mann, E. K.; Henon, S.; Langevin, D.; Meunier, J. *J. Phys. II* **1992**, *2*, 1683-1704.

(82) Noll, W.; Steinbach, H.; Sucker, C. *J. Polym. Sci. Polym. Symp.* **1971**, *No. 34*, 123-139.

(83) Fox, H. W.; Taylor, P. W.; Zisman, W. A. *J. Ind. Eng. Chem.* **1947**, *39*, 1401-1409.

(84) Buzin, A. I.; Godovsky, Y. K.; Makarova, N. N.; Fang, J.; Wang, X.; Knobler, C. M. *J. Phys. Chem. B* **1999**, *103*, 11372-11381.

(85) Fang, J.; Dennin, M.; Knobler, C. M.; Godovsky, Y. K.; Makarova, N. N.; Yokoyama, H. *J. Phys. Chem. B B* **1997**, *101*, 3147-3154.

(86) Granick, S.; Clarson, S. J.; Formoy, T. R.; Semlyen, J. A. *Polymer* **1985**, *26*, 925-929.

(87) Williams, A. A.; Day, B. S.; Kite, B. L.; McPherson, M. K.; Slebodnick, C.; Morris, J. R.; Gandour, R. D. *Chem. Commun.* **2005**, 5053-5055.

(88) Gabrielli, G.; Maddii, A. *J. Colloid Interface Sci.* **1978**, *64*, 19-27.

(89) Esker, A. R.; Mengel, C.; Wegner, G. *Science* **1998**, *280*, 892-895.

(90) Miyashita, T.; (Chisso Corp., Japan). Application: JP, 2007, p 21pp.

(91) Yang, H.; Zhu, P.; Yao, Y.; Gao, X.; Li, R.; Wu, D. *Gaofenzi Xuebao* **2007**, 93-96.

(92) Ievlev, A.; Verkhovskaya, K.; Fridkin, V. *Ferroelectr. Lett.* **2006**, *33*, 147-152.

(93) Tadros-Morgane, R.; Kliem, H. *J. Phys. D: Appl. Phys.* **2006**, *39*, 4872-4877.

(94) Peetla, C.; Graf, K.; Kressler, J. *Colloid. Polym. Sci.* **2006**, *285*, 27-37.

(95) Wegner, G. *Macromol. Chem. Phys.* **2003**, *204*, 347-357.

(96) Ringard-Lefebvre, C.; Baszkin, A. *Langmuir* **1994**, *10*, 2376-2381.

(97) Wilhelmy, L. *Ann. Physik* **1863**.

(98) Li, B., Ph. D. Thesis, Virginia Tech, 2007.

(99) Roberts, G. G. *Langmuir-Blodgett Films*; Plenum: New York, 1990.

(100) Atkins, P.; de Paula, J. *Physical Chemistry; 8 ed.*; W. H. Freeman: New York, 2006.

(101) Pallas, N. R.; Pethica, B. A. *Langmuir* **1985**, *1*, 509-513.

(102) Ni, S., Ph. D. Thesis, Virginia Tech, 2007.

(103) Adam, N. K. *Proc. R. Soc. London, Ser. A* **1922**, *101*, 516-531.

(104) Ruckenstein, E. *Colloids Surf., A* **2001**, *183-185*, 423-427.

(105) Loesche, M.; Sackmann, E.; Moehwald, H. *Ber. Bunsen Ges.* **1983**, *87*, 848-852.

(106) Adam, N. K. *Proc. R. Soc. London, Ser. A* **1922**, *101*, 452-472.

(107) Helm, C. A.; Moehwald, H.; Kjaer, K.; Als-Nielsen, J. *Europhys. Lett.* **1987**, *4*, 697-703.

(108) Dorshow, R. B.; Swofford, R. L. J. *Appl. Phys.* **1989**, *65*, 3756-3759.

(109) Kretzschmar, G. *J.Inf. Rec. Mater.* **1994**, *21*, 335-348.

(110) Langevin, D. *Adv. Colloid Interface Sci.* **2000**, *88*, 209-222.

(111) Sacchetti, M.; Yu, H.; Zografi, G. *Chin. J. Chem. Phys.* **1993**, *99*, 563-566.

(112) Sacchetti, M.; Yu, H.; Zografi, G. *Rev. Sci. Instrum.* **1993**, *64*, 1941-1946.

(113) Sacchetti, M.; Yu, H.; Zografi, G. *Langmuir* **1993**, *9*, 2168-2171.

(114) Brown, A. G.; Thuman, W. C.; McBain, J. W. *J. Coll. Sci.* **1953**, *8*, 491-507.

(115) Inokuchi, K. *Bull. Chem. Soc. Jpn.* **1956**, *29*, 490-497.

(116) Inokuchi, K. *Bull. Chem. Soc. Jpn.* **1955**, *28*, 453-465.

(117) Garrett, W. D.; Zisman, W. A. *J. Phys. Chem.* **1970**, *74*, 1796-1805.

(118) Kim, C. J.; Esker, A. R.; Runge, F. E.; Yu, H. *Macromolecules* **2006**, *39*, 4889-4893.

(119) Kim, C. J.; Yu, H. *Langmuir* **2003**, *19*, 4460-4464.

(120) Vollhardt, D.; Gutberlet, T.; Emrich, G.; Fuhrhop, J. H. *Langmuir* **1995**, *11*, 2661-2668.

(121) Lenk, T. J.; Lee, D. H. T.; Koberstein, J. T. *Langmuir* **1994**, *10*, 1857-1864.

(122) Esker, A. R.; Kim, C.; Yu, H. *Adv. Polym. Sci.* **2007**, *209*, 59-110.

(123) Esker, A. R.; Zhang, L. H.; Sauer, B. B.; Lee, W.; Yu, H. *Colloids Surf., A* **2000**, *171*, 131-148.

(124) Hård, S.; Neuman, R. D. *J. Colloid Interface Sci.* **1987**, *120*, 15-29.

(125) Kim, H.; Lalli, J. H.; Riffle, J. S.; Viers, B. D.; Esker, A. R. *ACS Symp. Ser.* **2007**, *964*, 268-289.

(126) Kawaguchi, M.; Sauer, B. B.; Yu, H. *Macromolecules* **1989**, *22*, 1735-1743.

(127) de Gennes, P.-G. *Scaling Concepts in Polymer Physics*; Cornell University: Ithaca NY, 1979.

(128) Esker, A. R., Ph. D Thesis, University of Wisconsin, 1996.

(129) Teraoka, I. *Polymer Solutions: An Introduction to Physical Properties*; John Wiley & Sons, Inc.: New York, 2002.

(130) Vilanove, R.; Rondelez, F. *Phys. Rev. Lett.* **1980**, *45*, 1502-1505.

(131) Armstrong, N. J.; Chari, K.; Penner, T. L. *J. Colloid Interface Sci.* **1996**, *183*, 617-618.

(132) Auvray, L. *J. Phys., Lett.* **1985**, *46*, 163-172.

(133) Smith, T. *J. Colloid Interface Sci.* **1967**, *23*, 27-35.

(134) Flory, P. J. *Principle of Polymer Chemistry*; Ithaca: New York, 1971.

(135) Le Guillou, J. C.; Zinn-Justin, J. *Phys. Rev. B: Condens. Matter* **1980**, *21*, 3976-3998.

(136) Duplantier, B.; Saleur, H. *Phys. Rev. Lett.* **1987**, *59*, 539-542.

(137) Stephen, M. J. *Mod. Phys. Lett. A* **1973**, *46*, 289-290.

(138) Cai, L. L.; Granick, S. *Adv. Colloid Interface Sci.* **2001**, *94*, 135-150.

(139) Monroy, F.; Ortega, F.; Rubio, R. G. *Phys. Rev. E: Stat. Phys., Plasmas, Fluids, Relat. Interdiscip. Top.* **1998**, *58*, 7629-7641.

(140) Takahashi, A.; Yoshida, A.; Kawaguchi, M. *Macromolecules* **1982**, *15*, 1196-1198.

(141) Thompson, W. *Philos. Mag.* **1871**, *42*, 368.

(142) Langevin, D. *Light Scattering by Liquid Surfaces and Compolementary Techniques*; Marcel Dekker: New York, 1992.

(143) Kramer, L. *J. Chem. Phys.* **1971**, *55*, 2097-2105.

(144) Goodrich, F. C. *J. Phys. Chem.* **1962**, *66*, 1858-1863.

(145) Lee, W., Ph. D Thesis, Virginia Tech, 2008.

(146) Mann, J. A., Jr. *Langmuir* **1985**, *1*, 10-23.

(147) Langevin, D. *J. Colloid Interface Sci.* **1981**, *80*, 412-475.

(148) Earnshaw, J. C.; Grattan, M. W. D.; Lunkenheimer, K.; Rosenthal, U. *J. Phys. Chem. B* **2000**, *104*, 2709-2713.

(149) Earnshaw, J. C.; McGivern, R. C.; McLaughlin, A. C.; Winch, P. J. *Langmuir* **1990**, *6*, 649-660.

(150) Earnshaw, J. C.; Nugent, C. P.; Lunkenheimer, K. *Langmuir* **1997**, *13*, 1368-1370.

(151) Earnshaw, J. C.; Sharpe, D. J. *J. Chem. Soc., Faraday Trans.* **1996**, *92*, 611-618.

(152) Runge, F. E.; Kent, M. S.; Yu, H. *Langmuir* **1994**, *10*, 1962-1970.

(153) Runge, F. E.; Yu, H. *Langmuir* **1993**, *9*, 3191-3199.

(154) Runge, F. E.; Yu, H.; Woermann, D. *Ber. Bunsen Ges.* **1994**, *98*, 1046-1055.

(155) Sauer, B. B.; Chen, Y. L.; Zografi, G.; Yu, H. *Langmuir* **1988**, *4*, 111-117.

(156) Sauer, B. B.; Kawaguchi, M.; Yu, H. *Macromolecules* **1987**, *20*, 2732-2739.

(157) Stokes, G. G. *Cambridge Trans.* **1845**, *8*, 287.

(158) Dorrenstein, R.; Koninkl, R. *Ned. Akad. Wetenshap. Proc.* **1951**, *B54*, 260.

(159) Dorrenstein, R.; Koninkl, R. *Ned. Akad. Wetenshap. Proc.* **1951**, *B54*, 350.

(160) Reynolds, O. *Br. Ass. Rep.* **1880**.

(161) Song, Y.; Lambert, S. M.; Prausnitz, J. M. *Ind. Eng. Chem. Res.* **1994**, *33*, 1047-1057.

(162) Hino, T.; Song, Y.; Prausnitz, J. M. *Macromolecules* **1995**, *28*, 5725-5733.

(163) Zoller, P.; Walsh, D. J. *Standard Pressure-Volume-Temperature Data for Polymers*; Technomic Publishing Co.: Lancaster, 1995.

(164) Brostow, W.; Chiu, R.; Kalogeras, I. M.; Vassilikou-Dova, A. *Mater. Lett.* **2008**, *62*, 3152-3155.

(165) Ruckdaeschel, H.; Rausch, J.; Sandler, J. K. W.; Altstaedt, V.; Schmalz, H.; Mueller, A. H. E. *Mater. Res. Soc. Symp. Proc.* **2007**, *977E*,

(166) Ratna, D. *J. Adhes. Sci. Technol.* **2008**, *22*, 101-110.

(167) Aristeia de Lima, J.; Felisberti, M. I. *Eur. Polym. J.* **2008**, *44*, 1140-1148.

(168) Joshi, M.; Butola, B. S. *J. Macromol. Sci., Polym. Rev.* **2004**, *C44*, 389-410.

(169) Wang, J.; Yang, X. *Colloid. Polym. Sci.* **2008**, *286*, 283-291.

(170) Torrey, J. D.; Bordia, R. K. *J. Am. Cer. Soc.* **2008**, *91*, 41-45.

(171) Meric, G.; Ruyter, I. E. *Acta Odontol. Scand.* **2007**, *65*, 306-312.

(172) Park, Y. J.; Park, S. R.; (Han Yang New Technology Co., Ltd., S. Korea). Application: KR.

(173) Ginzburg, V. V.; Singh, C.; Balazs, A. C. *Macromolecules* **2000**, *33*, 1089-1099.

(174) Haddad, T. S.; Stapleton, R.; Jeon, H. G.; Mather, P. T.; Lichtenhan, J. D.; Phillips, S. *Polym. Prepr. (Am. Chem. Soc., Div. Polym. Chem.)* **1999**, *40*, 496-497.

(175) Pittman, C. U., Jr.; Li, G.; Ni, H. *Macromol. Symp.* **2003**, *196*, 301-325.

(176) Scott, D. W. *J. Am. Chem. Soc.* **1946**, *68*, 356-358.

(177) Baney, R. H.; Itoh, M.; Sakakibara, A.; Suzuki, T. *Chem. Rev.* **1995**, *95*, 1409-1430.

(178) Haddad, T. S.; Viers, B. D.; Phillips, S. H. *J. Inorg. Organomet. Polym Mater.* **2002**, *11*, 155-164.

(179) Leu, C. M.; Chang, Y. T.; Wei, K. H. *Chem. Mater.* **2003**, *15*, 3721-3727.

(180) Leu, C. M.; Reddy, G. M.; Wei, K. H.; Shu, C. F. *Chem. Mater.* **2003**, *15*, 2261-2265.

(181) Leu, C. M.; Chang, Y. T.; Wei, K. H. *Macromolecules* **2003**, *36*, 9122-9127.

(182) Xiao, S.; Nguyen, M.; Gong, X.; Cao, Y.; Wu, H.; Moses, D.; Heeger, A. J. *Adv. Funct. Mater.* **2003**, *13*, 25-29.

(183) Jeon, H. G.; Mather, P. T.; Haddad, T. S. *Polym. Int.* **2000**, *49*, 453-457.

(184) Hoflund, G. B.; Gonzalez, R. I.; Phillips, S. H. *J. Adhes. Sci. Technol.* **2001**, *15*, 1199-1211.

(185) Gonzalez, R. I.; Phillips, S. H.; Hoflund, G. B. *J. Spacecraft Rockets* **2000**, *37*, 463-467.

(186) Zhang, C.; Babonneau, F.; Bonhomme, C.; Laine, R. M.; Soles, C. L.; Hristov, H. A.; Yee, A. F. *J. Am. Chem. Soc.* **1998**, *120*, 8380-8391.

(187) Choi, J.; Kim, S. G.; Laine, R. M. *Macromolecules* **2004**, *37*, 99-109.

(188) Choi, J.; Tamaki, R.; Kim, S. G.; Laine, R. M. *Chem. Mater.* **2003**, *15*, 3365-3375.

(189) Fu, B. X.; Zhang, W.; Hsiao, B. S.; Rafailovich, M.; Sokolov, J.; Johansson, G.; Sauer, B. B.; Phillips, S.; Balnski, R. *High Perform. Polymers* **2000**, *12*, 565-571.

(190) Laine, R. M.; Zhang, C.; Sellinger, A.; Viculis, L. *Appl. Organomet. Chem.* **1998**, *12*, 715-723.

(191) Xu, H.; Kuo, S. W.; Lee, J. S.; Chang, F. C. *Polymer* **2002**, *43*, 5117-5124.

(192) Haddad, T. S.; Lichtenhan, J. D. *Macromolecules* **1996**, *29*, 7302-7304.

(193) Pellice, S. A.; Fasce, D. P.; Williams, R. J. J. *J. Polym. Sci., Part B: Polym. Phys.* **2003**, *41*, 1451-1461.

(194) Soong, S. Y.; Cohen, R. E.; Boyce, M. C. *Polymer* **2007**, *48*, 1410-1418.

(195) Soong, S. Y.; Cohen, R. E.; Boyce, M. C.; Mulliken, A. D. *Macromolecules* **2006**, *39*, 2900-2908.

(196) Kopesky, E. T.; Haddad, T. S.; Cohen, R. E.; McKinley, G. H. *Macromolecules* **2004**, *37*, 8992-9004.

(197) Kopesky, E. T.; Haddad, T. S.; McKinley, G. H.; Cohen, R. E. *Polymer* **2005**, *46*, 4743-4752.

(198) Kopesky, E. T.; Boyes, S. G.; Treat, N.; Cohen, R. E.; McKinley, G. H. *Rheologica Acta* **2006**, *45*, 971-981.

(199) Kopesky, E. T.; McKinley, G. H.; Cohen, R. E. *Polymer* **2006**, *47*, 299-309.

(200) Fu, J.; Shi, L.; Chen, Y. L.; Yuan, S.; Wu, J.; Liang, X.; Zhong, Q. *J. Appl. Polym. Sci.* **2008**, *109*, 340-349.

(201) Voronkov, M. G.; Lavrent'yev, V. I. *Top. Curr. Chem.* **1982**, *102*, 199-236.

(202) Feher, F. J.; Newman, D. A.; Walzer, J. F. *J. Am. Chem. Soc.* **1989**, *111*, 1741-1748.

(203) Frye, C. L.; Collins, W. T. *J. Am. Chem. Soc.* **1970**, *92*, 5586-5588.

(204) Brown, J. F., Jr.; Vogt, L. H., Jr.; Prescott, P. I. *J. Am. Chem. Soc.* **1964**, *86*, 1120-1125.

(205) Brown, J. F., Jr.; Vogt, L. H., Jr. *J. Am. Chem. Soc.* **1965**, *87*, 4313-4317.

(206) Haddad, T. S.; Lichtenhan, J. D. *Macromolecules* **1996**, *29*, 7302-7304.

(207) Pyun, J.; Matyjaszewski, K. *Macromolecules* **2000**, *33*, 217-220.

(208) Mather, P. T.; Jeon, H. G.; Romo-U., A.; Haddad, T. S.; Lichtenhan, J. D. *Macromolecules* **1999**, *32*, 1194-1203.

(209) Tsuchida, A.; Bolln, C.; Sernetz, F. G.; Frey, H.; Muelhaupt, R. *Macromolecules* **1997**, *30*, 2818-2824.

(210) Lee, A.; Lichtenhan, J. D. *Macromolecules* **1998**, *31*, 4970-4974.

(211) Zheng, L.; Farris, R. J.; Coughlin, E. B. *Polym. Prepr. (Am. Chem. Soc., Div. Polym. Chem.)* **2001**, *42*, 885-886.

(212) Wu, J.; Haddad, T. S.; Kim, G.; Mather, P. T. *Macromolecules* **2007**, *40*, 544-554.

(213) Paul, R.; Esker, A. R. *Langmuir* **2006**, *22*, 6734-6738.

(214) Tuteja, A.; Choi, W.; Ma, M.; Mabry, J. M.; Mazzella, S. A.; Rutledge, G. C.; McKinley, G. H.; Cohen, R. E. *Science.* **2007**, *318*, 1618-1622.

(215) Hosaka, N.; Otsuka, H.; Hino, M.; Takahara, A. *Langmuir* **2008**, *24*, 5766-5772.

(216) Mitsuishi, M.; Zhao, F.; Kim, Y.; Watanabe, A.; Miyashita, T. *Chem. Mater.* **2008**, *20*, 4310-4316.

(217) Wilson, K. S.; Goff, J. D.; Riffle, J. S.; Harris, L. A.; St. Pierre, T. G. *Polym. Adv. Technol.* **2005**, *16*, 200-211.

(218) Knight, P. T.; Lee, K. M.; Qin, H.; Mather, P. T. *Biomacromolecules* **2008**, *9*, 2458-2467.

(219) Li, Q.; Hutcheson, S. A.; McKenna, G. B.; Simon, S. L. *J. Polym. Sci., Part B: Polym. Phys.* **2008**, *46*, 2719-2732.

(220) Fu, B. X.; Hsiao, B. S.; White, H.; Rafailovich, M.; Mather, P. T.; Jeon, H. G.; Phillips, S. H.; Lichtenhan, J. D.; Schwab, J. J. *Polym. Int.* **2000**, *49*, 437-440.

(221) Janowski, B.; Pielichowski, K. *Thermochimica Acta* **2008**, *478*, 51-53.

(222) Knischka, R.; Dietsche, F.; Hanselmann, R.; Frey, H.; Muelhaupt, R.; Lutz, P. J. *Langmuir* **1999**, *15*, 4752-4756.

(223) Kobayashi, H. *Makromol. Chem.* **1993**, *194*, 2569-2577.

(224) Kobayashi, H.; Owen, M. J. *Makromol. Chem.* **1993**, *194*, 1785-1792.

(225) Zhang, X.; Huang, Y.; Wang, T.; Liu, L. *J. Appl. Polym. Sci.* **2006**, *102*, 5202-5211.

(226) Deng, J.; Hottle, J. R.; Polidan, J. T.; Kim, H. J.; Farmer-Creely, C. E.; Viers, B. D.; Esker, A. R. *Langmuir* **2004**, *20*, 109-115.

(227) Paul, R.; Karabiyik, U.; Swift, M. C.; Hottle, J. R.; Esker, A. R. *Langmuir* **2008**, *24*, 4676-4684.

(228) Lee, C. W.; Josse, Y.; Hsu, C. H.; Nguyen, T. P. *Eur. Phys. J. Appl. Phys.* **2008**, *42*, 213-218.

(229) Mann, E. K.; Langevin, D. *Langmuir* **1991**, *7*, 1112-1117.

(230) Monroy, F.; Ortega, F.; Rubio, R. G.; Velarde, M. G. *Adv. Colloid Interface Sci.* **2007**, *134-135*, 175-189.

(231) Esker, A. R.; Zhang, L.; Olsen, C. E.; No, K. H.; Yu, H. *Langmuir* **1999**, *15*, 1716-1724.

(232) Johann, R.; Symietz, C.; Vollhardt, D.; Brezesinski, G.; Moehwald, H. *J. Phys. Chem. B* **2000**, *104*, 8512-8517.

(233) Linden, M.; Rosenholm, J. B. *Langmuir* **1995**, *11*, 4499-4504.

(234) Runge, F. E.; Yu, H.; Woermann, D. *Ber. Bunsen Ges.* **1994**, *98*, 1046-1055.

(235) Lodge, T. P. *Science* **2008**, *321*, 50-51.

(236) Batra, A. K.; Aggarwal, M. D.; Edwards, M. E.; Bhalla, A. *Ferroelectrics* **2008**, *366*, 84-121.

(237) Sorathia, U. *Adv. Fire Retar. Mater.* **2008**, 527-572.

(238) Marangoni, R.; Ramos, L.; Wypych, F. *J. Colloid Interface Sci.* **2009**, *330*, 303-309.

(239) Yogeswaran, U.; Thiagarajan, S.; Chen, S. *Sensors* **2008**, *8*, 7191-7212.

(240) Schaefer, D. W.; Justice, R. S. *Macromolecules* **2007**, *40*, 8501-8517.

(241) Lichtenhan, J. D. *Comments Inorg. Chem.* **1995**, *17*, 115-130.

(242) Schwab, J. J.; Lichtenhan, J. D. *Appl. Organomet. Chem.* **1998**, *12*, 707-713.

(243) Pielichowski, K.; Njuguna, J.; Janowski, B.; Pielichowski, J. In *Supramolecular Polymers Polymeric Betains Oligomers* 2006, p 225-296.

(244) Zhang, H.; Kulkarni, S.; Wunder, S. L. *J. Phys. Chem. B* **2007**, *111*, 3583-3590.

(245) Haddad, T. S.; Viers, B. D.; Phillips, S. H. *J. Inorg. Organomet. Polym.* **2002**, *11*, 155-164.

(246) Choi, J.; Harcup, J.; Yee, A. F.; Zhu, Q.; Laine, R. M. *J. Am. Chem. Soc.* **2001**, *123*, 11420-11430.

(247) Wei, J. H.; Coffey, D. C.; Ginger, D. S. *J. Phys. Chem. B FIELD Full Journal Title:Journal of Physical Chemistry B* **2006**, *110*, 24324-24330.

(248) Lee, J.; Sung, S.; Park, J. *Synth. Met.* **2001**, *117*, 271-272.

(249) Jiang, X.; Ding, J.; Kumar, A. *J. Membr. Sci.* **2008**, *323*, 371-378.

(250) Peterson, S. L.; McDonald, A.; Gourley, P. L.; Sasaki, D. Y. *J. Biomed. Mater. Res., Part A* **2005**, *72A*, 10-18.

(251) Yan, W.; Hsiao, V. K. S.; Zheng, Y.; Shariff, Y. M.; Gao, T.; Huang, T. *Thin Solid Films* **2009**, *517*, 1794-1798.

(252) Lotters, J. C.; Olthuis, W.; Veltink, P. H.; Bergveld, P. *J. Micromech. Microeng.* **1997**, *7*, 145-147.

(253) Zhao, H.; Fu, Z.; Li, P. B.; Zhao, Y. Z. *J. Adhes.* **2007**, *83*, 1003-1029.

(254) Chan, E. P.; Ahn, D.; Crosby, A. J. *J. Adhes.* **2007**, *83*, 473-489.

(255) Ngaile, G.; Botz, F. *J. Tribol.* **2008**, *130*, 021801/021801-021801/021807.

(256) Morrison, E. D.; Johnson, R. D.; Besse, M. l. E.; Man, V.; (Ecolab Inc., USA). Application: US, 2007, p 17pp.

(257) James, V. *Pitture e Vernici, Eur. Coat.* **2007**, *83*, 65-72.

(258) Urayama, K.; Miki, T.; Takigawa, T.; Kohjiya, S. *Chem. Mater.* **2004**, *16*, 173-178.

(259) Jarvis, N. L. *J. Phys. Chem.* **1966**, *70*, 3027-3033.

(260) Braslau, A.; Deutsch, M.; Pershan, P. S.; Weiss, A. H.; Als-Nielsen, J.; Bohr, J. *Phys. Rev. Lett.* **1985**, *54*, 114-117.

(261) Mazur, E.; Chung, D. *Physica A* **1987**, *147A*, 387-406.

(262) Sohn, B. H.; Cohen, R. E. *Chem. Mater.* **1997**, *9*, 264-269.

(263) Tamai, H.; Sakurai, H.; Hirota, Y.; Nishiyama, F.; Yasuda, H. *J. Appl. Polym. Sci.* **1995**, *56*, 441-449.

(264) Bulte, J. W.; Brooks, R. A.; Moskowitz, B. M.; Bryant, L. H., Jr.; Frank, J. A. *Magn Reson Med* **1999**, *42*, 379-384.

(265) Ivkov, R.; S., D.; Daum, W.; R., F. A.; C., G. R.; S., N. V.; L., D. G. *Clin Cancer Res* **2005**, *11*, 7093s-7103s.

(266) Vorotnikova, E.; Ivkov, R.; Foreman, A.; Tries, M.; Braunhut, S. J. *Int. J. Radiat. Biol.* **2006**, *82*, 549-559.

(267) Kondo, A.; Fukuda, H. *J. Ferment. Bioeng.* **1997**, *84*, 337-341.

(268) Needham, D.; McIntosh, T. J.; Simon, S. A.; Zhelev, D. *Curr. Opin. Colloid Interface Sci.* **1998**, *3*, 511-517.

(269) Mendenhall, G. D.; Geng, Y.; Hwang, J. *J. Colloid Interface Sci.* **1996**, *184*, 519-526.

(270) Pardoe, H.; Chua-anusorn, W.; St. Pierre, T. G.; Dobson, J. *J. Magn. Magn. Mater.* **2001**, *225*, 41-46.

(271) Harris, L. A.; Goff, J. D.; Carmichael, A. Y.; Riffle, J. S.; Harburn, J. J.; St. Pierre, T. G.; Saunders, M. *Chem. Mater.* **2003**, *15*, 1367-1377.

(272) Liu, X.; Kaminski, M. D.; Riffle, J. S.; Chen, H.; Torno, M.; Finck, M. R.; Taylor, L.; Rosengart, A. J. *J. Magn. Magn. Mater.* **2007**, *311*, 84-87.

(273) Woodward, R. C.; Heeris, J.; St. Pierre, T. G.; Saunders, M.; Gilbert, E. P.; Rutnakornpituk, M.; Zhang, Q.; Riffle, J. S. *J. Appl. Crystallogr.* **2007**, *40*, s495-s500.

(274) Zhang, Q.; Thompson, M. S.; Carmichael-Baranauskas, A. Y.; Caba, B. L.; Zalich, M. A.; Lin, Y.; Mefford, O. T.; Davis, R. M.; Riffle, J. S. *Langmuir* **2007**, *23*, 6927-6936.

(275) Dumazet-Bonnamour, I.; Le Perchec, P. *Colloids Surf., A* **2000**, *173*, 61-71.

(276) Wormuth, K. *J. Colloid Interface Sci.* **2001**, *241*, 366-377.

(277) Moeser, G. D.; Roach, K. A.; Green, W. H.; Laibinis, P. E.; Hatton, T. A. *Ind. Eng. Chem. Res.* **2002**, *41*, 4739-4749.

(278) Rutnakornpituk, M.; Thompson, M. S.; Harris, L. A.; Farmer, K. E.; Esker, A. R.; Riffle, J. S.; Connolly, J.; St. Pierre, T. G. *Polymer* **2002**, *43*, 2337-2348.

(279) Stevenson, J. P.; Rutnakornpituk, M.; Vadala, M.; Esker, A. R.; Charles, S. W.; Wells, S.; Dailey, J. P.; Riffle, J. S. *J. Magn. Magn. Mater.* **2001**, *225*, 47-58.

(280) Wilson, K. S.; Goff, J. D.; Riffle, J. S.; Harris, L. A.; St. Pierre, T. G. *Polym. Adv. Technol.* **2005**, *16*, 200-211.

(281) Sahoo, Y.; Pizem, H.; Fried, T.; Golodnitsky, D.; Burstein, L.; Sukenik, C. N.; Markovich, G. *Langmuir* **2001**, *17*, 7907-7911.

(282) Sun, S.; Zeng, H. *J. Am. Chem. Soc.* **2002**, *124*, 8204-8205.

(283) Dubault, A.; Veyssie, M.; Liebert, L.; Strzelecki, L. *Nature* **1973**, *245*, 94-95.

(284) Brooks, C. F.; Thiele, J.; Frank, C. W.; O'Brien, D. F.; Knoll, W.; Fuller, G. G.; Robertson, C. R. *Langmuir* **2002**, *18*, 2166-2173.

(285) Bruno, F. F.; Akkara, J. A.; Samuelson, L. A.; Kaplan, D. L.; Mandal, B. K.; Marx, K. A.; Kumar, J.; Tripathy, S. K. *Langmuir* **1995**, *11*, 889-892.

(286) Bubeck, C. *Thin Solid Films* **1988**, *160*, 1-14.

(287) Matmour, R.; Joncheray, T. J.; Gnanou, Y.; Duran, R. S. *J. Colloid Interface Sci.* **2007**, *311*, 315-321.

(288) Tsougeni, K.; Tserepi, A.; Gogolides, E. *Microelectron. Eng.* **2007**, *84*, 1104-1108.